

UNIVERSITÀ DEGLI STUDI DI NAPOLI FEDERICO II
Consiglio Nazionale delle Ricerche

Scuola Politecnica e delle Scienze di Base
Area Didattica di Scienze Matematiche Fisiche e
Naturali



Dipartimento di Biologia
Istituto per i Sistemi Agricoli e Forestali del Mediterraneo

Dottorato in
Biologia

XXXII CICLO
Phd Thesis

***ANTHROPOGENIC METHANE EMISSIONS IN CAMPANIA
REGION***

Tutor:

Prof.ssa Carmen Arena

Co-Tutor:

Dott.ssa Daniela Famulari

Dott. Vincenzo Magliulo

Candidato:

Daniele Gasbarra

Table of contents

Introduction.....	1
Chapter 1: Materials and Methods.....	10
1.1 Modified mass balance approach.....	10
1.2 The development of the Sky Arrow ERA airborne platform.....	11
1.3 The Eddy Covariance technique.....	14
1.4 The Borgo Cioffi field station.....	16
Chapter 2: The SKY Arrow ERA: a powerful instrument for the parameterization of meteorological and chemical models.....	20
2.1 Performance Analysis of Planetary Boundary Layer Parameterization Schemes in WRF Modeling Set Up over Southern Italy	21
2.2 Atmospheric Dynamics and Ozone Cycle during Sea Breeze in a Mediterranean Complex Urbanized Coastal Site.....	23
Chapter 3: Estimate of methane emissions from landfills: an approach based on airborne measurements.....	66
3.1 Locating and quantifying multiple landfills methane emission using aircraft data.....	66
Chapter 4: Agricultural GHGs measurements in Campania Region	
4.1 Greenhouse gases exchange over <i>Lolium italicum</i> and <i>Sorghum bicolor</i> crops.....	83
4.1.1 <i>Lolium italicum</i> crop.....	85
4.1.2 <i>Sorghum bicolor</i> crop.....	88
4.1.3 Discussion.....	95
4.2 Study of entericCH ₄ emission from water buffalo production in the Mediterranean area.....	96
4.2.1 Study site and method.....	98
4.2.2 Results.....	101
Conclusions.....	136

Introduction

Since the beginning of industrial age, human activities related to fossil fuel extraction and use, biomass burning and land use change have increased the globally averaged atmospheric carbon dioxide (CO₂) and methane (CH₄) concentration. Despite the smaller atmospheric concentration and the shorter atmospheric lifetime respect to CO₂, increasing CH₄ concentration in the atmosphere could have a substantial impact on the climate due its global warming potential that has been estimated 30 times larger than CO₂.

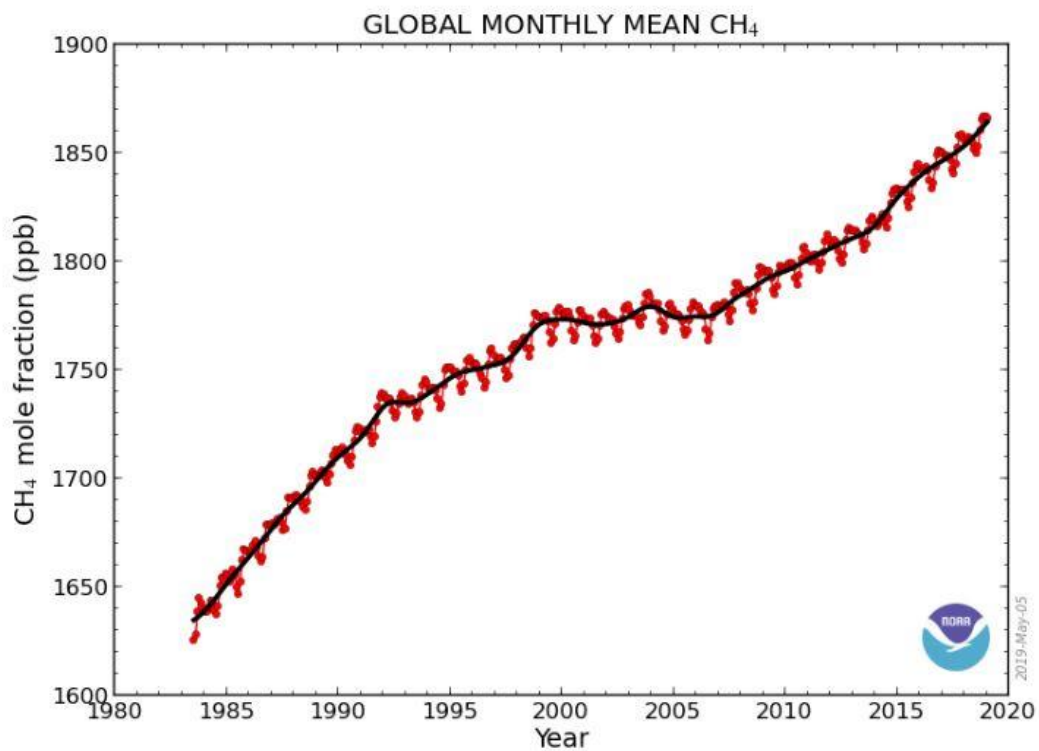


Figure 1 Globally-averaged monthly mean atmospheric methane mixing ratio

Last IPCC estimates has shown that together CO₂ and CH₄ account for more than 93% of the increase of radiative forcing by anthropogenic greenhouse gases. CH₄ is emitted naturally by wetlands, wildfires, grassland, coal beds and lake. The human anthropogenic sources of CH₄ emissions include municipal solid waste landfills, rice paddies, coal mining, oil and gas drilling and processing, cattle ranching, manure management, agricultural products and wastewater treatment. CH₄ concentration in the atmosphere remained stable for thousands of year before it began to rise in 19th

century. Globally averaged CH₄ surface concentrations have risen from 722 ± 25 ppb in 1750 to 1803 ± 2 ppb by 2011, over that time scale the rise is due predominantly to changes in anthropogenic-related CH₄ emissions [1]. Human activities associated with the agricultural and the energy sectors are the main sources of anthropogenic methane through enteric fermentation of livestock (17%), rice cultivation (7%), for the former, and coal mining (7%), oil and gas exploitation (12%), and waste management (11%), for the latter. On the other hand, natural sources of methane include wetlands (34 %), termites (4%), methane hydrates and ocean (3%) along with biomass burning (4%), a source of atmospheric methane that is both natural and anthropogenic [2],[3]. Methane is depleted at the surface by consumption by soil bacteria, in the marine boundary layer by reaction with chlorine atoms, in the troposphere by oxidation with the hydroxyl radical (OH), and in the stratosphere by reaction with chlorine atoms, O(1D), OH, and by photodissociation [4]. Due to its sinks, methane has important chemical impacts on the atmospheric composition. In the troposphere, oxidation of methane is a major regulator of OH [5] and is a source of hydrogen and of tropospheric ozone precursors such as formaldehyde and carbon monoxide [6]. In the stratosphere, methane plays a central role as a sink for chlorine atoms and as a source of stratospheric water vapour, an important driver of decadal global surface climate change [7]. Given its atmospheric lifetime, and its impact on radiative forcing and on atmospheric chemistry, methane is one of the primary targets for regulation of greenhouse gas emissions and climate change mitigation.

Several attempts and methodologies have been implemented and tested for the retrieval of CH₄ emissions from different environments. Flux measurements from enclosure techniques [8] consist in monitoring the increase in concentration of the target gas inside chambers placed in different locations. This technique has the big advantage that almost any terrestrial environment is suitable for being sampled, but it also presents some limitations: both temporally (discontinuous monitoring times, typically lasting from minutes to hours) and in terms of spatial coverage (0.5-1 m² surface covered by the enclosure), therefore they may not be fully representative of the whole study area. For example landfills are characterized by a large spatial heterogeneity in surface fluxes; CH₄ may escape directly into the atmosphere through cracks and broken pipes, causing large uncertainties in the flux estimates, even if based

on a large number of single measurements, as some emission pathways may remain undetected [9].

The Atmospheric Tracer Method (ATM) can be used to circumvent spatial heterogeneity by releasing a tracer gas from the emitting surface. This method is based on the assumption that a tracer gas released at a methane emission source will disperse in the atmosphere in the same way as the emitted methane. Assuming the air is well mixed, the methane emission rate can be calculated as a function of the ratio of the downwind measurements of methane and tracer gas concentrations. This method allows the integration of the fluxes in the whole domain, and is generally used in situations with no interfering or patchy sources [10].

Atmospheric dispersion models are considered useful tools to determine the emission strength of area sources. They can be coupled with point measurements and employed in forward or backward configuration to respectively validate the estimated emission or to derive source-receptor relationship [11]. After measuring the source strength, a Lagrangian dispersion model can be used to simulate the dispersion and the transport of particles in forward mode by knowing meteorological and turbulent information [12].

Eddy covariance (EC) is a well-established micrometeorological method for any trace gas net flux calculation, based on the covariance between vertical wind speed and gas concentration. This technique requires fast measurements of wind speed and gas concentration, typically 10 Hz, and fluxes are generally calculated at half-hour resolution. EC is preferable to enclosure techniques because it spatially integrates fluxes over larger areas corresponding to the footprint of the incoming turbulent atmospheric flow, and can provide a continuous time-series of emission measurements. For these reasons, EC would provide a means to greatly improve our understanding of the processes controlling greenhouse gas emissions in complex environments such as landfills [13][14]. However, the hypotheses for the application of EC may be quite constraining for sampling over landfills. EC results may be compromised e.g. by the complex orography of the study area, affecting the extension of the fetch, by the patchiness of the sources within the fetch, and by the low turbulent mixing in conditions of atmospheric stability.

Alternative techniques like the mass balance approach are often used to estimate the emissions from large area sources, e.g. cities or oil sands. A great number of studies reported different methods for the application of mass balance technique based on airborne measurements: estimated CH₄ and CO₂ emissions from the city of Indianapolis has been obtained by flying long horizontal transects at different heights perpendicular to the wind direction downwind of the city [15][16]. Emissions are calculated using wind speed and the difference between gas concentration measured in the plume and background concentration. Another approach is the so called “box method”, that is accomplished by flying a circle or a polygon around the emission source and repeating the pattern at different heights, in such a way that the mixing ratio of the species of interest can be interpolated between multiple heights to reconstruct a two-dimensional screen surrounding the emission area. Air pollutants emission rate over Alberta oil sands operations [17] has been inferred by flying a square at multiple heights surrounding the emission area. Emissions were then calculated by applying the divergence theorem in the control volume generated by the flight path. CO₂ emissions from Rome have been evaluated by flying circles around the city at three different heights and applying the mass conservation equation at the box edge surfaces and top surface [18]. A new airborne method to identify and quantify trace gas emissions has been deployed by performing an aircraft route pattern that generate a virtual cylinder around the source, and using Reynolds decomposition for the scalar concentrations, along with Gauss’s theorem to estimate the flux divergence through that cylinder [19]. This method accounted for the turbulent dispersion of the smaller scale plumes, which are generally ignored in the average mass balance approach.

In this work an estimation of anthropogenic CH₄ emission from the Campania region is presented by studying two different anthropic ecosystems that can be considered most relevant sources for the whole regional territory: landfills, which account for a percentage of about 45% of the total regional emission, and agricultural (crops and livestock activities) which account for a percentage of about 35% [20].

Campania region has been characterized since the 1980s by a reckless waste management that led to several waste crisis especially between the provinces of Naples and Caserta. The countryside of this area is well known in the media: urban waste combined with industrial toxic waste have been dumped and spilled in old quarries or

buried without any control or safety measure. This led to a patchy presence of waste and associated biogas sources, with several emitting hot spots on heterogeneous landscape. Several authorized site for the waste storage, equipped with pipes and tubes for the biogas recovery, has been destroyed by arsons causing release of additional contaminants into the atmosphere and posing serious health risk to citizens [21].

Despite several environmental issue associated with waste pollution events, agriculture is playing a very important role in regional CH₄ emissions, as it is one of the main sectors for the economic development of the region. Just the production of buffalo mozzarella, the typical cheese originating from this region, is providing a major economic activity, counting around 300k heads (in 2019) farmed regionally. Water buffalo farms are spread through the whole regional territory especially concentrated in two provinces, Caserta (near Naples), and Salerno, in the Southern part of the region. The dairy industry connected with the production of typical products thus need to be sustained by hundreds of farm providing huge CH₄ release from animals through enteric fermentation. Moreover, the slurry produced from farms is widely used as fertilizer in the fertile volcanic lands at the foothills of Mount Vesuvius and in the Sele Plain, producing CH₄ emission both during the stocking phase and in the fertilization processes.

In this work two different approaches were deployed for the retrievals of CH₄ fluxes. Landfills emissions are characterized by large heterogeneity, with several hot-spots emitting with different magnitude and spread over the whole landfills domain. In this context, point measurements cannot provide a reliable picture of the emission field and also the footprint of EC measurements cannot be considered representative for the whole study domain. Aircraft measurements could be considered a powerful instrument to overcome this issue, covering the entire study domain. For this purpose a novel biogas payload for airborne CH₄ measurements has been developed and it is described in Chapter 1. In chapter 2 has shown how airborne measurements could be a useful tool for the parameterization of meteorological and dispersion models at local/regional scale. These inputs are of fundamental importance for the reproduction of meteorological conditions and pollution patterns in complex orography as the urbanized coast of Campania region. The mass balance approach combined with Gaussian dispersion model (described in Chapter 3) is recognized as a suitable

approach to infer landfills emission from airborne measurements and to make an apportionment between different sources.

On the other hand, GHGs emissions from agricultural field, generally show a uniform emission pattern and EC technique (described in Chapter 1) could provide a reliable estimates of the emissions. The proximity of the measurements site with a water buffalo farm allowed also the investigations of CH₄ enteric emissions using measurements coupled with Lagrangian simulation (Chapter 4).

Specific objectives of this work are focussed on the evaluation of such CH₄ sources through measurements and modelling, from local to regional scale, as listed below:

Landfill Source

- Testing of a parameterization of meteorological and chemical dispersion models at a regional scale using aircraft observations (Chapter 2)
- The experimental development of an airborne biogas payload for the Sky Arrow ERA aircraft and measurements over the landfill environment (Chapter 3)
- The development and application of an airborne mass balance algorithm to provide an emission apportionment between different landfills closely located among them (Chapter 3)
- Evaluate methane (and other GHGs) fluxes from different crops located in typical climate of the Mediterranean basin , cultivated in rotation over different seasons
- Evaluate the contribution of CH₄ emissions from livestock by using Lagrangian simulations applied on a water buffalo farm, by using measurements taken on site.

BIBLIOGRAPHY

- [1] Myhre, G., D. Shindell, F.-M. Bréon, W. Collins, J. Fuglestvedt, J. Huang, D. Koch, J.-F. Lamarque, D. Lee, B. Mendoza, T. Nakajima, A. Robock, G. Stephens, T. Takemura and H. Zhang, 2013: Anthropogenic and Natural Radiative Forcing Supplementary Material. In: Climate Change 2013: The Physical Science Basis. Contribution of Working Group I to the Fifth Assessment Report of the Intergovernmental Panel on Climate Change. Available from www.climatechange2013.org and www.ipcc.ch.
- [2] Turner, A. J., Jacob, D. J., Wecht, K. J., Maasakkers, J. D., Lundgren, E., Andrews, A. E., Biraud, S. C., Boesch, H., Bowman, K. W., Deutscher, N. M., Dubey, M. K., Griffith, D. W. T., Hase, F., Kuze, A., Notholt, J., Ohyama, H., Parker, R., Payne, V. H., Sussmann, R., Sweeney, C., Velazco, V. A., Warneke, T., Wennberg, P. O., and Wunch, D.: Estimating global and North American methane emissions with high spatial resolution using GOSAT satellite data, *Atmos. Chem. Phys.*, 15, 7049–7069, <https://doi.org/10.5194/acp-15-7049-2015>, 2015.
- [3] Chen, Y.-H., and Prinn, R. G. (2006), Estimation of atmospheric methane emissions between 1996 and 2001 using a three-dimensional global chemical transport model, *J. Geophys. Res.*, 111, D10307, doi:10.1029/2005JD006058.
- [4] Kirschke, Stefanie & Bousquet, Philippe & Ciais, Philippe & Saunois, M. & Canadell, J.G. & Dlugokencky, E.J. & Bergamaschi, Peter & Bergmann, Daniel & Blake, D.R. & Bruhwiler, L. & Cameron-Smith, Philip & Castaldi, Simona & Chevallier, Frederic & Feng, Liang & Fraser, Annemarie & Heimann, Martin & Hodson, E. & Houweling, Sander & Josse, B. & Zeng, Guang. (2013). Three decades of global methane sources and sinks. *Nature Geoscience*. 6. 813-823. [10.1038/ngeo1955](https://doi.org/10.1038/ngeo1955).
- [5] Lelieveld, J., Peters, W., Dentener, F. J., and Krol, M. C., Stability of tropospheric hydroxyl chemistry, *J. Geophys. Res.*, 107(D23), 4715, doi:10.1029/2002JD002272, 2002.
- [6] Montzka, S., Dlugokencky, E. & Butler, J. Non-CO₂ greenhouse gases and climate change. *Nature* 476, 43–50 (2011). <https://doi.org/10.1038/nature10322>

- [7] Solomon Susan, Rosenlof, Karen H.Portmann, Robert W.Daniel, John S.Davis, Sean M. Sanford, Todd J.A Plattner, Gian-Kasper Plattner, Contributions of Stratospheric Water Vapor to Decadal Changes in the Rate of Global Warming, 2010, *J Science*, 1219-1223, Volume 327, <https://doi.org/10.1126/science.1182488>
- [8] Czepiel, P.M., Mosher, B., Harriss, R.C., Shorter, J.H., McManus, J.B., Kolb, C.E., Allwine, E., Lamb, B.K., 1996. Landfill methane emissions measured by enclosure and atmospheric tracer methods. *J. Geophys. Res.* 101 (D11), 16711.
- [9] Borjesson, G., Danielsson, A., Svensson, B.H., 2000. Methane fluxes from a Swedish landfill determined by geostatistical treatment of static chamber measurements. *Environ. Sci. Technol.* 34 (18), 4044e4050.
- [10] Lamb, B.K., Mcmanus, J.B., Shorter, J.H., Kolb, C.E., Mosher, B., Harriss, R.C., Allwine, E., Blaha, D., Howard, T., Guenther, A., et al., 1995. Development of atmospheric tracer methods to measure methane emissions from natural gas facilities and urban areas. *Environ. Sci. Technol.* 29 (6), 1468e1479.
- [11] Flesch, T. K., Wilson, J. D., and Yee, E.: 1995, 'Backward-Time Lagrangian Stochastic Dispersion Models, and their Application to Estimate Gaseous Emissions', *J. Appl. Meteor.* **34**, 1320–1332.
- [12] Marlies Hrad, Erwin Binner, Martin Piringer, Marion Huber-Humer, Quantification of methane emissions from full-scale open windrow composting of biowaste using an inverse dispersion technique, *Waste Management*, Volume 34, Issue 12, 2014, Pages 2445-2453, ISSN 0956-053X, <https://doi.org/10.1016/j.wasman.2014.08.013>.
- [13] Rinne, J., Pihlatie, M., Lohila, A., Thum, T., Aurela, M., Tuovinen, J.-P., Laurila, T., Vesala, T., 2005. Nitrous oxide emissions from a municipal landfill. *Environ. Sci. Technol.* 39 (20), 7790e7793.
- [14] Schroth, M.H., Eugster, W., Gomez, K.E., Gonzalez-Gil, G., Niklaus, P.A., Oester, P., 2012. Above and below ground methane fluxes and methanotrophic activity in a landfill-cover soil. *Waste Manag.* 32 (5), 879e889.

- [15] Mays, K., Shepson, P., Stirm, B., 2009. Aircraft-based measurements of the carbon footprint of Indianapolis- supplementary material. *Environ. Sci. Technol.* 43 (20), 7816e7823.
- [16] Cambaliza, M.O.L., Shepson, P.B., Bogner, J., Caulton, D.R., Stirm, B., Sweeney, C., Montzka, S.A., Gurney, K.R., Spokas, K., Salmon, O.E., et al., 2015. Quantification and source apportionment of the methane emission flux from the city of Indianapolis. *Elem. Sci. Anthr.* 3, 000037.
- [17] Mays, K., Shepson, P., Stirm, B., 2009. Aircraft-based measurements of the carbon footprint of Indianapolis- supplementary material. *Environ. Sci. Technol.* 43 (20), 7816e7823.
- [18] Cambaliza, M.O.L., Shepson, P.B., Bogner, J., Caulton, D.R., Stirm, B., Sweeney, C., Montzka, S.A., Gurney, K.R., Spokas, K., Salmon, O.E., et al., 2015. Quantification and source apportionment of the methane emission flux from the city of Indianapolis. *Elem. Sci. Anthr.* 3, 000037.
- [19] Conley, S., Faloon, I., Mehrotra, S., Suard, M., Lenschow, D. H., Sweeney, C., Herndon, S., Schwietzke, S., Pétron, G., Pifer, J., Kort, E. A., and Schnell, R.: Application of Gauss's theorem to quantify localized surface emissions from airborne measurements of wind and trace gases, *Atmos. Meas. Tech.*, 10, 3345–3358, <https://doi.org/10.5194/amt-10-3345-2017>, 2017.
- [20] ISPRA CAMPANIA, *Piano regionale di risanamento e mantenimento della qualità dell'aria*, http://www.sito.regione.campania.it/burc/pdf06/burcsp27_10_06/del167_06allpiano.pdf
- [21] Giulia Carriero, Luisa Neri, Daniela Famulari, Sara Di Lonardo, Daniela Piscitelli, Antonio Manco, Andrea Esposito, Adriano Chirico, Osvaldo Facini, Sandro Finardi, Gianni Tinarelli, Rossella Prandi, Alessandro Zaldei, Carolina Vagnoli, Piero Toscano, Vincenzo Magliulo, Paolo Ciccioli, Rita Baraldi, Composition and emission of VOC from biogas produced by illegally managed waste landfills in Giugliano (Campania, Italy) and potential impact on the local population, *Science of The Total*

Environment, Volumes 640–641, 2018, Pages 377-386, ISSN 0048-9697,
<https://doi.org/10.1016/j.scitotenv.2018.05.318>.

Chapter 1

Materials and Methods

1.1 Modified mass balance approach

In this work a novel mass balance approach has been developed for the retrievals of CH₄ emission from landfills. Landfills are usually characterized by complex orography with several emissive hot-spots that may lead to different CH₄ emission rates along the landfill domain. The eddy covariance measurements are integrated over a footprint of few hundred meters, therefore cannot be representative of the whole study domain, because of the inhomogeneous, patchy emission sources characterising these landfills. To overcome this issue, the evaluation of emissions from these landfills were performed using aircraft data in order to cover the entire study domain. An improvement of the existing mass balance approaches has been developed to make an emission apportionment between different sources closely located among them. The study area is a 5x5 km square domain in which four different landfills are located. The previously described mass balance approaches all measure the total emission of a study area enclosed by a control volume. In this case instead, the presence of multiple spatial sources within the same area poses a new challenge: to split the total emissions into individual ones and quantify them. An improvement to the mass balance algorithm uses a mass balance approach based on the box method using airborne measurements, coupled with a simple steady-state Gaussian dispersion model to retrieve an emission partitioning between different sources. This new approach allows to discriminate the emissions of the four landfills, and it is deployable in many similar contexts since landfills are usually characterized by irregular shape and several adjacent surfaces with possibly non-homogeneous waste age and composition. By flying gridded trajectories at different heights above the landfills, it is possible to reconstruct methane mixing ratios and wind vector, both at the edges and inside the sampled box volume, driving an optimization algorithm for individual sources separation.

1.2 The development of the Sky Arrow ERA airborne platform

Research aircraft are becoming increasingly important for biosphere and atmosphere research. Instrumented aerial platforms permit the efficient investigation of problems having spatial distributions ranging vertically well beyond the Planetary Boundary Layer (PBL) and horizontally up to hundreds of kilometres. Research aircrafts can assess the spatial variability of atmospheric properties over relatively large distances in a short period of time, integrating ground observations over large areas. This is of great importance especially for heterogeneous surfaces and complex terrains.

The Sky Arrow ERA (Environmental Research Aircraft) is a small aircraft produced by Iniziative Industriali Italiane (Rome, Italy) equipped with sensors to measure three-dimensional wind and turbulence, together with gas concentrations and other atmospheric parameters at a frequency of 50 Hz. It is a two seater aircraft made of carbon fiber and epoxy resin, powered by a 100 HP engine, with a wingspan of 9.6 m, length of 8.2 m, wing area of 13.1 m², and a maximum take-off mass of 650 kg. The aircraft has a cruise flight speed of 85 knots with an endurance of 3.5 h, covering flight distances of up to 400 km. Operating altitudes can range from 10 m above ground level to more than 3500 m a.s.l. The aircraft is equipped with the Mobile Flux Platform (MFP), developed by NOAA (National Oceanic and Atmospheric Administration) which consists of a set of sensors for atmospheric measurements. The MFP is designed to correct wind measurements relative to the aircraft that are performed by the BAT probe, for the movement of the aircraft and the sensor with respect to the Earth [1],[2]. Those corrections are made using a combination of GPS (Global Positioning System) velocity measurements and data from two sets of three-dimensional accelerometers mounted at the centre of gravity of the aircraft and in the centre of the pressure sphere. For this, a commercial differential GPS (Novatel, U.S.A., mod. RT20) is used in combination with a four antenna vectorial GPS system (Trimble, U.S.A., mod. Tans Vector) to measure three-dimensional ground speed, pitch, roll and yaw angles of the aircraft up to 10 Hz. A subsequent blending of GPS and accelerometer signals provides attitude and velocity data up to 50 Hz. Accordingly, atmospheric turbulence is measured fifty times per second that translates to a horizontal spacing of 0.7 m while the aircraft flies at 35 m s⁻¹ ground speed. In this way, eddies of wavelengths larger than 1.4 m can be resolved.

Scalars are also measured during flight operations. A microbead (thermocouple) temperature sensing element with a nominal time response of 0.02 s located at the centre of the pressure sphere is used to measure air temperature fluctuations at high frequency. A platinum resistance thermometer is used as a slow response air temperature reference.

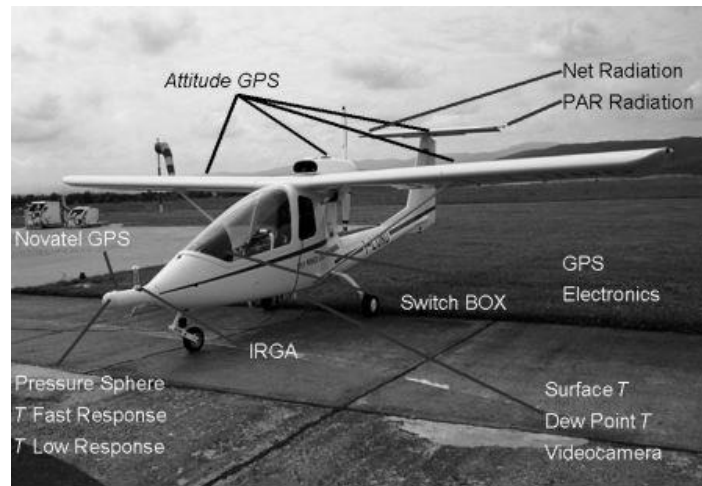


Figure 1.1 The Sky Arrow ERA

Atmospheric densities of CO₂ and water vapour are recorded at 50 Hz by an open path infrared gas analyser (Licor, U.S.A., mod. Li7500) installed on the aircraft nose (fig. 1). Low frequency air moisture measurements are made using a chilled mirror dew point sensor (EdgeTech, U.S.A., mod. 200). A net radiometer (Rebs, U.S.A., mod. Q*7) and upward and downward looking PAR (Photosynthetically Active Radiation) radiometers (Licor, U.S.A., mod. 200 s) are mounted on the aircraft horizontal stabilizer. Surface temperature is also measured at low frequency (1 Hz), using an infrared thermometer (Everest, U.S.A., mod. 4000.4 GH). The MFP platform has been developed leading to the creation of two different payloads: the air quality payload and the biogas payload.

The air quality payload consist of a series of sensors added to the MFP platform for the monitoring of most common pollutants. Ozone and NO_x measurements are performed respectively with 2BTech mod.202 and with 2BTech mod. 405 (2BTechnologies, Boulder, USA).



Figure 1.2 *The air quality payload on board the Sky Arrow ERA*

For particulate matter measurements an iso-kinetic inlet, located along the aircraft fuselage, has been connected to an optical particle counter Grimm mod. 1.109 (Grimm INC, Ainring, Deutschland) for the retrieval of particles densities in 32 size channels from 0.32 to 32 μm .

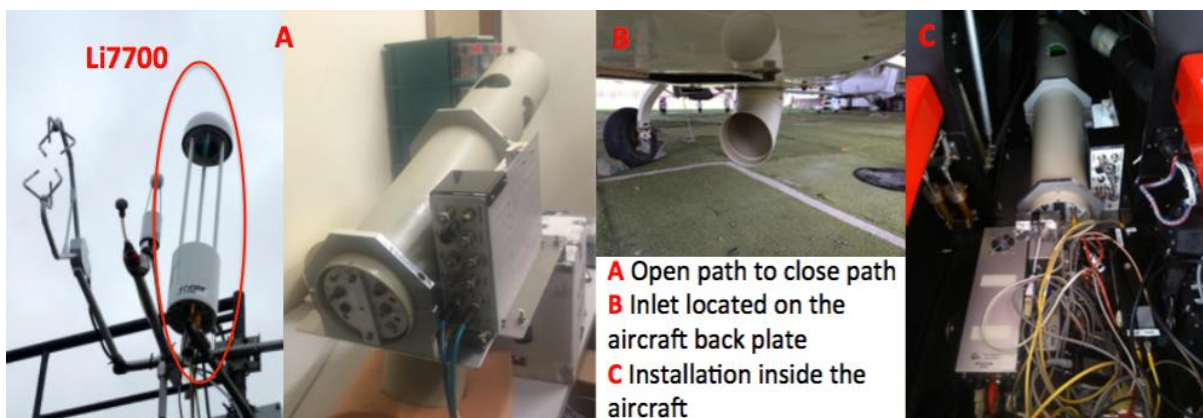


Figure 1.3 *The biogas payload on board the Sky Arrow ERA*

For CH_4 measurements, a new configuration of the Licor 7700 open path fast methane gas analyzer was developed (LiCor, Lincoln, NE, USA), based on enclosing the sensor within a cylinder exposed to the external air in-flow. The sensor is located in the back-plate of the Sky Arrow, above a trap door from which the air flow is conveyed to the instrument optical path. This set-up allows fast response measurements (50 Hz), avoiding external modifications to the aircraft, that would be subjected to restrictions. Signal from the sensor has been taken directly from DAC (digital analog converter),

without using Licor's softwares in order to obtain higher measurements frequency respect to the standard instrument operational configuration. Some flights tests have been performed before the measurement campaigns to check the reliability of the Licor 7700 new configuration. Mixing ratio measurements of methane have been carried out in vertical profiles up to 1500 meter ASL to prevent possible influences of temperature and pressure variations on the mixing ratio calculation and to verify that vibrations during the flight did not produce disturbance to laser multiple reflections inside the instrument optical path. No automatic cleaning for the mirrors was installed on board. Residual signal strength indicator (RSSI) of the instrument was observed to decrease gradually during the flight but remaining at values around 50% after landing, sufficient to preserve good data quality.

1.3 The Eddy Covariance Technique

The eddy covariance is a micrometeorological technique to infer the exchanges of energy, momentum and matter at the surface-atmosphere interface. The air flow in the planetary boundary layer can be imagined as a horizontal flow of numerous rotating eddies. Each eddy has 3-D motion components, including vertical movement of the air. If we look at one single sampling point, we can recognise two different situations (see Figure 1.4):

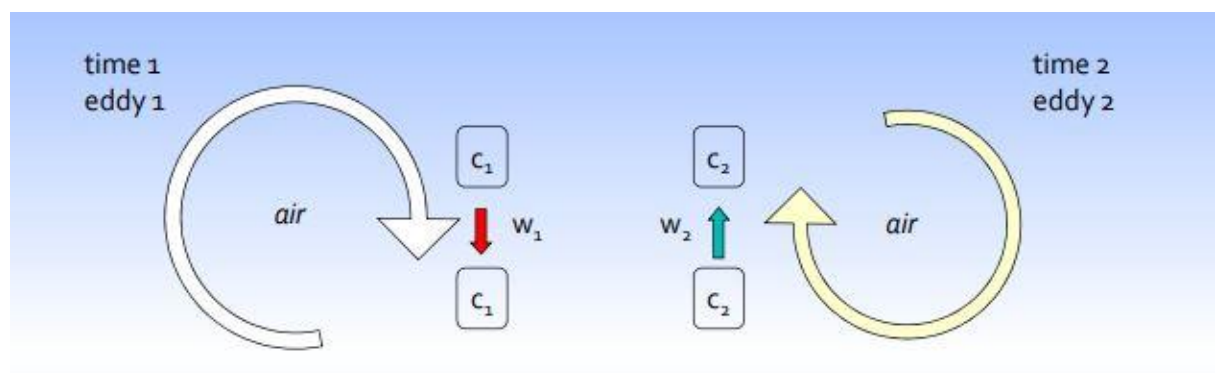


Figure 1.4 Simple representation of eddy covariance principles.

At one moment (time 1), eddy number 1 moves air parcel c_1 downward with the speed w_1 . At the next moment (time 2) at the same point, eddy number 2 moves air parcel c_2 upward with speed w_2 . Each air parcel has its own characteristics, such as gas concentration, temperature, humidity. If we could measure these characteristics and

the speed of the vertical air movement, we would know the vertical upward or downward fluxes of gas concentration, temperature, and humidity. For example, if at one moment we know that three molecules of CO₂ went up, and in the next moment only two molecules of CO₂ went down, then we know that the net flux over this time was upward, and equal to one molecule of CO₂ [3]. This is the general principle of Eddy Covariance measurements: covariance between the concentration of interest and vertical wind speed in the eddies following the equation:

$$F_c = \overline{w' C'} \quad \text{Equation 1.1}$$

Where F_c is the vertical turbulent flux of a gaseous concentration C , and w is the vertical component of the wind vector.

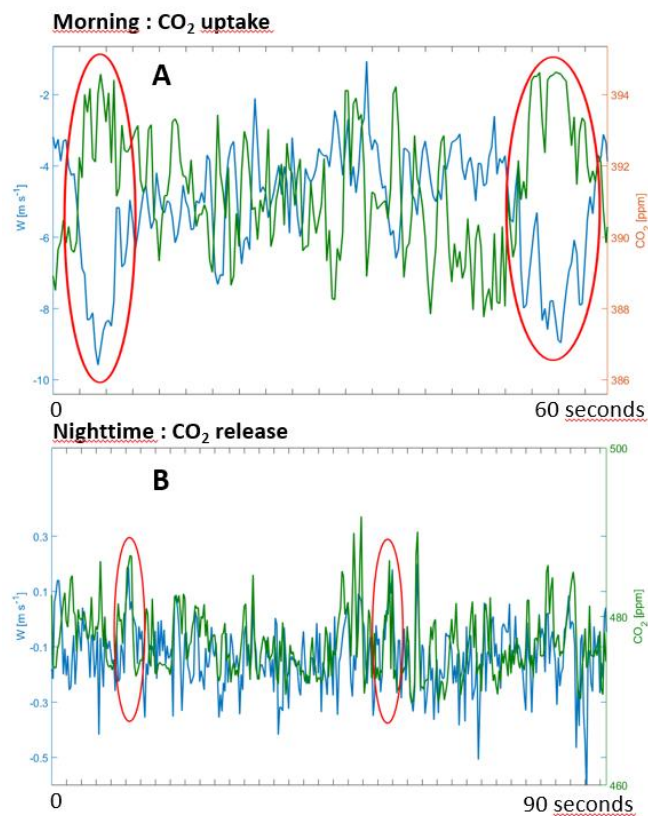


Figure 1.5 High frequency measurements of CO₂ mixing ratios and vertical wind component carried out at Borgo Cioffi. Blue lines represent the vertical wind speed, while green lines represent CO₂ mixing ratios.

Figure 1.5 shows a clear example of the eddy covariance measurements for CO₂ at Borgo Cioffi (see following section). In figure 1.5 A CO₂ mixing ratio and vertical wind component have a negative covariance indicating the presence of a flux towards the canopy. This is the distinguishing behaviour recorded during the photosynthesis activity that occur in the central hours of the day, during which the canopy absorb CO₂ from the atmosphere. In figure 1.5 B the covariance between the variables is positive revealing a CO₂ flux towards the atmosphere. This is the situation that characterized the night time hours, where the crop respiration produced a release of CO₂ in the atmosphere.

1.4 The Borgo Cioffi field station

The Borgo Cioffi field site (shown in figure 1.6) is located near Eboli (SA) in the Southern Italian Campania region (40° 31' N, 14° 57' E) and is the European southernmost cropland observation candidate site of ICOS (Integrated Carbon Observation System). The field station is located in a 15 ha field, irrigated by means of a central pivot system. The main cultivated species are corn (*Zea mays*), sorghum (*Sorghum bicolor*) and Alfalfa, along with some winter grass crops (*Lolium Italicum*), for fresh animal consumption, silage or hay.



Figure 1.6 Map of the field site in Borgo Cioffi. N-NE of the EC tower is the water buffalo farm.

The cropland site is located nearby a water buffalo farm (about 1000 animals). The farm area can be considered as representative of agricultural soils in this region where

water buffalo form an important part of the animal husbandry. The soil has an alluvial origin, deriving from the nearby Sele river, and it features a clay texture (clay: 52%, silt: 28%, sand: 20%), whereas in isolated patches localized in the SW area of the field, a coarse texture (clay:14%, silt:11% and sand: 75%) was detected. Soil pH is 7.5 and bulk density 1.2 g cm^{-3} , organic matter content $2.5 \pm 0.3\%$.

BIBLIOGRAPHY

[1] Crawford, T.L., Dobosy, R.J., 1992. A sensitive fast-response probe to measure turbulence and heat flux from any airplane. *Boundary-Layer Meteorol.* 59 (3), 257e278.

[2] Gioli, B., Miglietta, F., Vaccari, F.P., Zaldei, A., De Martino, B., 2006. The Sky arrow ERA, an innovative airborne platform to monitor mass, momentum and energy exchange of ecosystems, *Ann. Geophys.* 49 (1), 109e116.

[3] Burba, George & DJ, Anderson. (2010). A Brief Practical Guide to Eddy Covariance Flux Measurements: Principles and Workflow Examples for Scientific and Industrial Applications. 10.13140/RG.2.1.1626.4161.

Chapter 2

The SKY Arrow ERA: a powerful instrument for the parameterization of meteorological and chemical model

Air quality studies are generally supported by meteorological and chemical models in order to include those processes regulating severe air pollution episodes, such as atmospheric circulation and chemical transport. Reproducing and forecasting regional and local meteorological conditions is therefore of fundamental importance in order to replicate pollution patterns, and analyze the pollutants dispersion in complex orography. Air temperature, wind speed and direction and planetary boundary layer (PBL) height derived from numerical weather prediction (NWP) models are the fundamental parameters given as inputs to air quality models. In the framework of AriaSaNa (Air quality in Salerno and Naples districts) a deterministic air quality model forecast system has been developed and implemented for the Naples urban area and for the entire Campania region. The model chain is composed by the Flexible Air quality Regional Model (FARM) Chemical Transport Model [1] coupled with the WRF (Weather Research and Forecasting) meteorological model [2]. In this context, aircraft observations from the Sky Arrow ERA platform have been used to assess the performances of the meteorological simulations. In this chapter I show two different studies. The first is an evaluation of the performance of WRF modelling set up, comparing meteorological outputs with measurements by the Sky Arrow ERA. The second is a comparison and integration of aircraft measurements with high resolution modelling for meteorology and air quality in order to investigate local circulation and pollutant dynamics.

My role in both papers was related to the aircraft measurements. I was responsible for the measurement campaigns organization, for the correct functioning of the different payloads and of the aircraft data analysis.

2.1 Performance Analysis of Planetary Boundary Layer Parameterization Schemes in WRF Modelling Set Up over Southern Italy

A unique feature of the Sky Arrow ERA platform observations is to provide direct verification of model performances at the entire PBL scale for the wind vector, the potential temperature and the specific humidity by using different PBL parameterization schemes in the model. Usually, performances of PBL parameterizations have been verified either by means of surface observations - sometimes supplemented by a single vertical sounding [3]. Through this study, the sampling strategy was aimed at measuring at the local scale the vertical profiles of meteorological and micrometeorological variables at key locations of the study area, both inland and above the sea, at different times of the day, associated with different atmospheric conditions and sea breeze development phases. The Sky Arrow ERA measurements provided high resolution information, both on the temporal and spatial level, normally not available from radio sondes or larger aeroplanes that cannot fly at low altitude and with a low speed as the Sky Arrow.

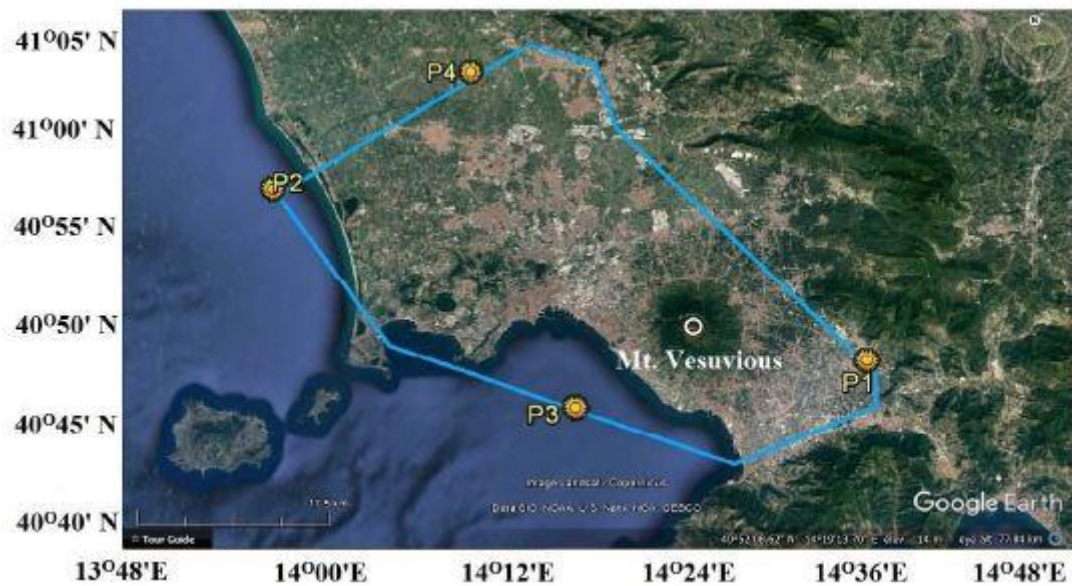


Figure 2.1. Flight tracks performed by the Sky Arrow ERA, yellow circles showed the location of the vertical profiles

The Sky Arrow performed five flights over the Campania region on 7-9 October 2014. The flight tracks were designed as a box encompassing inland and sea horizontal

transects with vertical soundings on each of the four corners. Inland profiles (P1 and P4 in figure 2.1) were performed from the minimum safety height (150 m ASL) up to the free troposphere (2000 m ASL), whereas sea profiles (P2 and P3 in figure 4) up to 1000 m ASL. The overall comparisons have shown that the main features of the vertical layering of the atmosphere are captured by the WRF simulations with all of the considered PBL parameterizations; furthermore the modelled boundary layer matches the vertical location of the most important temperature gradients, and captured correctly the upper layer temperature slopes. The selected PBL schemes (legend in figure 2.2) include three first-order closure PBL schemes (ACM, MRF, YSU) and four turbulent kinetic energy (TKE) closure schemes (MYJ, UV, MYNN2 and BouLac). However, some observations are not well reproduced by the model simulations, using any of the PBL parameterizations. The measured virtual potential temperature shows quite a stable slope in the PBL, while modelled profiles are uniform within the PBL, as it can be expected in well-mixed conditions. The modelled specific humidity is overestimated in the lower layers, and underestimated in the upper layers for all tested PBL schemes. The model reproduction of the vertical variation of the wind field is correct, showing the relevant decrease of wind speed alongside wind direction rotation in the shear layer, observed in this case between 500-900 m ASL.

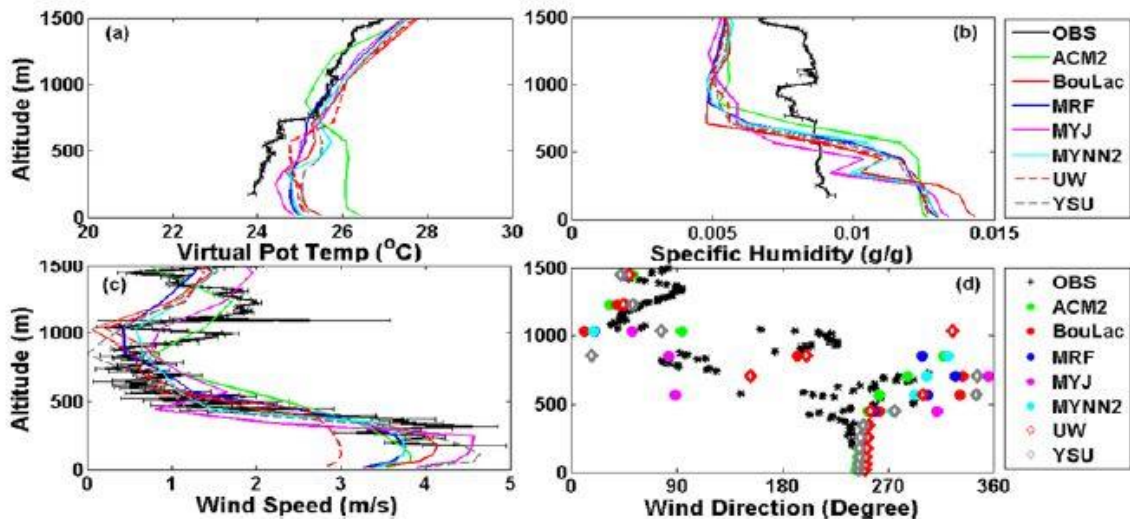


Figure 2.2 Vertical profile of (a) air temperature, (b) specific humidity (g/Kg), (c) wind speed and (d) wind direction. Black lines are the observations, coloured lined the simulations with different PBL schemes.

Some PBL schemes reproduced better wind profiles near the surface, but in general, measured wind field profiles show weak winds with strong vertical variability that the model is not able to reproduce. These discrepancies can be attributed to local features that are possibly transient and are connected to the development of the sea-breeze cell circulation, and in particular to the return current aloft.

The results of this study have been published in July 2018 in the paper “Performance Analysis of Planetary Boundary Layer Parameterization Schemes in WRF Modeling Set Up over Southern Italy”, that can be found in Appendix A of this chapter.

2.2 Atmospheric Dynamics and Ozone Cycle during Sea Breeze in a Mediterranean Complex Urbanized Coastal Site

It is well known that the Mediterranean Basin has a strong vulnerability to photochemical air pollution episodes, especially during the summer season when the Ozone (O_3) concentration over the Mediterranean is about three times higher than the hemispheric background level. The Italian peninsula is characterized by the presence of the Apennine mountains (range of altitude of the tops) located at moderate distance from the coast, favouring the development of breeze circulations on both Eastern and Western coasts. The district of Naples is one of the main urbanized areas of Southern Italy with more than three million inhabitants. Its vulnerability to O_3 pollution episodes is increased by intense agricultural activities over the inland plains and by forest areas extending farther inland over the Apennine chain and on Mount Vesuvius. Due to the prevalence of sea breeze regime during spring and summer, these vegetated areas are exposed to the urban plume with high NO_x concentrations that can lead to the photooxidation of BVOC enhancing the O_3 concentration. To reconstruct the atmospheric dynamics and the O_3 increase during a pollution episode, data from the Sky Arrow ERA are coupled with ground based measurements performed at the same time and model simulations (same model chain WRF+FARM described in the previous section) in a study domain centred in the city of Naples.

Four flights were performed on 15-16 July 2015 (figure 2.3) when a high pressure ridge of African origin affected the Mediterranean Basin causing high temperatures especially over the Italian peninsula.

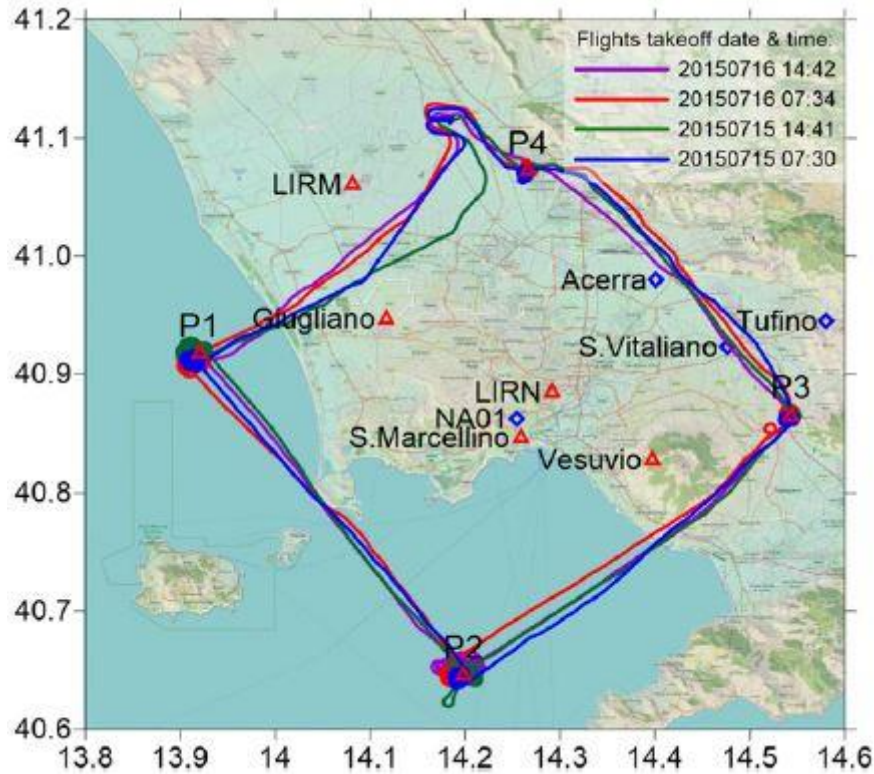


Figure 2.3. Flight tracks performed by the Sky Arrow ERA during the measurements campaigns. At each corners of the box a vertical soundings have been performed (P1, P2, P3 and P4).

Figure 4.2 shows the comparison between the O_3 concentrations measured by the Sky Arrow ERA during the vertical soundings and FARM model outputs for the O_3 concentrations during the morning hours (a,b,c,d) and during afternoon hours (e,f,g,h). P1 and P2 (a and b in figure 2.4), sea vertical profiles taken during the morning hours, showed a quite constant concentration above 400 m ASL with values close to $150 \mu\text{g m}^{-3}$; below this height concentration decreased towards the surface with values between 100 and $120 \mu\text{g m}^{-3}$. FARM simulations (red lines in figure 2.4) reproduced correctly the profile shapes with some underestimation of concentrations in the upper layers. This model results support the hypothesis of the low value of near surface O_3 concentration caused by NO_x rich and O_3 poor air masses from the urbanized coastal areas during the night, and early morning breeze regime. Morning inland profiles (c and d in figure 2.4) were well reproduced by the model showing high O_3 concentration ($150\text{-}175 \mu\text{g m}^{-3}$) within a layer of about 600 m ASL, with values similar to those measured at high altitude over the sea profiles. The afternoon O_3 profiles (e,f,g,h in figure 2.4) showed peculiar features. These profiles were characterized by a general

increase of O₃ concentration in the lower layer (below 600m?) compared to morning profiles, but the two northern profiles P1 and P4 (e and h in figure 2.4) showed an O₃ rich layer between 400 and 1000 m ASL, with maxima located at about 600 m ASL.

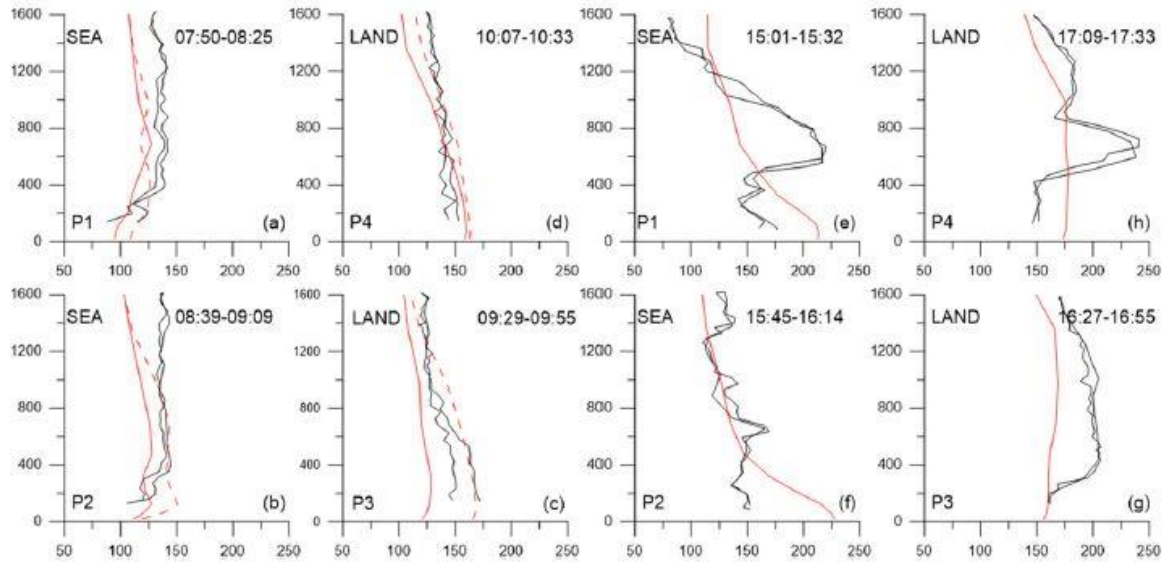


Figure 2.4. Vertical profiles of ozone concentration ($\mu\text{g m}^{-3}$) measured by the aircraft along its ascending and descending flight paths (black lines) at locations (a),(e) P1, (b),(f) P2, (c),(g) P3, and (d),(h) P4 during the morning [in (a)–(d)] and afternoon [in (e)–(h)] flights on 15 Jul 2015. Start and end times of the ascending and descending aircraft flight paths are indicated for each profile. FARM results extracted at the same location are reported for the closest hourly time frame (red solid lines) and with 1-h delay (red dashed lines, for the morning flight only).

These patterns were not reproduced by the model simulation: the transient nature of the observed phenomenon and the relatively low altitude of this O₃ rich layer support the hypothesis that it is caused by the local recirculation.

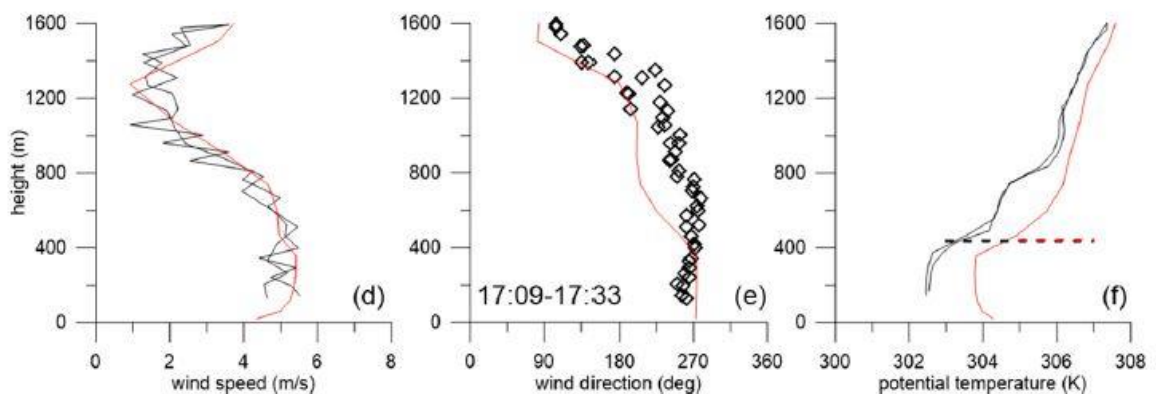


Figure 2.5. Vertical profile of wind speed, wind direction and potential temperature at location P4 measured (black lines) and modelled (red lines) during the afternoon of 15 July.

The O₃ rich layer observed in P4 (figure 2.4 h) is coincident with the residual layer located over the internal boundary layer as can be seen in figure 2.5 (f), where pollutants have been injected during late morning, before the arrival of the breeze front, and then remain trapped after the internal boundary layer development. During local recirculation events, the mismatch between observation and simulation is probably related to the limited difference between the modelled and measured wind direction (Figure 2.5 (e)). The advection of NO_x from Naples and its harbour towards the VOC rich inland planes caused a relevant O₃ production in the area; pollutants were vertically mixed inside the boundary layer, until the sea breeze front reached the inland plains near midday. The evening collapse of the boundary layer height formed a layered vertical structure of the lower atmosphere with high O₃ concentration trapped in the residual layer. This complex dynamics of the pollutants dispersion are strictly related to the local topography and to the local wind field rotation that the simulation is not able to reproduce correctly, also due to the ambiguity of this phenomenon, that e.g. did not occur in the following day. Results of this study have been published on January 2018, in the paper “Atmospheric Dynamics and Ozone Cycle during Sea Breeze in a Mediterranean Complex Urbanized Coastal Site”, which can be found in Appendix B of this chapter.

BIBLIOGRAPHY

[1] Silibello, C., G. Calori, G. Brusasca, A. Giudici, E. Angelino, G. Fossati, E. Peroni, and E. Buganza, 2008: Modelling of PM10 concentrations over Milano urban area using two aerosol modules. *Environ. Modell. Software*, 23, 333–343, <https://doi.org/10.1016/j.envsoft.2007.04.002>.

[2] Skamarock, W. C., and Coauthors, 2008: A description of the Advanced Research WRF version 3. NCAR Tech. Note NCAR/TN-4751STR, 113 pp., <http://dx.doi.org/10.5065/D68S4MVH>.

[3] Prasad, K.B.R.R. & C., Venkata Srinivas & Bagavath Singh, Anbalagan & Rao, S. & Ramakrishnan, Baskaran & Balasubramaniam, Venkatraman. (2014). Numerical simulation and intercomparison of boundary layer structure with different PBL schemes in WRF using experimental observations at a tropical site. *Atmospheric Research*. 145–146. 27-44. [10.1016/j.atmosres.2014.03.023](https://doi.org/10.1016/j.atmosres.2014.03.023).

Appendix A



Article

Performance Analysis of Planetary Boundary Layer Parameterization Schemes in WRF Modeling Set Up over Southern Italy

Bhishma Tyagi ^{1,2,*}, Vincenzo Magliulo ¹, Sandro Finardi ³, Daniele Gasbarra ^{1,4},
Pantaleone Carlucci ¹, Piero Toscano ⁵, Alessandro Zaldei ⁵, Angelo Riccio ⁶,
Giuseppe Calori ³, Alessio D'Allura ³ and Beniamino Gioli ⁵

¹ National Research Council, Institute for Agricultural and Forestry Systems in the Mediterranean (CNR-Isafom), ViaPatacca 85, 80040 Ercolano, Napoli, Italy; enzo.magliulo@cnr.it (V.M.); danielegasbarra@yahoo.it (D.G.); pantaleone.carlucci@gmail.com (P.C.)

² Department of Earth and Atmospheric Sciences, National Institute of Technology Rourkela, Rourkela 769008, India

³ Arianetsrl, viaGilino 9, 20128 Milano, Italy; s.finardi@aria-net.it (S.F.); g.calori@aria-net.it (G.C.); a.dallura@aria-net.it (A.D.)

⁴ Department of Vegetal Biology, University of Napoli Federico II, ViaForias 223, 80139 Napoli, Italy

⁵ National Research Council, Institute of Biometeorology (CNR-Ibimet), ViaCaproni 8, 50145 Firenze, Italy; p.toscano@ibimet.cnr.it (P.T.); A.Zaldei@ibimet.cnr.it (A.Z.); b.gioli@ibimet.cnr.it (B.G.)

⁶ Department of Applied Sciences, University of Naples "Parthenope", Centro Direzionale-Isola C4, 80143 Napoli, Italy; angelo.riccio@uniparthenope.it

* Correspondence: bhishmatyagi@gmail.com

Received: 17 April 2018; Accepted: 10 July 2018; Published: 17 July 2018



Abstract: Predictions of boundary layer meteorological parameters with accuracy are essential for achieving good weather and air quality regional forecast. In the present work, we have analyzed seven planetary boundary layer (PBL) parameterization schemes in a Weather Research and Forecasting (WRF) model over the Naples-Caserta region of Southern Italy. WRF model simulations were performed with 1-km horizontal resolution, and the results were compared against data collected by the small aircraft Sky Arrow Environmental Research Aircraft (ERA) during 7–9 October 2014. The selected PBL schemes include three first-order closure PBL schemes (*ACM2*, *MRF*, *YSU*) and four turbulent kinetic energy (TKE) closure schemes (*MYJ*, *UW*, *MYNN2*, and *BouLac*). A performance analysis of these PBL schemes has been investigated by validating them with aircraft measurements of meteorological parameters profiles (air temperature, specific humidity, wind speed, wind direction) and PBL height to assess their efficiency in terms of the reproduction of observed weather conditions. Results suggested that the TKE closure schemes perform better than first-order closure schemes, and the *MYNN2* closure scheme is close to observed values most of the time. It is observed that the inland locations are better simulated than sea locations, and the morning periods are better simulated than those in the afternoon. The results are emphasizing that meteorology-induced variability is larger than the variability in PBL schemes.

Keywords: aircraft measurements; WRF; vertical profile; weather prediction

1. Introduction

Regional scale meteorological modeling is important to improve our knowledge of the processes controlling atmospheric circulation, as well as actual air pollution levels and their impact on human health and ecosystems [1]. Routinely available meteorological and air quality observations are generally insufficient to properly identify the atmospheric phenomena driving severe air pollution conditions,

especially in complex terrain. Air quality studies are usually supported by chemistry and transport models, which use emission inventories over the region of interest, boundary conditions from a global forecast model, and meteorological fields from a numerical weather prediction (NWP) model [2]. Therefore, reproducing and forecasting regional and local meteorological conditions are key tasks to accurately replicate the pollution patterns and analyze the dispersion of pollutants in the area of interest [2–4]. Air temperature, wind, specific humidity, and planetary boundary layer (PBL) height derived from NWP models are the fundamental parameters given as inputs to air quality models, which are affecting the forecasting of air pollution [5]. The performance of numerical models can be improved, among other factors, through using higher spatial and temporal grid resolutions, appropriate parameterizations, or the data assimilation of observed meteorological parameters [6–8].

Weather Research and Forecasting (WRF) is a widely used NWP model for meteorological and air quality predictions all over the world [9,10]. The present study is aimed at assessing the performance of different WRF boundary layer parameterizations over a large conurbation sited in a complex coastal area, based on atmospheric aircraft observations and modeling performed within the project AriaSaNa (Air quality in Salerno and Napoli districts), integrating regional ground-based and airborne measurements with state-of-the-art meteorological and air quality modeling. A deterministic air quality modeling forecast system has been developed and implemented for the Naples urban area and Campania region, based on the Flexible Air quality Regional Model (FARM) Chemical Transport Model [11–13] coupled with the WRF meteorological model, which has been working operationally since July 2014. Numerical modeling system performance was assessed against upper in situ observations collected using the Sky Arrow Environmental Research Aircraft (ERA) experimental aircraft [14] during multiple days of intensive flight campaigns. These observations enabled a unique occasion to verify model performances at the entire PBL scale, including wind components. Moreover, aircraft measurements allowed sampling at a level of spatial and temporal detail that is normally not available from radio sonde or larger aeroplanes. The sampling strategy was aimed at measuring the vertical profiles of meteorological and micrometeorological variables in key locations of the study area, which are located both inland and above sea, and at different times of the day, which is associated with different atmospheric conditions and sea breeze development phases.

Previous analyses of PBL parameterizations performances have been mainly based on surface observations sometimes supplemented by a single vertical sounding [15–22], or have been focused on the mesoscale [23–27]. Our study is focused on the local scale, and based on the availability of nearly simultaneous vertical profiles measured at different locations of the target area, which allows a thorough analysis of three-dimensional (3D) circulation in coastal breeze conditions. The specific objectives of this study are to: (i) assess whether a single PBL scheme may be identified as capable of providing better performance across all of the study area; (ii) assess the variability in model outputs related to various PBL schemes with respect to the variability related to different atmospheric circulations or different areas of the domain; and (iii) provide an experimental and modeling framework for the benchmarking and optimal configuration of mesoscale models. Overall, this work aims at improving meteorological and air quality assessment capability, which is especially important for forecasting severe pollution episodes associated with extreme weather conditions.

2. Materials and Methods

2.1. Study Area

Aircraft observations were performed over an area of circa 1300 km², situated in Campania region (Southern Italy) and roughly centered in the city of Naples (40°51' N, 14°21' E), which is bounded by the Appennini and anti-Appennini mountains to the east and southeast, and by Naples Bay and Tyrrhenian sea to south and west (Figure 1). The surface encompassed by flights is mainly made of flat land that is part of the two plains extending northwest of Naples and southeast of Mount Vesuvius and is surrounding the strip of conurbation that spreads from Naples to Caserta. This urban area is

recognized as the largest metropolitan area in the Mediterranean Basin [28]; it is often affected by high pollution due to anthropogenic activities associated with calm and stagnant air masses, and its effect on health is a concern for the scientific community and policy makers [29–32]. The remaining surface is occupied by agricultural land and small industrial districts [33].

The climate is typically Mediterranean, with mild winter providing most of the rainfall and a relatively dry and hot summer. Prevalent winds blow along the northeast to southwest direction, in a local breeze circulation pattern. The presence of Mount Vesuvius complicates this basic frame, since air masses are forced to move around its foothills, thus creating areas of relatively calm air downwind [33].



Figure 1. Flight tracks performed by the Sky Arrow aircraft on 8 October 2014 (sky blue color lines). Locations of four profiles (PRF), i.e., P1 ($40^{\circ}47'39.35''$ N, $14^{\circ}37'52.82''$ E), P2 ($40^{\circ}57'05.68''$ N, $13^{\circ}56'19.41''$ E), P3 ($40^{\circ}45'12.89''$ N, $14^{\circ}18'00.54''$ E), and P4 ($41^{\circ}04'22.49''$ N, $14^{\circ}10'06.27''$ E) are outlined by yellow circles (image source: Google Earth).

2.2. Aircraft Data

The Sky Arrow Environmental Research Aircraft (ERA) is a small airplane equipped with sensors to measure three-dimensional wind vectors (u , v , w), together with temperature, water vapor, trace gas concentrations, and other atmospheric parameters at high temporal frequency [14]. It has a cruise speed of 170 km/h and can fly up to a height of about 3000 m. The wind components are measured by means of a pressure sphere recording an airspeed velocity vector (e.g., relative to aircraft frame) that is post-processed to subtract aircraft motion, obtaining an absolute (i.e., relative to earth) wind vector following [34,35]. Details of the Sky Arrow ERA meteorological instrumentation relevant to this study is summarized in Table 1.

High-frequency (50 Hz) observational data streams were then block-averaged to obtain 4 s average values. The Sky Arrow performed five flights on 7–9 October 2014 (Table 2). The flight track was designed as a box encompassing inland and sea horizontal transects, with a vertical sounding profile on each of the four corners (Figure 1): Profile 1 (referred as PRF1 hereafter) at ($40^{\circ}47'39.35''$ N, $14^{\circ}37'52.82''$ E) and Profile 4 (referred as PRF4 hereafter) at ($41^{\circ}04'22.49''$ N, $14^{\circ}10'06.27''$ E) were obtained over land, while Profile 2 (referred as PRF2 hereafter) at ($40^{\circ}57'05.68''$ N, $13^{\circ}56'19.41''$ E) and Profile 3 (referred as PRF3 hereafter) at ($40^{\circ}45'12.89''$ N, $14^{\circ}18'00.54''$ E) were made over the sea. On PRF1 to PRF4, the aircraft flew a vertical profile from the minimum safety height (~ 150 m) up to the free troposphere (~ 2000 m above land and ~ 1000 m above sea), both upward and downward, performing spirals with about a 1.5-km diameter. Profiles of wind speed, wind direction, air temperature, and specific humidity were obtained by extracting ascending and descending legs from the flight paths for the subsequent comparison with model data.

Table 1. Details of meteorological instrumentation used during Sky Arrow Environmental Research Aircraft (ERA) flights.

Serial Number	Instrument	Parameters Measured	Accuracy
75H 0590	LI-COR-7500-LI-COR/LI-COR Biosciences, Lincoln, NE, USA	CO ₂ and H ₂ O densities of air	Within 1% of reading for CO ₂ and within 2% of reading for H ₂ O
ATDD03-3	Best Aircraft Turbulence (BAT) probe/NOAA, Silver Spring, MD, USA; Airborne Research Australia, Adelaide, Australia	3D wind speed (u, v, w) with respect to aircraft	The ratio of standard deviation of w ~5%
LD90-3300HR	Riegl Laser Altimeter LD90-3/RIEGL Laser Measurement Systems GmbH, Horn, Austria	Aircraft flying height from the ground	Typically 0.5 m at highest range and 10 cm at minimum range
CM1480	C-MIGITS (Accelerometer)/Syston Donner Inertial, Concord, CA, USA	Position, velocity, and attitude information	Position (Spherical Error Probable-SEP): 3.9 m, Velocity (1 sigma, horiz/vert): 0.1/0.1 m/s, Pitch and roll (1 sigma): 1.0 mrad, Time mark output 1 pps: 1 microsecond, Heading (1 sigma, in motion): 1.5 mrad
2003-004	GPS OEM4 Family/Novatel, Calgary, AB, Canada	Position, velocity, altitude ASL (Above Sea Level) and GPS time	Position accuracy 1.8 m, velocity accuracy 0.03 RMS, time accuracy 20 ns RMS
Q03045	LI-190SA Photosynthetically Active Radiation (PAR)-Radiometer/LI-COR Biosciences, Lincoln, NE, USA	Photosynthetic photon flux density (PPFD)	Sensitivity: Typically 5 μA to 10 μA per 1000 $\mu\text{mol s}^{-1} \text{m}^{-2}$ Linearity: Maximum deviation of 1% up to 10,000 $\mu\text{mol s}^{-1} \text{m}^{-2}$

Table 2. Aircraft flights and profiles details; the time of each profile is the average of the UTC time during the profile measurement interval, typically about 5 min to 15 min.

Serial Number	Flight	Date and Time	Profiles
1	Flight 1	7 October 2014, 08:39–10:58 UTC	1 (09:05 UTC), 2 (09:46 UTC), 3 (10:23 UTC), 4 (11:12 UTC)
2	Flight 2	7 October 2014, 12:38–16:56 UTC	1 (14:42 UTC), 2 (13:50 UTC), 3 (13:16 UTC), 4 (14:12 UTC)
3	Flight 3	8 October 2014, 12:47–14:46 UTC	1 (13:09 UTC), 2 (14:11 UTC), 3 (14:39 UTC), 4 (13:45 UTC)
4	Flight 4	9 October 2014, 08:39–10:37 UTC	1 (08:56 UTC), 2 (09:36 UTC), 3 (10:06 UTC), 4 (10:55 UTC)
5	Flight 5	9 October 2014, 12:09–14:24 UTC	1 (14:19 UTC), 2 (13:17 UTC), 3 (12:46 UTC), 4 (13:40 UTC)

2.3. Meteorological Model

The Advanced Research Weather Research and Forecasting model (WRF-ARW) version 3.5.1 has been configured with four nested domains, keeping the outermost domain at the continental scale, and the inner domains at the national and local scales (Figure 2).

The model domains use a grid of 3 km \times 3 km resolution in Domain 3, and a 1 km \times 1 km resolution in the innermost domain, i.e., Domain 4, with 41 vertical levels stacked closest near the ground, and approximately 11 vertical levels below 1 km above-ground level. WRF simulations have been driven by National Oceanic and Atmospheric Administration (NOAA)/National Centre for Environmental Prediction (NCEP)-Global Forecast System (GFS) global scale meteorological forecast with a horizontal spatial resolution of one degree and with time resolution of 3 h. The dynamics and physics schemes used by WRF forecast are resumed in Table 3.

Surface model results depend on the proper definition of land cover and soil composition. The land cover description has been improved by the introduction of the European Coordination of Information on the Environment (CORINE) land cover at 250-m resolution (<http://land.copernicus.eu>),

while no information was available to enhance the soil composition description with respect to the standard worldwide WRF database.

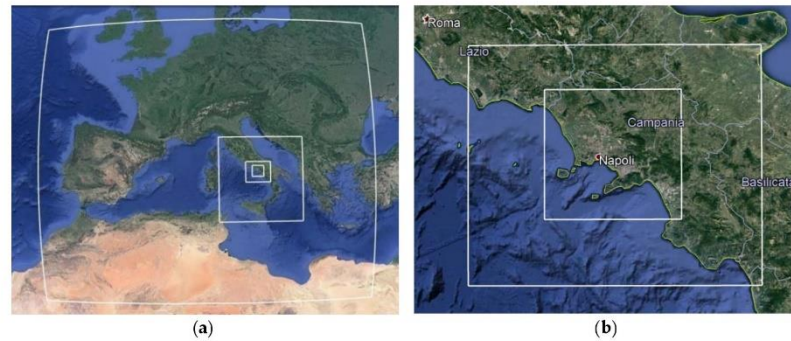


Figure 2. Geographic location of Weather Research and Forecasting (WRF) four nested domains (a) and a zoom over the two inner ones, covering the Campania Region and Naples (b). Image source: Google Earth.

Table 3. Overview of WRF model configuration presently used for the Air quality in Salerno and Napoli districts (AriaSaNa) project. PBL: planetary boundary layer.

Dynamics	Non Hydrostatic
Data	NCEP GFS
Interval	3 h
Gridsize and Resolution	Domain1: $(80 \times 57) \times 34$; 27 km \times 27 km Domain2: $(95 \times 95) \times 34$; 9 km \times 9 km Domain3: $(69 \times 69) \times 34$; 3 km \times 3 km Domain4: $(69 \times 69) \times 34$; 1 km \times 1 km
Map projection	Lambert Conformal
Horizontal grid system	Arakawa-C grid
Integration time step	225 s
Vertical coordinates	Terrain-following hydrostatic pressure vertical co-ordinate with 34 vertical levels
Time integrationscheme	Third order Runge–Kutta Scheme
Spatial differencingscheme	Sixth order center differencing
Land surface option	Noah land surface scheme
Microphysics	WSM six-class graupelscheme
Shortwaveradiation	(old) Goddardshortwavescheme
Longwaveradiation	Rapid Radiative Transfer Model (RRTM) scheme
Cumulus parameterization	Kain–Fritsch scheme in Domain 1 and 2 and no scheme in Domain 3 and 4
Surface layer physics	Monin–Obukhovsimilaritytheory
PBL schemes tested in present work	ACM2, BouLac, MRF, MYJ, MYNN2, UW, YSU

The WRF ARW version 3.5.1 has 13 PBL schemes [36], which can be mainly grouped based on Richardson Number (Ri) or turbulent kinetic energy (TKE) criterion, which is commonly referred as first-order closure and TKE closure schemes [16] for PBL turbulence modeling and PBL height determination. PBL height is considered as the vertical limit where heat, moisture, and momentum are mixed in NWP models [37], affecting the reconstruction of dispersion and ground concentrations of various pollutants [2]. Different PBL schemes use different criteria to estimate PBL height, but the choice of the specific PBL scheme to be implemented is often made arbitrarily. Performance analysis of PBL parameterizations has been reported for specific regions in the last decade [15,16,19,21–24].

For the present study, three first-order closure PBL schemes (ACM2; MRF; YSU) and four TKE closure schemes (MYJ; UW; MYNN2; BouLac) have been chosen, based on the findings of previous studies [21,22,25,26]. A brief description and physical working principle of each of the chosen scheme is given hereunder.

2.3.1. The Asymmetrical Convective Model Version 2 (ACM2) Scheme

ACM2 is a first-order, non-local closure scheme [38] that was obtained as a modification of the ACM1 scheme of the MM5 model, which was derived from the Blackadar scheme [39]. The scheme has an eddy-diffusion component, in addition to the explicit non-local transport of ACM1.

The non-local mixing term dominates the local mixing term through most of the depth of the convective PBL, but the local mixing term can be larger near the top of the PBL where the wind shear might be greater. The non-local transport term is set to zero, and local closure is used in stable conditions [26]. The scheme is found to have high accuracy in reproducing the vertical profiles of velocity and potential temperature by considering non-local and local closure for vertical mixing together [38]. ACM2 determines PBL height where the bulk Richardson number (Rib) exceeds a threshold value of 0.25.

2.3.2. Medium-Range Forecast (MRF) Scheme

MRF is a non-local first-order closure scheme [40] that incorporates a counter-gradient correction term into down-gradient diffusion defined by local mixing only [41]. Compared to local schemes, MRF showed higher accuracy in simulating the deeper mixing within unstable PBL, where larger eddies entrain higher potential temperatures above the PBL into the PBL [42,43]. The PBL height is calculated iteratively where Rib exceeds a threshold value of 0.50.

2.3.3. Yonsei University (YSU) Scheme

YSU is a first-order, non-local scheme [44]. It comes after a modification from the MRF scheme [40] of the MM5 model [21]. It uses a parabolic K -profile in an unstable mixed layer with the addition of an explicit term to treat the entrainment layer at the top of the PBL [22]. The buoyancy-driven PBLs with shallower mixing in strong-wind regimes are better simulated by YSU compared to MRF [26,44]. YSU determines PBL height where Rib exceeds a threshold value of 0.

2.3.4. Mellor–Yamada–Janjic (MYJ) Scheme

The classification of the Mellor–Yamada (MY) family schemes can be understood as “simplified second-order closure” [45], which is often indicated as “1.5-order” because they implement a reduced set of second-order moment equations [46]. The term “1.5-order” usually means a first-order closure with eddy viscosity K -coefficients dependent on TKE, which in turn is calculated from a budget equation. MY Level 3 and higher use a full set of second-moment budgets with proper closure hypotheses simplified by a scale analysis based on a departure from isotropy metric and the application of the so-called “boundary layer approximation” to obtain simpler models. The widely-used MY Level 2.5 model is based on the solution of the TKE budget equation only, and is usually indicated as a “1.5 order”. The MYJ scheme comes after modification from the MM5 model’s ETA scheme [47]. It solves a prognostic equation for TKE with a diagnostic estimation of potential temperature, water vapor variance, and covariances [48]. The scheme is considered to improve the Mellor–Yamada Level 2.5 local scheme [49,50] without particularly large computational expense [26]. It determines PBL height by the level where TKE decreases to a prescribed small value ($0.2 \text{ m}^2 \text{ s}^{-2}$).

2.3.5. Mellor–Yamada–Nakanishi–Niino Level 2.5 (MYNN2) Scheme

MYNN2 also comes under MY family scheme, which can be termed as a “simplified second order” [45]. It is a variation of the Mellor–Yamada Level 2.5 scheme [49,50], which uses liquid water potential temperature and total water content as the thermodynamic variables. It also takes into account the effects of buoyancy in the diagnosis of the pressure covariance terms, and uses closure constants in the stability functions and mixing length formulations that are based on large eddy simulation (LES) results instead of observational datasets [48]. Furthermore, the MYNN2 model considers the effect of stability on the turbulent length scale, obtaining a mixing length formulation

that is considered more flexible across the stability spectrum compared to *MYJ* [51–53]. *MYNN2* determines PBL height, where the TKE falls below a critical value of $1.0 \times 10^{-6} \text{ m}^2 \text{ s}^{-2}$ [21].

2.3.6. Bougeault–Lacarrere (*BouLac*) Scheme

BouLac is a 1.5-order, local closure scheme [54] with a TKE prediction formulation designed to extend PBL turbulence parameterizations to orography-induced turbulence and, within WRF, to be used with the Building Environment Parameterization multi-layer, urban canopy model [55]. The *BouLac* scheme has been found to better represent the PBL in regimes of higher static stability compared to non-local schemes [16]. PBL height determination with this scheme is achieved at a level where prognostic TKE reaches a sufficiently small value (e.g., $0.005 \text{ m}^2 \text{ s}^{-2}$).

2.3.7. University of Washington (*UW*) Scheme

The *UW* scheme is a 1.5-order, local TKE closure scheme [56–58]. The *UW* scheme has been originally developed for climate modeling application. It uses moist-conserved variables, TKE as a diagnostic rather than a prognostic variable, and an explicit entrainment closure to diagnose effective entrainment diffusivity at the edge of convective layers [57]. *UW* has been found to better reproduce the night-time stable boundary layer and sub-stratocumulus layers. PBL height determination by *UW* scheme is based on the Rib threshold (0.25) used in all cases of stability.

The applicability of the previously listed PBL parameterizations in a non-hydrostatic model at 1-km grid spacing could be considered questionable because the mentioned space resolution falls within the so-called “Terra Incognita” zone [59,60]. Nonetheless, it is common practice to apply WRF and other non-hydrostatic models down to 1-km grid spacing for regional to urban scale applications. This is generally considered acceptable, even if we should keep into account that the daily convective eddies can have a size of the order of the horizontal grid spacing, and could be partially resolved. The effective spatial resolution of WRF that has been evaluated by Skamarock [61] to be of the order of 7 dx, should anyway tend to guarantee that PBL parameterizations can still be considered reliable at 1-km grid spacing.

2.4. Model Performance Assessment

The model-simulated air temperature, specific humidity, wind speed, and wind direction obtained by different PBL parameterization simulations were directly compared to observational data collected by the Sky Arrow. WRF-ARW outputs have been stored with hourly frequency. The simulated vertical profiles of meteorological variables have been extracted at the corresponding aircraft profile locations, selecting the nearest available time frame and applying bilinear interpolation among the four surrounding grid points on each model level. PBL height obtained from the model as a diagnostic parameter is also compared with the PBL height obtained from the vertical profile soundings of the aircraft. The observed PBL heights are subjectively estimated by visualizing the profiles of potential temperature and water vapor [62]. By applying the potential temperature profile criterion, which is indicating atmospheric static stability, the PBL height can be taken as the level where maximum gradient occurs. In case of water vapor profiles, the PBL height is taken as the level of the minimum vertical gradient, with a noteworthy reduction in atmospheric moisture [63]. We have also validated our results of PBL height values by using bulk Richardson number criterion [64]. The results have been statistically analyzed using root mean square error (RMSE) and Pearson correlation (r). Model results were extracted from the innermost domain (1-km grid-spacing domain), horizontally interpolating model results to measurement points and time. The RMSE has been defined as follows:

$$\text{RMSE} = \sqrt{\frac{1}{N} \sum_{i=1}^N (M_i - O_i)^2}$$

And Pearson correlation (r) has been calculated as:

$$r = \frac{\sum_{i=1}^N (M_i - \bar{M}_i)(O_i - \bar{O}_i)}{\sqrt{\sum_{i=1}^N (M_i - \bar{M}_i)^2} \sqrt{\sum_{i=1}^N (O_i - \bar{O}_i)^2}}$$

where M_i = model-simulated values, O_i = observed values, and N = number of points.

Statistical parameters were also averaged across multiple flights performed over the sea, over inland areas, in the morning and the afternoon. This was done to assess the importance of the error variability related to geographical features (i.e., sea versus land) or to meteorological conditions (i.e., morning versus afternoon flights) with respect to error variability related to the different PBL schemes under investigation.

In order to compute an empirical total performance index integrating the performance of each PBL scheme on all of the flights and for all of the examined variables, RMSE and r were at first computed for all of the flights, obtaining one value for each variable; then, these values were normalized over the average of all of the PBL schemes, and finally averaged for all of the variables. Normalized RMSE and r were then obtained in a way that the mean of all of the schemes is equal to one.

3. Results and Discussion

Measurements of meteorological parameters (air temperature, specific humidity, wind speed, and wind direction) from all profiles of Sky Arrow flights were compared with the corresponding WRF output. It is worth mentioning that the comparison of model results with high-frequency aircraft measurements recorded inside the boundary layer is not a straightforward and consolidated practice. The model based on Reynolds-averaged Navier–Stokes (RANS) equations provide results that are representative of the space and time averages of the meteorological variables. The effective space and time resolution of WRF depends on the computational domain grid spacing and the numerical advection scheme [61], and it is the usual practice to compare the results of model simulation with grid spacing of a few kilometers with the observed variables' time averages of the order of 1 h, implicitly assuming that the averaging time window is large enough to sample the whole boundary layer turbulence spectrum. This approach cannot be applied to local scale PBL airborne measurements due to the speed of the aircraft. Short time window averages do not completely filter out PBL turbulence, especially in neutral to convective conditions. Therefore, we should expect observations to include short wavelength fluctuations and possibly transient structures that cannot be reproduced by model simulations. Moreover, shallow layers characterized by relevant specific humidity variations are expected to be removed by buoyancy over timescales that are comparable with the average values and representative of model results. Nevertheless, the strategy adopted here, e.g., treating measured profiles as quasi-instantaneous representations of vertical atmospheric variability and comparing them with the model output interpolated at the time of the measurements, is only capable of giving observational evidence of atmospheric properties, and is commonly adopted whenever comparing aircraft in-situ measurements with model data.

The model performance is analyzed for each variable on multiple profiles over different areas of the innermost domain (i.e., sea versus inland) and at different times of the day (i.e., morning versus afternoon). The results are reported at the single profile detail level only for one flight (Flight 3), which is quite representative of the encountered conditions during the three days of the campaign. Afterwards, aggregated performance indexes considering all of the profiles of all of the flights are presented and discussed.

3.1. Synoptic and Local Circulation Conditions during Flights

To understand the synoptic weather situations during the aircraft observational period, we have analyzed the surface pressure charts showing pressure and weather fronts at 00:00 UTC on 8–10 October 2014 provided by the Met Office (available at <http://www.wetterzentrale.de>), and the

thickness isopleths for the layer (500–1000) hPa (dam) and temperature at 850 hPa (°C) at 00:00 UTC of 8–10 October 2014 provided by European Centre for Medium Range Weather Forecast (ECMWF) reanalysis (ERA-Interim) (available at <http://www.meteociel.fr>).

Weather conditions for the measurement period (7–9 October 2014) showed a reinforcing high pressure system over northeastern Africa extending northeastward and linking to the Blocking Highs over Russia while a deeply cyclonic vortex persisted over the United Kingdom (UK) and much of the North Atlantic area, with the polar front jet stream forced way south across the Atlantic toward northwestern Africa before returning northeastward across the western Mediterranean Basin and Central Europe (Figure 3 panel a-b-c). These complicated patterns lead to an increasingly warm southwesterly flow over the study area, with temperatures rising well above average and higher than average stability conditions for the season (Figure 3 panel a1-b1-c1).

The limited pressure gradient that occurred over southern Italy favored the development of a sea breeze circulation characterized by surface winds blowing from S–SW during the daytime and N–NE during the night-time over the Naples region. Local meteorological conditions are described by the observations of the Napoli Capodichino airport meteorological station (International Civil Aviation Organization (ICAO) code LIRN) reported in Figure 4. The pressure shows high values with a slowly growing trend during 7–8 October 2014 becoming stationary from 8 October 2014 onward. The daily variability of wind speed and direction has a cyclic structure that characterizes coastal breeze circulation. Daily maximum wind speeds ranging between 3 m s^{-1} and 4 m s^{-1} are recorded during the early afternoon, and associated with directions from S–SW, while weak nightly currents blow from N–NE. These directions are determined by the gulf of Naples' local circulation. The temperature and relative humidity daily cycles are quite regular, with a slight growing trend of daytime maximum temperature, confirming the absence of relevant cloudiness.

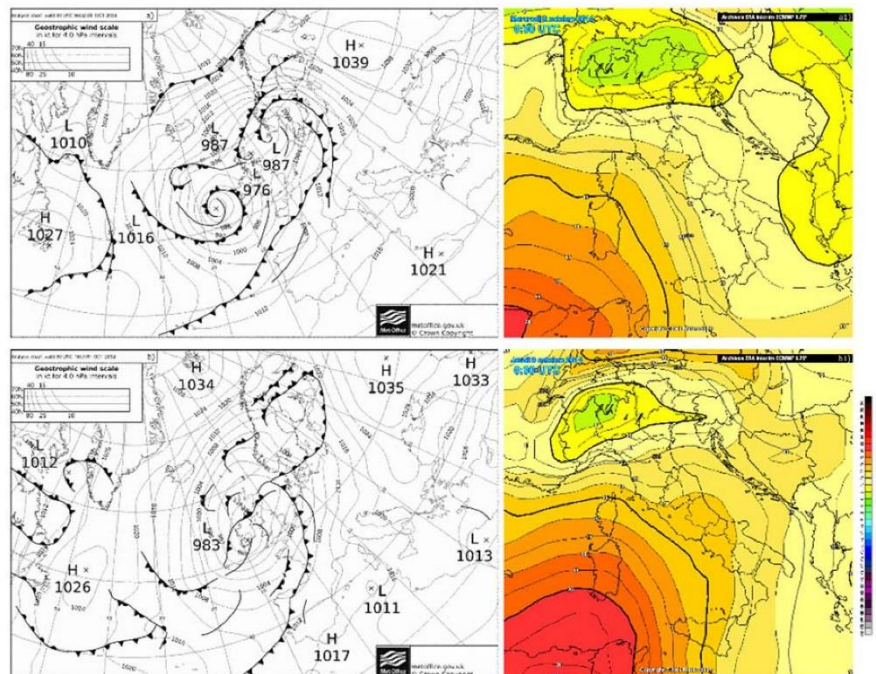


Figure 3. Cont.

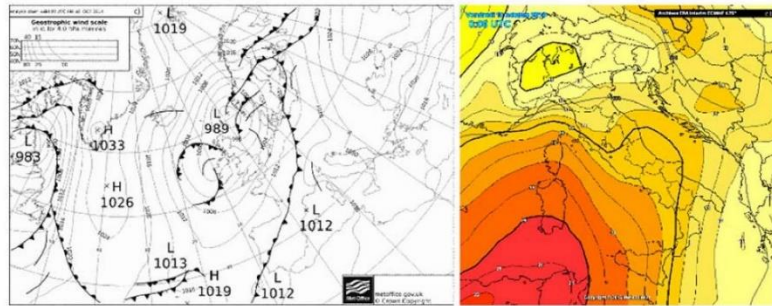


Figure 3. Surface pressure charts showing pressure and weather fronts at 00:00 UTC of 8–10 October 2014 (left panel a–c). Charts are provided by the Met Office and available at <http://www.wetterzentrale.de>. Thickness isopleths for the layer (500–1000) hPa (dam) and temperature at 850 hPa (°C) at 00:00 UTC of 8, 9 and 10 October 2014 (right panel a1–c1). Charts are provided by ECMWF reanalysis (ERA-Interim) and available at <http://www.meteociel.fr>.

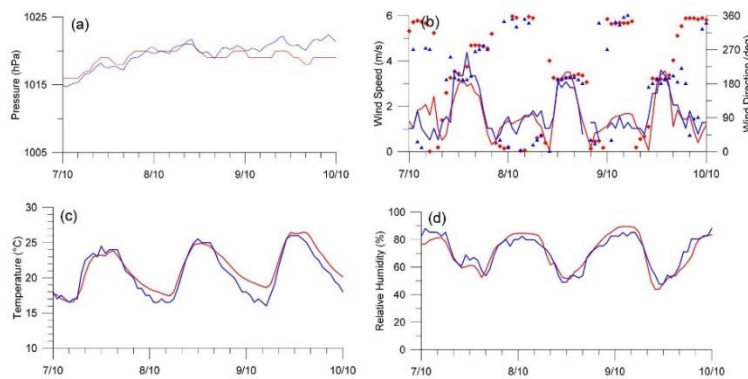


Figure 4. Napoli Capodichino airport (LIRN) surface meteorological observations (blue) and WRF simulation results with the Mellor–Yamada–Nakanishi–Niino Level 2.5 (MYNN2) planetary boundary layer (PBL) scheme (red) for: (a) pressure; (b) wind speed and direction; (c) air temperature; and (d) relative humidity.

WRF simulations were able to satisfactorily reconstruct the main features of the near surface meteorological variables with all of the tested PBL parameterizations. Figure 4 shows the results of WRF run with the MYNN2 scheme, which resulted as the best performing, with a correct reconstruction of all of the variables except for a tendency to overestimate night-time minimum temperature and surface pressure during the last day. The coastal breeze wind speed and direction cycle is particularly nicely reconstructed (Figure 4b). The results obtained with the different PBL schemes were hardly distinguishable when superposed in the same figure, except for MYJ, which showed an overestimation of daytime maximum wind speed with an overall BIAS = 0.19 m s⁻¹. BIAS, RMSE, and correlation obtained with the different PBL schemes ranged within the following intervals: wind speed: BIAS = -0.19–0.19 m s⁻¹; RMSE = 0.54–0.68 m s⁻¹; r = 0.77–0.86; temperature: BIAS = 0.66–1.06 K; RMSE = 1.21–1.39 K; r = 0.95–0.96; relative humidity: BIAS = ((-3.36)–(-0.39))%; RMSE = (5.09–7.09)%;

$r = 0.86\text{--}0.93$. The comparison of WRF results with surface observations confirms the capability of the model to describe the circulation structure during coastal breeze conditions over the investigated area, as it has been already verified during different midsummer episodes by Finardi et al. [11].

3.2. Vertical Profiles of Air Temperature, Specific Humidity, Wind Speed, and Direction

To get insights regarding the chosen PBL schemes with respect to observations, we have selected Flight 3 profiles in the present work. As mentioned earlier, Profile 1 (Figure 5) is overland, whereas Profile 2 (Figure 6) and 3 (Figure 7) are over sea, and Profile 4 (Figure 8) is again over land. The overall comparison shows that the main features of the vertical layering of the atmosphere are captured by WRF simulations with all of the considered PBL schemes. The wind speed is everywhere decreasing with height, with a SW direction near the surface and a strong shear in both direction and speed between 500–1000 m agl. Weak winds are observed from NE–SE in the upper monitored layers. The development of the modeled boundary layer matches the vertical location of the major temperature gradient, and correctly reproduced the upper layer temperature slopes. This generally indicates a reasonable reconstruction of the PBL depth and its time variation, even if the virtual potential temperature is generally overestimated in the lower atmospheric layers located within the PBL. It is worthwhile to remember that the growth of the PBL is not monotonic over land due to the development of the thermal internal boundary layer, which follows the sea breeze front penetration.

Some peculiar features of the observations are not reproduced by WRF with any of the PBL parameterizations. The measured virtual potential temperature shows a stable slope within the boundary layer that is particularly evident over sea (Figures 6 and 7), while modeled profiles are nearly uniform within the PBL, as expectable in well-mixed conditions. The specific humidity is overestimated in the lower layers and underestimated in the upper layers at Profile 1 and 3 (Figures 5 and 7), where observations show limited variation with height and relatively high values in the upper layers with respect to the other measured profiles. No model simulation is capable of reproducing the NW wind direction that is detected by measurements at Profile 4 (Figure 8), which is at variance with all of the other profiles measuring winds from directions around E, as predicted by the models. These discrepancies can be attributed to local features that are possibly transient, and are connected to the development to the breeze cell circulation and in particular, to the return current aloft. It can be noticed that WRF predicts a higher specific humidity over the sea than over land within the boundary layer, while measurements show variable conditions without clear sea/land differences. This behavior can be attributed to the near-coast location of the profiles measured over the sea.

Looking in more detail at the differences shown by the WRF results with the different PBL schemes, it can be observed that at the PRF1 inland vertical profile (Figure 5a), all of the schemes are overlapping each other in the lowest 600 m, and they all overestimate measured values of less than 1 °C. ACM2 shows a different vertical profile and a larger overestimation of the order of 2 °C. The observed (OBS) air virtual potential temperature between 600–1000 m is warmer than in the lower layers, and is roughly coincident with the model-simulated profiles. Only ACM2 shows temperatures colder than the measurements in this layer. All of the schemes' results are coincident above 1000 m, where they overestimate measurements of less than 1 °C, reproducing its vertical slope. The model reproduction of the vertical variation of wind is correct, showing the relevant decrease of wind speed and wind direction rotation in the shear layer observed between 500–900 m (Figure 5c,d). The trend of wind profiles near to the surface is better reproduced by ACM2 and MYNN2, while also MRF and BouLac schemes are able to reproduce the observed profile to a good extent. UW underestimates near surface winds, while MYJ and YSU overestimate them. The virtual potential temperature measured by PRF2 over sea (Figure 6a) is well reproduced by all of the schemes, with MYJ and BouLac showing the largest overestimation above 500 m agl, but being nearest to the observations in the lower layers. The observed wind speed profile (Figure 6c) shows generally weak winds, with a strong vertical variability and many pockets of high wind speed at 200 m, 400 m, 650 m, and 850 m. These features, which are not reproduced by simulations, make it difficult to rank the performances of the different PBL

schemes. However, it can be argued that *MYNN2*, *MRF*, and *UW* perform better than the other schemes, while *MYJ*, *BouLac*, and *YSU* overestimate wind speed, and *ACM2* underestimates it. The vertical profile of the wind speed observed at PRF3 above sea (Figure 7c) is correctly described by WRF with all of the PBL schemes. *MYNN2*, *ACM2*, and *MRF* produce wind speed that is better comparable with values measured below 200 m, while all of the other schemes show a tendency to overestimate them, which is particularly pronounced for *MYJ*, *BouLac*, and *YSU*.

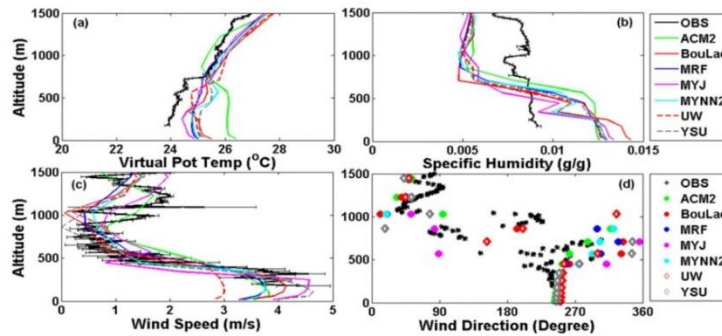


Figure 5. Vertical profile of (a) air temperature (°C); (b) wind speed (m/s); (c) specific humidity (g/kg); and (d) wind direction (degree) on 8 October 2014 during Flight 3: Profile 1 up. Error bars in observations are standard deviation values.

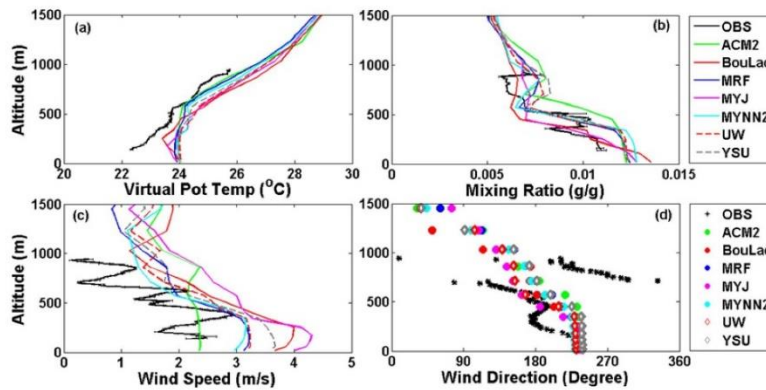


Figure 6. Vertical profile of (a) air temperature (°C); (b) wind speed (m/s); (c) specific humidity (g/kg); and (d) wind direction (degree) on 8 October 2014 during Flight 3: Profile 2 up. Error bars in observations are standard deviation values.

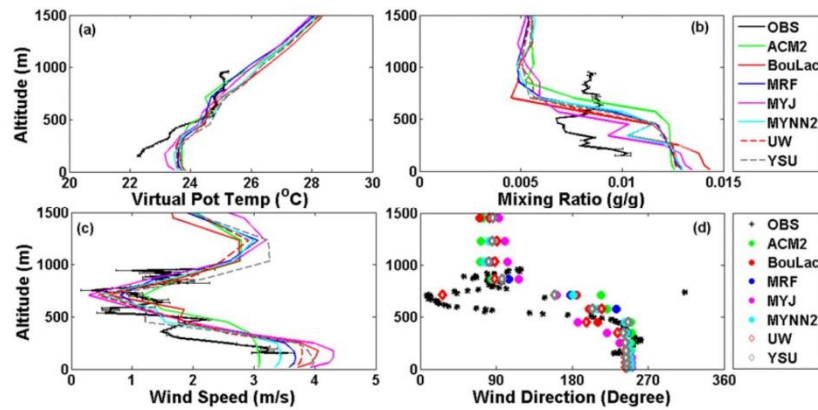


Figure 7. Vertical profile of (a) air temperature (°C); (b) wind speed (m/s); (c) specific humidity (g/kg); and (d) wind direction (degree) on 8 October 2014 during Flight 3: Profile 3 up. Error bars in observations are standard deviation values.

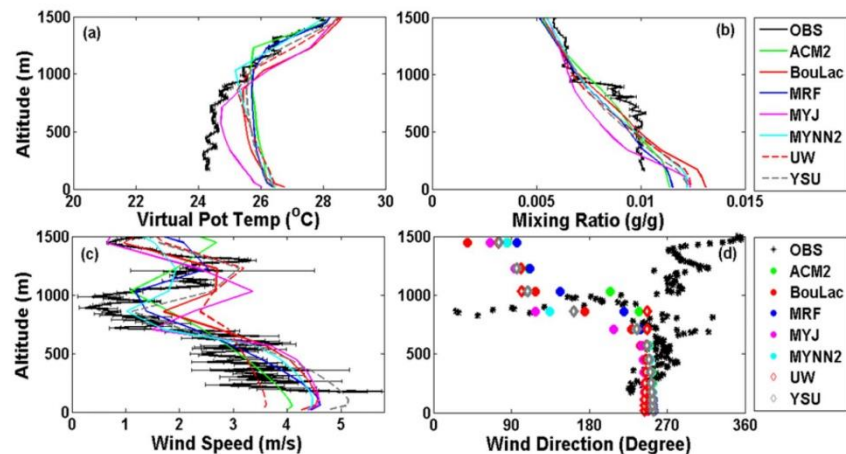


Figure 8. Vertical profile of (a) air temperature (°C); (b) wind speed (m/s); (c) specific humidity (g/kg); and (d) wind direction (degree) on 8 October 2014 during Flight 3: Profile 4 up. Error bars in observations are standard deviation values.

The detailed comparison of the different PBL schemes’ performance with virtual potential temperature measured at PRF4 above land (Figure 8a) show similar results in the lower 1000 m for all parameterization, while *MYJ* is closer to the measurements. On the other hand, *MYJ* and *BouLac* show larger errors over 1000 m, where *MRF*, *ACM2*, and *MYNN2* better fit the virtual potential temperature measurements. *MYJ* shows also larger discrepancies than the other schemes with respect to specific humidity below 1000 m (Figure 8b). Wind speed (Figure 8c) observations are quite fluctuating along the entire profile, which is a feature that makes their comparison with model results difficult. The observed fluctuations must be considered a subgrid variation considering both horizontal and vertical resolution. The overall variation of wind speed with height is reproduced by almost all of the PBL schemes, with *ACM2*, *MYNN2*, and *MRF* performing best, and the tendency of *YSU* to overestimate near surface wind speed.

Model and data compared at different locations within the same area in the central hours of the day flight (Flight 3) show a highly dynamic situation, with a non-uniform sea breeze penetration and the presence of circulation layers: the southern profiles of the domain, PRF1 over land and PRF3 over sea (Figures 5 and 7), both show a strong return flow with a wind turning from westerly (up to 700 m) to easterly (above 700 m) direction, which is correctly reproduced by all of the schemes. The northern profiles, PRF4 over land and PRF2 over sea, show a stronger sea breeze penetration (Figures 6 and 8) that is not entirely reproduced by WRF, as a likely consequence of a non-optimal simulation of the timing of sea breeze penetration in a dynamic context. The complexity of the atmospheric flow and the PBL structure during sea breeze inland penetration is illustrated in Figure 9 by the results of WRF simulations on 8 October 2014 at 13:00 GMT with *MYNN2* and *YSU* schemes. The sea breeze front is clearly detectable where the wind speed gradient is located just upwind of the maximum value of the PBL height. The overlap of the flight track helps to realize the intrinsic difficulty to compare local profiles with modeled atmospheric fields characterized by relevant space and time variability.

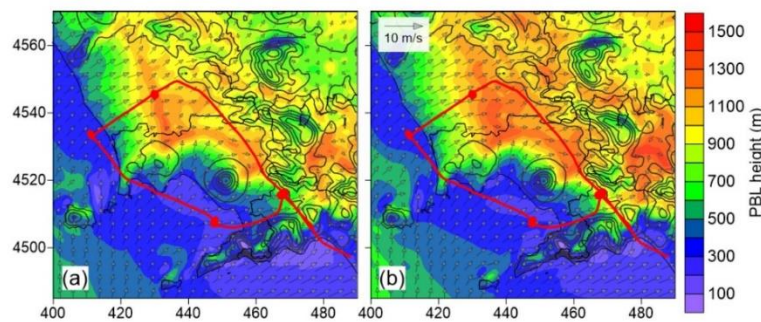


Figure 9. PBL height (m) predicted by WRF model simulations for 8 October 2014 at 13:00 GMT with *MYNN2* (panel a) and Yonsei University (*YSU*) (panel b) PBL parameterization. Wind field at 10-m height is represented by grey arrows (one arrow out of four). The red line superposed represents the flight track.

Overall, a larger variability among the schemes is observed for the wind vector than for temperature and specific humidity, while the observed and modeled variability among schemes is always lower than the variability among the different profiles for all of the variables. The observed and modeled profiles of air temperature, specific humidity, winds, and PBL height from flights 1, 2, 4, and 5 (not shown here) have also been analyzed, revealing similar behavior of the various schemes in reproducing atmospheric circulations, with respect to Flight 3 reported above (Figures 5–8). Performance across the full set of flights is analyzed in the following section.

3.3. Spatial and Temporal Assessment of Model PBL Schemes

When grouping the observed profiles for all of the flights with respect to their location (i.e., over the sea or over the inland, Figure 1), and with respect to the time of the day (i.e., morning or afternoon flights, Table 2), significantly better performance is overall achieved at inland sites with respect to the sea, and at morning with respect to afternoon flights (Figures 10 and 11). However, important differences are observed among the variables: higher correlation coefficients and lower RMSE are obtained especially for specific humidity and temperature (Figure 10a,d and Figure 11a,d). For specific humidity analysis, it is observed that RMSE is lower during morning flights and over sea flights compared to those in the afternoon or over land. The wind direction (in degree) (Figure 10e,f and Figure 11e,f), shows better simulated profiles over sea, whereas afternoon and morning simulations

perform similarly. Wind speeds are better simulated in the morning compared to the afternoon (Figure 10g,h and Figure 11g,h). The reasons for this difference in performance is likely related to difficulty in reproducing vertical variability at sea, where very shallow PBL develop that may not be entirely reproduced, as also confirmed by the detailed analysis of sea profiles from Flight 3 (Figures 5–8). This result is also consistent with simulated PBL depths at sea locations that exhibit a larger bias with respect to observations at inland locations with well developed convective boundary layers (Table 4). The reasons for the better performance at morning with respect to afternoon flights are likely related to the model capability of fully reproducing sea breeze development, and the interface between sea breeze and the synoptic circulation. Since inland profile locations PRF1 and PRF4 are relatively close to the coastal line, even relatively small errors in space and time in reproducing sea breeze penetration may lead to a significant bias in the model results (extracted at the requested point) with respect to observational values. Moreover, the model shows generally high values of specific humidity in the lower 500 m for profiles observed over the sea during all of the flights (Figures 5–8).

Table 4. Performance statistics of PBL height prediction according to the seven configurations of PBL schemes for all of the profiles of the Sky Arrow flights. The best performances are highlighted in a bold red color, and the second best is highlighted in blue. Other values within ± 60 m (1/2 of WRF grid spacing at 500 m) are reported in green. The profiles for which we cannot determine PBL height from observations are left blank in the *OBS* column.

Schemes	ACM2	BouLac	MRF	MYJ	MYNN2	UW	YSU	OBS
Profiles								
Flight 1: 7 October 2014, 08:39–10:58 UTC								
p1	1047	1040	912	995	1000	889	983	980
p2	586	671	601	628	528	439	517	700
p3	702	715	593	671	494	518	568	750
p4	1441	1390	1398	1435	1323	1392	1387	-
Flight 2: 7 October 2014, 12:38–16:56 UTC								
p1	1135	879	925	686	751	682	848	-
p2	770	630	871	743	762	694	773	450
p3	888	540	788	638	702	439	640	600
p4	1331	1142	1225	1017	1151	1159	1195	-
Flight 3: 8 October 2014, 12:47–14:46 UTC								
p1	1002	901	850	744	705	830	949	1000
p2	464	390	382	356	364	425	418	360
p3	365	319	320	312	297	284	309	200
p4	972	859	799	790	877	1016	856	830
Flight 4: 9 October 2014, 08:39–10:37 UTC								
p1	421	445	302	392	347	403	390	400
p2	226	200	142	106	144	129	135	480
p3	128	183	161	145	141	138	147	500
p4	774	923	765	902	770	816	862	820
Flight 5: 9 October 2014, 12:09–14:24 UTC								
p1	654	653	441	472	381	557	449	1005
p2	268	198	240	203	201	190	204	400
p3	186	169	184	132	161	131	188	310
p4	770	754	614	446	538	670	570	680

BouLac, *UW*, *MYNN2*, and *ACM2* proved to be the better schemes for simulating specific humidity profiles over land (Figures 10 and 11). However, the overall variability between morning and afternoon flights, and between sea and inland profile sites, always exceeds the variability among different PBL schemes. This indicates the importance of the underlying meteorological model that overwhelms the importance of PBL scheme choice. *YSU* (first-order closure) and *MYNN2* (TKE closure) are proved to be

the best schemes for all of the profiles (Figure 12). Among the first-order closure schemes, *YSU* proved to be the best scheme for simulating the wind speed profiles of all of the flights. The *MYNN2* scheme, which predicts TKE terms at subgrid levels, provided the best simulation overall, considering all of the meteorological variables and all of the observed profiles (Figure 12). *MYNN2* uses a unique surface layer scheme, and was reported to better simulate surface heat fluxes (Banks et al. 2016) [22]. Madala et al. [19] also found that *MYNN2* was better performing when compared against eddy covariance energy flux observations. *MRF*, *YSU*, and *ACM2* have the ability of simulating deep convection/deep PBL in their formulation, which explains their relatively low performance over the sea, when compared with flight observations [26,48]. It has been observed [48] that *MYJ* produces a shallower PBL height than the non-local schemes during the daytime. The potential temperature profiles are showing a warm bias near the ground and a cool bias starting near 0.75 km and reaching above the PBL height by *MYJ* [48]. This might be the reason for the under performance of *MYJ* in the present study compared to *MYNN2*. *MYNN2*, *UW*, and *BouLac* showed improved reproduction of the observed profiles compared to other PBL schemes; however, the subtle difference in the base formulation results in the different performance of the three schemes. The *UW* is developed by taking into account stratocumulus clouds and their influence on PBL, and is therefore more suitable for climate runs with longer time steps, diagnosing rather than forecasting turbulent kinetic energy (TKE), and simulating layers determined by the vertically varying stability of the thermodynamic profile [26]. The *BouLac* scheme is better suited for cases with terrain-induced turbulence to study its impact on PBL [16]. It can be observed that the *MYJ* and *MYNN2*-simulated profiles for potential temperature, specific humidity, and wind speed are showing significant differences among each other, although the *MYJ* and *MYNN2* base formulation is the same [49,50]. This can be explained by the difference in *MYNN2* formulation constraints. It has been observed that *MYJ* is having a tendency to underestimate boundary layer height during upstream locations of convection, while *MYNN2* improves this drawback over non-local PBL schemes and supports deep convection [48]. The mixing length formulations used in *MYNN2* are also more flexible for the static stability regimes compared to *MYJ* [26]. This difference in formulation results in appreciable differences in the simulated profiles also in the present work (Figures 5–8). Over land (profiles 1 and 4), the *MYNN2*-simulated profiles are showing a better reproduction of observed profiles compared to *MYJ*. Also, the afternoon simulated profiles show an improvement of *MYNN2* compared to *MYJ* (Figures 10 and 11) for all of the flights. It is worth noticing here that no modification on any of the PBL schemes used in the present study was made, keeping them in their original form, as provided in the WRF model.

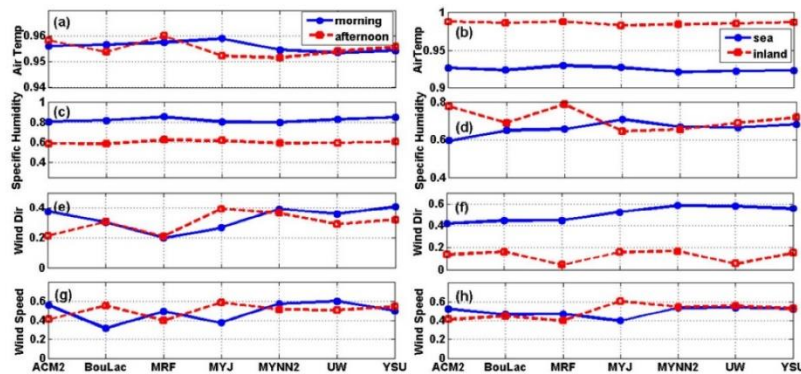


Figure 10. Variation of Pearson coefficient for PBL schemes used in the present study for all of the flights (flights 1–5) for air temperature, specific humidity, wind direction, and wind speed for morning/afternoon (a,c,e,g) and over sea/inland (b,d,f,h) respectively.

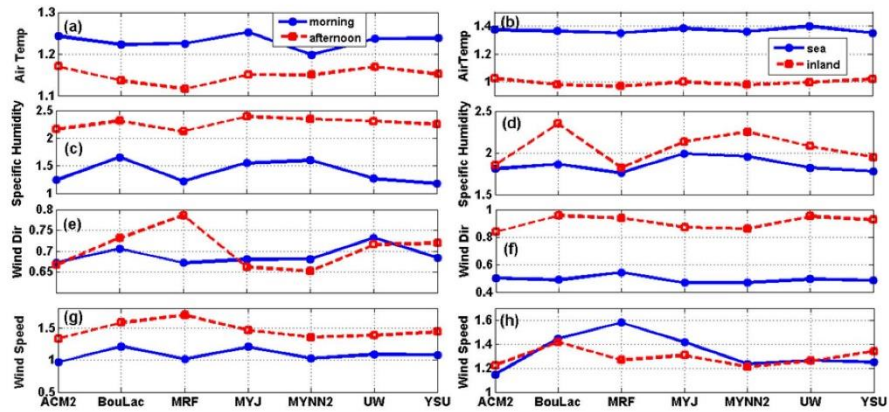


Figure 11. Variation of root mean square error (RMSE) for PBL schemes used in the present study for all flights (flights 1–5) for air temperature, specific humidity, wind direction, and wind speed for morning/afternoon (a,c,e,g) and over sea/inland (b,d,f,h) respectively.

As all of the profiles were observed during the day time when a surface heated convective boundary layer was already developed, it was possible for the TKE closure schemes to provide an overall good performance. It was found that the TKE closure schemes performed better than the first-order closure schemes for the CASES-99 experiment study over the Kansas area in the United States (U.S.) [16]. In our work, *YSU* performs better among first-order closure schemes. The *YSU* scheme increases the thermally-induced mixing and allows for the early development of PBL before noon, which is helpful for this scheme in comparison to *ACM2* and *MRF* to better simulate the PBL height (Table 4). When we analyze the performance of TKE closure schemes, the *MYNN2* scheme is ranked as the best in all of the flights and conditions (Figure 12).

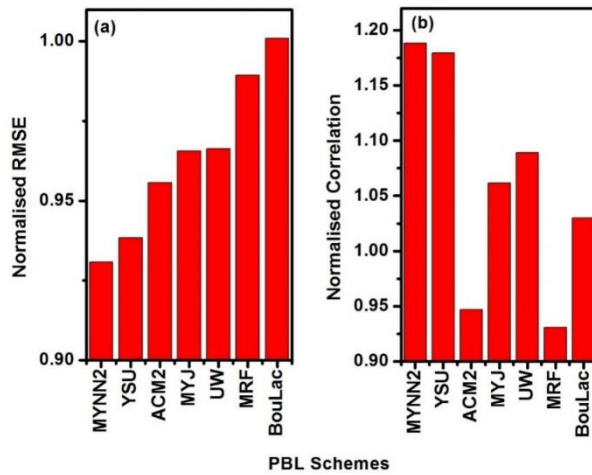


Figure 12. Variation of normalized RMSE (a) and normalized correlation (b) for PBL schemes used in the present study for all of the meteorological variables and profiles.

The normalized RMSE and correlation values for Figure 12 are obtained using the ratio of RMSE/correlation value of a particular scheme divided by the mean value of all of the schemes. This normalization allows values to go above or below 1, as the average value (by considering all of the schemes) is lower/higher than an individual scheme value that is performing better/worse than the average. In case of normalized RMSE, *MYNN2* is the best-performing scheme (Figure 12a), as the value of RMSE for *MYNN2* is less than the average value calculated, which gives the lowest normalized RMSE value for *MYNN2*. Similarly, Figure 12b shows that *MYNN2* again is having the highest correlation (greater than one in this case), which is a result of normalization.

However, our findings do not allow for the identification of a specific scheme providing a better performance in any condition. As evidenced by the discussion of WRF results at each measured profile location, the variability in model errors is more related to both the spatial and temporal variability of atmospheric properties than to the behavior of the different PBL schemes. Overall, our findings are consistent with Gioli et al. [65], indicating that sea breeze transition is a critical phenomenon to be correctly simulated in time and space with a WRF-based modeling setup. However, these results allow the identification of a subset of PBL schemes that perform comparably, and constitute useful data to constrain the choice of the PBL scheme in the setup of a WRF modeling chain for meteorological or air quality predictions.

3.4. Comparison of Observed and Modeled PBL Height

The PBL height predicted by the different schemes and available within the WRF standard output is hardly comparable, because different computational methods can produce different estimates of the PBL height, even with the same meteorological input fields. This condition makes it difficult to distinguish differences due to the method to compute PBL height from those due to the meteorological fields produced by WRF with different parameterizations. Therefore, PBL height has been re-computed for each profile by analyzing potential temperature and wind profiles through the application of a criterion based on the bulk Richardson number (Sorensen 1998) [64] as implemented by the WRF post-processor called UPP (<https://dtcenter.org/upp/users/index.php>), developed by the National Centers for Environmental Prediction (NCEP). This approach produces comparable results, and differences can be attributed to the structure of the meteorological fields in the lower atmospheric layers. Simulated and measured values are compared and presented in Table 4 for all of the profiles. It is observed that no single scheme can be chosen as the best-performing for PBL height simulation in all of the examined conditions.

MYNN2, which performs better in simulating other meteorological variables, is not always the best-performing scheme in predicting PBL height. *BouLac*, *MYJ*, *YSU*, and *ACM2* are able to simulate PBL height in equal good proportion considering all of the flights. However, it can be observed from Table 4 that the simulated PBL heights are closer to observations over land compared to sea. At the same time, the vertical grid spacing of the WRF computational mesh should also be kept into account, which grows with height and is roughly 120 m deep at 500 m agl. The model grid spacing intrinsically limits the precision of the PBL height estimation, and should make consider comparable values within the grid spacing range.

The values resumed in Table 4 illustrate the strong space and time variability of the boundary layer depth over the investigated area. The coastal location, the complex terrain, and the non-uniformity of land cover—as the Naples–Caserta conurbation is characterized by mixed urban and agricultural areas—cause the horizontal variation of the boundary layer structure. The dominant breeze circulation regime characterizing fair weather conditions introduces a time variability that is usually characterized by a decrease of the PBL depth over the inland areas when they are reached by the sea breeze front. These features are partially reproduced by the model whose accuracy is limited by its space resolution, together with the PBL parameterization scheme features.

4. Conclusions

WRF model simulations using different PBL schemes have been compared with aircraft observations and analyzed to assess model performance over a complex coastal study area with associated sea breeze circulations. We have presented a comparison of WRF results with observed vertical profiles of air temperature, specific humidity, wind speed, wind direction, and PBL height, and computed statistical scores for each PBL scheme. The overall performance of WRF with all of the selected schemes is assessed on vertical profiles that indirectly indicate the reconstruction of local scale circulation and sea breeze development. The performance criteria for meteorological model results [66,67] were able to distinguish the better-performing PBL schemes out of all of the model runs. As the aircraft observations include high frequency PBL turbulence fluctuations that are filtered out in the WRF model results as a subgrid scale turbulent component of meteorological variables, this reproduction is proving the model's ability to simulate the conditions on a smaller scale aptly. Overall, the findings of the present study are consistent with Gioli et al. [65], indicating that the sea breeze transition is a critical phenomenon to be correctly simulated in time and space with a WRF-based modeling setup.

No single boundary layer turbulence scheme can be termed as the optimal PBL scheme for all of the tests performed at different times and in different locations within the present study. However, the TKE closure scheme *MYNN2* was the best performing in regard to simulating meteorological variables in accordance with normalized cumulated statistical indexes. The results from this study constitute a solid framework that could be followed for the initial performance assessment of a modeling chain, and the identification of the optimal setup for a specific study area. However, aircraft measurements should be also made in different seasons of the year in order to verify the consistency of results. Besides other factors that shall be considered when identifying the PBL scheme to be used in a WRF modeling chain, such as the computational performance, the methodology proposed here can add a level of information to better drive such choice, which is often made arbitrarily. The limitations to all of the PBL schemes and the WRF configuration presented here arise from the model capacity of reproducing sea breeze circulations and the presence of return current layers. The wind speed and direction representation for the lowest 500 m is generally excellent for the better PBL schemes, while the sudden change of wind direction due to the presence of circulation layers is not well reproduced by any of the schemes at all of the locations monitored by vertical profiles, where local differences are detected. Our findings point out that a valid modeling methodology to reduce uncertainties would be running model ensembles of the better-performing PBL schemes and deploying modeling architectures that are commonly used in Earth system sciences [68], although at the cost of a higher demand of computing power.

Author Contributions: Conceptualization, B.G., V.M., B.T., S.F., D.G., P.C., P.T., A.Z., A.R., G.C. and A.D.; Writing—original draft, B.T.; Writing—review & editing, B.T., S.F. and B.G.

Funding: This research was funded by Government of Regione Campania.

Acknowledgments: Authors want to acknowledge the Government of Regione Campania, Italy, for providing financial resources to carry on this study. Authors are also thankful to the team members of AriaSaNa project who dedicated their time and efforts to make the experiment successful.

Conflicts of Interest: The authors declare no conflict of interest.

References

1. Schmale, J.; Schindell, D.; von Schneidemesser, E.; Chabay, I.; Lawrence, M. Air Pollution: Clean up our skies. *Nature* **2014**, *515*, 335–337. [[CrossRef](#)] [[PubMed](#)]
2. Zhang, Y.; Sartelet, K.; Wu, S.Y.; Seigneur, C. Application of WRF/Chem-MADRID and WRF/Polyphemus in Europe—Part 1: Model description, evaluation of meteorological predictions, and aerosol-meteorology interactions. *Atmos. Chem. Phys.* **2013**, *13*, 6807–6843. [[CrossRef](#)]
3. Angevine, W.M.; Eddington, L.; Durkee, K.; Fairall, C.; Bianco, L.; Brioude, J. Meteorological Model Evaluation for CalNex 2010. *Mon. Weather Rev.* **2012**, *140*, 3885–3906. [[CrossRef](#)]

4. Kim, Y.; Sartelet, K.; Raut, J.C.; Chazette, P. Evaluation of the Weather Research and Forecast/Urban Model over Greater Paris. *Bound.-Layer Meteorol.* **2013**, *149*, 105–132. [[CrossRef](#)]
5. Govardhan, G.; Nanjundiah, R.S.; Satheesh, S.K.; Krishnamoorthy, K.; Kotamarthi, V.R. Performance of WRF-Chem over Indian region: Comparison with measurements. *J. Earth Syst. Sci.* **2015**, *124*, 875–896. [[CrossRef](#)]
6. Arunachalam, S.; Holland, A.; Do, B.; Abraczinskas, M. A quantitative assessment of the influence of grid resolution on predictions of future year air quality in North Carolina, USA. *Atmos. Environ.* **2006**, *40*, 5010–5026. [[CrossRef](#)]
7. Borge, R.; Alexandrov, V.; del Vas, J.J.; Lumbreras, J.; Rodriguez, E. A comprehensive sensitivity analysis of the WRF model for air quality applications over the Iberian Peninsula. *Atmos. Environ.* **2008**, *42*, 8560–8574. [[CrossRef](#)]
8. Misemis, C.; Zhang, Y. An examination of sensitivity of WRF/Chem predictions to physical parameterizations, horizontal grid spacing, and nesting options. *Atmos. Res.* **2010**, *97*, 315–334. [[CrossRef](#)]
9. Skamarock, W.C.; Klemp, J.B.; Dudhia, J.; Gill, D.O.; Barker, D.M.; Duda, M.G.; Huang, X.Y.; Wang, W.; Powers, J.G. *A Description of the Advanced Research WRF Version 3*; National Centre of Atmospheric Research: Boulder, CO, USA, 2008.
10. Yver, C.E.; Graven, H.D.; Lucas, D.D.; Cameron-Smith, P.J.; Keeling, R.F.; Weiss, R.F. Evaluating transport in the WRF model along the California coast. *Atmos. Chem. Phys.* **2013**, *13*, 1837–1852. [[CrossRef](#)]
11. Finardi, S.; Agrillo, G.; Baraldi, R.; Calori, G.; Carlucci, P.; Ciccioli, P.; D'Allura, A.; Gasbarra, D.; Gioli, B.; Magliulo, V.; et al. Atmospheric dynamics and ozone cycle during seabreeze in a Mediterranean complex urbanized coastal site. *J. Appl. Meteorol. Climatol.* **2018**, *57*, 1083–1099. [[CrossRef](#)]
12. Silibello, C.; Calori, G.; Brusasca, G.; Giudici, A.; Angelino, E.; Fossati, G.; Peroni, E.; Buganza, E. Modelling of PM₁₀ Concentrations over Milano Urban Area Using Two Aerosol Modules. *Environ. Model. Softw.* **2008**, *23*, 333–343. [[CrossRef](#)]
13. Kukkonen, J.; Olsson, T.; Schultz, M.; Baklanov, A.; Klein, T.; Miranda, I.; Monteiro, A.; Hirtl, M.; Tarvainen, V.; Boy, M.; et al. A review of operational, regional-scale, chemicalweatherforecastingmodels in Europe. *Atmos. Chem. Phys.* **2012**, *12*, 1–87. [[CrossRef](#)]
14. Gioli, B.; Miglietta, F.; Vaccari, F.P.; Zaldei, A.; DeMartino, B. The Sky Arrow ERA, an innovative airborne platform to monitor mass, momentum and energy exchange of ecosystems. *Ann. Geophys.* **2006**, *49*, 109–116.
15. Zhong, S.; In, H.; Clements, C. Impact of turbulence, land surface, and radiation parameterizations on simulated boundary layer properties in a coastal environment. *J. Geophys. Res.* **2007**, *112*. [[CrossRef](#)]
16. Shin, H.H.; Hong, S.Y. Intercomparison of Planetary Boundary-Layer Parametrizations in the WRF Model for a Single Day from CASES-99. *Bound.-Layer Meteorol.* **2011**, *139*, 261–281. [[CrossRef](#)]
17. Mohan, M.; Bhati, S. Analysis of WRF Model Performance over Subtropical Region of Delhi, India. *Adv. Meteorol.* **2011**, *2011*, 621235. [[CrossRef](#)]
18. Xie, B.; Fung, J.C.H.; Chan, A.; Lau, A. Evaluation of nonlocal and local planetary boundary layer schemes in the WRF model. *J. Geophys. Res.* **2012**, *117*, D12103. [[CrossRef](#)]
19. Madala, S.; Satyanarayana, A.N.V.; Srinivas, C.V.; Kumar, M. Mesoscale atmospheric flow field simulations for air quality modeling over complex terrain region of Ranchi in eastern India using WRF. *Atmos. Environ.* **2015**, *107*, 315–328. [[CrossRef](#)]
20. Madala, S.; Satyanarayana, A.N.V.; Srinivas, C.V.; Tyagi, B. Performance Evaluation of PBL Schemes of WRF-ARW Model in the Simulating Thermo-Dynamical Structure of Pre-monsoon convective Episodes over Kharagpur using STORM Data Sets. *Pure Appl. Geophys.* **2016**, *173*, 1803–1827. [[CrossRef](#)]
21. Banks, R.F.; Tiana-Alsina, J.; Rocadenbosch, F.; Baldasano, J.M. Performance Evaluation of the Boundary-Layer Height from Lidar and the Weather Research and Forecasting Model at an Urban Coastal Site in the North-East Iberian Peninsula. *Bound.-Layer Meteorol.* **2015**, *157*, 265–292. [[CrossRef](#)]
22. Banks, R.F.; Tiana-Alsina, J.; Baldasano, J.M.; Rocadenbosch, F.; Papayannis, A.; Solomos, S.; Tzanis, C.G. Sensitivity of boundary-layer variables to PBL schemes in the WRF model based on surface meteorological observations, lidar, and radiosondes during the HygrA-CD campaign. *Atmos. Res.* **2016**, *176–177*, 185–201. [[CrossRef](#)]
23. Li, X.; Pu, Z. Sensitivity of numerical simulation of early rapid intensification of hurricane Emily (2005) to cloud microphysical and planetary boundary layer parameterizations. *Mon. Weather Rev.* **2008**, *136*, 4819–4838. [[CrossRef](#)]

24. Hu, X.M.; Nielson-Gammon, J.W.; Zhang, F. Evaluation of three Planetary Boundary Layer schemes in the WRF model. *J. Appl. Meteorol. Climatol.* **2010**, *49*, 1831–1844. [CrossRef]
25. Garcia-Diez, M.; Fernandez, J.; Fita, L.; Yague, C. Seasonal dependence of WRF model biases and sensitivity to PBL schemes over Europe. *Q. J. R. Meteorol. Soc.* **2013**, *139*, 501–514. [CrossRef]
26. Cohen, A.E.; Cavallo, S.M.; Coniglio, M.C.; Brooks, H.E. A review of planetary boundary layer parameterization schemes and their sensitivity in simulating southeastern U.S. cold season severe weather environments. *Weather Forecast.* **2015**, *30*, 591–612. [CrossRef]
27. Qian, Y.; Yan, H.; Berg, L.; Hagos, S.; Feng, Z.; Yang, B.; Huang, M. Assessing impacts of PBL and surface layer schemes in simulating the surface-atmosphere interactions and precipitation over the tropical ocean using observations from AMIE/DYNAMO. *J. Clim.* **2016**, *29*, 8191–8210. [CrossRef]
28. Demographic Balance Data. 2014. Available online: <http://demo.istat.it> (accessed on 22 June 2018).
29. Martuzzi, M.; Mitis, F.; Bianchi, F.; Minichilli, F.; Comba, P.; Fazzo, L. Cancer mortality and congenital anomalies in a region of Italy with intense environmental pressure due to waste. *Occup. Environ. Med.* **2009**, *66*, 725–732. [CrossRef] [PubMed]
30. Fazzo, L.; de Santis, M.; Mitis, F.; Benedetti, M.; Martuzzi, M.; Comba, P.; Fusco, M. Ecological studies of cancer incidence in an area interested by dumping waste sites in Campania (Italy). *Ann. Ist. Super. Sanita* **2011**, *47*, 181–191. [PubMed]
31. Pirastu, R.; Zona, A.; Ancona, C.; Bruno, C.; Fano, V.; Fazzo, L.; Iavarone, I.; Minichilli, F.; Mitis, F.; Pasetto, R.; et al. Mortality results in SENTIERI Project. *Epidemiol. Prev.* **2011**, *35*, 29–152. [PubMed]
32. Triassi, M.; Alfano, R.; Illario, M.; Nardone, A.; Caporale, O.; Montuori, P. Environmental Pollution from Illegal Waste Disposal and Health Effects: A Review on the “Triangle of Death”. *Int. J. Environ. Res. Public Health* **2015**, *12*, 1216–1236. [CrossRef] [PubMed]
33. Barone, G.; D’Ambra, P.; di Serafino, D.; Giunta, G.; Murli, A.; Riccio, A. Application of a parallel photochemical air quality model to the Campania region (southern Italy). *Environ. Model. Softw.* **2000**, *15*, 503–511. [CrossRef]
34. Vellinga, O.S.; Dobosy, R.J.; Dumas, E.J.; Gioli, B.; Elbers, J.A.; Hutjes, R.W.A. Calibration and quality assurance of flux observations from a small research aircraft. *J. Atmos. Ocean. Technol.* **2013**, *30*, 161–181. [CrossRef]
35. Dobosy, R.; Dumas, E.J.; Senn, D.L.; Baker, B.; Seyres, D.S.; Witinski, M.F.; Healy, C.; Munster, J.; Anderson, J.G. Calibration and quality assurance of an airborne turbulence probe in an aeronautical wind tunnel. *J. Atmos. Ocean. Technol.* **2013**, *30*, 182–196. [CrossRef]
36. WRF User Manual, 2015 ARW Version 3 Modeling System User’s Guide. January 2015. Available online: http://www2.mmm.ucar.edu/wrf/users/docs/user_guide_V3.5/ARWUsersGuideV3.pdf (accessed on 22 June 2018).
37. Vogelezang, D.H.P.; Holtslag, A.A.M. Evaluation and model impacts of alternative boundary-layer height formulations. *Bound.-Layer Meteorol.* **1996**, *81*, 245–269. [CrossRef]
38. Pleim, J.E. A combined local and non-local closure model for the atmospheric boundary layer. Part 1: Model description and testing. *J. Appl. Meteorol. Climatol.* **2007**, *46*, 1383–1395. [CrossRef]
39. Blackadar, A.K. Modeling pollutant transfer during daytime convection. In *Preprints Fourth Symposium on Atmospheric Turbulence, Diffusion, and Air Quality*; American Meteorological Society: Reno, NV, USA, 1978; pp. 443–447.
40. Hong, S.Y.; Pan, H.L. Nonlocal boundary layer vertical diffusion in a medium-range forecast model. *Mon. Weather Rev.* **1996**, *124*, 2322–2339. [CrossRef]
41. Troen, L.; Mahrt, L. A simple model of the atmospheric boundary layer: Sensitivity to surface evaporation. *Bound.-Layer Meteorol.* **1986**, *37*, 129–148. [CrossRef]
42. Wyngaard, J.C.; Brost, R.A. Top-down and bottom-up diffusion of a scalar in the convective boundary layer. *J. Atmos. Sci.* **1984**, *41*, 102–112. [CrossRef]
43. Stull, R.B. Review of non-local mixing in turbulent atmospheres: Transilient turbulence theory. *Bound.-Layer Meteorol.* **1993**, *62*, 21–96. [CrossRef]
44. Hong, S.Y.; Noh, Y.; Dudhia, J. A new vertical diffusion package with an explicit treatment of entrainment processes. *Mon. Weather Rev.* **2006**, *134*, 2318–2341. [CrossRef]
45. Loboeki, L. Mellor-Yamada simplified second-order closure models: Analysis and application of the generalized von Karman local similarity hypothesis. *Bound.-Layer Meteorol.* **1992**, *59*, 83–109. [CrossRef]

46. Janjic, Z. *Nonsingular Implementation of the Mellor-Yamada Level 2.5 Scheme in the NCEP Meso Model*; NCEP Office Note, No. 437; National Centers for Environmental Prediction: College Park, MD, USA, 2002; p. 61.
47. Janjic, Z. The step-mountain coordinate: Physical package. *Mon. Weather Rev.* **1990**, *118*, 1429–1443. [[CrossRef](#)]
48. Coniglio, M.C.; Correia, J., Jr.; Marsh, P.T.; Kong, F. Verification of convection-allowing WRF model forecasts of the planetary boundary layer using sounding observations. *Weather Forecast.* **2013**, *28*, 842–862. [[CrossRef](#)]
49. Mellor, G.L.; Yamada, T. A hierarchy of turbulence closure models for planetary boundary layers. *J. Atmos. Sci.* **1974**, *31*, 1791–1806. [[CrossRef](#)]
50. Mellor, G.L.; Yamada, T. Development of a turbulence closure model for geophysical fluid problems. *Rev. Geophys. Space Phys.* **1982**, *20*, 851–875. [[CrossRef](#)]
51. Nakanishi, M. Improvement of the Mellor–Yamada turbulence closure model based on large-eddy simulation data. *Bound.-Layer Meteorol.* **2001**, *99*, 349–378. [[CrossRef](#)]
52. Nakanishi, M.; Niino, H. An improved Mellor–Yamada level-3 model with condensation physics: Its design and verification. *Bound.-Layer Meteorol.* **2004**, *112*, 1–31. [[CrossRef](#)]
53. Nakanishi, M.; Niino, H. Development of an improved turbulence closure model for the atmospheric boundary layer. *J. Meteorol. Soc. Jpn.* **2009**, *87*, 895–912. [[CrossRef](#)]
54. Bougeault, P.; Lacarrere, P. Parameterization of orography-induced turbulence in mesoscale model. *Mon. Weather Rev.* **1989**, *117*, 1872–1890. [[CrossRef](#)]
55. Martilli, A.; Clappier, A.; Rotach, M.W. An urban surface exchange parameterisation for mesoscale models. *Bound.-Layer Meteorol.* **2002**, *104*, 261–304. [[CrossRef](#)]
56. Grenier, H.; Bretherton, C.S. A moist PBL parameterization for large-scale models and its application to subtropical cloud-topped marine boundary layers. *Mon. Weather Rev.* **2001**, *129*, 357–377. [[CrossRef](#)]
57. Bretherton, C.; Park, S. A new moist turbulence parameterization in the community atmosphere model. *J. Clim.* **2009**, *22*, 3422–3448. [[CrossRef](#)]
58. Gent, P.R.; Danabasoglu, G.; Donner, L.J.; Holland, M.M.; Hunke, E.C.; Jayne, S.R.; Lawrence, D.M.; Neale, R.B.; Rasch, P.J.; Vertenstein, M.; et al. The Community Climate System Model Version 4. *J. Clim.* **2011**, *24*, 4973–4991. [[CrossRef](#)]
59. Wyngaard, J.C. Toward Numerical Modeling in the “Terra Incognita”. *J. Atmos. Sci.* **2004**, *61*, 1816–1826. [[CrossRef](#)]
60. Ito, J.; Niino, H.; Nakanishi, M.; Moeng, C. An Extension of the Mellor–Yamada Model to the TerraIncognita Zone for Dry Convective Mixed Layers in the Free Convection Regime. *Bound.-Layer Meteorol.* **2015**, *157*, 23–43. [[CrossRef](#)]
61. Skamarock, W.C. Evaluating Mesoscale NWP Models Using Kinetic Energy Spectra. *Mon. Weather Rev.* **2004**, *132*, 3019–3032. [[CrossRef](#)]
62. Wang, X.Y.; Wang, K.C. Estimation of atmospheric mixing layer height from radiosonde data. *Atmos. Meas. Tech.* **2014**, *7*, 1701–1709. [[CrossRef](#)]
63. Seidel, D.J.; Ao, C.O.; Li, K. Estimating climatological planetary boundary layer heights from radiosonde observations: Comparison of methods and uncertainty analysis. *J. Geophys. Res.* **2010**, *115*. [[CrossRef](#)]
64. Sorensen, J.H. Sensitivity of the DERMA long-range Gaussian dispersion model to meteorological input and diffusion parameters. *Atmos. Environ.* **1998**, *32*, 4195–4206. [[CrossRef](#)]
65. Gioli, B.; Gualtieri, G.; Busillo, C.; Calastrini, F.; Gozzini, B.; Miglietta, F. Aircraft wind measurements to assess a coupled WRF-CALMET mesoscale system. *Meteorol. Appl.* **2014**, *21*, 117–128. [[CrossRef](#)]
66. Thunis, P.; Georgieva, E.; Galmarini, S. A Procedure for Air Quality Models Benchmarking, FAIRMODE Report Version 2. 2011. Available online: <http://fairmode.jrc.ec.europa.eu/> (accessed on 22 June 2018).
67. Enhanced Meteorological Modeling and Performance Evaluation for Two Texas Ozone Episodes. Available online: <https://www.tceq.texas.gov/assets/public/implementation/air/am/contracts/reports/mm/EnhancedMetModelingAndPerformanceEvaluation.pdf> (accessed on 22 June 2018).
68. Yuan, X.; Wood, E.F. On the clustering of climate models in ensemble seasonal forecasting. *Geophys. Res. Lett.* **2012**, *39*. [[CrossRef](#)]



Atmospheric Dynamics and Ozone Cycle during Sea Breeze in a Mediterranean Complex Urbanized Coastal Site[Ⓞ]

SANDRO FINARDI,^a GIUSEPPE AGRILLO,^b RITA BARALDI,^c GIUSEPPE CALORI,^a
PANTALEONE CARLUCCI,^b PAOLO CICCIOI,^c ALESSIO D'ALLURA,^a DANIELE GASBARRA,^{b,c}
BENIAMINO GIOLI,^d VINCENZO MAGLIULO,^b PAOLA RADICE,^a PIERO TOSCANO,^d AND
ALESSANDRO ZALDEI^d

^aARIANET S.R.L., Milan, Italy

^bCNR/ISAFOM, Ercolano, Italy

^cCNR/IBIMET, Bologna, Italy

^dCNR/IBIMET, Florence, Italy

^eUniversità di Napoli Federico II, Naples, Italy

(Manuscript received 3 May 2017, in final form 15 January 2018)

ABSTRACT

Persistent high pressure conditions over the Mediterranean Basin favor the occurrence of sea breezes that can lead to ozone transport through complex recirculation patterns. These features were investigated during an ozone episode with hourly concentrations exceeding $200 \mu\text{g m}^{-3}$ that occurred on July 2015 in Naples (Italy), one of the largest and densest conurbations in the Mediterranean region. Aircraft measurements were taken at heights from 150 to 1500 m AGL and compared and integrated with high-resolution meteorological and air quality model simulations to investigate local circulation and pollutants dynamics. The integration of airborne measurements, surface observations, and modeling established a framework to assess the photochemical phenomena in the area. Sea breezes and local emissions triggered ozone production at inland areas, causing high concentrations between the coast and the Apennine chain. Ozone was then injected into the upper boundary layer and transported toward the sea by the wind rotation occurring above 500 m AGL, causing a complex vertical layering of concentrations, with maxima between 500 and 800 m AGL. Vertical growth of the ozone concentration profile was also caused by the decrease of the boundary layer depth occurring when the breeze front reached the inland area carrying NO_x -rich air from the densely populated coast and favoring titration near the surface. Although the whole airshed was a net ozone producer, local surface concentrations were determined by a complex interaction of atmospheric flow and chemistry at different scales, supporting the need for coordinated efforts to control smog precursors over wide areas.

1. Introduction

Ozone is a photochemical air pollutant with harmful effects on humans, animals, and plants. Recent epidemiological studies showed that both long- and short-term exposure to elevated ozone concentrations result in increased morbidity and mortality (WHO 2013; Henschel and Chan 2013). Ozone absorption damages plant cells, impairing their functionality and affecting agricultural yields and forest growth (Paoletti 2006;

Calfapietra et al. 2009). Although ozone is a major indicator of photochemical smog itself, its production is connected to the abundance of other organic and inorganic reactive species potentially harmful for human beings and plants, being associated with an increase of the oxidative capacity of the atmosphere and secondary aerosol formation (Atkinson 2000; Kanakidou et al. 2005).

The vulnerability of the Mediterranean Basin to photochemical air pollution is well known; for example, Lelieveld et al. (2002) found summer ozone concentrations over the Mediterranean 2.5–3 times as high as the hemispheric background level. Satellite observations of tropospheric ozone highlight that the Mediterranean Basin is among the most noticeable production and accumulation zones at global scale (Ziemke et al. 2011).

[Ⓞ] Supplemental information related to this paper is available at the Journals Online website: <https://doi.org/10.1175/JAMC-D-17-0117.s1>.

Corresponding author: Sandro Finardi, s.finardi@aria-net.it

DOI: 10.1175/JAMC-D-17-0117.1

© 2018 American Meteorological Society. For information regarding reuse of this content and general copyright information, consult the AMS Copyright Policy (www.ametsoc.org/PUBSReuseLicenses).

The analysis of long-term ozone measurements does not indicate a stable reduction trend for the photochemical pollution (Parrish et al. 2012; Sicard et al. 2013). The consistent reduction in anthropogenic precursors emissions achieved in the European Union has not led to the expected reduction in ozone concentrations (European Environment Agency 2015). Different factors contributed to this result: the increase in intercontinental transport of ozone and its precursors in the Northern Hemisphere, which drove an increase in hemispheric background concentrations (Bach et al. 2014); the reduction in emissions of nitrogen oxides (NO_x), which led to an increase in ozone concentrations inside highly urbanized areas because of the reduced titration effect (Sicard et al. 2013; Querol et al. 2014). Ozone therefore remains one of the pollutants of major concern in southern Europe. The potential health impact of ozone is particularly severe for large cities, where it combines with that of other air pollutants, and of the changing climate, as weather is expected to become increasingly warm and dry over the Mediterranean Basin in the next decades (IPCC 2007, 2014; Giorgi and Lionello 2008; Gualdi et al. 2013; Lionello et al. 2014).

Summertime atmospheric circulation in the western Mediterranean Basin is characterized by distinctive features: the presence of mountains close to coastal areas favors the combination of land-sea breezes, mountain-valley breezes, and slope winds, generating return flows possibly across several layers (Millán et al. 2000). Daytime compensatory subsidence over the coast and sea can be superimposed on large-scale subsidence because of the anticyclonic circulation over the basin. Nighttime land breeze can transport polluted air masses above the maritime boundary layer building reservoirs that may be advected onshore during the following day (Millán et al. 1997, 2000, 2002, 2005; Gangoiti et al. 2001; Ancellet and Ravetta 2005; Jiménez et al. 2006; Castell et al. 2008). The land-sea breeze cycle can drive pollutant recirculation for prolonged periods and contribute to ozone formation via both local and regional sources. Local NO_x emissions are considered to have a major role in ozone formation near the surface, while longer-range transport is more relevant at higher levels (Richards et al. 2013). Emissions of biogenic volatile organic compounds (BVOC) also impact ozone concentration over the Mediterranean Basin (Liakakou et al. 2007) and may increase summertime daily maxima by 5–10 ppbv at different locations (Thunis and Cuvelier 2000; Curci et al. 2009). Shipborne measurements showed high ozone levels over the open sea during summer anticyclonic conditions: in particular, ozone concentration over the southeastern Tyrrhenian Sea was found to be driven by the presence of photochemically

“aged” air masses containing ozone precursors emitted in the Rome and Naples areas (Velchev et al. 2011). The influence of sea-breeze circulation on the evolution of ozone abundance has also been described in other areas of the world (see, e.g., McKendry and Lundgren 2000; Cheng 2002; Sills et al. 2011), showing similarities with the Mediterranean dynamics summarized here.

The Italian peninsula presents a peculiar condition within the Mediterranean because of the presence of the high Apennine mountain chain at moderate distance from the coast, favoring the development of breeze circulations on both its western and eastern coasts. Anthropogenic activities in the densely populated coastal areas cause an injection of precursors into recirculating air masses that may be already ozone rich. This atmospheric dynamic is considered one of the reasons why the European Union (EU) limit for the protection of human health and vegetation (European Union 2008) is not attained in Italy (European Environment Agency 2015).

The relationships between summer circulation and ozone production have been studied in different areas of southern Italy on the basis of surface observations (Ciccioli et al. 1987; Mangia et al. 2010; Schipa et al. 2009; Schürmann et al. 2009), while no investigation was based on upper-air observations within the atmospheric boundary layer (ABL) that can provide insights into topography and stratified circulation effects on coastal ozone dynamics.

Naples is the main conurbation of southern Italy and one of the largest urbanized areas on the Mediterranean shores, with more than three million inhabitants and a population density exceeding $10\,000\text{ km}^{-2}$ in some municipalities. Its vulnerability to ozone pollution is increased by intense agriculture spread over the inland plains and by forest areas extending farther inland over the Apennine chain and on Mount Vesuvius. Because of their geographical location and the prevalence of a sea-breeze wind regime during spring and summer, the agricultural and natural vegetation areas are exposed to the urban plume and can be affected by high ozone concentrations. On the other hand, forests may enhance ozone concentrations because of the photooxidation of BVOC emissions in the presence of NO_x (Fuentes et al. 2000; Atkinson and Arey 2003; Kemper Pacheco et al. 2014).

The Naples region has never been thoroughly investigated despite its vulnerability and its major role as source of ozone precursors; therefore, an assessment of the mechanisms regulating photochemical pollutants production and transport is desirable to identify possible measures to limit VOC and NO_x emissions and reduce human and ecosystems' exposure. This study analyses the ozone dynamics over the city of Naples and its surroundings. Surface and airborne meteorological and

trace gases observations have been combined with regional and local-scale meteorological and air quality modeling to interpret the observed summer ozone cycles. Upper-air measurements were taken by the SkyArrow Environmental Research Aircraft (ERA) research aircraft (Gioli et al. 2006), which provided meteorological and air quality observations within the ABL and free troposphere, finally assessing the meteorological and photochemical processes controlling ozone formation, transport, and layering in urbanized coastal areas.

2. Observations and model simulations

This study was part of the Aria Salerno Napoli (Air in Salerno and Napoli district) (AriaSaNa) project, integrating regional ground-based and airborne measurements with state-of-the-art meteorological and air quality modeling. Within the project framework, a specific field campaign was planned to study the atmospheric circulation and emissions conditions favoring the occurrence of high ozone episodes.

a. Airborne measurements

The Sky Arrow ERA is a small, certified aircraft equipped with sensors to measure three-dimensional wind and turbulence at high frequency, together with gas concentrations and other atmospheric parameters (Gioli et al. 2006). The instrumentation deployed in this study included: a best aircraft turbulence (BAT) measuring 3D wind speed and air temperature at 50-Hz frequency; an open-path infrared gas analyzer (IRGA; Licor 7500) to measure H_2O and CO_2 concentration at 50 Hz; a laser altimeter (Riegl LD90-3) measuring aircraft above ground altitude; a UV analyzer (2B Technologies 202) to measure ozone concentration at 1 Hz with an accuracy of ~ 1 ppb.

The campaign was planned on the basis of weather forecasts and performed on 15–16 July 2015, when a high pressure ridge of African origin affected the Mediterranean Basin and continental Europe (see Fig. S1 in the online supplemental material), causing high temperatures in different areas of the continent. Satellites showed clear-sky conditions over southern Italy and the western and central Mediterranean (see, e.g., the MODIS image in supplemental Fig. S1). The aircraft performed four flights during the morning and afternoon of 15 and 16 July 2015, including both horizontal transects and vertical profiles, at a cruise speed of ~ 150 km h^{-1} . Transects were flown at an average height of 150 m AGL along a counterclockwise square track with side length of about 30 km enclosing Naples, its gulf, and Mount Vesuvius (Fig. 1). Four vertical upward and downward profiles (P1 to P4) were made at each of the track vertexes, from near

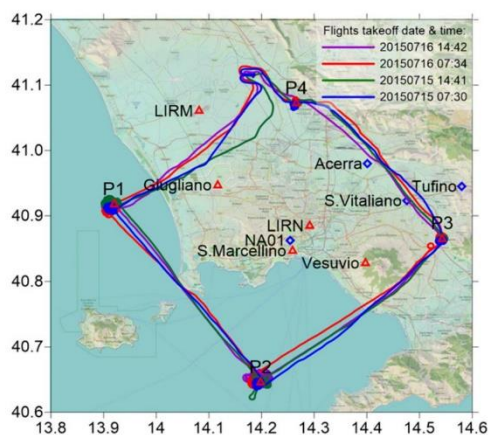


FIG. 1. Meteorological (red triangles) and air quality (blue diamonds) station locations, flight tracks, and location of the vertical profiles (P1–P4). Takeoff dates and local solar times are indicated in the legend. The axes show geographic coordinates.

ground up to a height of about 1500 m AGL, reaching the free troposphere between 0800 and 1700 local solar time (LST). P1 and P2 were located over the sea, while P3 and P4 were over land (Fig. 1).

The high-frequency observational data stream was then low-pass filtered to compute 30-s average values of wind speed WS , wind direction WD , air temperature T , and ozone concentration, to be compared with corresponding model data associating each average measured value to the spatially and temporally closest model gridcell value. The value of 30 s to apply low-pass filtering was chosen as the best compromise to maintain high-resolution spatial information from flight data and to average high-frequency fluctuations associated with turbulent structures that are not resolved by numerical models (Gioli et al. 2004). The 30-s interval corresponds to an average horizontal flight path of about 1.3 km, which is well comparable to model spatial gridcell size (1 km). Nevertheless, averaged aircraft measurements can still include temporal variability of atmospheric fields that, being in some circumstances related to non-stationary conditions, may be scarcely representative on model spatial and temporal scales.

b. Ground-based meteorological and air quality observations

While no information is routinely available on the vertical structure of the atmosphere, several ground-based meteorological and air quality stations are in operation in the study area (Fig. 1). Meteorological measurements were provided by the World Meteorological Organization

TABLE 1. WRF-ARW physics options.

WRF physics scheme	Description
Microphysics	Single-moment 6-class scheme (ice, snow, and graupel processes)
Longwave radiation	Rapid Radiative Transfer Model
Shortwave radiation	Goddard shortwave
Cumulus parameterization	Kain–Fritsch scheme (deep and shallow convection)
Land surface	Noah land surface model
Surface layer	Eta similarity (based on Monin–Obukhov theory)
Planetary boundary layer	Mellor–Yamada–Janjić eta operational scheme

(WMO) stations of Napoli Capodichino [International Civil Aviation Organization (ICAO) code LIRN] and Grazzanise (ICAO code LIRM) airports. Further surface micrometeorological measurements were made at the San Marcellino site, at roof level in Naples city center (40.8473°N, 14.2578°E), and at the northwestern periurban site of Giugliano (40.9471°N, 14.1171°E), which were both equipped with sonic anemometers.

The Naples conurbation air quality is monitored by the Regional Environmental Protection Agency of Campania Region (<http://www.arpacampania.it/>) measuring concentrations of pollutants regulated by the European air quality directives (European Union 2008). Routinely available measurements were integrated by supplementary air quality stations located at the San Marcellino site and at the Vesuvius Observatory (<http://www.ov.ingv.it/>; 40.8279°N; 14.3973°E).

c. Meteorological and air quality models

The AriaSaNa air quality forecast system for Naples city and the surrounding Campania region is based on the Flexible Air Quality Regional Model (FARM) chemical transport model (Silibello et al. 2008; Mircea et al. 2014) coupled with the Weather Research and Forecasting (WRF) Model (Skamarock et al. 2008). Pollutant emissions were modeled starting from the national emission inventory (Taurino et al. 2018), disaggregated at municipal level through activity-based proxies and supplemented by local information concerning industries and road and maritime traffic. WRF simulations were driven by the NOAA/NCEP GFS global-scale meteorological forecast, downloaded with 0.5° grid spacing every 6 h. Air quality boundary conditions were provided by the QualeAria air quality forecast system (Kukkonen et al. 2012; <http://www.qualearia.it/>), which uses the air quality model FARM and runs at European and national scale driven by the Copernicus Atmosphere Monitoring Service (CAMS) global air quality forecast (<https://atmosphere.copernicus.eu/>). The physics schemes used by the WRF-ARW (version 3.5.1) forecast are summarized in Table 1. FARM gas phase chemistry implements

the Statewide Air Pollution Research Center, version 1999 (SAPRC-99), model (Carter 2000).

The modeling system was configured to provide high-resolution results on a target domain that encompasses all the measurement flight tracks, covering the central Campania region that includes all the major cities, the whole inland plains area, and a large percentage of the region's population (Fig. 2). Both WRF and FARM use two-way nesting. WRF was configured with four nested domains (Table 2), from continental scale down to the local target area, using a grid spacing of 3 km in the third domain, covering the whole Campania region, and of 1 km in the innermost fourth domain. FARM used two nested domains covering Campania and the target area with grid spacings of 4 and 1 km, respectively. Model results were stored at hourly frequency. Surface values and vertical profiles of meteorological variables and pollutants concentrations were extracted at the surface stations and at aircraft profile locations, by selecting the nearest available time frame and applying bilinear interpolation among the four surrounding grid points on each model level.

Backward trajectories have been computed using RIP4, a WRF postprocessor developed by the National Center for Atmospheric Research (NCAR) and by the University of Washington (Stoelinga 2009), which includes the capability to compute backward/forward trajectories from WRF simulation results.

3. Atmospheric circulation over the Gulf of Naples

Local atmospheric circulation during the campaign was characterized by the typical sea–land breeze cycle, as detected by the LIRN observation tower (Fig. 3). Sea-breeze southerly winds were observed during the late morning and the central hours of the day, with maximum speed ranging from 4 to 6 m s⁻¹. Beginning in the late afternoon the wind turned from westerly to northerly, assuming the local land-breeze direction with decreasing speed and reaching nearly calm conditions at night (Fig. 3a). These breeze circulation features are similar to

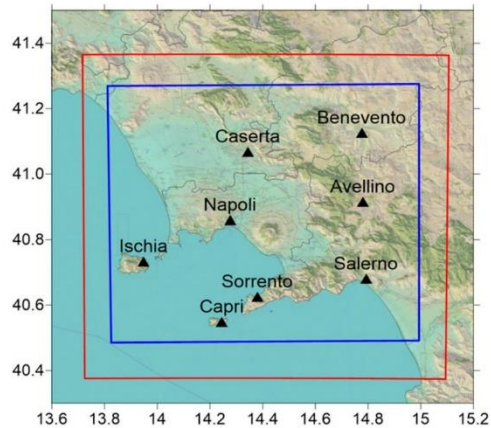


FIG. 2. Inner computational domains of the WRF (red) and FARM models (blue). Major cities and geographical locations are indicated by triangles.

those observed at other coastal sites (Millán et al. 2000; Adame et al. 2010; David and Nair 2011). Surface pressure showed a slowly increasing trend over the study period, evidencing subsidence due to the high pressure ridge persistence over the western Mediterranean (Fig. 3b). Air temperature showed a slight increasing trend in its daily maximum value, which exceeded 35°C on 17 July (Fig. 3c). Relative humidity had a general decreasing trend with short-term fluctuations (Fig. 3d). The surface winds were fairly well reproduced by the WRF Model simulation, which satisfactorily described the daily temperature cycles, decreasing relative humidity trend, and rising pressure (Figs. 3a–d). Surface energy and momentum fluxes measured with eddy covariance at the Giugliano rural site, northwest of Naples, were also correctly reproduced (Fig. 4), confirming a reliable reconstruction of near-surface weather conditions. The SkyArrow aircraft performed two flights a day to monitor circulation and air quality conditions during morning and afternoon hours. Weak winds with variable directions were measured during the 15 July morning flight (Fig. 5a), which lasted from 0730 to 1040 LST. WRF simulation confirmed the winds

variability, but only partially reproduced aircraft measurements along the northwest and southeast legs, while relevant differences in wind direction were found along the southwest leg, over the sea, and the northeast leg, over the land (Fig. 5a). This result could be expected during the morning transition between land and sea-breeze circulation, when local slope flows, residual land breezes, and transient phenomena can be dominant. The overall atmospheric circulation conditions predicted by WRF are depicted by the cross section at 180-m height AGL of the wind field computed at 0900 LST, showing large spatial variability over the domain (Fig. 5c).

Measured winds showed a well-developed sea-breeze circulation during the afternoon flight (from 1443 to 1739 LST) with prevailing west-southwest direction and an average speed of 5.9 m s^{-1} along the horizontal legs of the aircraft trajectory, flown at an average height of 157 m AGL (Fig. 5b). Local wind features were quite well reproduced by WRF, while significant discrepancies were only observed in the wake of Mount Vesuvius, where local orographic effects were dominant and strong turbulence conditions were recorded in the pilot report and confirmed by high-frequency wind fluctuation measurements. The turbulent kinetic energy in the Mount Vesuvius wake area showed an average value 40% larger than that measured along the overland portions of the horizontal flight legs. Horizontal wind spatial variability observed along the flight path can be interpreted from the analysis of the correspondent modeled wind field at 180 m AGL (Fig. 5d): the eastward wind rotation along the western leg of the flight is caused by the wake of Ischia Island, while the wind acceleration and convergence observed southeast and northeast of Mount Vesuvius can be attributed to topographic channeling and wake effect. The morning and afternoon flights on 16 July (not shown) confirmed a similar atmospheric circulation, with a slightly earlier development of the sea breeze and a prevailing southeast wind direction over the Gulf of Naples, which improved the agreement between observations and WRF simulations during the morning hours.

The measured vertical profiles, extending to a height of about 1600 m AGL, included the whole ABL and the first section of the adjacent free troposphere. P4 profiles

TABLE 2. WRF-ARW nested grid spacing.

Grid No.	Horizontal grid spacing (km)	Vertical level No.	Cumulus parameterization
1	45	41	Kain–Fritsch scheme
2	9	41	Kain–Fritsch scheme
3	3	41	None
4	1	41	None

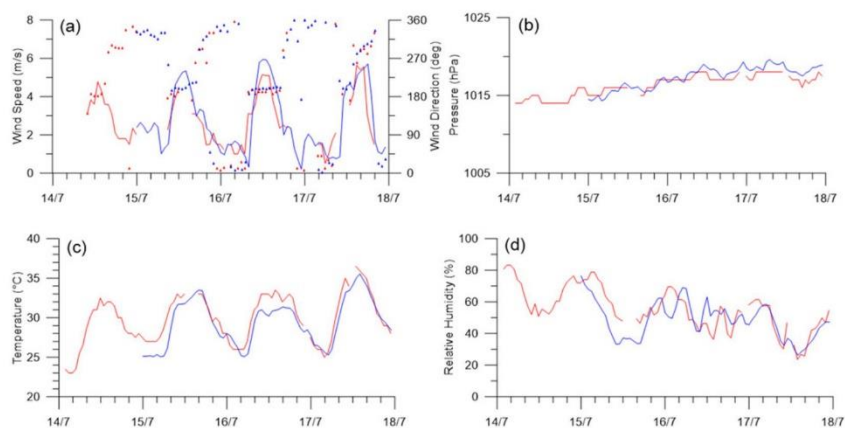


FIG. 3. Napoli Capodichino (LIRN) meteorological observations (red) and WRF simulation results (blue): (a) wind speed and direction, (b) sea level pressure, (c) air temperature, and (d) relative humidity.

(Fig. 6) are particularly interesting because of their location (Fig. 1), which is representative of the sea-breeze development and penetration over the inland plains area where high ozone concentrations are often recorded. The 15 July morning profile was measured from 1007 to 1033 LST, when a convective ABL is usually already well developed in summer fair-weather conditions. Both measured and modeled potential temperature profiles showed an adiabatic lapse rate up to 800–1000 m (Fig. 6c). The ABL depth has been evaluated applying the Sorensen (1998) method, as the height where the bulk Richardson number grows above a critical threshold value set to 0.25. This approach has been

applied to both measured and modeled profiles for consistency. The ABL depth computed from WRF results at this location was 735 m at 1000 LST, with an underestimation of about 9% with respect to the value of 808 m computed from airborne measurements (Fig. 6c). Very weak winds with wide direction variability were measured by the aircraft within the boundary layer, without a definable prevailing direction (Figs. 6a,b). Wind speed increased from 1 to 2 m s^{-1} to roughly 6 m s^{-1} from 800 to 1600 m, with a well-defined east-northeast direction. The WRF simulation correctly reproduced such wind speed variation with height, and predicted the east-southeast direction in the

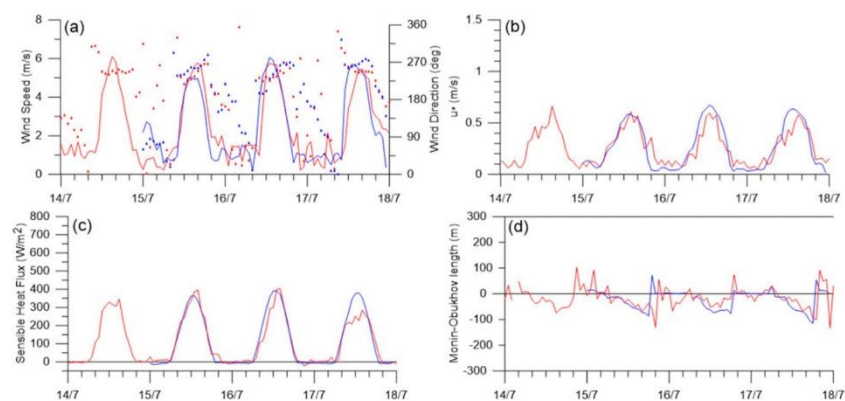


FIG. 4. Giugliano sonic anemometer observations (red) and WRF simulation results (blue): (a) wind speed and direction, (b) friction velocity, (c) sensible heat flux, and (d) Monin–Obukhov length.

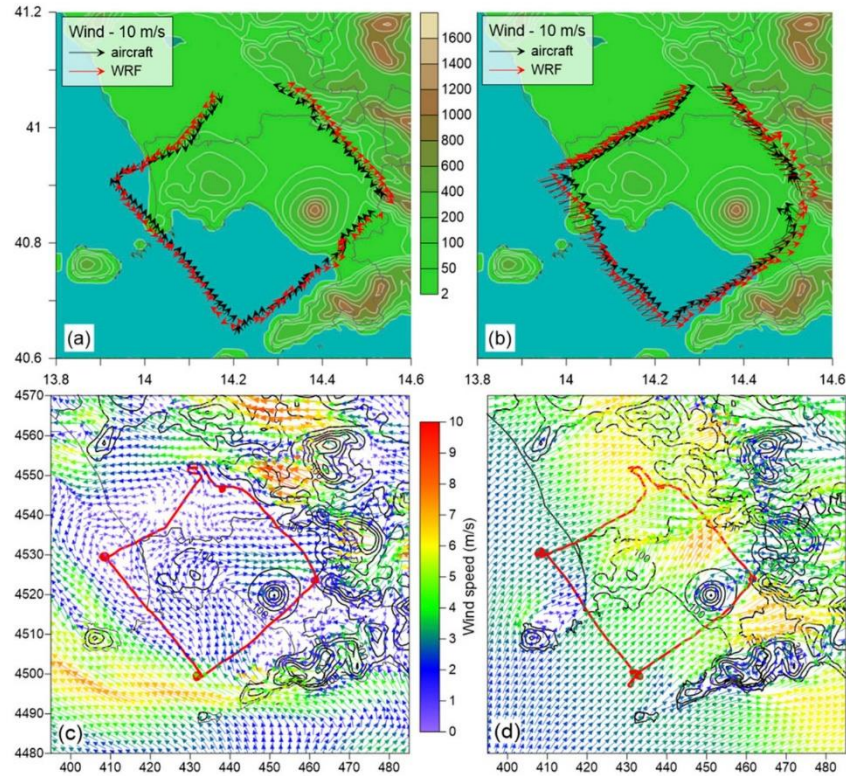


FIG. 5. Wind speed and direction measured by the aircraft during 15 Jul (a) morning and (b) afternoon along the horizontal flight legs (black arrows) compared with WRF results (red arrows). Color scale refers to topography height. Wind fields predicted by WRF simulations at 180 m AGL at (c) 0900 and (d) 1500 LST 15 Jul. The superimposed red line indicates the flight track.

upper layers and west-southwest direction below 400 m, showing an earlier sea-breeze front penetration with respect to aircraft observations.

The 15 July afternoon flight measurements showed sea-breeze winds with west-west-southwest direction up to about 1000 m, turning counterclockwise until becoming east at 1600 m (Figs. 6d,e). The wind speed was around 5 m s^{-1} in the lower 500 m, decreasing at higher levels, up to about 1200 m, where a layer characterized by relevant wind direction shear and slowly growing speed was observed up to 1600 m (Figs. 6d,e). The wind profile was well reproduced by WRF predictions, with a limited difference between 600 and 1200 m, where the modeled direction was southwest, with a difference of about 45° with respect to observations. It is worthwhile to note that the potential temperature profile showed an inversion at low elevation, between 400 and 600 m, that

was also reproduced by WRF, with an overestimation of about 1.2°C in the lower layers. The ABL depth of 440 m diagnosed from WRF results was substantially coincident with the value of 436 m estimated from measurements (Fig. 6f). As expected, the sea-breeze penetration over the inland plains caused a collapse of the ABL depth (Fig. 6f) with respect to the late morning values (Fig. 6c) because of the formation of a thermal internal boundary layer (Garratt 1990). This feature can be important to understanding ozone dynamics because of the possible trapping in the residual layer of pollutants dispersed vertically in the deeper boundary layer before the sea-breeze front arrival (Millán et al. 2000).

P3 was strongly influenced by its geographical location, east of Mount Vesuvius, measuring a south-southeast wind with speed decreasing with height in the lower 500 m during both morning and afternoon flights (Figs. 7a,d).

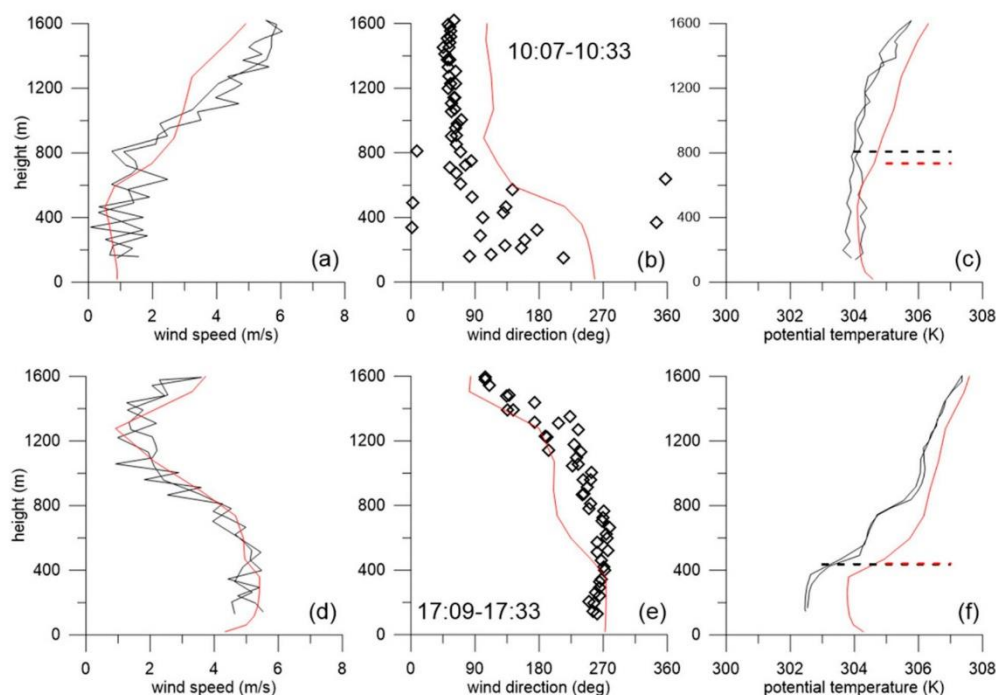


FIG. 6. Vertical profiles of (a),(d) wind speed, (b),(e) wind direction, and (c),(f) potential temperature measured by the aircraft on 15 Jul along its ascending and descending flight paths (black line and symbols) at location P4 compared with WRF results (red lines) extracted from the closest hourly time frame, at the same location. Morning flights are shown in (a)–(c) and afternoon flights are shown in (d)–(f); reference time intervals are indicated in (b) and (e). Dashed lines in (c) and (f) show the boundary layer height estimated from measured and computed meteorological profiles using the bulk Richardson number criterion.

Above this layer, the wind speed increased with height, blowing from the east during the morning and northwest during the afternoon. Potential temperature profiles (Figs. 7c,f) confirmed the presence of a mixing layer roughly 600 m deep as confirmed by the wind direction shear observed and correctly modeled at this height (Figs. 7b,e). The overall structure of the lower tropospheric flow and its time evolution were reconstructed by WRF, whose fields confirmed the influence of the Mount Vesuvius wake and flow channeling between the volcano and the Sorrento Peninsula on the sea-breeze development (Fig. 5). The differences between predicted and measured wind and temperature values were higher in the lower layers, where the mountain wake effect was too strong to be entirely reproduced at the model grid-space resolution. Near-surface values can be also influenced by the poor initialization of soil temperature and moisture. While local land-cover description has been improved by the introduction of the European Coordination of Information

on the Environment (CORINE) land cover at 250-m resolution, no information was available to enhance the soil composition description.

All wind profiles measured on 15 July were characterized by directions between northeast and southeast in their upper layers (Figs. 6b,e and 7b,e), with minimum height of the easterly flow depending on location and time of day and ranging between 800 and 1400 m. Model simulations confirmed this wind direction pattern up to about 3000 m. This upper airflow behaves as a return current, potentially transporting pollutants seaward in the upper layers. The height of this layer is also compatible with return current observations made in other locations (see, e.g., Tijm et al. 1999; Millán et al. 2000).

4. Ozone production and distribution

Surface ozone observations were compared with the air quality model results (Fig. 8): a general increase of

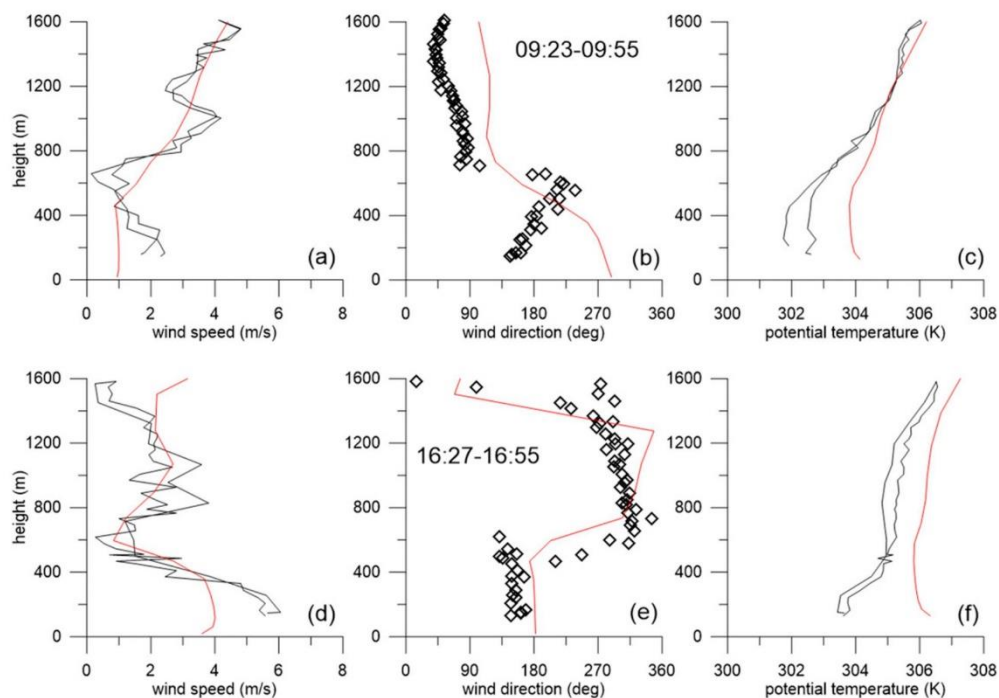


FIG. 7. As in Fig. 6, but for location P3.

daily maximum values can be observed moving from Naples near-coast city stations (San Marcellino and NA01; Fig. 1) to the inland plains area at increasing distance from the coast (Acerra, San Vitaliano, and Tufino; Fig. 1). Measurements in Naples were fairly well reproduced by FARM simulations (Figs. 8a,b), with a tendency to overestimate daily maxima and a correct reproduction of nighttime concentration levels, which confirms a correct reproduction of NO_x emissions driving nightly titration effect. The short-term time variability of measured concentration at San Marcellino and its relatively low daily maximum value (Fig. 8a) can be explained by the position of the station at roof level, about 500 m from the port, which exposes it to the plumes of large cargo and cruise ships. The model result verification at the urban background station NA01 is limited by missing observations during the experimental campaign (Fig. 8b). The ozone concentration and its time variability were correctly reproduced by the model at the Mount Vesuvius station (Fig. 8c) located at 608 m MSL on the southwestern slopes of the volcano (Fig. 1), where local anthropogenic emissions are scarce, as

confirmed by the limited daily modulation of ozone concentration and elevated minimum nighttime values. The good performance of the modeling system at this background station confirms the effective reproduction of the atmospheric circulation over the studied area. The inland stations showed a relevant spatial variability of ozone concentrations (Figs. 8d–f), reflecting the complex land use that includes scattered urban areas, major motorways, and industrial sites within a landscape that is mainly agricultural. Moreover, during sea-breeze flow the area is downwind of Naples, receiving plumes of pollutants emitted in the highly urbanized coastal strip. The model simulations were able to describe part of the variability observed among the inland stations (e.g., variation of maximum values), while they showed difficulties in reproducing nighttime ozone concentrations, which were generally overestimated. This behavior indicates that present knowledge of emissions in the Naples hinterland is insufficient to support a complete reconstruction of events controlled by local emissions like titration during nightly stagnation conditions.

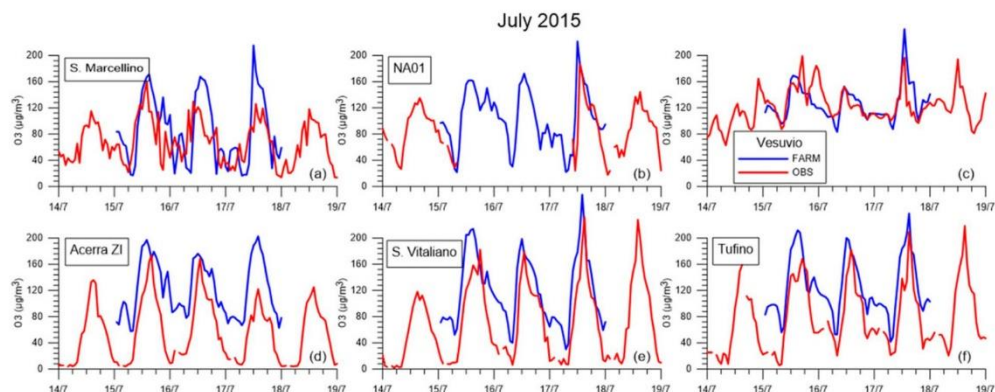


FIG. 8. Ozone concentrations measured (red) and computed by the FARM model (blue) at the monitoring stations of (a) San Marcellino and (b) NA01 located in Naples city; (c) on Mount Vesuvius; and in (d) Acerra, (e) San Vitaliano, and (f) Tufino on the inland plains.

Aircraft flights allowed to analyze ozone space and time variability over the Gulf of Naples and the inland plains area. The morning flight showed minimum ozone concentrations along the northwest leg (Fig. 9a), while the aircraft was flying over land before 0800 LST in nearly calm wind conditions (Fig. 5a). At this time of the day, during the transition between land and sea-breeze circulation conditions, titration due to local NO_x emissions can still be dominant. Concentrations grew to $100\text{--}140\ \mu\text{g m}^{-3}$ over the sea (Fig. 9a), with a sharp increase as soon as the shoreline was crossed. Highest overland concentrations were recorded along the eastern portion of the trajectory, over the area northeast of Mount Vesuvius, with values up to $170\ \mu\text{g m}^{-3}$.

Concentration values mostly over $140\ \mu\text{g m}^{-3}$ were recorded along the northeastern horizontal leg (Fig. 9a).

An increase in ozone concentration levels was observed over the whole afternoon flight path (Fig. 9b) with respect to the morning values (Fig. 9a). Maximum values exceeding $200\ \mu\text{g m}^{-3}$ were measured over the inland area northeast of Naples city center and north of Mount Vesuvius (Fig. 9b). It can also be noticed that concentration values recorded over the sea were higher north of Ischia Island than over the Gulf of Naples (Fig. 9b). This could be associated with the higher NO_x concentration detected over the Gulf of Naples (not shown) that can be attributed to the emissions of the intense shipping traffic during the tourist season, which

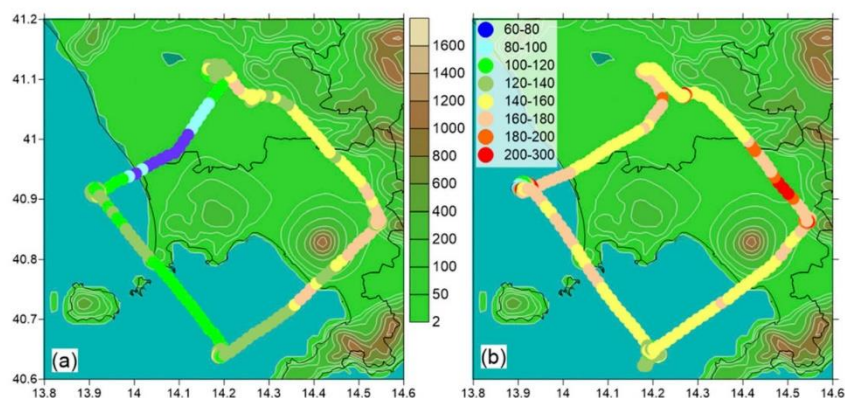


FIG. 9. Ozone concentrations ($\mu\text{g m}^{-3}$) measured along the horizontal legs of the SkyArrow (a) morning and (b) afternoon flights on 15 Jul 2015. Measurements were taken at cruise height of about 150 m AGL. Measured ozone values are superimposed on the topography height used by the models.

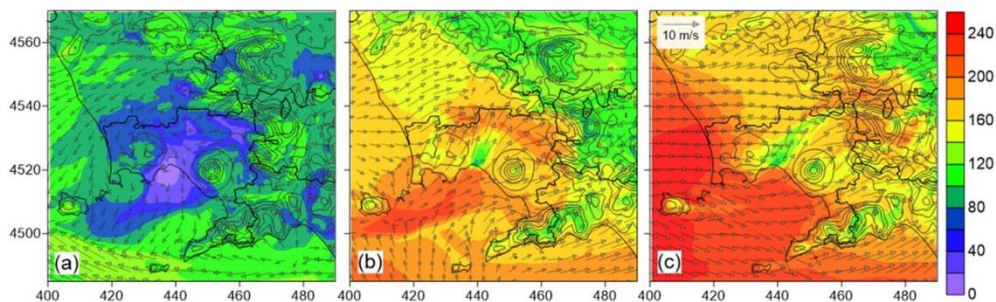


FIG. 10. Near-surface ozone concentrations ($\mu\text{g m}^{-3}$) predicted by FARM model simulations for 15 Jul 2015 at (a) 0800, (b) 1200, and (c) 1700 LST. Wind field at 10-m height is represented by gray arrows.

involves both local ferries to the islands and large cruise and cargo ships.

The analysis of model concentration fields allowed us to identify the main ozone production area and its transport pathways (Fig. 10). During the morning, the atmospheric flow was dominated by weak land-breeze conditions transporting pollutants from the coastal area to the sea (Fig. 10a). The urban area of Naples, the inland plains, and a portion of the gulf facing the main port area were characterized by a minimum of ozone concentration due to the prevailing effect of titration at nighttime and in the early morning (Fig. 10a). From late morning to midday, the main areas of ozone production were the plains inland from Naples and between Mount Vesuvius and the Sorrento Peninsula (Fig. 10b). High concentrations were also predicted over the northern part of the Gulf, where ozone precursors have previously been advected by the land-breeze flow. Later in the afternoon, the sea-breeze penetration transported pollutants over the mountain slopes, locally reducing concentrations over the inland plains by dilution. Moreover, surface concentration fields showed an enlarged area influenced by the Naples plume that, being rich in NO_x , caused a local reduction in ozone concentrations by a titration effect (Fig. 10c). At the same time, the coastal strip was reached by ozone advected from the sea and originating from an offshore reservoir, whose presence during sea breezes and summer high pressure conditions has been documented, for example, by Velchev et al. (2011).

The vertical ozone profiles measured by the aircraft over the sea (P1 and P2) during the morning hours (Figs. 11a,b) showed nearly constant concentration above 400 m with values close to $150 \mu\text{g m}^{-3}$. Below this height, concentration decreased toward the surface with values between 100 and $120 \mu\text{g m}^{-3}$. The FARM simulation reproduced the profile shape, with some underestimation of concentrations

in the upper layers (Figs. 11a,b). Model results support the interpretation of the low value of near-surface ozone concentration as caused by NO_x -rich and ozone-poor air masses originating from the urbanized coastal area and advected by land breezes during the night and early morning (Fig. 10a). The morning profile P3, measured over land (Fig. 11c), showed high ozone concentrations ($150\text{--}175 \mu\text{g m}^{-3}$) within a layer about 600 m deep, reducing to values similar to those detected over the sea at higher vertical levels. The northeastern profile P4 over land showed ozone concentration slowly and regularly decreasing with height (Fig. 11d). The analysis of P4 meteorological measurements and model results evidenced the occurrence of a convective ABL with a depth of about 800 m (Fig. 6c). FARM simulations showed the tendency to underestimate P3 ozone values near the ground (Fig. 11c). This confirms the previous analysis of the time variation of modeled air pollutants showing a slight delay in the prediction of ozone growth, which is especially evident for P3. The comparison of model results with measurements in fact improved for all the profiles if a 1-h delayed time frame (e.g., 1100 LST instead of 1000 LST for P3) was extracted from model results (see dashed lines in Figs. 11a–d). Wind, surface energy, and momentum fluxes (Figs. 3c and 4a–c) do not show any delay, while a slight time shift is observed in the daily growth of temperature in the urban environment (Fig. 3c). A possible cause of the ozone concentration growth delay can be the emissions time modulation, which is based on statistical analyses of anthropogenic activities and cannot guarantee an accurate reconstruction of the actual emissions time variability during a specific day.

The afternoon ozone profiles showed peculiar features. An increase of concentration in the lower 400 m was detected from the comparison of morning and afternoon profiles over water (P1 and P2; Figs. 11a,b,e,f), that was overestimated by the model (Figs. 11e,f). This discrepancy can be partially attributed to the western

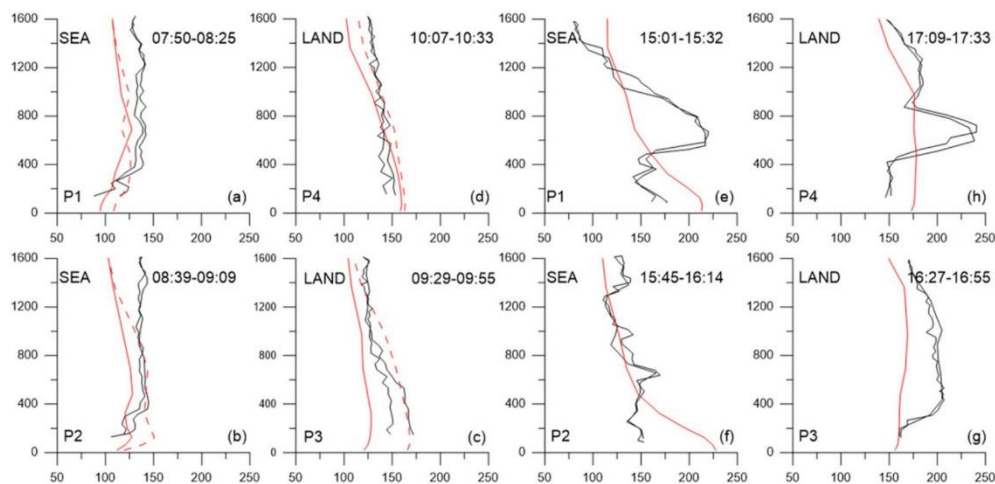


FIG. 11. Vertical profiles of ozone concentration ($\mu\text{g m}^{-3}$) measured by the aircraft along its ascending and descending flight paths (black lines) at locations (a),(e) P1, (b),(f) P2, (c),(g) P3, and (d),(h) P4 during the morning [in (a)–(d)] and afternoon [in (e)–(h)] flights on 15 Jul 2015. Start and end times of the ascending and descending aircraft flight paths are indicated for each profile. FARM results extracted at the same location are reported for the closest hourly time frame (red solid lines) and with 1-h delay (red dashed lines, for the morning flight only).

boundary conditions, provided by the continental-scale model, injecting ozone-rich air masses that were advected onshore by the southwesterly breeze (Fig. 10c). The two northern profiles (P1 and P4) showed an ozone-rich layer between 400 and 1000 m (Figs. 11e,h), with concentrations higher than at the surface and maxima located around 600 m. This pattern was neither reproduced by the model nor repeated on the second day of measurements, when ozone concentration was decreasing with height and nearly constant within the mixing layer (see supplemental material Fig. S2e). The transient nature of the observed phenomenon and the relatively low altitude of the ozone-rich layer support the hypothesis that it is caused by local recirculation rather than subsidence associated with the high pressure system over the Mediterranean (Millán et al. 2000, 2002; Richards et al. 2013). The ozone-rich layer observed over land (P4; Fig. 11h) is coincident with the residual layer located over the internal boundary layer (Fig. 6f), where pollutants have been injected during late morning, before the arrival of the breeze front, and could then remain trapped after the internal boundary layer development. During local recirculation events, a limited difference in predicted wind direction was probably the reason of the mismatch between modeled and measured profiles.

The possible origin of such ozone-rich layer was further investigated with the help of back-trajectories computed using RIP4 (Stoelinga 2009) from WRF

wind fields on the third computational domain covering the whole Campania region with 3-km horizontal grid spacing. Trajectories arriving at P1, with vertical positions ranging from 356 to 734 m, have been computed on both 15 and 16 July at 1500 LST to investigate the origin of air masses possibly carrying the elevated ozone-rich layer. The trajectories showed that air mass recirculation was more pronounced on 15 July (Fig. 12a) than on the following day (Fig. 12b). Trajectories reaching P1 during the afternoon westerly flow actually originated over land and traveled across some potentially ozone-rich layers over the Gulfs of Naples and Salerno (Fig. 12a). They can therefore confirm the hypothesis of local recirculation origin of the elevated concentration maxima. On 16 July the air masses arriving at P1 during the afternoon started over the open sea at the southern boundary of the computational domain (Fig. 12b), transporting background offshore concentrations that did not include any elevated maximum. Elevated ozone reservoir layers were observed by Lin et al. (2007, 2010) during sea-breeze circulation in Taiwan; however, the different climatic and circulation features, together with the presence of the Naples conurbation along the coastline, make it difficult to establish reliable similarities with the Mediterranean episode we analyzed.

The aircraft vertical profiles did not extend high enough to clearly detect pollutants transport toward the sea caused by the sea-breeze return current.

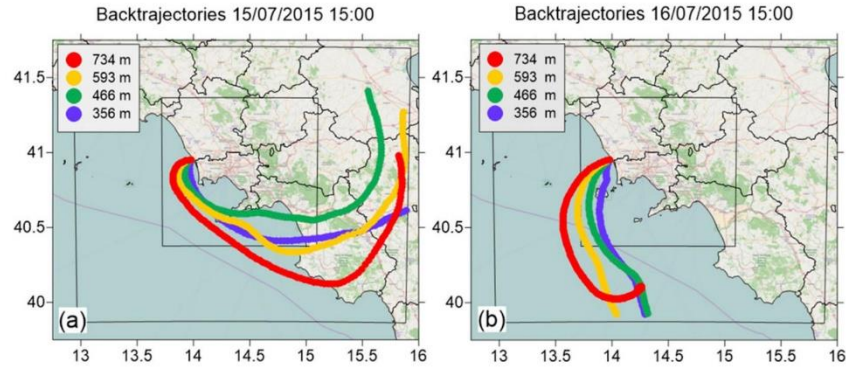


FIG. 12. Back trajectories arriving at profile P1 location from 356 to 734 m MSL at 1500 LST on (a) 15 Jul 2015 and (b) 16 Jul 2015. Color indicates trajectory height at the arrival point. Trajectories are followed for 24 h travel time.

Nonetheless, all meteorological profiles measured east-erly winds at the upper levels, that is, over about 1400 m, during the whole day (Figs. 6 and 7). WRF simulations showed easterly currents up to about 3000 m, with maximum intensities around 2000 m. Figure 13 shows a vertical cross section of ozone concentration computed by FARM along the northwestern transect of the flight track on 15 July at 1800. The concentration pattern suggests seaward transport of ozone with maximum values between 1000 and 2000 m (Fig. 13). The recirculation of pollutants was driven by the vertical dispersion of pollutants over the inland plains and by the vertical transport forced by the Apennine mountain range, which contributed to their injection into the high troposphere and finally to their transport seaward by the upper-air easterly current.

Ozone mass balance over the Naples area

Even in the presence of differences between model results and observations, the main features of the complex atmospheric circulation and ozone dynamics within the study area have been reconstructed, permitting us to use FARM model results to provide an estimation of the mass balance and the overall ozone production during sea-breeze daily cycles. The mass balance computation was performed within the inner model domain (Fig. 2) with a horizontal size of $99 \times 87 \text{ km}^2$ and vertical depth of 10 km. For each hour, the following integrated values were computed: total mass variation within the domain (TMV), net variation associated with chemical reactions production/removal (Chemistry), dry deposition flux (DryDep), and net flux through the lateral and top

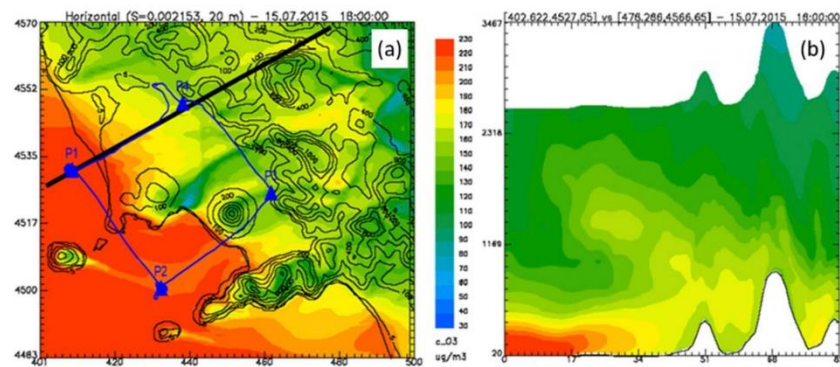


FIG. 13. Ozone concentration ($\mu\text{g m}^{-3}$) in the (a) near-surface field and (b) vertical cross section across the shoreline. The concentration fields refer to 1800 LST 15 Jul 2015. The aircraft flight path (blue line) and vertical cross section position (black line) are superimposed on the horizontal cross section.

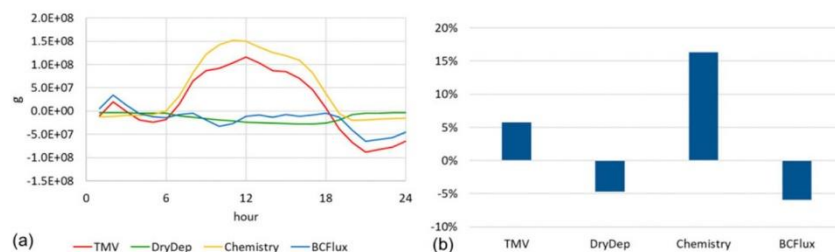


FIG. 14. Ozone mass balance within the FARM model inner computational domain. (a) Hourly and (b) daily integrated values for 15 Jul 2015. Hourly values are expressed in grams, while daily values are reported as fraction of the total mass within the computational domain.

boundaries (BCFlux). Hourly and daily values of different contributions to the mass balance showed the expected daily cycle of atmospheric chemistry, producing ozone during the day and destroying it at night (Fig. 14a). The time variation of the total ozone mass reflected the same cycle, increasing during the day and decreasing at night. The dry deposition sink was more relevant during the day, when surface concentrations were higher and turbulence more intense. The local chemistry production, together with mesoscale circulation, caused prevailing ozone export conditions. The daily integrated values showed that ozone net production can be quantified as about 16% of the daily average mass contained within the computational domain volume (Fig. 14b). The net daily ozone mass gain resulting from chemical production, after subtraction of the deposition sink effect, was almost equally distributed between an increase of the total mass within the computational domain and the export through the boundaries, toward the nearby geographical areas. The contributions to the overall daily mass balance remained similar for the three days covered by model simulation (15–17 July 2015), causing an overall 23% increase of the ozone mass within the computational domain because of chemical production (45% of the initial mass) partially compensated by deposition and outflow.

5. Discussion and conclusions

The Naples area is considered one of the major anthropogenic sources of ozone precursors in the Mediterranean Basin. Its geographical location on the Italian peninsula near the high Apennine mountain chain favors the export of pollutants over the sea, where ozone accumulation has been detected from surface and satellite observations and from atmospheric modeling investigations. The integration of extensive measurements and model simulations

allowed us to investigate the ozone production and transport during summer sea breeze and to identify the key role played by the inland plains areas, where agriculture is mixed with scattered urbanization, in controlling ozone and other secondary pollutants production. The advection of NO_x and other primary pollutants from Naples and its harbor area to the VOC-rich inland plains caused a relevant production of ozone in the area. Pollutants were vertically mixed in the convective boundary layer, up to a height of about 1 km, until the sea-breeze front reached the inland plains around midday. A collapse of the boundary layer depth was then observed associated with the development of an internal boundary layer driven by the breeze penetration, creating a layered vertical structure of the lower atmosphere with high concentrations possibly trapped within the elevated residual layer. The sea-breeze penetration reduced surface ozone concentrations over the inland plains because of the joint effect of increased ventilation and advection of NO_x -rich air masses, locally increasing the titration effect. Ozone was then transported eastward, over the Apennines, where BVOCs emitted by natural vegetation further triggered photochemical production. The mountain-breeze circulation reinforced the vertical transport of pollutants that were then advected westward toward the sea by the return currents above 1500 m. The nightly land-breeze circulation carried ozone precursors from the densely inhabited coastal area to the sea within near-surface atmospheric layers. Nighttime titration conditions dominated over Naples city, the inland plains area, and the Gulf of Naples.

The observed complex flow and layered structure of the atmosphere is quite similar to that described by Millán et al. (2002) for eastern Spanish coasts, with differences induced by local topography that caused the intense ozone production over the inland plains located downwind of the city during sea breezes.

Model simulations confirmed the role of the Naples conurbation as a regional source of ozone through a net production and direct export of ozone, together with its anthropogenic and biogenic precursors, as predicted by Velchev et al. (2011). Sea-breeze coastal circulation, together with the vertical atmospheric motion induced by the Apennine mountain chain, favors the recirculation within the coastal region and its transport toward the western Mediterranean, as clearly described by Millán et al. (1997).

Despite the relevant chemical ozone production occurring locally, the daily increase of the total ozone mass within the computational domain was less than 6% (Fig. 14b), with a slight increment of daily maximum concentration detectable in some of the surface observations. The local surface concentration is determined by a complex interaction of atmospheric flow and chemistry from the continental to the local scale. The regional background concentration of ozone and its precursors (entering the chemical transport model simulation through the initial and boundary conditions) have a dominant role in establishing local concentration levels, and especially their daily maxima. Different studies have already shown that local emission precursors control policies would have a limited or even negative effect on summer ozone episodes [see, e.g., Escudero et al. (2014) or Schipa et al. (2009) and Schürmann et al. (2009) for investigations in coastal locations of southern Italy]. Regardless, the coordinated reduction of pollutants' emission from the major conurbations located on or near the Mediterranean coasts is one of the main approaches to achieve an ozone concentration reduction at the regional scale and especially over the sea, where this pollutant accumulates during persistent high pressure conditions. The slight decreasing trend observed at background stations during recent years (Sicard et al. 2013; European Environment Agency 2015) is in fact an encouraging, albeit limited, sign of the possible effects of the EU air pollution control strategy. Efforts to reduce photochemical smog precursors' emissions should therefore be continued and extended from the continental to the global scale, taking into account the global emission trends (Miyazaki et al. 2017) and the negative effect of the expected climate warming over the Mediterranean (Giorgi and Lionello 2008; Gualdi et al. 2013; Sillmann et al. 2013).

REFERENCES

- Adame, J. A., E. Serrano, J. P. Bolívar, and B. A. De la Morena, 2010: On the tropospheric ozone variations in a coastal area of southwestern Europe under a mesoscale circulation. *J. Appl. Meteor. Climatol.*, **49**, 748–759. <https://doi.org/10.1175/2009JAMC2097.1>.
- Ancellet, G., and F. Ravetta, 2005: Analysis and validation of ozone variability observed by lidar during the ESCOMPTE-2001 campaign. *Atmos. Res.*, **74**, 435–459. <https://doi.org/10.1016/j.atmosres.2004.10.003>.
- Atkinson, R., 2000: Atmospheric chemistry of VOCs and NO_x. *Atmos. Environ.*, **34**, 2063–2101. [https://doi.org/10.1016/S1352-2310\(99\)00460-4](https://doi.org/10.1016/S1352-2310(99)00460-4).
- , and J. Arey, 2003: Gas phase tropospheric chemistry of biogenic volatile organic compounds: A review. *Atmos. Environ.*, **37** (Suppl. 2), 197–219. [https://doi.org/10.1016/S1352-2310\(03\)00391-1](https://doi.org/10.1016/S1352-2310(03)00391-1).
- Bach, H., and Coauthors, 2014: Services to assess the reasons for non-compliance of ozone target value set by Directive 2008/50/EC and potential for air quality improvements in relation to ozone pollution. ECORYS Final Rep., 50 pp. http://ec.europa.eu/environment/air/pdf/Final_ozone_report.pdf.
- Calfapietra, C., S. Fares, and F. Loreto, 2009: Volatile organic compounds from Italian vegetation and their interaction with ozone. *Environ. Pollut.*, **157**, 1478–1486. <https://doi.org/10.1016/j.envpol.2008.09.048>.
- Carter, W. P. L., 2000: Documentation of the SAPRC-99 chemical mechanism for VOC reactivity assessment. California Air Resources Board Final Rep., Air Pollution Research Center and College of Engineering Center for Environmental Research and Technology, University of California, Riverside, CA, 230 pp. <http://www.cert.ucr.edu/~carter/absts.htm#saprc99>.
- Castell, N., E. Mantilla, and M. M. Millán, 2008: Analysis of tropospheric ozone concentration on a western Mediterranean site: Castellon (Spain). *Environ. Monit. Assess.*, **136**, 3–11. <https://doi.org/10.1007/s10661-007-9723-1>.
- Cheng, W. L., 2002: Ozone distribution in coastal central Taiwan under sea-breeze conditions. *Atmos. Environ.*, **36**, 3445–3459. [https://doi.org/10.1016/S1352-2310\(02\)00307-2](https://doi.org/10.1016/S1352-2310(02)00307-2).
- Ciccioli, P., E. Brancaleoni, C. Di Paolo, A. Brachetti, and A. Cecinato, 1987: Daily trends of photochemical oxidants and their precursors in a suburban forested area. A useful approach for evaluating the relative contributions of natural and anthropogenic hydrocarbons to the photochemical smog formation in rural areas of Italy. *Physico-Chemical Behaviour of Atmospheric Pollutants*, G. Angeletti and G. Restelli, Eds., Springer, 551–559.
- Curci, G., M. Beekmann, R. Vautard, G. Smiatek, R. Steinbrecher, J. Theloke, and R. Friedrich, 2009: Modelling study of the impact of isoprene and terpene biogenic emissions on European ozone levels. *Atmos. Environ.*, **43**, 1444–1455. <https://doi.org/10.1016/j.atmosenv.2008.02.070>.
- David, L. M., and P. R. Nair, 2011: Diurnal and seasonal variability of surface ozone and NO_x at a tropical coastal site: Association with mesoscale and synoptic meteorological conditions. *J. Geophys. Res.*, **116**, D10303. <https://doi.org/10.1029/2010JD015076>.
- Escudero, M., A. Lozano, J. Hierro, J. del Valle, and E. Mantilla, 2014: Urban influence on increasing ozone concentrations in a characteristic Mediterranean agglomeration. *Atmos. Environ.*, **99**, 322–332. <https://doi.org/10.1016/j.atmosenv.2014.09.061>.
- European Environment Agency, 2015: Air quality in Europe—2015 report. EEA Rep. 5/2015, 64 pp. https://www.eea.europa.eu/publications/air-quality-in-europe-2015/at_download/file.
- European Union, 2008: Directive 2008/50/EC of the European Parliament and of the Council of 21 May 2008 on ambient air quality and cleaner air for Europe. EU, 44 pp. <http://eur-lex.europa.eu/legal-content/EN/TXT/PDF/?uri=CELEX:32008L0050&from=en>.
- Fuentes, J. D., and Coauthors, 2000: Biogenic hydrocarbons in the atmospheric boundary layer: A review. *Bull. Amer. Meteor. Soc.*, **81**, 1537–1575. [https://doi.org/10.1175/1520-0477\(2000\)081<1537:BHITAB>2.3.CO;2](https://doi.org/10.1175/1520-0477(2000)081<1537:BHITAB>2.3.CO;2).
- Gangoiti, G., M. M. Millán, R. Salvador, and E. Mantilla, 2001: Long-range transport and re-circulation of pollutants in the

- western Mediterranean during the project Regional Cycles of Air Pollution in the West-Central Mediterranean Area. *Atmos. Environ.*, **35**, 6267–6276, [https://doi.org/10.1016/S1352-2310\(01\)00440-X](https://doi.org/10.1016/S1352-2310(01)00440-X).
- Garratt, J. R., 1990: The internal boundary layer—A review. *Bound.-Layer Meteorol.*, **50**, 171–203, <https://doi.org/10.1007/BF00120524>.
- Gioli, B., and Coauthors, 2004: Comparison between tower and aircraft-based eddy covariance fluxes in five European regions. *Agric. For. Meteorol.*, **127**, 1–16, <https://doi.org/10.1016/j.agrformet.2004.08.004>.
- , F. Miglietta, F. P. Vaccari, A. Zaldei, and B. De Martino, 2006: The Sky Arrow ERA, an innovative airborne platform to monitor mass, momentum and energy exchange of ecosystems. *Ann. Geophys.*, **49**, 109–116, <https://doi.org/10.4401/ag-3159>.
- Giorgi, F., and P. Lionello, 2008: Climate change projections for the Mediterranean region. *Global Planet. Change*, **63**, 90–104, <https://doi.org/10.1016/j.gloplacha.2007.09.005>.
- Gualdi, S., and Coauthors, 2013: The CIRCE simulations: Regional climate change projections with realistic representation of the Mediterranean Sea. *Bull. Amer. Meteor. Soc.*, **94**, 65–81, <https://doi.org/10.1175/BAMS-D-11-00136.1>.
- Henschel, S., and G. Chan, 2013: Health risks of air pollution in Europe—HRAPIE project: New emerging risks to health from air pollution—Results from the survey of experts. World Health Organization Regional Office for Europe, 65 pp., http://www.euro.who.int/_data/assets/pdf_file/0017/234026/e96933.pdf?ua=1.
- IPCC, 2007: *Climate Change 2007: The Physical Science Basis*. Cambridge University Press, 996 pp., https://www.ipcc.ch/pdf/assessment-report/ar4/wg1/ar4_wg1_full_report.pdf.
- , 2014: *Climate Change 2014: Synthesis Report*. Cambridge University Press, 151 pp., https://www.ipcc.ch/pdf/assessment-report/ar5/syr/SYR_AR5_FINAL_full.pdf.
- Jiménez, P., J. Lelieveld, and J. M. Baldasano, 2006: Multiscale modeling of air pollutants dynamics in the northwestern Mediterranean basin during a typical summertime episode. *J. Geophys. Res.*, **111**, D18306, <https://doi.org/10.1029/2005JD006516>.
- Kanakidou, M., and Coauthors, 2005: Organic aerosol and global climate modelling: A review. *Atmos. Chem. Phys.*, **5**, 1053–1123, <https://doi.org/10.5194/acp-5-1053-2005>.
- Kemper Pacheco, C., S. Fares, and P. Ciccioli, 2014: A highly spatially resolved GIS-based model to assess the isoprenoid emissions from key Italian ecosystems. *Atmos. Environ.*, **96**, 50–60, <https://doi.org/10.1016/j.atmosenv.2014.07.012>.
- Kukkonen, J., and Coauthors, 2012: A review of operational, regional-scale, chemical weather forecasting models in Europe. *Atmos. Chem. Phys.*, **12**, 1–87, <https://doi.org/10.5194/acp-12-1-2012>.
- Lelieveld, J., and Coauthors, 2002: Global air pollution crossroads over the Mediterranean. *Science*, **298**, 794–799, <https://doi.org/10.1126/science.1075457>.
- Liakakou, E., M. Vrekoussis, B. Bonsang, C. Donousis, M. Kanakidou, and N. Mihalopoulos, 2007: Isoprene above the eastern Mediterranean: Seasonal variation and contribution to the oxidation capacity of the atmosphere. *Atmos. Environ.*, **41**, 1002–1010, <https://doi.org/10.1016/j.atmosenv.2006.09.034>.
- Lin, C.-H., C.-H. Lai, Y.-L. Wu, P.-H. Lin, and H.-C. Lai, 2007: Impact of sea breeze air masses laden with ozone on inland surface ozone concentrations: A case study of the northern coast of Taiwan. *J. Geophys. Res.*, **112**, D14309, <https://doi.org/10.1029/2006JD008123>.
- , Y.-L. Wu, and C.-H. Lai, 2010: Ozone reservoir layers in a coastal environment—A case study in southern Taiwan. *Atmos. Chem. Phys.*, **10**, 4439–4452, <https://doi.org/10.5194/acp-10-4439-2010>.
- Lionello, P., F. Abrantes, M. Gacic, S. Planton, R. Trigo, and U. Ulbrich, 2014: The climate of the Mediterranean region: Research progress and climate change impacts. *Reg. Environ. Change*, **14**, 1679, <https://doi.org/10.1007/s10113-014-0666-0>.
- Mangia, C., I. Schipa, A. Tanzarella, D. Conte, G. P. Marra, M. M. Miglietta, and U. Rizza, 2010: Numerical study of the effect of sea breeze circulation on photochemical pollution over a highly industrialized peninsula. *Meteor. Appl.*, **17**, 19–31, <https://doi.org/10.1002/met.147>.
- McKendry, I. G., and J. Lundgren, 2000: Tropospheric layering of ozone in regions of urbanized complex and/or coastal terrain: A review. *Prog. Phys. Geogr.*, **24**, 329–354, <https://doi.org/10.1177/030913330002400302>.
- Millán, M. M., R. Salvador, E. Mantilla, and G. Kallos, 1997: Photooxidant dynamics in the Mediterranean basin in summer: Results from European research projects. *J. Geophys. Res.*, **102**, 8811–8823, <https://doi.org/10.1029/96JD03610>.
- , E. Mantilla, R. Salvador, A. Carratala, M. J. Sanz, L. Alonso, G. Gangoi, and M. Navazo, 2000: Ozone cycles in the western Mediterranean basin: Interpretation of monitoring data in complex coastal terrain. *J. Appl. Meteor. Climatol.*, **39**, 487–508, [https://doi.org/10.1175/1520-0450\(2000\)039<0487:OCITWM>2.0.CO;2](https://doi.org/10.1175/1520-0450(2000)039<0487:OCITWM>2.0.CO;2).
- , M. J. Sanz, R. Salvador, and E. Mantilla, 2002: Atmospheric dynamics and ozone cycles related to nitrogen deposition in the western Mediterranean. *Environ. Pollut.*, **118**, 167–186, [https://doi.org/10.1016/S0269-7491\(01\)00311-6](https://doi.org/10.1016/S0269-7491(01)00311-6).
- , and Coauthors, 2005: Climatic feedbacks and desertification: The Mediterranean model. *J. Climate*, **18**, 684–701, <https://doi.org/10.1175/JCLI-3283.1>.
- Mircea, M., and Coauthors, 2014: Assessment of the AMS-MINNI system capabilities to predict air quality over Italy for the calendar year 2005. *Atmos. Environ.*, **84**, 178–188, <https://doi.org/10.1016/j.atmosenv.2013.11.006>.
- Miyazaki, K., H. Eskes, K. Sudo, K. F. Boersma, K. Bowman, and Y. Kanaya, 2017: Decadal changes in global surface NO_x emissions from multi-constituent satellite data assimilation. *Atmos. Chem. Phys.*, **17**, 807–837, <https://doi.org/10.5194/acp-17-807-2017>.
- Paoletti, E., 2006: Impact of ozone on Mediterranean forests: A review. *Environ. Pollut.*, **144**, 463–474, <https://doi.org/10.1016/j.envpol.2005.12.051>.
- Parrish, D. D., and Coauthors, 2012: Long-term changes in lower tropospheric baseline ozone concentrations at northern mid-latitudes. *Atmos. Chem. Phys.*, **12**, 11 485–11 504, <https://doi.org/10.5194/acp-12-11485-2012>.
- Querol, X., and Coauthors, 2014: 2001–2012 trends on air quality in Spain. *Sci. Total Environ.*, **490**, 957–969, <https://doi.org/10.1016/j.scitotenv.2014.05.074>.
- Richards, N. A. D., S. R. Arnold, M. P. Chipperfield, G. Miles, A. Rap, R. Siddans, S. A. Monks, and M. J. Hollaway, 2013: The Mediterranean summertime ozone maximum: Global emission sensitivities and radiative impacts. *Atmos. Chem. Phys.*, **13**, 2331–2345, <https://doi.org/10.5194/acp-13-2331-2013>.
- Schipa, I., A. Tanzarella, and C. Mangia, 2009: Differences between weekend and weekday ozone levels over rural and urban sites in southern Italy. *Environ. Monit. Assess.*, **156**, 509–523, <https://doi.org/10.1007/s10661-008-0501-5>.
- Schürmann, G. J., A. Algieri, I. M. Hedgecock, G. Manna, N. Pirrone, and F. Sprovieri, 2009: Modelling local and synoptic scale influences on ozone concentrations in a topo-

- graphically complex region of southern Italy. *Atmos. Environ.*, **43**, 4424–4434, <https://doi.org/10.1016/j.atmosenv.2009.06.017>.
- Sicard, P., A. De Marco, F. Troussier, C. Renou, N. Vas, and E. Paoletti, 2013: Decrease in surface ozone concentrations at Mediterranean remote sites and increase in the cities. *Atmos. Environ.*, **79**, 705–715, <https://doi.org/10.1016/j.atmosenv.2013.07.042>.
- Silibello, C., G. Calori, G. Brusasca, A. Giudici, E. Angelino, G. Fossati, E. Peroni, and E. Buganza, 2008: Modelling of PM10 concentrations over Milano urban area using two aerosol modules. *Environ. Modell. Software*, **23**, 333–343, <https://doi.org/10.1016/j.envsoft.2007.04.002>.
- Sillmann, J., V. V. Kharin, F. W. Zwiers, X. Zhang, and D. Bronaugh, 2013: Climate extremes indices in the CMIP5 multimodel ensemble: Part 2. Future climate projections. *J. Geophys. Res. Atmos.*, **118**, 2473–2493, <https://doi.org/10.1002/jgrd.50188>.
- Sills, D. M. L., J. R. Brook, I. Levy, P. A. Makar, J. Zhang, and P. A. Taylor, 2011: Lake breezes in the southern Great Lakes region and their influence during BAQS-Met 2007. *Atmos. Chem. Phys.*, **11**, 7955–7973, <https://doi.org/10.5194/acp-11-7955-2011>.
- Skamarock, W. C., and Coauthors, 2008: A description of the Advanced Research WRF version 3. NCAR Tech. Note NCAR/TN-475+STR, 113 pp., <http://dx.doi.org/10.5065/D68S4MVH>.
- Sorensen, J. H., 1998: Sensitivity of the DERMA long-range Gaussian dispersion model to meteorological input and diffusion parameters. *Atmos. Environ.*, **32**, 4195–4206, [https://doi.org/10.1016/S1352-2310\(98\)00178-2](https://doi.org/10.1016/S1352-2310(98)00178-2).
- Stoelinga, M. T., 2009: A users' guide to RIP version 4.5: A program for visualizing mesoscale model output. University of Washington, 82 pp., <http://www2.mmm.ucar.edu/wrf/users/docs/ripug.pdf>.
- Taurino, E. and Coauthors, 2018: Italian Emission Inventory 1990–2016 Informative Inventory Report 2018. Istituto Superiore per la Protezione e la Ricerca Ambientale Annual Rep., 195 pp., <http://www.sinanet.isprambiente.it/it/sia-ispra/serie-storiche-emissioni/informative-inventory-report/view>.
- Thunis, P., and C. Cuvelier, 2000: Impact of biogenic emissions on ozone formation in the Mediterranean area—A BEMA modelling study. *Atmos. Environ.*, **34**, 467–481, [https://doi.org/10.1016/S1352-2310\(99\)00313-1](https://doi.org/10.1016/S1352-2310(99)00313-1).
- Tijm, A. B. C., A. A. M. Holtslag, and A. J. Van Delden, 1999: Observations and modeling of the sea breeze with the return current. *Mon. Wea. Rev.*, **127**, 625–640, [https://doi.org/10.1175/1520-0493\(1999\)127<0625:OAMOTS>2.0.CO;2](https://doi.org/10.1175/1520-0493(1999)127<0625:OAMOTS>2.0.CO;2).
- Velchev, K., F. Cavalli, J. Hjorth, E. Marmer, E. Vignati, F. Dentener, and F. Raes, 2011: Ozone over the western Mediterranean Sea—Results from two years of shipborne measurements. *Atmos. Chem. Phys.*, **11**, 675–688, <https://doi.org/10.5194/acp-11-675-2011>.
- WHO, 2013: Review of evidence on health aspects of air pollution—REVIHAAP project. World Health Organization Regional Office for Europe Tech. Rep., 309 pp., http://www.euro.who.int/__data/assets/pdf_file/0004/193108/REVIHAAP-Final-technical-report-final-version.pdf.
- Ziemke, J. R., S. Chandra, G. J. Labow, P. K. Bhartia, L. Froidevaux, and J. C. Witte, 2011: A global climatology of tropospheric and stratospheric ozone derived from Aura OMI and MLS measurements. *Atmos. Chem. Phys.*, **11**, 9237–9251, <https://doi.org/10.5194/acp-11-9237-2011>.

Chapter 3

Estimate of methane emissions from landfills: an approach based on airborne measurements

3.1 Locating and quantifying multiple landfills methane emission using aircraft data

Emission of methane (CH_4) into the atmosphere is a serious environmental issue associated with the landfilling of municipal waste, especially when landfills are not equipped with biogas recovery systems. This study is conducted on a 5x5 km spatial domain between the Naples and Caserta districts, in an area known as “terra dei fuochi”, in which four different illegal landfills are encompassed.

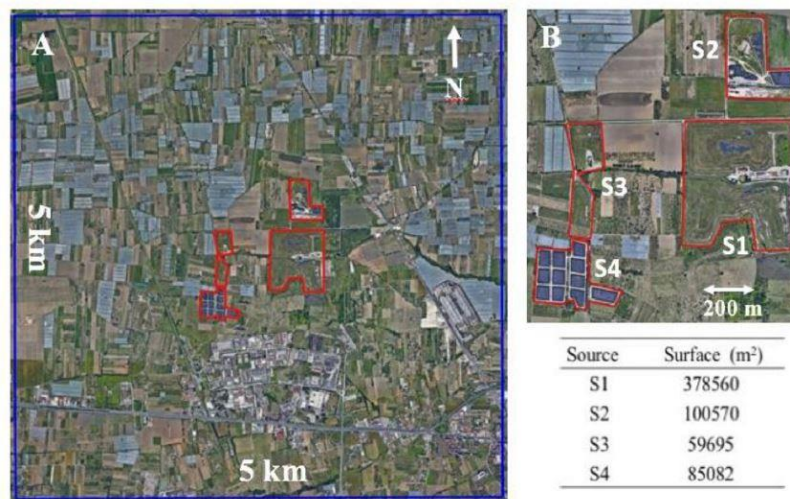


Figure 3.1 Location (panel A) of the four landfills (red polygons) inside the study domain (blue rectangle). Panel B shows the detail of the emissive area, with the surface extension.

The surroundings are well known in the media: urban, industrial and toxic waste were spilled and dumped in old dismissed quarries or buried without any control or safety measures for decades. This led to a patchy presence of waste with consequent spread CH_4 sources with several emitting hot spots. The heterogeneous landscape that characterizes this area, in combination with the widespread presence of CH_4 sources, make it a difficult spot for the assessment of CH_4 emission using the common measurements techniques. The presence of several hot spots with different magnitude

of emission poses a problem for chamber measurement techniques, as they become less representative due to low spatial coverage of the measurements and their temporal discontinuity. The eddy covariance technique is generally suitable for the measurement of CH₄ emissions from landfill, but the orography and the presence of four distinct landfills closely located within the domain affect the application of this technique as well.

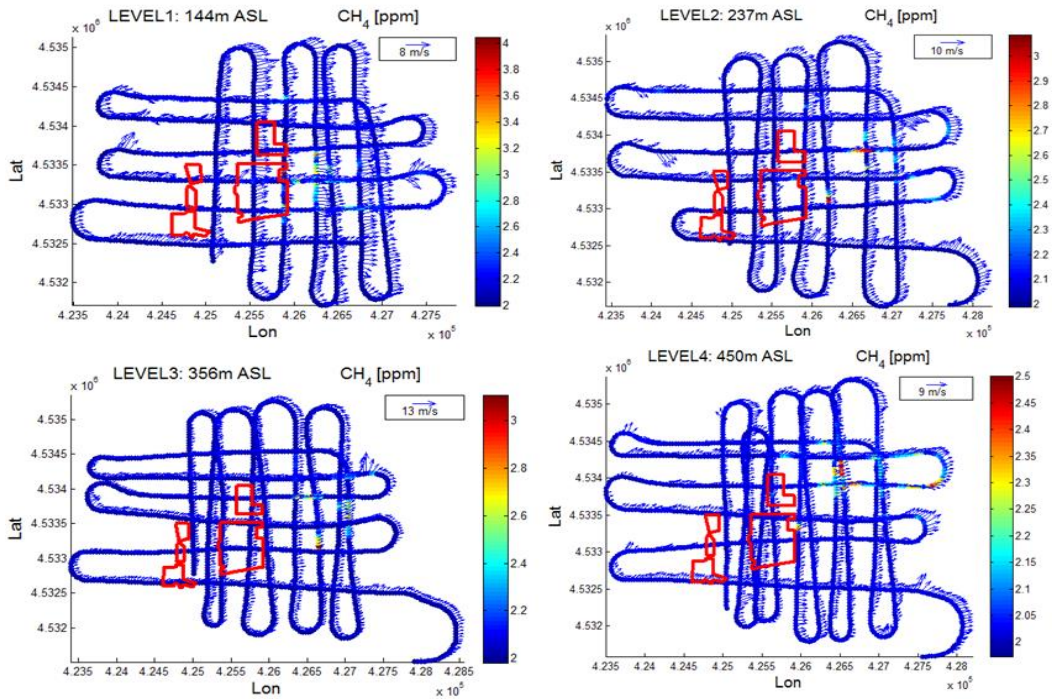


Figure 3.2 Typical flight path of the Sky Arrow ERA during the measurement campaigns above the landfills.

To overcome these issues the airborne platform Sky Arrow ERA, equipped with the biogas payload described in Chapter 1, has been used for the estimate of landfill emissions. Eight flights were performed above the landfills following the same flight path, a series of grids repeated at different heights above the landfills as shown in figure 3.2. Flying grids instead of flying a circle or a polygon around the sources (as performed in the classical mass balance approach) allow to reconstruct both methane densities and wind components not only at the edge of the study area, but also inside the domain.

Figure 3.3 shows the typical trend of CH₄ mixing ratios versus heights measured during each flight. Multiple strong plumes were measured above the study area at

different heights; the CH₄ signal above the landfills decreased gradually with altitude, although during daytime convective conditions, mixing ratios greater than background values were still measured even at the highest level, confirming the presence of strong emission sources at the ground.

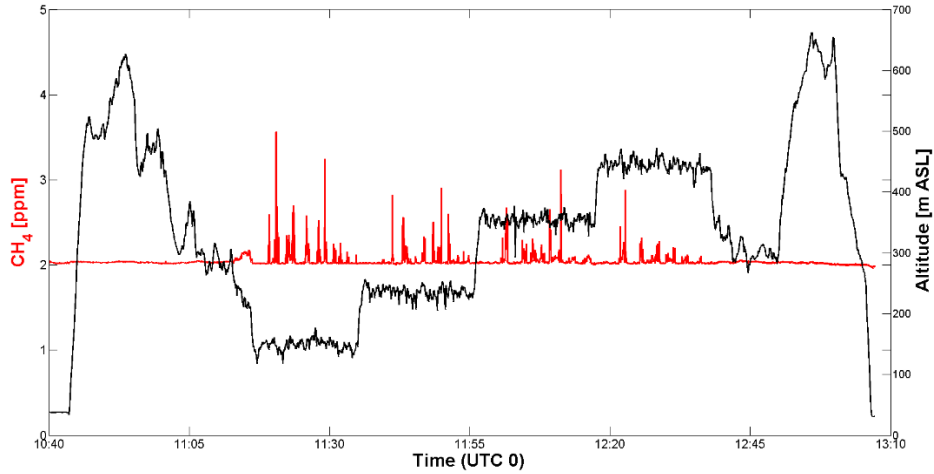


Figure 3.3 Time series of CH₄ mixing ratio measured during one of the flights at 1 Hz resolution. Flight pattern portions at constant height correspond to the grids performed above the study domain.

CH₄ densities and wind data were then interpolated on a grid encompassing the flight domain, extending vertically from the surface to an altitude at which plumes are no longer sampled (Z_{TOP}). Gridded data were computed at 50 meter horizontal resolution and 20 meter vertical resolution, using an inverse distance weighting (IDW) to a power (squared) algorithm. This algorithm is based solely on the assumption that close data points are more related to each other than distant points, not relying on any spatial or temporal relationship:

$$C_{est}^j = \frac{\sum_{i=1}^n \frac{C_i}{d_{ij}^2}}{\sum_{i=1}^n \frac{1}{d_{ij}^2}} \quad \text{Equation 3.1}$$

where C_{est}^j is the estimated value of CH₄ densities or wind data for location j , C_i are the values of the neighbouring points i and d^2 the squared distance between grid note

j and neighbouring points. Following equation 3.1, we obtained a gridded dataset of CH_4 density and wind speed.

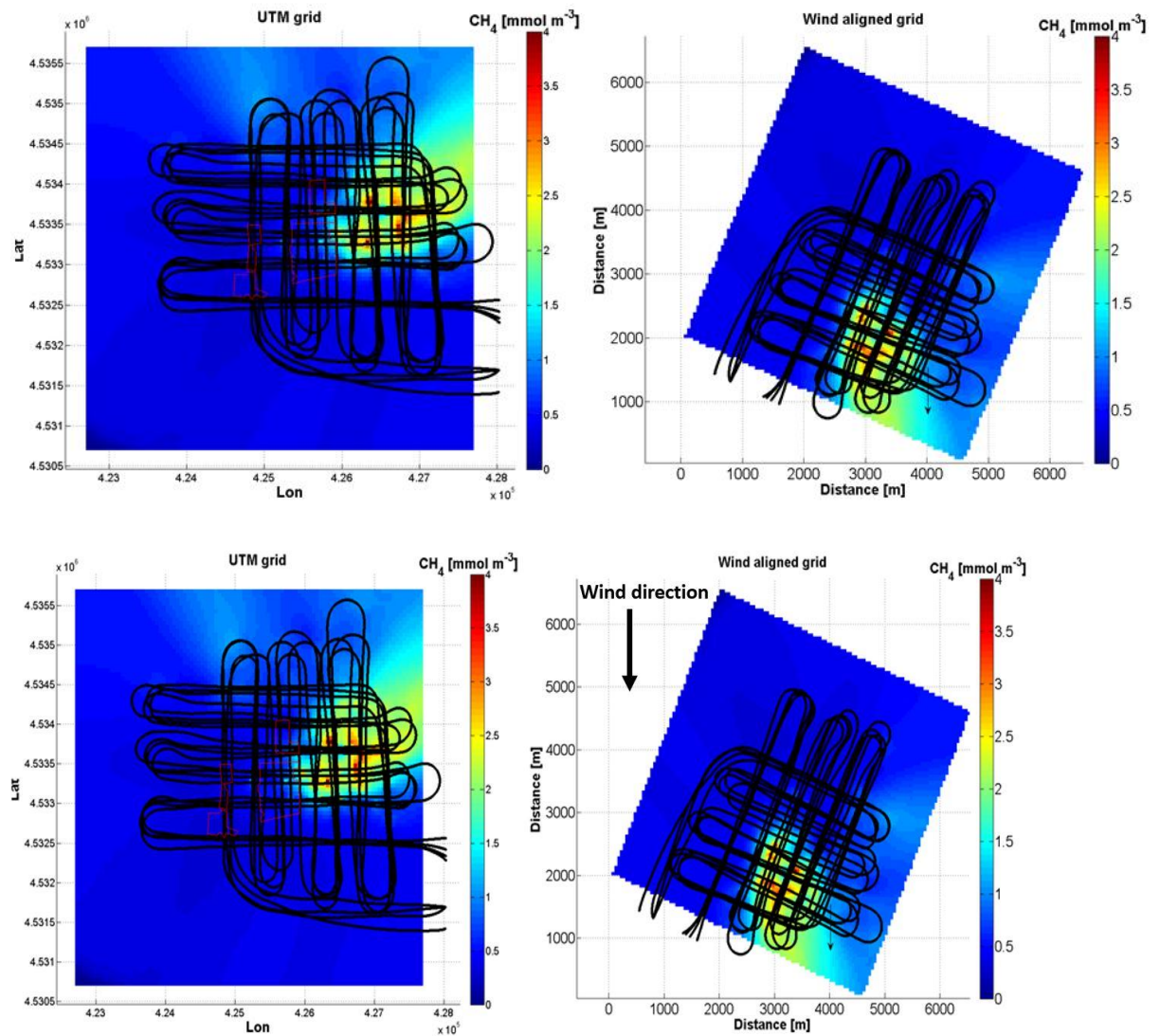


Figure 3.4 CH_4 density map integrated along the z direction obtained from one of the flights (F6) after 3D interpolation. The dimensions of the study area are reported on x and y axes. Black lines represent the flight paths above the landfills. The grid is rotated to align with the mean wind direction.

Wind and CH_4 density grids were rotated for each flight, according to the mean wind direction of each flight, obtaining a wind-aligned box domain (Fig. 3.4). The CH_4 net mass flow was then obtained multiplying gridded densities by rotated wind speed. The total mass flow (MF) (g s^{-1}) along and across the wind aligned direction was then calculated as the integral of the net MF along y - z (parallel to mean wind direction) and

along x-z (perpendicular to mean wind direction) using equations (3.2) and (3.3), to obtain MF along and across wind direction, respectively:

$$MF_ALONG(x) = \int_0^{Z_{TOP}} \int_{y_1}^{y_2} C_{ij} \cdot V_{ij} dy dz \quad \text{Equation 3.2}$$

$$MF_ACROSS(y) = \int_0^{Z_{TOP}} \int_{x_1}^{x_2} C_{ij} \cdot V_{ij} dx dz \quad \text{Equation 3.3}$$

where Z_{TOP} is the top height of the box, x_1 - x_2 and y_1 - y_2 are the horizontal boundaries of the study area (5x5 km domain), dy dx and dz are horizontal and vertical grid spacing respectively ($dy, dx = 50m$, $dz = 20m$). C_{ij} and V_{ij} are the CH_4 molar densities and wind speed, where i and j are horizontal and vertical grid cell indices. Total flow rates obtained from equations (3.2) and (3.3) were calculated for each flight based only on aircraft measurements, with no information or assumption on the underlying sources. A steady-state Gaussian dispersion model was deployed to compute CH_4 density $C(x,y,z)$ at any point of the study domain as follows:

$$C(x,y,z) = \frac{Q}{2\pi\sigma_y\sigma_z U} * \exp\left(-\frac{y^2}{2\sigma_y^2}\right) \frac{1}{\sqrt{2\pi}\sigma_z} * \exp\left[-\frac{(z-L)^2}{2\sigma_z^2}\right] \quad \text{Equation 3.4}$$

where x and y represent the downwind and the crosswind distance from the emitter, and z the vertical distance from the ground. The two Gaussian exponential terms describe the dispersion of the plume in the horizontal and vertical direction respectively, Q is the emission rate of the source that is considered constant in time and magnitude, L is the height of the emitter and U is the wind speed that defines the x direction. The meteorological conditions used as inputs for the Gaussian model (mixing height, temperature, wind speed and direction) were obtained for each flight directly from the aircraft observations, by considering the mean values measured during the lowest grid performed above the landfills. The Gaussian model was then applied separately for each landfill on the same grid described above for the actual measurements. Each surface grid cell (50 x 50 m) included in any landfill area was considered an emissive cell at location $x = y = 0$, with a point source at the centre of

the square. By then multiplying the gridded CH₄ density - obtained from the Gaussian model - and the wind, we obtained CH₄ mass flows associated to each landfill, and unit grid cell emission. Those mass flows were then integrated along z and subsequently along both x and y to retrieve, for each landfill, 1-d modeled mass flow (MMF_i, where i is the number of landfills) signatures along and across wind direction, similarly to those computed from observations (figure 3.5).

An optimization approach by General Linear Model (GLM) was used to separate the contribution of each individual landfill through the equation:

$$\left| MF - \sum_{i=1}^4 (MMF_i \cdot \alpha_i) \right| = \min \quad \text{Equation 3.5}$$

where i = 4 is the number of landfills, MF is the CH₄ mass flow calculated for each flight over the entire domain, obtained with equations (3.2) and (3.3), and MMF_i are the flight specific modelled mass flows for each landfill. Equation (3.5) allows the estimation of landfill emission coefficients α_i that minimize the absolute difference between total measured mass flow (MF) and total modelled mass flow ($\sum_{i=1}^4 MMF_i \cdot \alpha_i$). Emission rates for each individual source were then obtained by multiplying 1-d modeled mass flow by its relative coefficient α_i .

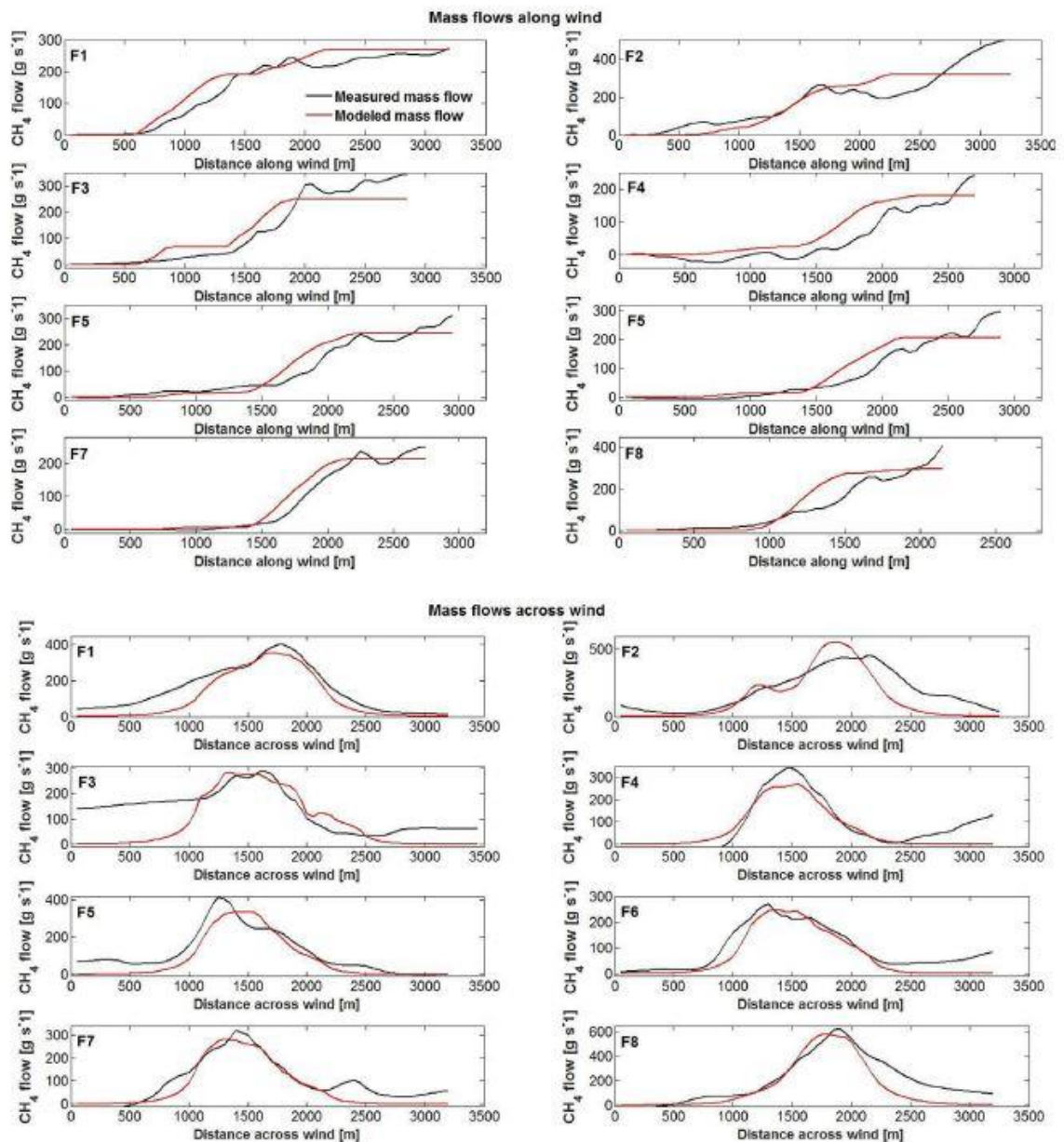


Figure 3.5 Comparison between modeled and measured mass flows. Black lines show computed mass flows for the study area down (upper panel) and across (lower panel) wind for each flight. The red lines show the estimates of CH_4 mass flows obtained from the Gaussian dispersion model through the solution of equation 3.5

Emission partitioning shown in figure 3.6 revealed that S1 was the strongest CH_4 source, with a mean emission covering 40% of the total and ranging from $30.7 \pm 2.6 \text{ g m}^{-1} \text{ day}^{-1}$ (F1) to $63.1 \pm 3.1 \text{ g m}^{-1} \text{ day}^{-1}$ (F8). S2 accounted for almost 30% of total emissions and values were quite steady for all flights, ranging between 31 and $48 \text{ g m}^{-1} \text{ day}^{-1}$. For F8 no emission was estimated from S2, as this flight was characterized by

a single and strong CH₄ plume located downwind of S1 and partially S3. S3 and S4 were the weaker sources accounting for 12% and 19% of the total emission. Emissions from S3 ranged from $54.0 \pm 19.1 \text{ g m}^{-2} \text{ day}^{-1}$ (F1) to $0.0 \pm 14. \text{ g m}^{-2} \text{ day}^{-1}$ (F4); for S4 the maximum emission was recorded during F2 ($58.3 \pm 27.1 \text{ g m}^{-2} \text{ day}^{-1}$) while the minimum during F8 ($3.0 \pm 9.8 \text{ g m}^{-2} \text{ day}^{-1}$).

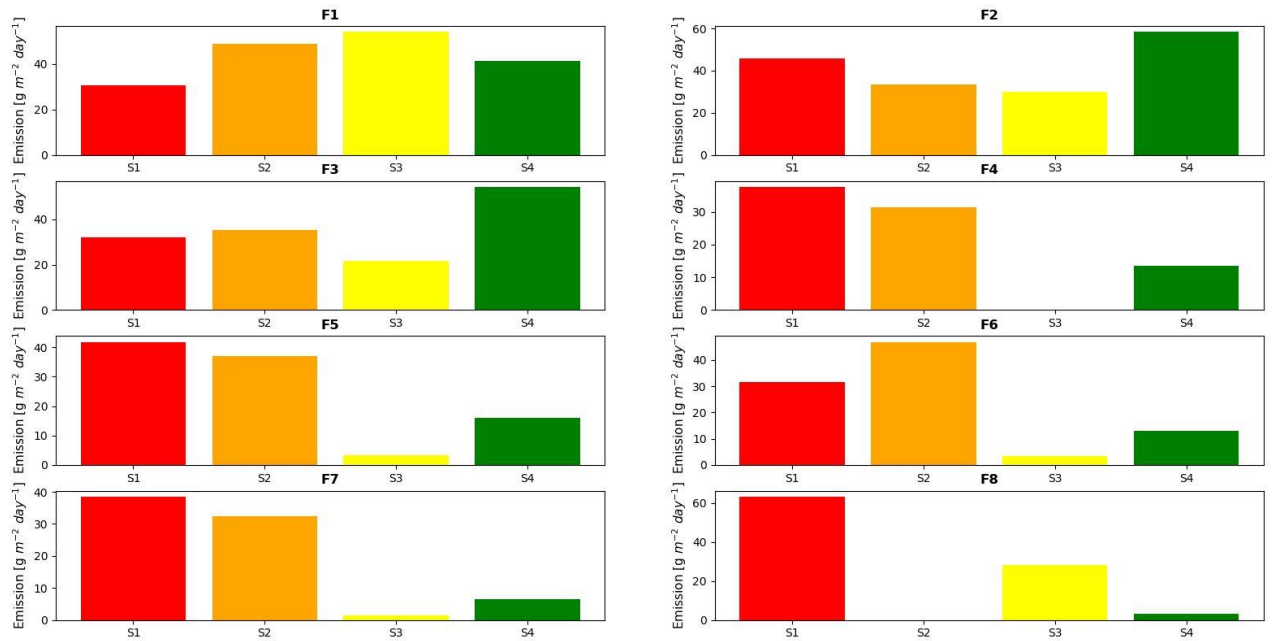


Figure 3.6 Emissions partitioning of each flight among the different landfills.

Results of this study have been published in August 2019, in the paper “Locating and quantifying multiple landfills methane emission using aircraft data”, which can be found in Appendix A of this chapter.



Contents lists available at ScienceDirect

Environmental Pollution

journal homepage: www.elsevier.com/locate/envpol



Locating and quantifying multiple landfills methane emissions using aircraft data[☆]



D. Gasbarra^{a, c, *}, P. Toscano^b, D. Famulari^a, S. Finardi^d, P. Di Tommasi^a, A. Zaldei^b, P. Carlucci^e, E. Magliulo^a, B. Gioli^b

^a ISAFOM-CNR, Institute for Mediterranean Agricultural and Forest Systems, National Research Council, Via Patacca 85, 80056 Ercolano, NA, Italy

^b IBE-CNR, Institute for Bioeconomy, National Research Council, Via G. Caproni 8, 50145, Italy

^c Department of Vegetal Biology, University of Napoli Federico II, Via Foria 223, 80139 Napoli, Italy

^d Arianet Srl, Via Gilino 9, 20128 Milan, Italy

^e ISAC-CNR, Institute of Atmospheric Sciences and Climate, National Research Council, Via Fosso del Cavaliere 100, 00133 Roma, Italy

ARTICLE INFO

Article history:

Received 25 February 2019

Received in revised form

30 July 2019

Accepted 30 July 2019

Available online 2 August 2019

Keywords:

Landfill emission

Airborne measurements

Mass balance

ABSTRACT

A mass balance approach to quantify methane (CH₄) emission of four co-located landfills by means of airborne measurements and dispersion modelling was proposed and assessed. By flying grids at different heights above the landfills, atmospheric CH₄ densities and wind components were measured along the edges and inside the study atmospheric volume, in order to calculate mass flows in the along- and across-wind directions. A steady-state Gaussian dispersion model was applied to build the concentration fields associated to unit emission from each landfill, while the contribution of each one to the total emission was assessed using a General Linear Model approach, minimizing the difference between measured and modeled mass flows. Results showed that wind spatial and temporal variability is the main factor controlling the accuracy of the method, as a good agreement between measured and modeled mass flows was mainly found for flights made in steady wind conditions. CH₄ emissions of the entire area ranged from 213.5 ± 33.5 to $317.9 \pm 90.4 \text{ g s}^{-1}$ with a mean value of $252.5 \pm 54.2 \text{ g s}^{-1}$. Contributions from individual sources varied from 17.5 to $40.1 \text{ g m}^{-2} \text{ day}^{-1}$ indicating a substantial heterogeneity of the different landfills, which differed in age and waste composition. The proposed method was validated against tower eddy covariance flux measurements made at one of the landfills, revealing an overall agreement within 20%.

© 2019 The Authors. Published by Elsevier Ltd. This is an open access article under the CC BY-NC-ND license (<http://creativecommons.org/licenses/by-nc-nd/4.0/>).

1. Introduction

Emission of CH₄ into the atmosphere is a serious environmental issue associated with landfilling of municipal waste. Decomposition of waste occurs through a complex series of microbial reactions, leading to the production of “landfill gas”, a gaseous mixture composed mainly of methane (CH₄) (50–60%) and carbon dioxide (CO₂) (40–50%), with traces of several other compounds (Themelis and Ulloa, 2007; Molino et al., 2013). Since CH₄ has a global warming potential 25 times higher than CO₂ over a 100 year time horizon (U.S. EPA, 2018), the global warming impact of landfills in terms of GHG is dominated by CH₄ emissions (~96–98%) while CO₂ emissions have a minor effect (~2–4%).

[☆] This paper has been recommended for acceptance by Admir Créso Targino.
* Corresponding author. ISAFOM-CNR, Institute for Mediterranean Agricultural and Forest Systems, National Research Council, Via Patacca 85, 80056 Ercolano, NA, Italy.
E-mail address: daniele.gasbarra@isafom.cnr.it (D. Gasbarra).

Several methods have been implemented and tested for estimating landfill emissions. Flux measurements from enclosure techniques (Czepiel et al., 1996; Schroth et al., 2012; Rachor et al., 2013) rely on monitoring the increase in mixing ratios of the target gas inside chambers placed directly on the ground. This technique presents limitations both in temporal resolution, being sporadic in time with sampling intervals sampling of the order of minutes to hours, and in spatial resolution, since the small sampled surface can be poorly representative of the larger scale surrounding area. Landfills are in fact characterized by high spatial heterogeneity causing large uncertainties in chamber flux estimates, even when relying on a large number of samples (Borjesson et al., 2000). The Atmospheric Tracer Method (ATM) is based on the assumption that a metered release of a tracer gas at the same location of an unknown emission source will identically disperse in the atmosphere. Assuming the air is well mixed, the emission rate is then calculated as a function of the ratio between the source and tracer gas mixing ratios measured downwind (Czepiel et al., 1996; Lamb

<https://doi.org/10.1016/j.envpol.2019.112987>

0269-7491/© 2019 The Authors. Published by Elsevier Ltd. This is an open access article under the CC BY-NC-ND license (<http://creativecommons.org/licenses/by-nc-nd/4.0/>).

et al., 1995).

Eddy covariance (EC) is a micrometeorological technique aimed at assessing turbulent exchange of mass, energy and momentum, based on the calculation of the covariance between vertical wind speed and gas density (Aubinet et al., 2012). EC is generally preferred to enclosure techniques because it integrates fluxes over wider areas due to the larger footprint of the turbulent atmospheric flow, and is suitable to provide continuous time-series of emission measurements (Schroth et al., 2012; Lohila et al., 2007; Rinne et al., 2005). However, reliable EC measurements of landfill surfaces may be difficult to achieve due to the complex orography and the lack of uniformity in the flux footprint area. Techniques based on the mass balance approach are often used to estimate emissions from large source areas, with several studies reporting applications based on airborne measurements. Mays et al. (2009) and Cambaliza et al. (2015) calculated CH₄ and CO₂ emissions from the city of Indianapolis by flying long horizontal transects downwind of the city, perpendicular to the wind direction and at different altitudes, measuring wind speed and the difference between background and within-plume gas mixing ratios. The same approach was used by O'Shea et al. (2014) to retrieve emissions of CH₄, CO₂ and carbon monoxide (CO) from Greater London. At a smaller spatial scale, Hacker et al. (2016) used airborne measurements to quantify the emissions of CH₄ and ammonia (NH₃) from feedlots in Australia. Transects were flown downwind of the source, at various heights and at different distances, and emissions calculated following the computational framework described in Bovensmann et al. (2014). A different measurement protocol is the 'box method', accomplished by flying in a circle or polygon at different heights around the emission source, in such a way that the mixing ratio of the species of interest is interpolated between multiple heights to reconstruct two-dimensional wind and concentration fields around the emission area. Gordon et al. (2015) inferred air pollutants emission rates over Alberta oil sands by flying in a square shape at multiple heights surrounding the area, and computing emissions by applying the divergence theorem in the control volume generated by the flight path. Gioli et al. (2014) evaluated CO₂ emissions from the city of Rome by flying in circles around the city at different heights and applying the mass conservation equation at the edge and top surfaces of the box. All these studies focused on the measurement of total emissions from a study area enclosed by a control

volume, generally not allowing for the separation into different, smaller spatial sources within the area. This study addresses this issue by adopting a mass balance approach based on the box method coupled with the implementation of a dispersion model, building an optimization framework to retrieve CH₄ emissions from individual landfills located close to each other within the domain. This novel approach was designed to be deployable in similar contexts, since landfills are usually characterized by irregular shapes, with several adjacent areas filled with waste of non-homogeneous age and composition. By flying gridded trajectories at different heights above the study area, CH₄ density and wind vector fields were reconstructed at the boundaries and within the box volume and an optimization algorithm was implemented to assess the strength of individual sources. The calculated emissions were validated against eddy covariance measurements from one of the landfills. The applicability and limitations of this approach in terms of study area geometry and meteorological conditions are finally discussed.

2. Materials and methods

2.1. Study area

This study is focused on a 5 × 5 km spatial domain near Naples, Italy (40° 55' N, 14° 11' E), inside an area known as "Terra dei fuochi" (Land of fires) due to the frequent occurrence of illegal open air waste burning. The climate of the area is typically Mediterranean, with mild winters when most of the yearly rain falls and relatively dry and hot summers; air temperatures measured during flights ranged from 12.4 °C in December to 22.6 °C in June (Table 1). Prevailing winds rotate from southwest to northeast direction, in a local breeze daily circulation pattern. The surrounding region is inhabited by about two million people over an area of 1000 km², making it among the most densely populated areas in Europe. The countryside is also well-known in the media as urban waste combined with industrial toxic waste has been dumped and spilled in old quarries or buried without control or safety measures since the 1980s (Bove et al., 2011). This led to a patchy presence of waste and associated biogas sources, with several emitting hot spots on a very heterogeneous landscape further associated with uncontrolled, small-scale waste burning, causing release of additional

Table 1

Maximum values of mixing ratio, mean temperature, mean wind speed and direction, total CH₄ mass flows from the entire area and emissions from individual landfills, measured during each flight along with their standard deviations. The last column on the right represents the root mean square error between measured and modeled mass flows of the entire study domain.

Flight	Date and time (UTC 0)	Max CH ₄ (ppm)	Mean Temp. (°C)	Mean wind Speed (m s ⁻¹)	Mean wind dir. (degrees)	Total Emission (g s ⁻¹)	S1 emission (g m ⁻² d ⁻¹)	S2 emission (g m ⁻² d ⁻¹)	S3 emission (g m ⁻² d ⁻¹)	S4 emission (g m ⁻² d ⁻¹)	RMSE (g s ⁻¹)
F1	27/10/2015 10:24–12:56	5.0	17.7	2.2 ± 0.4	59 ± 4	269.4 ± 48.5	30.7 ± 2.6	48.9 ± 9.2	54.0 ± 19.1	41.3 ± 13.7	43.9
F2	04/11/2015 13:15–15:57	5.8	17.2	1.6 ± 0.4	229 ± 24	317.9 ± 90.4	45.8 ± 5.3	33.6 ± 17.6	30.1 ± 29.4	58.3 ± 27.1	86.8
F3	02/12/2015 13:31–15:29	5.4	15.0	1.2 ± 0.5	235 ± 36	249.6 ± 64.8	31.9 ± 4.6	35.2 ± 8.5	21.8 ± 25.9	54.3 ± 8.5	69.7
F4	07/06/2016 11:05–13:58	4.2	22.3	5.2 ± 1.3	247 ± 3	214.8 ± 46.7	37.6 ± 2.6	31.5 ± 11.1	0.0 ± 14.8	13.4 ± 12.3	47.5
F5	08/06/2016 11:12–13:50	4.4	22.6	5.4 ± 1.2	239 ± 4	244.3 ± 51.4	41.8 ± 3.1	37.1 ± 12.4	3.3 ± 17.1	15.9 ± 12.3	42.4
F6	29/09/2016 10:43–13:08	3.6	21.1	3.4 ± 1.3	253 ± 4	208.1 ± 38.7	31.6 ± 2.4	46.8 ± 8.4	3.3 ± 13.3	13.1 ± 9.1	35.7
F7	19/10/2016 12:01–14:18	5.1	17.9	3.3 ± 0.9	245 ± 1	213.5 ± 33.5	38.4 ± 2.2	32.3 ± 7.2	1.3 ± 11.3	6.5 ± 7.6	32.4
F8	15/12/2016 10:52–13:06	4.5	12.4	4.1 ± 0.8	56 ± 9	299.1 ± 59.2	63.1 ± 3.1	0.0 ± 15.2	28.2 ± 26.7	3.0 ± 9.8	45.2
Mean methane emission						252.5 ± 54.2	40.1 ± 3.3	34.0 ± 11.2	17.5 ± 19.6	25.2 ± 12.6	

contaminants into the atmosphere and posing serious health risks to citizens (Carriero et al., 2018).

There are four landfills in the area (blue box in Fig. 1), with a total surface of about 620,000 m². S4 is a baled waste deposit while S1, S2 and S3 are landfills covered with plastic sheeting in the 1990s and with tubes for recovering biogas and drainage pipes for the collection of leaching waters (Fig. 1). Several arson attacks occurred in recent years, which destroyed most of the collection pipes and caused large openings in the plastic cover: as a result, none of the landfills is presently suitable for biogas recovery. No historical data quantifying the amount, chemical and physical properties of the deposited waste are available.

2.2. Airborne measurements

Airborne measurements were made with a Sky Arrow ERA (Environmental Research Aircraft) equipped with a Mobile Flux Platform (MFP), consisting of a pressure sphere, GPS (Novatel. U.S.A. mod. RT20) and inertial navigation systems. Three dimensional wind components were inferred on the basis of absolute and differential pressure data, measured at a frequency of 50 Hz by the Best Aircraft Turbulence (BAT) probe, a hemispherical 9 holes pressure sphere, retrieving wind angles of attack and sideslip (Crawford and Dobosy, 1992; Gioli et al., 2006). Raw data were recorded and synchronized on board during flights, while wind components were derived in post-processing. For CH₄ measurements, a new configuration of the LI7700 (Li-Cor, Inc.) open path gas analyzer was developed, based on enclosing the sensor within a cylinder exposed to the external air in-flow. The sensor was located on the back-plate of the Sky Arrow, above a trap door from which the air flow is conveyed to the instrument optical path. This setup allows for fast response measurements due to the high flow rate generated by aircraft movement, avoiding external modifications to the aircraft that would be subjected to severe restrictions. Signal strength of the laser (RSSI) was observed to decrease gradually during a flight likely because of dust deposition, but it always retained values around 50% after landing, which are adequate to preserve good data quality. CH₄ number density in $\mu\text{mol m}^{-3}$ and mixing ratio in $\mu\text{mol mol}^{-1}$ were logged from the instrument.

Eight flights were performed above the landfills from October 2015 to December 2016, at a cruise speed of 40 m s⁻¹ around midday, inside a well-mixed and developed Planetary Boundary Layer (PBL). The flight plan was repeated for each flight with an average duration of two and a half hours and consisted of repeated grids performed at different heights, namely 150, 250, 350 and 450 m asl, in order to resolve both horizontal and vertical spatial variability of CH₄ signals produced from landfill emissions.

2.3. Eddy covariance measurements

Turbulent flux measurements were taken from June 2015 to November 2016 in the S1 landfill (Fig. 1). The eddy covariance system was installed on a tower placed at the center of the landfill at 30 m height, and consisted of a USA-1 (Metek) sonic anemometer, a LI-7700 CH₄ open path analyzer and a CO₂/H₂O LI-7500 (Li-Cor, Inc.) open path analyzer. Raw data were acquired at 20 Hz and half-hourly fluxes were computed using the EddyPro® software package (https://www.licor.com/env/products/eddy_covariance/eddypro.html). A despiking procedure was specifically tuned to remove erroneous data (especially under rainy and foggy conditions); high-pass filtering with linear detrending was adopted (Aubinet et al., 1999); coordinate two-axis rotations were applied as described in Aubinet et al. (1999); corrections of CH₄ fluxes for air density fluctuations were implemented following Webb et al. (1980); QA/QC stationarity and integral turbulence tests were applied following Foken et al. (2004). Data outliers were removed by applying a 5- σ criterion in accordance with Chebyshev's theorem, which implies at least 96% of the acceptable data being within these boundaries without restrictions related to data distribution (Amidan et al., 2005). Finally, quality controlled CH₄ half hourly emissions were computed for the whole period, including the specific time of aircraft measurements.

2.4. Data gridding

In order to apply the mass budget method proposed here, three dimensional continuous grids of CH₄ and horizontal wind speed were obtained from the flight tracks. CH₄ atmospheric background

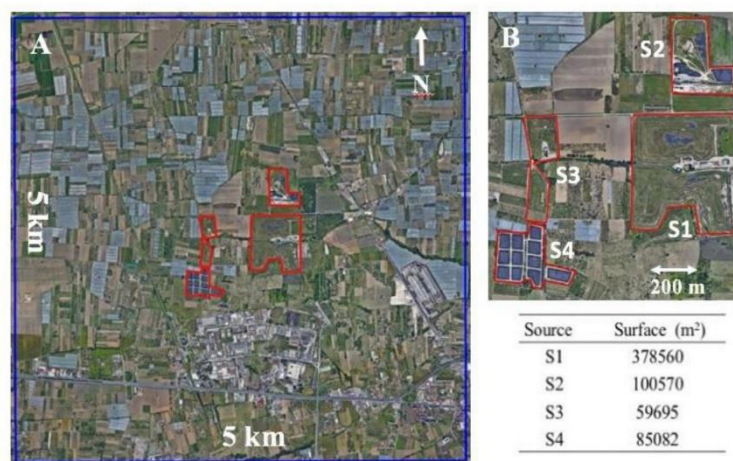


Fig. 1. Location (panel A) of the four landfills (red polygons) inside the study domain (blue rectangle). Panel B is a zoom of the emissive area. (For interpretation of the references to colour in this figure legend, the reader is referred to the Web version of this article.)

density was computed for each flight and subtracted from each measurement to better isolate landfill plume signatures. CH₄ resulting densities and wind data were then interpolated on a grid encompassing the flight domain and extending vertically from the surface to an altitude at which plumes are no longer sampled (Z_{TOP}). Gridded data were computed at 50 m horizontally and 20 m vertically resolution, using an inverse distance weighting (IDW) to a power (squared) algorithm (Ninyerola and Roure, 2007; Chen and Liu, 2012). IDW technique is based solely on the assumption that close data points are more related each other than distant points, not relying on any spatial relationship (Davis, 1986), as:

$$C_{est}^j = \frac{\sum_{i=1}^n \frac{C_i}{d_{ij}^2}}{\sum_{i=1}^n \frac{1}{d_{ij}^2}} \quad (1)$$

where C_{est}^j is the estimated value of CH₄ densities or wind data for location j , C_i are the values of the neighboring points i and d^2 the squared distance between grid note j and neighboring points. Following eq. (1), we obtained a gridded dataset of CH₄ density and wind speed. For each point, a spheroid neighboring volume was chosen with a horizontal axis of 1500 m and vertical axis of 200 m. Considering that the distance between aircraft horizontal transects was around 250–300 m, and the vertical spacing between flight level was around 150 m, for each interpolation several measured points fall within the spheroid, minimizing the impact of short-term fluctuations due to turbulent structures detected by high frequency measurements. To verify the appropriateness of this choice, we computed the variance of densities over the domain on a 250×250 m (x-y) window, and then compared them to those obtained from the application of a steady state Gaussian dispersion model (described in the following section). The comparison gave very similar results (data not shown), confirming that the interpolated densities were not on average affected by the presence of short term turbulent fluctuations.

2.5. Total emissions (mass flows)

Proceeding from upwind to downwind in the wind direction, the total CH₄ mass transported downwind starts to rise (above the background) when hitting the first landfill emission plume, then continues to rise as the other plumes are encountered, reaching a maximum at the downwind distance where all the landfills plume signatures are included. The shape of such monotonic behavior depends on the underlying landfills geometry and emission rates. Similarly, integrating the CH₄ flow across the wind direction at the same downwind distance, a cross wind signature of the landfills plumes is obtained. The idea behind our method is: i) to compute these two 'signatures' of integral mass flows measured along the wind direction x (with integration on y) and across wind (with integration along x); ii) to compute the same signatures with a Gaussian dispersion model run with unit emission at each grid mesh enclosed in the landfill perimeter and iii) to retrieve model emission multiplicative factors for each landfill in order to minimize the difference between observed and modeled signatures. The method is then evaluated in two ways: i) by comparing observed and modeled integral signatures (e.g. Gaussian model predictions), referring to the cumulative response of all the landfills; ii) by comparing retrieved S1 emissions with eddy covariance fluxes measured at the S1 landfill.

Wind and CH₄ density grids were rotated for each flight, according to mean wind direction, obtaining a wind-aligned box domain (Fig. 2). The CH₄ net mass flow was then obtained multiplying gridded densities by rotated wind speed. The total mass flow

(MF) ($g s^{-1}$) along and across the wind aligned direction was then calculated as the integral of the net MF along y - z (parallel to mean wind direction) and along x - z (perpendicular to mean wind direction) using equations (2) and (3), to obtain MF along and across wind direction, respectively:

$$MF_ALONG(x) = \int_0^{Z_{TOP}} \int_{y_1}^{y_2} C_{ij} \cdot V_{ij} \, dy \, dz \quad (2)$$

$$MF_ACROSS(y) = \int_0^{Z_{TOP}} \int_{x_1}^{x_2} C_{ij} \cdot V_{ij} \, dx \, dz \quad (3)$$

where Z_{TOP} is height of the top of the box, x_1 - x_2 and y_1 - y_2 are the horizontal boundaries of the study area (5x5 Km domain), dy dx and dz are horizontal and vertical grid spacing respectively (dy , $dx = 50$ m, $dz = 20$ m). C_{ij} and V_{ij} are the CH₄ molar densities and wind speed, where i and j are horizontal and vertical grid cell indices. Total flow rates obtained from equations (2) and (3) were calculated for each flight based only on aircraft measurements, without information or assumption on the underlying emission sources.

2.6. Gaussian model

A steady-state Gaussian dispersion model was deployed to compute CH₄ density $C(x,y,z)$ at any point of the study domain as follows:

$$C(x,y,z) = \frac{Q}{2\pi\sigma_y\sigma_zU} * \exp\left(-\frac{y^2}{2\sigma_y^2}\right) \frac{1}{\sqrt{2\pi\sigma_z}} * \exp\left[-\frac{(z-L)^2}{2\sigma_z^2}\right] \quad (4)$$

where x and y represent the downwind and the crosswind distance from the emitter, and z the vertical distance from the ground. The two Gaussian exponential terms describe the dispersion of the plume in the horizontal and vertical direction respectively, Q is the emission rate of the source that is considered constant in time and magnitude, L is the height of the emitter and U is the wind speed that defines the x direction. Dispersion coefficients σ_y and σ_z are

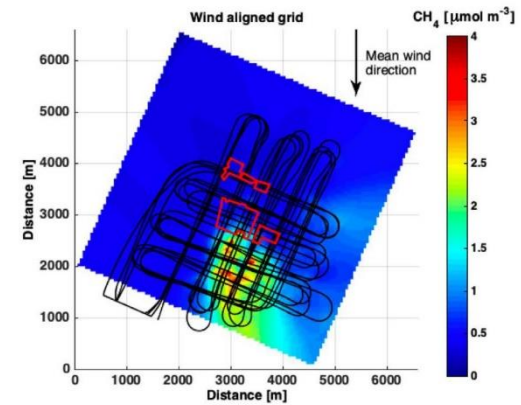


Fig. 2. CH₄ density map integrated along z direction obtained from one of the flights (F6) after 3D interpolation. The dimensions of the study area are reported on x and y axes. Black lines represent the flight paths above the landfills. The grid is rotated to align with the mean wind direction.

defined by the distance from the emitter and by atmospheric Guifford-Pasquill stability classes (Pasquill, 1961), chosen for each flight by considering wind speed at the lowest aircraft grid height, cloud cover and radiation intensity measured at the EC tower. The meteorological conditions used as inputs for the Gaussian model (mixing height, temperature, wind speed and direction) were obtained for each flight directly from the aircraft observations, by considering the mean values measured during the lowest grid performed above the landfills. The Gaussian model was then applied separately for each landfill on the same grid described above for the actual measurements. Each surface grid cell (50 × 50 m) included in any landfill area was considered an emissive cell at location $x = y = 0$, with a point source at the center of the square. By then multiplying the gridded CH₄ density obtained from Gaussian model and wind, we obtained CH₄ mass flows associated to each landfill and unit grid cell emission. Those mass flows were then integrated along z and subsequently along both x and y to retrieve, for each landfill, 1-d modeled mass flow (MMF_{*i*}, where i is the number of landfills) signatures along and across wind direction, similarly to those computed from observations.

2.7. Partitioned emissions

An optimization approach by General Linear Model (GLM) was used to separate the contribution of each individual landfill through the equation:

$$|MF - \sum_{i=1}^4 (MMF_i \cdot \alpha_i)| = \min \tag{5}$$

where $i = 4$ is the number of landfills, MF is the CH₄ mass flow calculated for each flight over the entire domain, obtained with equations (2) and (3), and MMF_{*i*} are the flight specific modeled mass flows for each landfill. Equation (5) allows the estimation of landfill emission coefficients α_i that minimize the absolute difference between total measured mass flow (MF) and total modeled mass flow ($\sum_{i=1}^4 MMF_i \cdot \alpha_i$). Emission rates for each individual source were then obtained by multiplying 1-d modeled mass flow by its relative coefficient α_i . All the (background corrected) CH₄ mass flows measured downwind were assumed to be attributable to surface emission only. Root Mean Square Error (RMSE) was calculated from measured and modeled mass flows for each flight according to:

$$RMSE = \sqrt{\sum_{i=1}^n (O_i - E_i)^2} \tag{6}$$

where O_i and E_i are observed and simulated mass flows values respectively, n is the number of grid squares.

Uncertainties in mass flow calculation are computed as the standard deviations of $n = 1000$ bootstrap samples generated by applying parametric bootstrap to the residuals between measured and modeled values (Flores-agreda and Cantoni, 2019).

3. Results

The wind regime during the measurement campaigns was fairly steady with a prevailing south-westerly direction; mean direction ranged between 229 and 253° for six of the eight flights, without any seasonal cycle (Table 1). Only F1 and F8 showed a prevailing north-easterly wind (59 and 56° N, respectively), due to land-sea breeze regime development. Wind speeds varied between

1.2 m s⁻¹ measured during F3 and 5.4 m s⁻¹ during F5, as expected showing an increase with altitude for each flight. Flights characterized by low winds (F2 and F3) were associated to more variable conditions. Mean wind direction for these flights showed high uncertainties of 24 and 36° respectively (Table 1), induced by pronounced wind differences observed among the measurements taken at different heights.

CH₄ mixing ratios increased, as expected, downwind of the landfills, with maxima ranging from 3.6 ppm (F6) to 5.8 ppm (F2) corresponding to an increase of about 200% and 300% over the normal ambient background value (Table 1). The results reported here in detail are for flight F6, which is representative of the typical behavior of CH₄ mixing ratios observed during all the measurement campaigns. Multiple strong plumes were measured above the study area at different heights; the CH₄ signal above the landfills decreased gradually with altitude, although during daytime convective conditions, mixing ratios greater than background values were still measured even at the highest level, confirming the presence of strong emission sources at the ground (Fig. 3).

Fig. 4 shows the horizontal extent of the plume: five transects

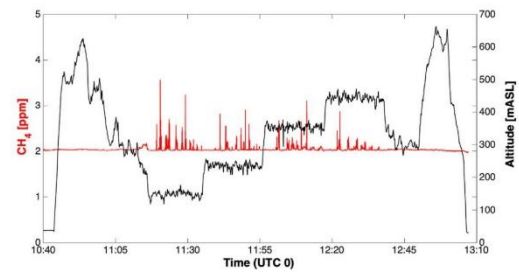


Fig. 3. Time trends of CH₄ mixing ratio measured during one of the flights (F6) at 1 Hz resolution. Flight pattern portions at constant height correspond to the grids performed above the study domain.

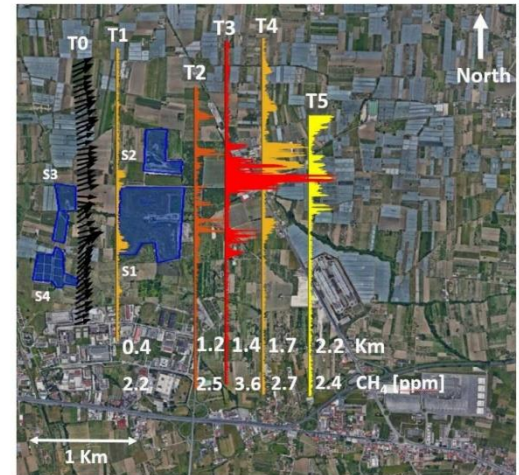


Fig. 4. Horizontal transects flown during one of the flights (F6), performed at 140 m asl. Black arrows signify wind direction and magnitude along the trajectory T0. Colored lines are proportional to CH₄ mixing ratio while numbers at the bottom represent distances from T0 and maximum mixing ratio values measured for each transect.

were flown over the landfills with a steady westerly wind of around 4 m s^{-1} at a height of 140 m. The CH_4 plume was still clearly visible at a distance of 2.2 km from the western boundaries of S3 and S4, with a maximum measured mixing ratio of 2.4 ppm (T5 in Fig. 4). At 1.4 km downwind of the farthest source, the CH_4 plume shows the maximum magnitude with mixing ratios reaching 3.6 ppm, representing an increase of 85% above the background of 1.9 ppm. Proceeding from upwind to downwind, the T1 transect lied downwind of landfills S3 and S4 and upwind of S1 and S2 (Fig. 4), therefore the two weak plumes that were measured along it can be attributed to S3 and S4, located about 400 m upwind. As expected, these were the weaker sources, due both to their small size and type of landfill, since S4 is a baled waste deposit. The T2 transect showed several low intensity plumes; emissions from S3 and S4 produced limited mixing ratio increases with respect to T1 measurements, as the

aircraft did not intercept the plume produced by S1 and S2 that became clearly visible along T3, where the highest values of CH_4 mixing ratios could be detected. The crosswind structure of the plume was well defined at this distance from the sources, with maximum values located between S1 and S2 (T2 in Fig. 4). T4 and T5 exhibit spatially increasing plumes due to the horizontal and vertical dispersion farther downwind from the sources (Fig. 4).

Results for F6 confirmed the findings suggested by observed patterns, revealing that S1 (33%) and S2 (50%) emissions accounted for about 80% of total (Table 1). CH_4 emissions have also been computed for the other flights, on the basis of CH_4 mass flows along and across wind direction computed from observations according to equations (2) and (3), and obtained from the optimization equation (5) (Fig. 5). Total surface CH_4 emission of the entire study area for each flight ranged from $208.1 \pm 38.7 \text{ g s}^{-1}$ (F6) to

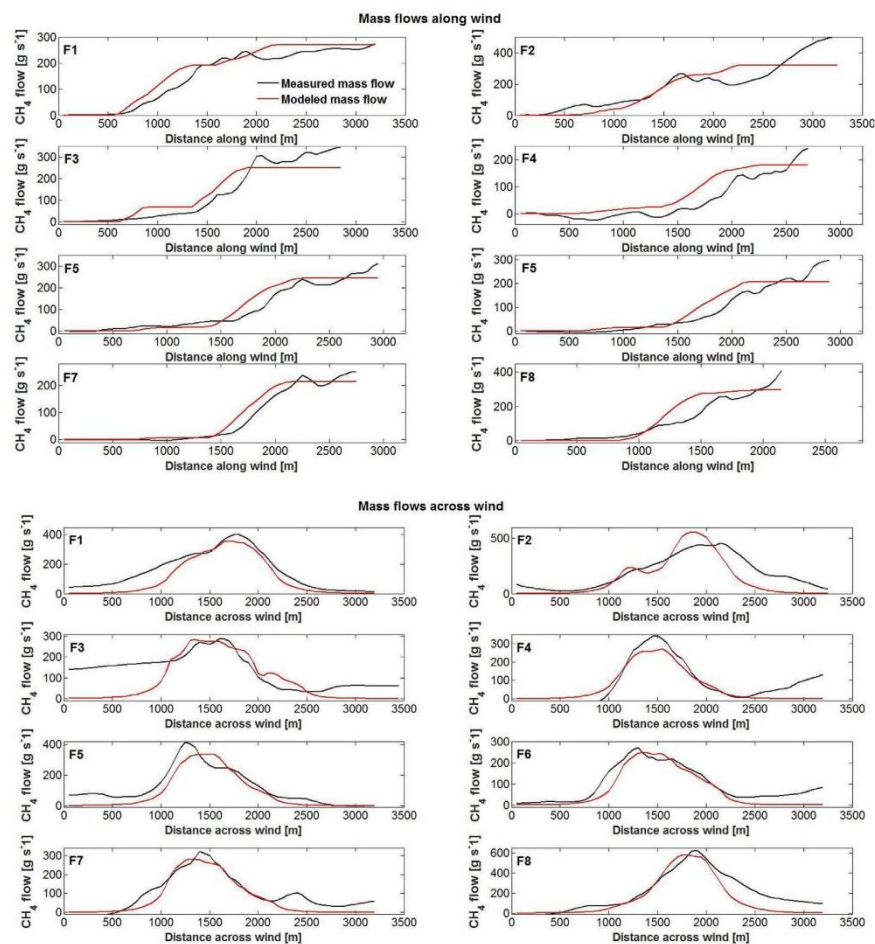


Fig. 5. Comparison between modeled and measured mass flows. Black lines show computed mass flows for the study area down (upper panel) and across (lower panel) wind for each flight. The red lines show the estimates of CH_4 mass flows obtained from the Gaussian dispersion model through the solution of equation (5). (For interpretation of the references to colour in this figure legend, the reader is referred to the Web version of this article.)

$317.9 \pm 90.4 \text{ g s}^{-1}$ (F2), with a mean value of $252.5 \pm 54.2 \text{ g s}^{-1}$ (see Table 1). RMSE between measured and modeled mass flows followed the wind field variability. Flights performed with a steady wind regime showed similar RMSE, between 40 and 50 g s^{-1} , while wind field rotation occurring in F2 and F3 produced an enhancement of RMSE (Table 1).

Emission partitioning revealed that S1 was the strongest CH_4 source, with a mean emission covering 40% of the total and ranging from $30.7 \pm 2.6 \text{ g m}^{-2} \text{ day}^{-1}$ (F1) to $63.1 \pm 3.1 \text{ g m}^{-2} \text{ day}^{-1}$ (F8). S2 accounted for almost 30% of total emissions and values were quite steady for all flights, ranging between 31 and $48 \text{ g m}^{-2} \text{ day}^{-1}$. For F8 no emission was estimated from S2, as this flight was characterized by a single and strong CH_4 plume located downwind of S1 and partially S3. S3 and S4 were the weaker sources accounting for 12% and 19% of the total emission. Emissions from S3 ranged from $54.0 \pm 19.1 \text{ g m}^{-2} \text{ day}^{-1}$ (F1) to $0.0 \pm 14.8 \text{ g m}^{-2} \text{ day}^{-1}$ (F4); for S4 the maximum emission was recorded during F2 ($58.3 \pm 27.1 \text{ g m}^{-2} \text{ day}^{-1}$) while the minimum during F8 ($3.0 \pm 9.8 \text{ g m}^{-2} \text{ day}^{-1}$) (Table 1).

A comparison of airborne derived emissions with EC fluxes from S1 was made for the different flights (Fig. 6). The two methods resulted in fairly good agreement as both fluxes always showed the same order of magnitude; the best match between airborne and ground data was observed during F6, with an airborne CH_4 flux of $22.7 \mu\text{mol m}^{-2} \text{ s}^{-1}$ and a flux at the tower during flight time of $23.0 \mu\text{mol m}^{-2} \text{ s}^{-1}$. An accurate match was also observed for F1 and F3, while the greatest discrepancies were found during summer flights (F4 and F5).

4. Discussion

In this paper we proposed a method based on airborne

measurements to retrieve individual CH_4 emissions from four closely located landfills. The approach uses a steady state Gaussian dispersion model to separate the contribution of the different landfills to the emissions, while the total emission intensity of the study domain is inferred from the airborne measurements. Computed fluxes appeared consistent, with mean values across multiple flights for each landfill ranging from 17.5 to $40.1 \text{ CH}_4 \text{ g m}^{-2} \text{ day}^{-1}$, values that are well comparable with previous studies on landfill emissions. Mønster et al. (2015), using ATM, reported CH_4 fluxes in the range of $0.7\text{--}13.2 \text{ g m}^{-2} \text{ day}^{-1}$ from 15 Danish landfills with gas extraction systems or employing biocovers to reduce gas escapes. With the same method, Borjesson et al. (2000) evaluated emissions from seven active Swedish landfills with gas collection systems. CH_4 fluxes ranged from 3.71 to $20.6 \text{ g m}^{-2} \text{ day}^{-1}$. Mosher et al. (1999) compared ATM approach with enclosure techniques obtaining excellent agreement between the two methods, and the measured CH_4 emissions in two landfills in the USA ranged from $9.1 \text{ g m}^{-2} \text{ day}^{-1}$ for an active site with biogas retrieval to $130 \text{ g m}^{-2} \text{ day}^{-1}$ for an active site without gas recovery. Nozhevnikova et al. (1993) measured CH_4 fluxes from several uncontrolled landfills around Moscow by enclosure methods, in a situation similar to that of our study domain, obtaining emissions as high as $32 \text{ g m}^{-2} \text{ day}^{-1}$. Our findings confirm that biogas recapture strategy is the main driver of CH_4 emission to the atmosphere, which can be one order of magnitude higher on sites that do not deploy recovery technology.

All observed mass flows, i.e. the mass of CH_4 advected downwind of the landfills, increased with distance from the sources reaching their maxima around 1.5 km downwind of the emissive area, due to the dispersion of pollutants emitted at ground level (see e.g. Fig. 4). This behavior confirms that the landfill plume development was correctly captured within the area sampled by

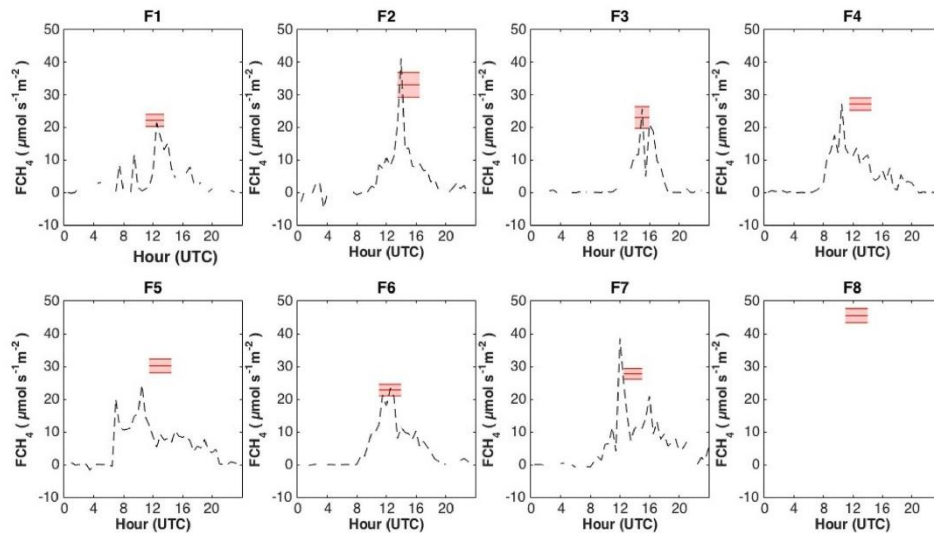


Fig. 6. Comparison between half-hourly fluxes of CH_4 measured by the eddy covariance flux station (black dashed lines) and mass flows from S1 landfill obtained from aircraft measurements (red lines), with their related uncertainties (shaded red region). No data are available from the tower in coincidence with flight F8. (For interpretation of the references to colour in this figure legend, the reader is referred to the Web version of this article.)

the flights, and that the presence of other relevant CH₄ sources at the boundaries of the domain can be excluded.

The method proposed here aims to optimize the agreement between modeled and observed CH₄ mass flows (i.e. CH₄ mass advected downwind of the emission areas) by means of a simple dispersion model to estimate the plume development down and across wind. The advantage of using the mass flow as the optimized variable is its robustness, since it is always monotonic proceeding from upwind to downwind (in the presence of source-only areas without sinks), and its shape changes only according to the underlying surface emissions geometry and rate. Using the mixing ratio to directly retrieve surface emissions (i.e. as in a classical atmospheric inversion framework) would have made the method much more sensitive to specific dispersion conditions, since the mixing ratio varies markedly within emission plumes and decreases with turbulent dispersion and dilution, thus increasing the uncertainties.

Our results point out that wind direction stability and wind field magnitude variability are crucial factors for the reliability of the approach proposed here. The agreement between measured and estimated mass flows is rather good for flights made in stationary conditions, as no strong wind rotation along the vertical occurs, and the high CH₄ gradients are clustered. In the absence of a steady wind regime, measured mass balances may show a non-monotonic increase (see F2 and F3 in Fig. 5), widening the discrepancy between estimated and measured values, as observed for F2 and F3 characterized by weak winds just above 1 m s⁻¹ (Table 1). The lack of a stationary wind field also induces mixing of the plumes produced by different portions of the landfill, making the Gaussian model less effective in reproducing the distribution of atmospheric CH₄ mixing ratios; a simple meteorological parameterization cannot in fact reproduce the real conditions encountered in flight. The 3-D interpolations of CH₄ density also become less effective in such conditions, due to the proximity of high CH₄ measured values inside the spheroid leading to distortion effects in the interpolated field. Emissions estimated here refer to the whole landfill areas, and cannot therefore provide information about the presence of emissive hot spots or spatial heterogeneity within a specific landfill, which would require higher spatial density measurements. The use of unmanned aerial vehicles (UAV) for these kinds of studies has recently been carefully assessed and allows high spatial resolution of the measurements flying at low speed and low altitude (Allen et al., 2014). Allen et al. (2018) used UAV for the measurements of CH₄ flux from landfill hotspots by means of a mass balance approach tailored for UAV measurements, and found comparable emissions to ours, between 50 and 140 g s⁻¹. Their approach presents limitations on larger study domains, due to poor wind field characterization (they used a sonic anemometer positioned at the launch location) and the inherent lower flight autonomy of UAVs. Fixed wing UAV equipped with wind measurement probes are necessary to adequately measure wind vectors (Reuder et al., 2009); however, such platforms typically have very limited payload capacity, making the installation of any gas sensor of sufficient accuracy a challenge.

The comparison between EC fluxes and airborne-derived emissions showed a good agreement overall. During flights F4 and F5, EC tower fluxes showed lower values than aircraft, that can be related to wind speed magnitude. These flights were in fact characterized by more sustained wind above 5 m s⁻¹, typical of the summer sea-land breeze regime, whereas the other flights showed mean values below 3.4 m s⁻¹ (Table 1). The high wind speed caused the flux footprint to extend farther upwind of the tower, likely integrating areas outside the landfill and hence reducing the emission rate per unit surface. Airborne derived emissions were instead always integrated over the same ground area, regardless of

wind conditions during each flight, thus producing a more robust estimate.

Possible improvements of the validation strategy for this method may consist in the installation of additional EC towers in other emissive landfills, or in the alternate deployment of a single EC tower at different landfills for different sub periods.

5. Conclusions

Rapid economic and demographic growth has made the land-filling of municipal waste and consequent biogas release to the atmosphere a serious environmental issue. In our research we proposed an alternative mass balance approach based on airborne measurements, able to distinguish individual contributions from four different landfills located near one another. For this purpose, we computed CH₄ mass flows in combination with simulated CH₄ emissions obtained through a steady state Gaussian dispersion model. High emissions from the entire study area were measured, with a mean value of $252.5 \pm 54.2 \text{ g s}^{-1}$, while releases from single landfills ranged from 17.5 to 40.1 g m⁻² day⁻¹. EC tower fluxes measured over the same study area were successfully compared with airborne retrieved emissions. A future upgrade of this approach could involve the use of more complex and advanced dispersion models based on Computational Fluid Dynamics (CFD) for the emission partitioning, which may be capable of an improved simulation of the actual dispersion flows. The retrieval of emissions sources is challenging in heterogeneous landscapes such as landfills, and CFD models can overcome these issues, by including the effects of complex site topography (Sonderfeld et al., 2017). A more effective simulation of dispersion patterns could also be assessed by CALPUFF, a well established non-steady state model considering the effect of time, weather and topographic conditions (Wang et al., 2019). Lagrangian simulations (Flesch et al., 1995; Seibert and Frank, 2004) are finally a potential tool to derive improved relationships between measured mixing ratios and source strength in backward configuration, where particles trajectories are modeled from the sensor to the emission source using turbulence and meteorological parametrizations derived from aircraft data.

Declarations of interest

None.

Acknowledgement

This work was partly funded by project MIUR PON Cluster OT4CLIMA.

Appendix A. Supplementary data

Supplementary data to this article can be found online at <https://doi.org/10.1016/j.envpol.2019.112987>.

References

- Allen, G., Gallagher, M.W., Hollingsworth, P., Illingworth, S., Kabbabe, K., Percival, C.J., 2014. Feasibility of Aerial Measurements of Methane Emissions from Landfills. Environment Agency, Bristol, UK.
- Allen, G., Hollingsworth, P., Kabbabe, K., Pitt, J.R., Mead, M.L., Illingworth, S., Roberts, G., Bourn, M., Shallcross, D.E., Percival, C.J., 2018. The development and trial of an unmanned aerial system for the measurement of methane flux from landfill and greenhouse gas emission hotspots. Waste Manag. 87, 883–892.
- Amidan, B.G., Ferryman, T.A., Cooley, S.K., 2005. Data outlier detection using the Chebyshev theorem. IEEE Aerosp. Conf. Proc. 3–8.
- Aubinet, M., Vesala, T., Papale, D., 2012. Eddy Covariance: a Practical Guide to Measurement and Data Analysis. Springer, ISBN 978-94-007-2350-4.
- Aubinet, M., Grelle, A., Ibrom, A., Rannik, Ü., Moncrieff, J., Foken, T., Kowalski, A.S., Martin, P.H., Berbigier, P., Bernhofer, C., et al., 1999. Estimates of the annual net

- carbon and water exchange of forests: the EUROFLUX methodology. *Adv. Ecol. Res.* 30, 113–175.
- Bovensmann, H., Krings, T., Gerilowski, K., Neininger, B., Ruhtz, T., Lindemann, C., 2014. C-MAPEX Final Report (ESA Study).
- Borjesson, G., Danielsson, A., Svensson, B.H., 2000. Methane fluxes from a Swedish landfill determined by geostatistical treatment of static chamber measurements. *Environ. Sci. Technol.* 34 (18), 4044–4050.
- Bove, M.A., Ayuso, R.A., De Vivo, B., Lima, A., Albanese, S., 2011. Geochemical and isotopic study of soils and waters from an Italian contaminated site: agro aversano (campania). *J. Geochem. Explor.* 109 (1–3), 38–50.
- Cambaliza, M.O.L., Shepson, P.B., Bogner, J., Caulton, D.R., Stirn, B., Sweeney, C., Montzka, S.A., Gurney, K.R., Spokas, K., Salmon, O.E., et al., 2015. Quantification and source apportionment of the methane emission flux from the city of Indianapolis. *Elem. Sci. Anthr.* 3, 000037.
- Carriero, G., Neri, L., Famulari, D., Di, S., Piscitelli, D., Manco, A., Esposito, A., Chirico, A., Facini, O., Finardi, S., et al., 2018. Composition and emission of VOC from biogas produced by illegally managed waste landfills in giugliano (Campania, Italy) and potential impact on the local population. *Sci. Total Environ.* 640–641, 377–386.
- Chen, F.W., Liu, C.W., 2012. Estimation of the spatial rainfall distribution using inverse distance weighting (IDW) in the middle of taiwan. *Paddy Water Environ.* 10 (3), 209–222.
- Crawford, T.L., Dobosy, R.J., 1992. A sensitive fast-response probe to measure turbulence and heat flux from any airplane. *Boundary-Layer Meteorol.* 59 (3), 257–278.
- Czepiel, P.M., Mosher, B., Harriss, R.C., Shorter, J.H., McManus, J.B., Kolb, C.E., Allwine, E., Lamb, B.K., 1996. Landfill methane emissions measured by enclosure and atmospheric tracer methods. *J. Geophys. Res.* 101 (D11), 16711.
- Davis, J.C., 1986. *Statistics and Data Analysis in Geology*. John Wiley & Sons Inc., New York. ISBN 9781601195838.
- Flesch, T.K., Wilson, J.D., Yee, E., 1995. Backward-time Lagrangian stochastic dispersion models and their application to estimate gaseous emissions. *J. Appl. Meteorol.* 34 (6), 1320–1332.
- Flores-agreda, D., Cantoni, E., 2019. Bootstrap estimation of uncertainty in prediction for generalized linear mixed models. *Comput. Stat. Data Anal.* 130, 1–17.
- Foken, T., Gockede, M., Mauder, M., Mahr, L., Amir, B., Munger, W., 2004. Post-field data quality control. *Handb. Micrometeorol.* 29, 181–208, 1988.
- Gioli, B., Carfora, M.F., Magliulo, V., Metallo, M.C., Poli, A.A., Toscano, P., Miglietta, F., 2014. Aircraft mass budgeting to measure CO₂ emissions of Rome, Italy. *Environ. Monit. Assess.* 186 (4), 2053–2066.
- Gioli, B., Miglietta, F., Vaccari, F.P., Zaldei, A., De Martino, B., 2006. The Sky arrow ERA, an innovative airborne platform to monitor mass, momentum and energy exchange of ecosystems. *Ann. Geophys.* 49 (1), 109–116.
- Gordon, M., Li, S.M., Staebler, R., Darlington, A., Hayden, K., O'Brien, J., Wolde, M., 2015. Determining air pollutant emission rates based on mass balance using airborne measurement data over the Alberta oil sands operations. *Atmos. Meas. Tech.* 8 (9), 3745–3765.
- Hacker, J.M., Chen, D., Bai, M., Ewenz, C., Junkermann, W., Lief, W., McManus, B., Neininger, B., Sun, J., Coates, T., et al., 2016. Using airborne technology to quantify and apportion emissions of CH₄ and NH₃ from feedlots. *Anim. Prod. Sci.* 56 (3), 190–203.
- Lamb, B.K., McManus, J.B., Shorter, J.H., Kolb, C.E., Mosher, B., Harriss, R.C., Allwine, E., Blaha, D., Howard, T., Guenther, A., et al., 1995. Development of atmospheric tracer methods to measure methane emissions from natural gas facilities and urban areas. *Environ. Sci. Technol.* 29 (6), 1468–1479.
- Lohila, A., Laurila, T., Tuovinen, J.P., Aurela, M., Hatakka, J., Thum, T., Pihlatie, M., Rinne, J., Vesala, T., 2007. Micrometeorological measurements of methane and carbon dioxide fluxes at a municipal landfill. *Environ. Sci. Technol.* 41 (8), 2717–2722.
- Mays, K., Shepson, P., Stirn, B., 2009. Aircraft-based measurements of the carbon footprint of Indianapolis—supplementary material. *Environ. Sci. Technol.* 43 (20), 7816–7823.
- Molino, A., Nanna, F., Ding, Y., Bikson, B., Braccio, G., 2013. Biomethane production by anaerobic digestion of organic waste. *Fuel* 103, 1003–1009.
- Mønster, J., Samuelsson, J., Kjeldsen, P., Scheutz, C., 2015. Quantification of methane emissions from 15 Danish landfills using the mobile tracer dispersion method. *Waste Manag.* 35, 177–186.
- Mosher, B.W., Czepiel, P.M., Harriss, R.C., Shorter, J.H., Kolb, C.E., McManus, J.B., Allwine, E., Lamb, B.K., 1999. Methane emissions at nine landfill sites in the northeastern United States. *Environ. Sci. Technol.* 33 (12), 2088–2094.
- Ninyerola, M., Roure, J.M., 2007. Objective air temperature mapping for the Iberian Peninsula using spatial interpolation and GIS. *Int. J. Climatol.* 27 (January), 1231–1242.
- Nozhevnikova, A.N., Lifshitz, A.B., Lebedev, V.S., Zavarzin, G.A., 1993. Emission of methane into the atmosphere from landfills in the former USSR. *Chemosphere* 26 (1), 401–417.
- Pasquill, F., 1961. The estimation of the dispersion of windborne material. *Meteorol. Mag.* 90, 33–49.
- Rachor, I.M., Gebert, J., Gröngroft, A., Pfeiffer, E.M., 2013. Variability of methane emissions from an old landfill over different time-scales. *Eur. J. Soil Sci.* 64 (1), 16–26.
- Reuder, J., Brisset, P., Jonassen, M., Müller, M., Mayer, S., 2009. The small unmanned meteorological observer SUMO: a new tool for atmospheric boundary layer research. *Meteorol. Z.* 18 (2), 141–147.
- Rinne, J., Pihlatie, M., Lohila, A., Thum, T., Aurela, M., Tuovinen, J.-P., Laurila, T., Vesala, T., 2005. Nitrous oxide emissions from a municipal landfill. *Environ. Sci. Technol.* 39 (20), 7790–7793.
- Schroth, M.H., Eugster, W., Gómez, K.E., Gonzalez-Gil, G., Niklaus, P.A., Oester, P., 2012. Above and below ground methane fluxes and methanotrophic activity in a landfill-cover soil. *Waste Manag.* 32 (5), 879–889.
- Seibert, P., Frank, A., 2004. Source-receptor matrix calculation with a Lagrangian particle dispersion model in backward mode. *Atmos. Chem. Phys. Discuss.* 3, 4515–4548.
- Shea, S.J.O., Allen, G., Fleming, Z.L., Bauguitte, S.J., Percival, C.J., Gallagher, M.W., Lee, J., Helfter, C., Nemitz, E., 2014. Area fluxes of carbon dioxide, methane, and carbon monoxide derived from airborne measurements around greater London: a case study during summer 2012. *J. Geophys. Res. Atmos.* 119, 4940–4952.
- Sonderfeld, H., Bosch, H., Jeanjean, A.P.R., Riddick, S.N., Allen, G., Ars, S., Davies, S., Harris, N., Humpage, N., Leigh, R., et al., 2017. CH₄ emission estimates from an active landfill site inferred from a combined approach of CFD modelling and in situ FTIR measurements. *Atmos. Meas. Tech.* 10 (10), 3931–3946.
- Themelis, N.J., Ulloa, P.A., 2007. Methane generation in landfills. *Renew. Energy* 32 (7), 1243–1257.
- U.S. EPA, 2018. *Inventory of U.S. Greenhouse Gas Emissions and Sinks (1990–2016)*. United States Environ. Prot. Agency.
- Wang, Q., Zuo, X., Xia, M., Xie, H., He, F., Shen, S., Bouazza, A., Zhu, L., 2019. Field investigation of temporal variation of volatile organic compounds at a landfill in Hangzhou, China. *Environ. Sci. Pollut. Res.* 26, 18162–18180.
- Webb, E.K., Pearman, G.I., RG, L., 1980. Correction of flux measurements for density effects due to heat and water-vapor transfer. *Q. J. R. Meteorol. Soc.* 106, 85–100.

Chapter 4

Agricultural GHGs emissions measurements in Campania Region

[The contents of this section have been published in Gasbarra, D., et al. (2019). Land-Atmosphere exchange of N₂O, CH₄ and CO₂ from a Mediterranean rotation cropland. 2019 IEEE International Workshop on Metrology for Agriculture and Forestry (MetroAgriFor), 68–71 and can be found in Appendix A of this chapter]

4.1 Greenhouse gases exchange over *Lolium italicum* and *Sorghum bicolor* crops in the Mediterranean

Agroecosystems play an important role in the global anthropogenic influence on climate through the variation of carbon storage potential of the ecosystems and exchange of greenhouse gases (GHGs) such as methane, carbon dioxide and nitrous dioxide.

N₂O is one of the most important long-lived GHG and soils account, globally for about 60% of the total N₂O release to the atmosphere. Microbial nitrification and denitrification in soils are the major sources of atmospheric N₂O. Under anaerobic conditions, incomplete denitrification produce N₂O whereas the terminal step of denitrification consumes N₂O. Hence, microbial N₂O production and consumption can occur simultaneously in soil via the activities of different microorganisms or even by a single denitrifying cell. In addition, within the soil profile and in the soil air-filled pores, N₂O can be further reduced to N₂ during its transport to the soil surface. Soil physical and biochemical factors influence the balance between soil N₂O production and consumption, and consequently the net N₂O flux to the atmosphere.

Direct, ground-based measurements of in situ CH₄ fluxes with high measurement frequency are important for understanding the responses of CH₄ fluxes to environmental factors including climate, for providing validation datasets for the land surface models used to infer global CH₄ budgets, and for constraining CH₄ budgets. Borgo Cioffi site is a part of a new coordination activity for flux tower CH₄ measurements organized by the Global Carbon Project (GCP) in collaboration with

regional flux networks and FLUXNET. The goal of the activity is to develop a global database for eddy covariance CH₄ observations to answer regional and global questions related to CH₄ cycling. Detailed description of the first results of this new activity coordination have been published (S. Knox, D. Gasbarra et al., 2019) and can be found in Appendix B of this chapter.

In particular, GHG continuous measurements from crops in the Mediterranean are of primary importance in order to validate emission inventories, which often rely on very few studies performed in this kind of climate. Water buffalo (*Bubalus bubalis*) farms play an important role in this region, both economically, for the production of mozzarella cheese typical of the Campania region, and environmentally, in terms of impacts of: animal husbandry, crops to feed the animals, and dairy production.

Here we present flux measurements carried out at the Borgo Cioffi site, that has been described in detail in Chapter 1, with the primary aim to identify and compare the most significant sources of GHGs from a typical cropland in the Mediterranean environment with particular focus on emissions sources associated with fertiliser application and management practices on a rotating crop.

Date	Crop Management			Tilling depth
	Event	Crop variety	N [kg ha ⁻¹]	
10/10/17	Fertilisation	<i>Lolium italicum</i>	75	–
25/10/17	Fertilisation	<i>Lolium italicum</i>	75	–
28/10/17	Ploughing	<i>Lolium italicum</i>	–	35 cm
31/10/17	Harrowing and sowing	<i>Lolium italicum</i>	–	–
28/4 - 1/5/18	Fertilisation	<i>Sorghum bicolor</i>	75	–
15/5/18	Ploughing with incorporation	<i>Sorghum bicolor</i>	–	<20 cm
18/5/18	Fertilisation	<i>Sorghum bicolor</i>	75	–
17/6/18	Harrowing and sowing	<i>Sorghum bicolor</i>	–	–

Table 4.1 Agricultural practices at Borgo Cioffi

N-fertiliser application rates have been approximately 300 Kg N ha⁻¹ yr⁻¹ (regional regulation impose a maximum of 340, including grazed areas). The fertilizer used is

slurry produced by the water-buffalo farm located nearby (see Section 4.2 for details). For what concerns soil management, greater soil disturbance, such as that caused by ploughing, can cause rapid respiration and loss of large amounts of soil carbon which would otherwise decompose more slowly. Inversion ploughing will turn the soil upside down, and the disturbance will depend on the depth of ploughing. Repeated mechanical operations cause soil microorganisms to become more compromised, reducing their potential, and inversion can help oxygenate soil, making methane and nitrous oxide emissions from anaerobic soils less likely. According to the tillage classes, defined by France National Institute for Agricultural Research (INRA), the measured tillage events on the field site can be defined as double-layer ploughing (inversion of the soil to a depth of about 15 cm and loosening to about 30 cm) and/or non-inversion (10-25 cm depth). The tilling depth and modality at the Borgo Cioffi site changes: at times incorporating residual crop, and less deep; according to the farmer necessities (weather over the season, pesticide usage, etc.).

Measurements took place over two different periods: in the first period (30 October 2017- 22 April 2018) *Lolium italicum*, grown for fodder, it constitutes the usual choice of a winter crop in this region. In the second period (12 May- 20 August 2018), *Sorghum bicolor*, very common species of grain grown in this region, as it is drought- and heat- resistant species: also grown for fodder, it constitutes a common alternative to maize in scarcely irrigated areas.

1.4.1 Field deployment of the eddy covariance tower

The eddy covariance station is setup approximately in the centre of the field, which has a rectangular shape with dimension of 300x600 m. The height of the sonic anemometer varied from 2.15 to 2.60 m according to vegetation growth stages. The terrain is flat with a gentle slope of approximately 2% toward south (see figure 4.1.1). A CW-QCL TILDAS (Aerodyne Research Inc., Billerica, MA, USA) was used for the fast, simultaneous measurements of N₂O, CH₄ and H₂O mixing ratios, whereas a LICOR7200 (LiCor, Lincoln, NE, USA) monitored CO₂ and H₂O: all gas were sampled at 10 Hz frequency.

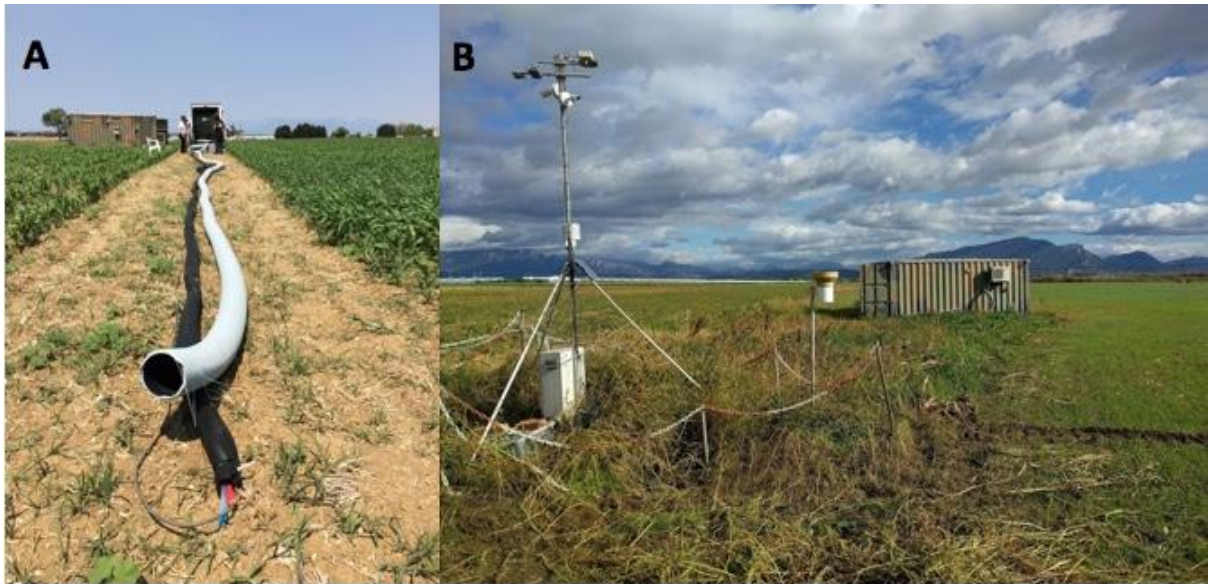


Figure 4.1.1 Preparation of the sampling line which connect the eddy covariance tower to the container where sensors are located. This picture refer to the set-up of the station, at the beginning of the work. For this reason the sampling line still laid on the soil.

The instrumentation was placed in an air conditioned sea container. A Gill R3 Ultrasonic anemometer (Gill Instruments Ltd., Lymington, Hampshire, UK) functioning at 10 Hz was used to measure the wind vector. A heated and insulated PTFE sampling line of 32.6 m length with a pipe diameter 3/8'' ran from the sonic anemometer to the CW-QCL inside the container, air was drawn with a turbulent flow rate greater than 18 l/min (Reynold number of 4236). All system logged data to a CR3000 data logger (Campbell Scientific Inc., Logan, UT, USA) by a custom made program storing synchronous raw data. In addition, meteorological data were recorded above the canopy: photosynthetic photon flux by Li-190 (LI-COR, Lincoln, NE, USA), air temperature and relative humidity by CS215-L (Campbell Scientific, Logan UT, USA). The site was also equipped with a rain gauge TE525-L (Campbell Scientific, Logan UT, USA) to measure precipitations and a barometric pressure transducer Setra 278 (Setra System Inc., Boxborough MA, USA) to measure air pressure.

4.1.1 *Lolium italicum* crop

Meteorology

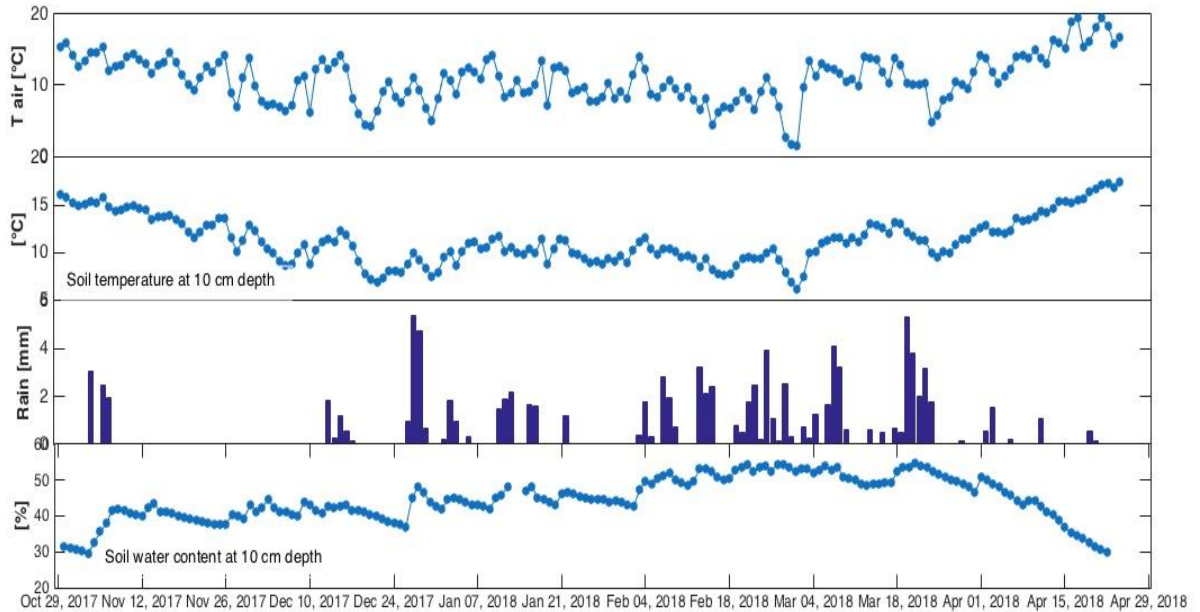


Figure 4.1.2 From top to bottom: air *T*, soil *T*, rainfall and volumetric soil water content at a depth of 10 cm.

Figure 4.1.2 shows the meteorology of the first measurement campaign (30 October 2017- 22 April 2018). Mean temperature of the whole period was 10.9 °C with a minimum value of 1.5 °C measured on February and a maximum value of 19.5 °C measured in April. Soil temperature followed a similar behaviour to the air temperature, ranging from 6.1 °C to 17.4 °C. Mean volumetric water soil content was about 46% throughout the observation period, showing a strong decrease to 30% from the end of March 2018 until the end of the measurement campaign corresponding to the temperatures increase. Artificial irrigation was not necessary in this season due to the frequent rainfall events. The wind field (figure 4.1.3) shows the typical pattern of winter sea-land breeze circulation, with a prevalent North-East direction and highest wind speed of about 12 ms⁻¹ measured in December 2017.

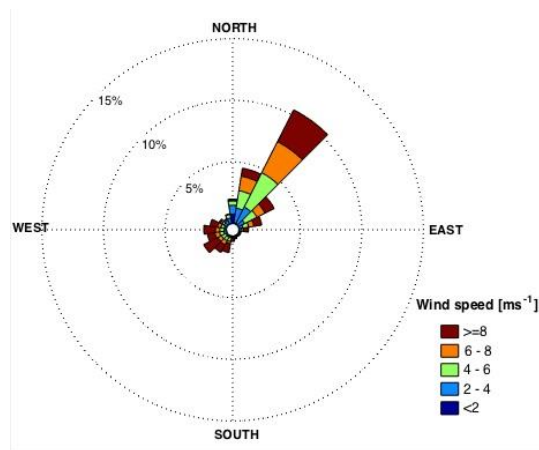


Figure 4.1.3 Wind field measured during the campaign.

GHGs fluxes

In figure 4.1.4 the half-hourly averages of CO₂ fluxes for the whole measurements period are reported. CO₂ uptake from the crop is clearly evident in the central hours of the day with maximum values around -30 μmol m⁻² s⁻¹ reached during the vegetation phase. Crop act as sink during this phase with a daily mean uptake of about -7.5 μmol m⁻² s⁻¹.

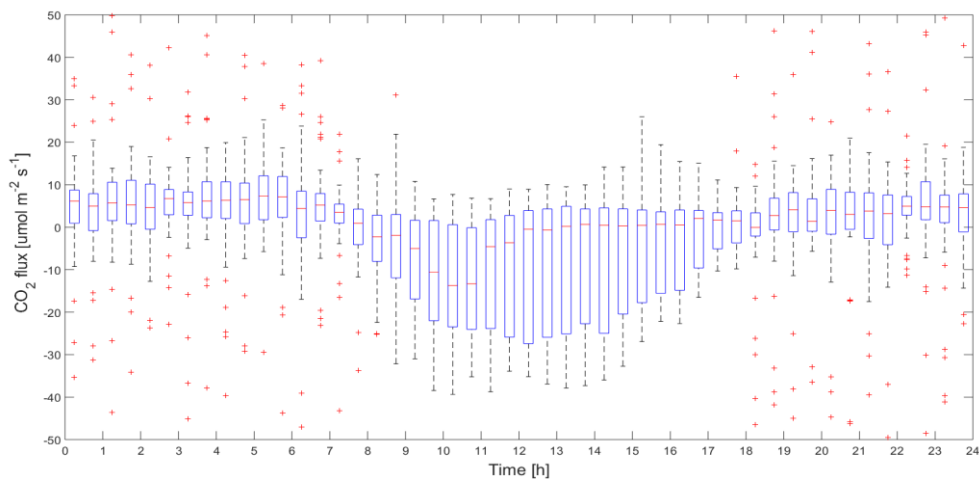


Figure 4.1.4 Daily cycles of CO₂ fluxes from 30 October 2017 to 22 April 2018. On each box, the central mark indicates the median, and the bottom and top edges of the box indicate the 25th and 75th percentiles, respectively. The whiskers extend to the most extreme data points not considered outliers. Data points are considered outliers if they are greater than $q_3 + w \times (q_3 - q_1)$ or less than $q_1 - w \times (q_3 - q_1)$, where w is the maximum whisker length, and q_1 and q_3 are the 25th and 75th percentiles of the sample data, respectively.

In Fig. 4.1.5 daily N_2O fluxes showed very small emission response after every operation performed on the field, in fact on average, N_2O emission during the whole measurements campaign was about $0.8 \text{ nmol } N_2O \text{ m}^{-2} \text{ s}^{-1}$, while the highest N_2O fluxes were observed following the spreading of buffalo slurry with a maximum of $7 \text{ nmol } N_2O \text{ m}^{-2} \text{ s}^{-1}$. These fluxes are very close to zero, and it can be concluded that the emissive contribution of the *lolium italicum* crop in the winter season was negligible, by comparison to the emissive character of the following season (see next section). This is likely due to the very different nature of the fertiliser used in the two different season: the N content of the autumn event was very low, as the fertiliser was very diluted liquid fraction of the buffalo slurry, while the spring event was solid fraction slurry, very rich in organic matter content.

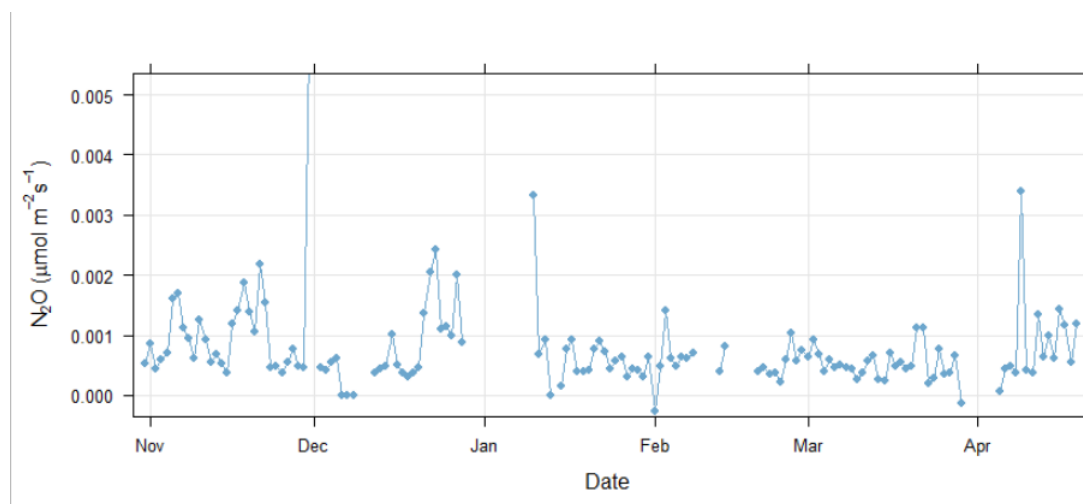


Figure 4.1.5 Mean daily fluxes of N_2O from 30 October 2017 to 22 April 2018.

CH_4 fluxes measured during the field campaign were negligible, no significant signal was detected also after the fertilization process, probably because liquid, diluted slurry was used in this occasion, without the solid, organic matter rich part. Figure 4.1.6 shows that the higher CH_4 mixing ratios measured during the campaign are related to a wind direction between 50 and 70 degrees, showing that the concentrations increase is due to transport phenomena from the livestock that is outside the tower footprint. These advection episodes occurred mainly during night hours, when stability was prevalent, while during daytime hours, the mixing re-established stationary conditions.

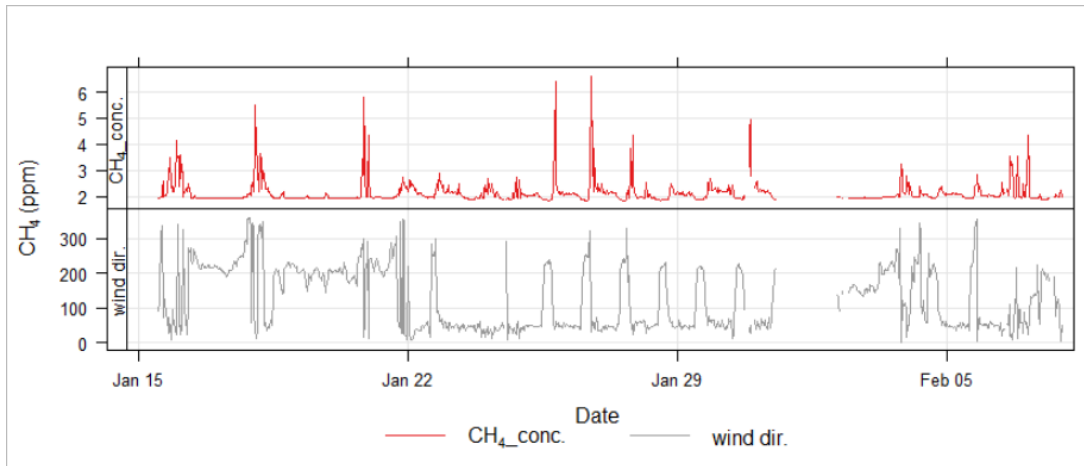


Figure 4.1.6 Time series of CH_4 concentrations (top panel) and wind direction (bottom), showing plumes of methane originating from the nearby paddocks.

4.1.2 *Sorghum bicolor* crop

Meteorology.

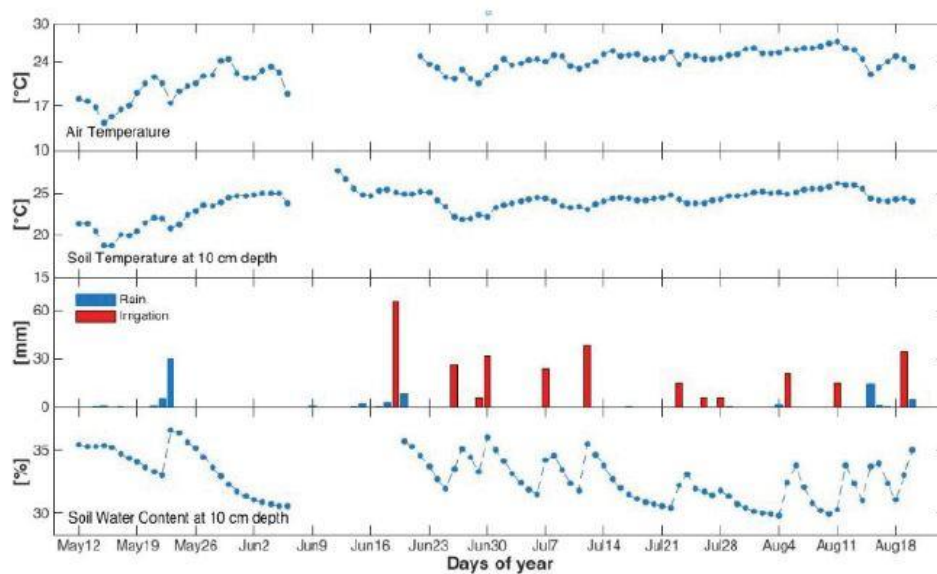


Figure 4.1.7 From top to bottom: air T , soil T , rainfall (blue) and irrigation (red) rates, volumetric soil water content at a depth of 10 cm and wind rose. Data refer to the whole measurements period.

Figure 4.1.7 shows the meteorology of the second measurements campaign period, relative to the growth of *Sorghum bicolor* (from 12 May to 20 August 2018). Daily temperatures show mean value around 25 °C during the summer period, while mean soil temperatures rise from 20 °C to 23 °C during summer. The lack of rainfall during

the summer at the site requires artificial irrigation, therefore the soil water content follows the irrigation events on the crop, remaining below 35% volumetric water content throughout the observation period.

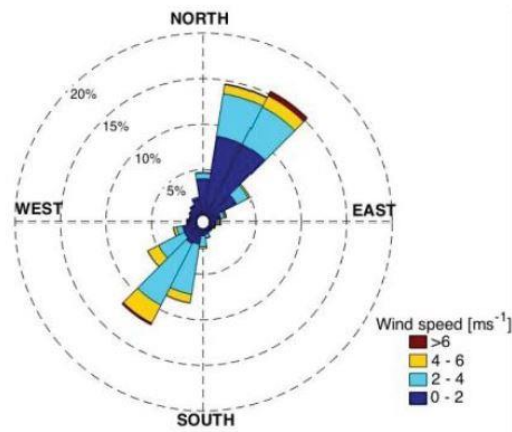


Figure 4.1.8 Wind rose recorded at Borgo Cioffi during the whole measurement period.

The wind field at Borgo Cioffi (figure 4.1.8) shows a typical sea land breeze regime with North East to South West prevalent direction, with mean values ranging from 0.5 to 9.4 m s⁻¹.

GHGs fluxes

In figure 4.1.9 are reported the half-hourly averages of CO₂ fluxes of the whole measurements period. Plant photosynthesis process is clearly evident during daytime hours, characterized by sunlight, through the uptake of CO₂ from the atmosphere by the canopy showing a maximum absorption during the central hours of the day of about 30 μmol m⁻² s⁻¹ (see green line in Fig. 4.1.9). CO₂ fluxes show that the field acts as a sink of C during the vegetated stages, with average daily net uptake value of -12.5 μmol m⁻² s⁻¹.

On the other hand, during the post-tillage phase, the measured CO₂ fluxes show an emissive character, due to the carbon loss from the soil. This lasted until vegetation re-established full photosynthetic activity (grey line in Fig.4.1.9).

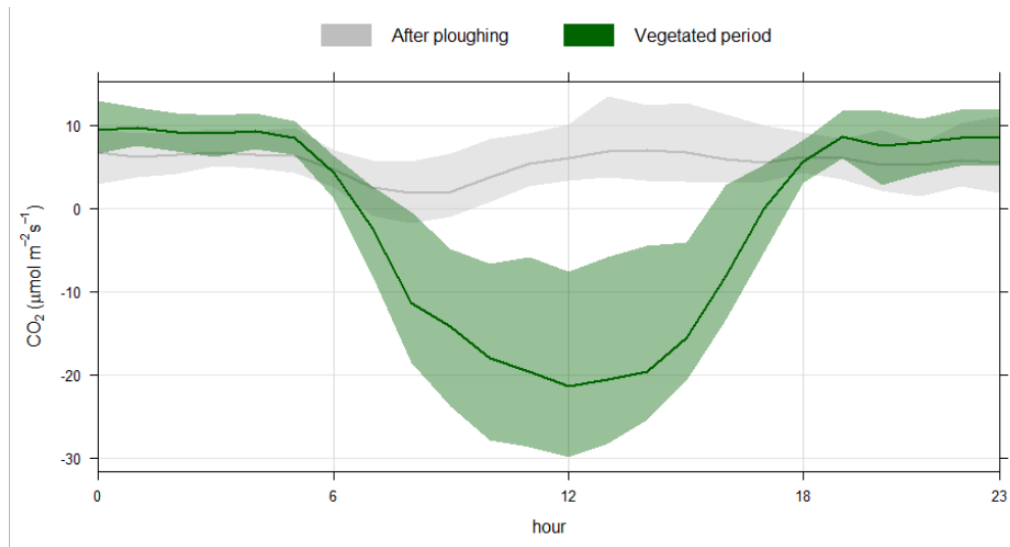


Figure 4.19 Daily cycles of CO₂ fluxes from 12 May to 20 August. The central lines indicate the median, and areas around indicate the 25th and 75th percentiles, respectively. The green line indicates the behaviour of CO₂ fluxes during the vegetated period, the grey line the period post-ploughing event.

After the tillage event, the mean flux measured was $7 \mu\text{mol m}^{-2} \text{s}^{-1}$ during that period. Time series of N₂O daily fluxes (figure 4.1.10) show an important emission feature, following the tillage and the fertilisation events. Before the ploughing event fluxes were close to zero: the fertilization event triggered the highest response, while both irrigation and tillage (any type of tilling) were followed by relatively small increase of emission.

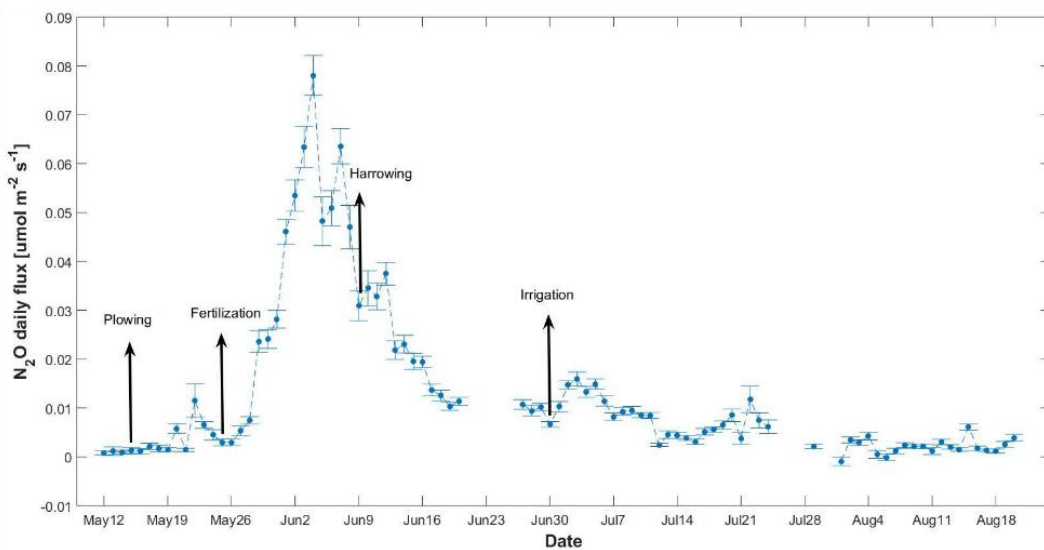


Figure 4.1.10 Mean daily fluxes of N₂O from 12 May to 20 August 2018. The most important farming operations performed on the field are reported in the graph.

N₂O fluxes showed an emission response after every operation performed on the field, and emissions were recorded both after ploughing and harrowing of the field.

Average N₂O emission during the whole measurements campaign was about 23 nmol N₂O m⁻² s⁻¹ while the highest N₂O fluxes were observed following the spreading of buffalo slurry with a maximum of 78 nmol N₂O m⁻² s⁻¹, ten days after fertilization.

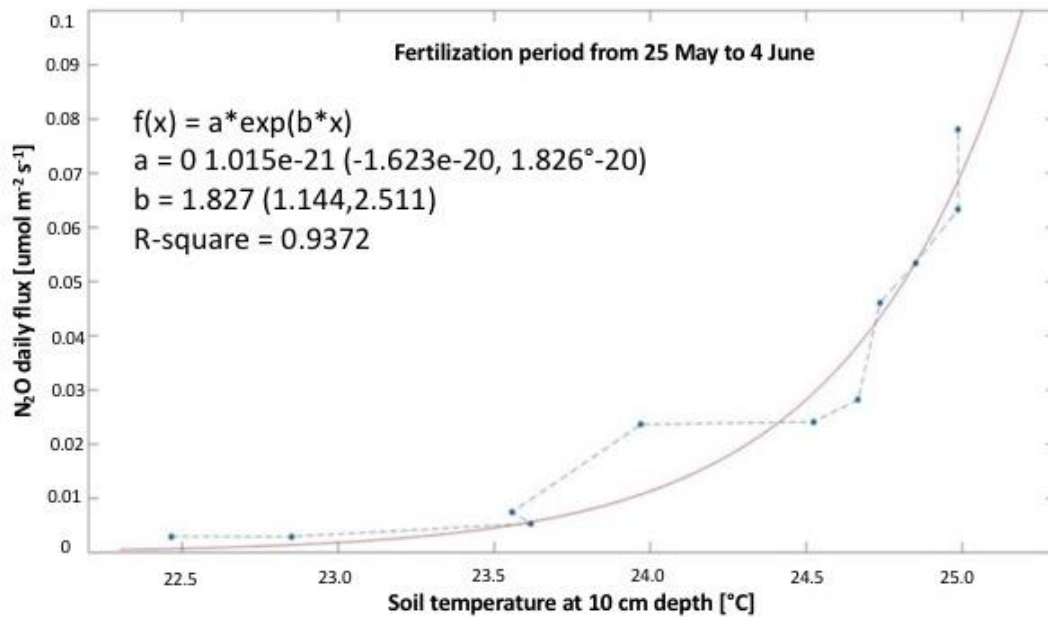


Figure 4.1.11 Relation between N₂O emissions and soil temperatures during the 25th May-4th June 2018 fertilization period.

In order to underpin the causes of N₂O release, environmental variables measured on site has been correlated with N₂O fluxes during the fertilization period, showing that soil T at 10 cm depth has the clearest relationship (figure 4.1.11) respect both to temperature at deeper depth and to water soil content.

CH₄ average concentrations were 2.6 ppm (figure 4.1.12), well above the background level of about 1.9 ppm. This is explicable by the vicinity of the buffalo farm, an important source of CH₄ influencing the area: in fact, during stable conditions, the cumulated CH₄ at the animal houses gets advected to the field, at the measurement tower, hence enhancing considerably the measured methane concentrations.

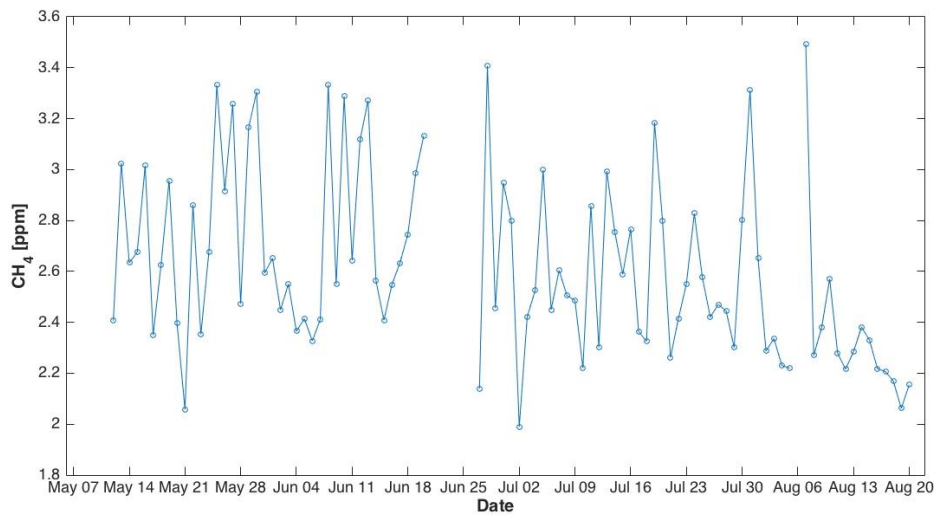


Figure 4.1.12 Daily mean CH_4 mixing ratios measured during the field campaign

Despite the high CH_4 mixing ratios measured at the site, very low fluxes from the ground have been measured, with a mean value of $0.027 \mu\text{mol m}^{-2} \text{s}^{-1}$ (figure 4.1.13).

Flux data were rejected according to the hypotheses of the eddy covariance method, for the advection phenomena from the livestock housing due to night time atmospheric stagnation.

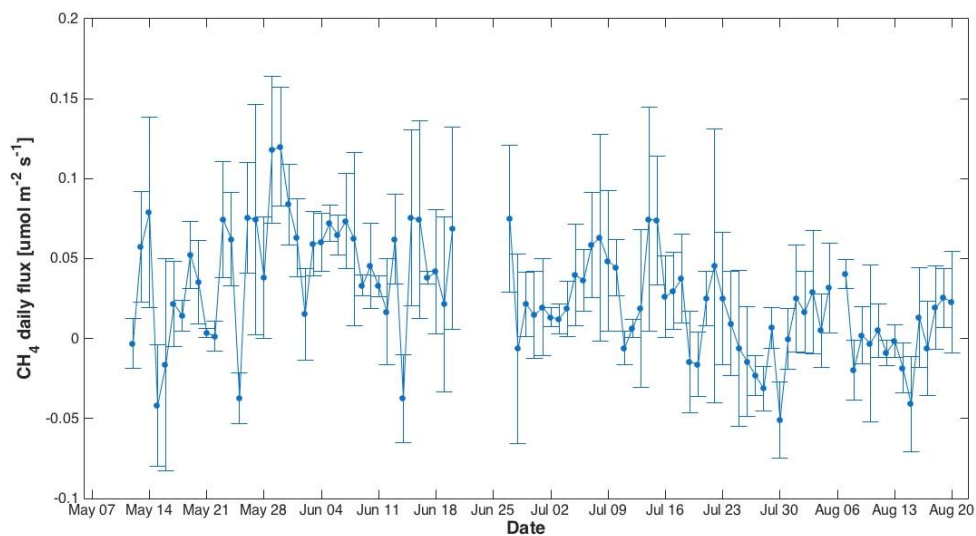


Figure 4.1.13 Daily mean of CH_4 fluxes measured during the field campaign

A small increase has been observed simultaneously to the fertilization process at the end of May, these small fluxes could be related to a direct emission from the slurry that had been spread on the field, as shown in Fig. 4.1.14.

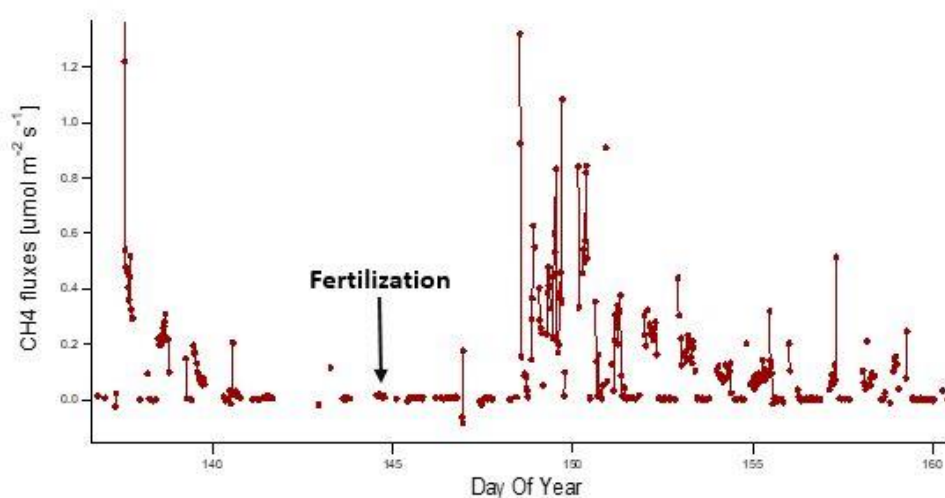


Figure 4.1.14 Time series of half-hourly CH₄ fluxes recorded in the weeks after the tillage and fertilisation events.

4.1.3 Discussion

The tilled field acted as a source for all measured GHG during the period following the soil disturbance event in the spring 2018, mostly for N₂O and CO₂, and marginally for CH₄. CO₂ emissions were of the order of 7 μmol m⁻² s⁻¹.

Both agricultural practices, tillage and fertilisation, occur at a very short distance, if not simultaneously, if considering the overall field. This poses a challenge when trying to distinguish the impact of the individual event, be it fertilising or disturbing the soil. CH₄ and N₂O emissions were both higher during the spring event, though in general, the CH₄ contribution was very small, and it can be concluded that the impact of CH₄ emissions from both crops is negligible. Further investigation on the CH₄ advection from the livestock can be found in section 4.2, addressing the importance of livestock in terms of CH₄ emissions.

Highest N₂O fluxes were observed during the days following the spreading of buffalo slurry mixed with solid as fertilizer (spring 2018), where maximum emission reached 78 nmol N₂O /m²s ten days after fertilization.

In general, both crops acted as a source for CH₄ and N₂O, and as a sink for CO₂, as reported in Table 4.2 below.

Table 4.2 Average values of GHG fluxes recorded at Borgo Cioffi for both crops.

	CO ₂	CH ₄	N ₂ O
Lolium 2017-2018	-7.5 $\mu\text{mol m}^{-2} \text{s}^{-1}$	0.027 $\mu\text{mol m}^{-2} \text{s}^{-1}$	0.8 $\text{nmol m}^{-2} \text{s}^{-1}$
Sorghum 2018	-12.5 $\mu\text{mol m}^{-2} \text{s}^{-1}$	0.1 $\mu\text{mol m}^{-2} \text{s}^{-1}$	23 $\text{nmol m}^{-2} \text{s}^{-1}$

4.2 Study of enteric methane emissions from water buffalo production in the Mediterranean area

Introduction

The production of greenhouse gases (GHG) from livestock provides a significant contribution to anthropogenic global warming ([1], [2], [3]) and economic development in many countries is expected to expand the demand for meat and dairy products, potentially resulting in increased GHG release to the environment (Garnett, 2009). According to United Nations Food And Agriculture Organization estimates [5] the global livestock sector is responsible for 14.5% of total anthropogenic emissions. Considering the main greenhouse gases, worldwide, livestock farms would be responsible for the emission of about 9% of carbon dioxide, 37% of methane and 65% of nitrous oxide. Steinfeld et al. [6] reports that the livestock sector is responsible for 18% of anthropogenic emissions, corresponding to about 80% of GHG emissions from all other agricultural sectors.

The main source of ruminant greenhouse gases is represented by the enteric fermentation process, in which the feeds are decomposed in the animal's rumen by microbial activity, with consequent production and release of high quantities of methane (CH₄). Other associated sources of CH₄ include manure and sewage storage and soil application.

Water buffalo (*Bubalus bubalis*) is a species widely present throughout the world, with a total population of 200 million, mainly localized in Southeast Asia.

The swamp buffalo type is used as draft power and as a meat source while the river buffalo features elevated milk production. The total number of water buffalo raised in

Mediterranean area, primarily for cheese production, is about 4.7 million, representing 2.4% of the world population. European buffaloes, named Mediterranean buffalo and belonging to the river type, are mainly found in Italy, Romania, Bulgaria, Greece, Albania, Germany and Republic of Macedonia. There are about 407,000 Italian buffaloes, with a total milk production of 92,000 tons. However, there is a consistent positive trend in Italian buffalo numbers, with a net increase in population of 52 % from 2005 to 2013. This increase is due to the rising market reputation of its typical cheese, “Mozzarella di Bufala”.

In response to the growing demand for dairy products, the buffalo farming system in Italy has evolved in the last decades, moving from extensive to intensive husbandry, similar to that of the dairy cattle industry [7], with the implication of enhanced environmental footprint due to air-quality and greenhouse gases emissions. Despite the increased industry size and economic interest, there are very few specific studies on the quantification of greenhouse and air-quality gas emissions from water buffalo [8]. Current estimates for inventory purposes are based on Intergovernmental Panel on Climate Change (IPCC) Tier 1, Tier 2 and Tier 3 schemes. The evaluations are based on the application of expected emissions factors or on computations based on gross energy intake and/or methane conversion factors (IPCC, 2006). In particular, the experimental determination of CH₄ emissions from water buffalo production has not been reported.

Several different approaches can be followed to quantify the amount of trace gases emitted by animals [9]. Storm et al. [10], reviewed specific procedures for measuring methane emission from ruminants, discussing the diverse conditions for application and their advantages and disadvantages. Enclosed chambers and tracer-ratio systems are commonly adopted, but their use can impact on animal normal behavior. Non-interference techniques, like microclimate methods, provide a more appropriate approach and classical micrometeorological procedures such as flux gradient, eddy covariance, relaxed eddy accumulation and boundary layer budgeting - based on measuring fluxes of gases in the free atmosphere and relate these to animal emissions - have been widely used to assess CH₄ fluxes ([11], [12], [13], [14], [15], [16]).

Harper et al.[17] focus on inverse dispersion analysis, a more flexible approach to measure emissions from small paddocks or whole farms, as it only requires gas concentration measurements at a point upwind and a point downwind and wind statistics provided by a three-dimensional sonic anemometer. Flesch et al. [18] developed a variant of Lagrangian stochastic models, the bLS dispersion model, providing a better ability to represent wind features near the ground and their role in gas transport. The technique has been widely used to calculate methane emissions from feedlots [19], paddocks [15]and entire farms ([20], [21]). This technique has been validated using tracer gases by many authors with an average accuracy of $98\% \pm 5\%$ [21].

The purpose of this study is to evaluate enteric CH₄ emissions of a buffalo herd under highly-intensive production in Mediterranean conditions.

4.2.1 Study site and method

The research was carried out at the Borgo Cioffi site described above and in Chapter 1, at the zootechnical farm specialized in rearing water buffalos. The location hosts a long term monitoring station belonging to the FLUXNET global network of ecological sites (<http://fluxnet.ornl.gov>). The high frequency data collected in the field described in section 4.1 were processed and averaged to provide records at half hourly intervals. The farm hosts about 1000 animals in total and at the time of the study about 360 lactating heads, divided into different production groups.

Inverse Dispersion (bLS) Technique

The most appropriate approach for the measurement and calculation of gaseous releases in the atmosphere are non-interference techniques [17]. In this study we use an inverse-dispersion analysis technique to calculate emissions: by measuring the concentration of a pollutant and the turbulence parameters at a location nearby a source, it is possible to evaluate the entity of the source Q (Fig. 4.2.1).

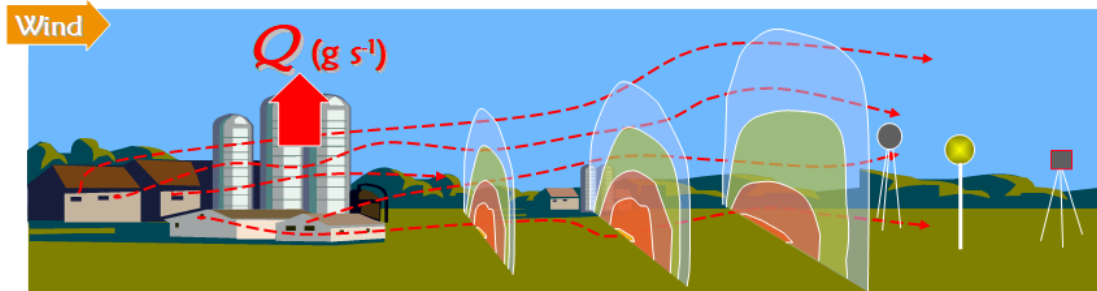


Figure 4.2.1. A scheme of the bLS technique, showing a source Q being dispersed in the vicinity and the monitoring station of concentration and wind located downwind the source.

A backward Lagrangian stochastic analysis (bLS) technology was combined with the measurements made by a gas analyser and a sonic anemometer for necessary wind statistics [20], [22]. This technique has a number of proven accuracy evaluations in calculating emissions from farm environments [17] and in this study we applied it to methane gas. In the bLS measurement technique [23], CH₄ concentration is needed upwind and downwind of the source along with wind information. Methane concentration was measured at only one spot close to the farm (described in section 4.1); consequently, an estimate of ‘background’ was made by selecting records featuring wind directions coming from the Mediterranean Sea, where no potential sources between the farm and the coastline were present (wind direction between 150 and 220 degrees, see map, Fig. 4.2.2a). For evaluating the source strength, wind sectors were chosen to address samples which came from the target area (wind direction between 350 and 45 degrees, see fig. 4.2.2b).



Figure 4.2.2 Left (a) Wind sector of air coming from the sea (red area) for background concentration estimate Right (b) Wind sector of air coming from the farm buildings.

For the bLS evaluation, the required information includes:

1. gas concentration estimated upwind (since upwind measurements were not available) and downwind of the source (farm)
2. wind measurements (taken well away from the farm so as not to be influenced by the farm structures)
3. a map of the farm indicating the location of CH₄ emissions sources (e.g., paddocks, houses) and the sensor locations.

The concentrations as well as friction velocity u^* , the Obukhov length L , and the surface roughness length z_0 (see [23]) were measured at the measurement tower described in section 4.1. In Fig 4.2.3 is shown a map of the different sources located at the farm.



Figure 4.2.3 Map of the different sources and the measurement station located at Borgo Cioffi.

The “WindTrax” (Thunder Beach Scientific, Nanaimo, Canada) software was used to make the calculation relating downwind concentration to the emission rate. This software combines the bLS model described by Flesch et al [23] with an interface allowing the farm emission sources and concentration sensors to be conveniently mapped. In the bLS model, thousands of model trajectories for the prevailing wind conditions. The important information relating the concentration to the emissions is

the set of trajectory intersections with ground (“touchdowns”, see an example in Fig. 4.2.4).

$$Q = \frac{C - C_b}{\frac{1}{n} \times \sum \left| \frac{z}{w_0} \right|}$$

where Q is the farm emission rate ($\text{kg m}^{-2} \text{s}^{-1}$), C is the downwind concentration of (kg m^{-3}), C_b is the upwind (background) concentration (kg m^{-3}), n is the number of computed bLS trajectories, w_0 is the vertical velocity of the trajectory at touchdown (m s^{-1}), and the summation covers all touchdowns occurring within the designated source area. The touchdowns map the concentration “footprint”, i.e., the ground area where emissions influence C . The areal emission rate, Q , calculated in the above formula is multiplied by the source area and is reported as an integrated whole-farm emission rate with units of $\text{kg-CH}_4 \text{ hr}^{-1}$.

The study farm is represented as a collection of surface area sources (Fig. 4.2.3). The farm emission rate, Q , was calculated using $n = 750,000$ trajectories. Not all observation periods give good Q calculations, and therefore the filtering strategy of Flesch et al. [24] was used. Three criteria identify periods when the bLS dispersion model is likely to be inaccurate and such periods were not used if:

- $u_* \leq 0.05 \text{ m s}^{-1}$ (low winds),
- $|L| \leq 10 \text{ m}$ (strongly stable/unstable atmospheric stratification),
- $z_0 \geq 0.2 \text{ m}$

For some wind directions, the farm plume only “glances” the downwind sensor. This leads to three problems: the plume edge is associated with greater Q uncertainty due to the difficulty of modeling lateral dispersion; emission measurements are weighted toward the unrepresentative farm edge; and slight errors in wind observations (particularly wind direction) can result in dramatic errors in Q . Therefore periods are not used where the concentration touchdowns cover less than 40% of designated source area (WindTrax calculates the fraction of source pixels displayed as touchdowns, see Fig. 4.2.3 for example). The bLS calculation of Q assumes CH_4 is a passive tracer with no deposition to the downwind surface and no chemical

transformation between the farm and the laser line. Given the short distances between the farm and the lasers (150 m), this assumption is realistic.

4.2.2 Results

The dataset used for application of WindTrax is the season from 1st November 2017 to 19th April 2018, when the planted crop was *Lolium Italicum* on the Borgo Cioffi field site (see for a full description section 4.1.1). The input data consisted of concentrations of CH₄ and turbulent wind variables measured from the eddy covariance tower.

The model run provided, for different stability conditions and different wind directions detected at the site, different sets of “touch-downs”. As shown in Fig. 4.2.4, the different atmospheric conditions mean that the measured concentration is describing different portions of the source area (the green polygon covering the whole farm area).



Figure 4.2.4 Touch downs (red dots) maps accounting for the same source in different stability conditions: unstable, neutral, stable (from left to right respectively).

In order to assess the background concentration from the data collected at the eddy covariance station, CH₄ concentrations coming from the direction of the sea were considered the best estimate of a plausible background, free from the influence of other local sources. The wind sector chosen ranged from 150° to 210°: the measurements showed a temporally non-constant background.

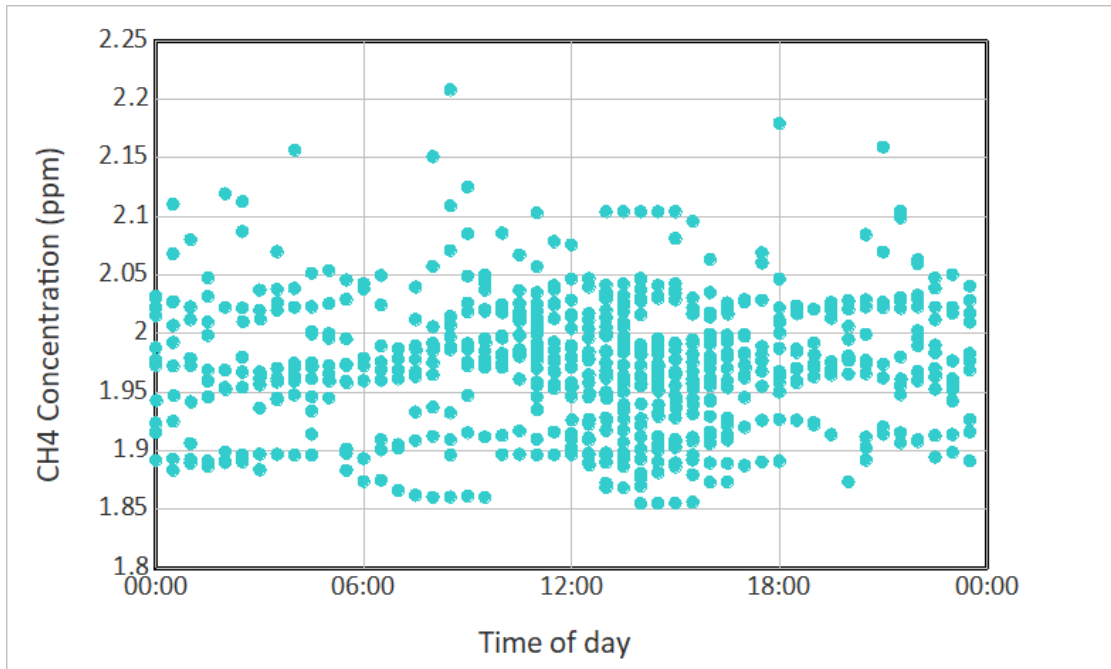


Figure 4.2.5 Background concentrations of methane, estimated from half-hourly values measured from the sea-wind sector at Borgo Cioffi.

However, by looking at the daily cycle of CH₄ concentrations, shown in Fig. 4.2.5, no structure was detected connected to the time of the day, and the values ranged from a minimum of 1.88 ppm to a maximum of 2.2 ppm. The mean value of such dataset spanning over the whole measuring period was 1.98 ppm, and it was used as model input (C_b) for the calculations.

The model run on an input of just under 6 months long dataset of half-hourly data for concentration and wind. The data were filtered according to selective criteria on turbulence mentioned in the previous section: the threshold values were fixed for friction velocity 0.05 m/s; for the Obukhov length 2, for the mean wind speed had to be 1 m/s, wind direction was restricted to the sector 350° - 30°. After the filtering described above, the output dataset consisted of 392 values.

The outcome of the model run is shown in Fig.4.2.6: the farm behaved in all cases as a source of methane, with emission rates ranging from -1.8 kg/hr to 83 kg/hr. The negative values represented 0.3% of all output data, and they are probably due to the estimate of the background, which has been chosen as a fixed value throughout the period, because of the lack of a continuous, independent CH₄ background measurement.

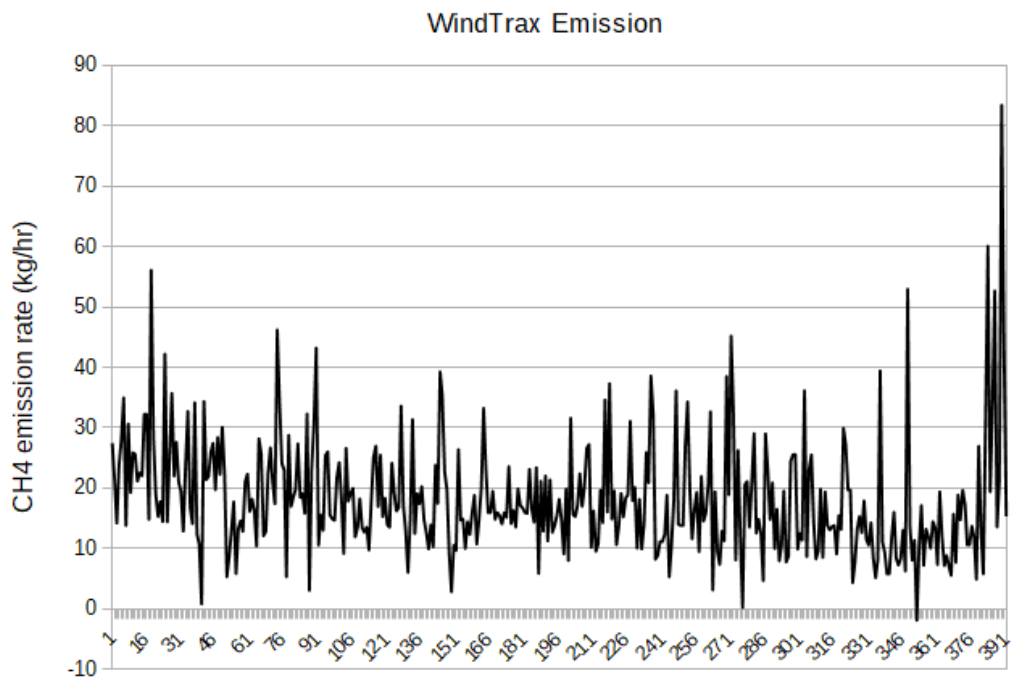


Figure 4.2.6 WindTrax model output simulating the methane emission rate from the buffalo farm at Borgo Cioffi.

In Fig. 4.2.7 is shown the daily cycle of the same dataset: the chart shows that no particular daily pattern is present, suggesting that variability could be linked more to the background assessment rather than attributable to feeding patterns of the animals.

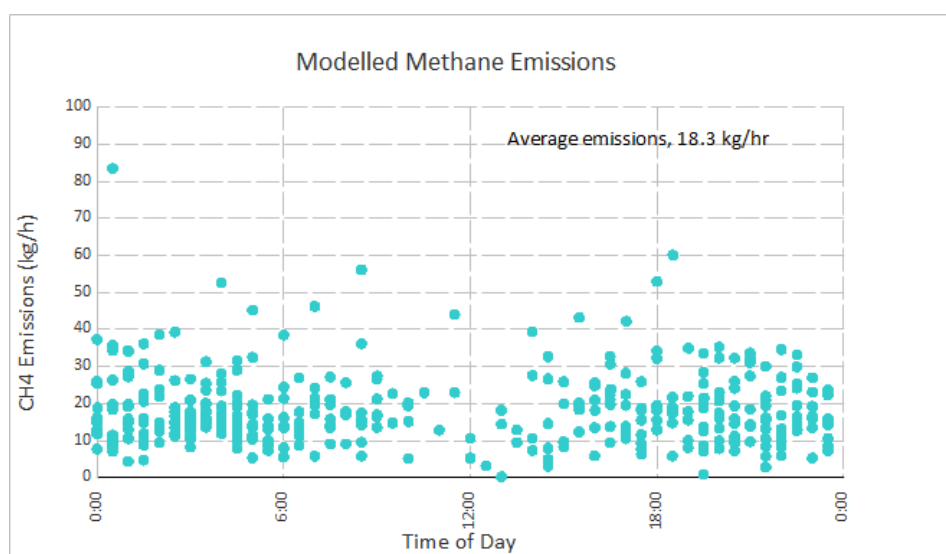


Figure 4.2.7 Daily cycle of emission fluxes from the farm output by the model.

The emission calculations from WindTrax found an average emission source strength of 18.3 kg/hr, with a standard deviation of about 9 kg/hr. The high uncertainty of the output is possibly due to: a lack of knowledge about where the gas source areas are within the farm and which parts are weaker/stronger (e.g. paddocks of lactating vs young calves); a large uncertainty over the Cb values at any instant (taking into account the contribution of surrounding sources).

However, despite the large uncertainty of this WindTrax calculation, the emission outcome shows quite good agreement in terms of magnitude of emission from a dairy farm of about 1000 heads. Further work is required to compare the emission obtained by WindTrax with the more theoretical approach of the IPCC emission calculation.

BIBLIOGRAPHY

- [1] McMichael AJ, Powles JW, Butler CD, Uauy R., 2007. Food, livestock production, energy, climate change, and health. *Lancet*. 370:1253–1263.
- [2] Gerber PJ, Steinfeld H, Henderson B, Mottet A, Opio C, Dijkman J, Falcucci A, Tempio, 2013. *G. Tackling climate change through livestock: a global assessment of emissions and mitigation opportunities*. Rome: Food and Agriculture Organization of the United Nations (FAO), pp 115.
- [3] Reisinger, A., H. Clark, 2018. How much do direct livestock emissions actually contribute to global warming? *Glob. Chang. Biol.*, 24, pp. 1749-1761.
- [4] Garnett, T. , 2009. Livestock-related greenhouse gas emissions: impacts and options for policy makers. *Environ. Sci. Pol.*, 12, pp. 491-503
- [5] Food and Agriculture Organization of the United Nations, Statistics Division (2018), <http://www.fao.org/faostat/>.
- [6] Steinfeld, H. ; Gerber, P. ; Wassenaar, T. ; Castel, V. ; Rosales, M. ; de Haan, C., 2006. *Livestock's long shadow*,. FAO, Rome 2006.
- [7] Sabia, E., F. Napolitano, S. Claps, A Braghieri, N. Piazzolla (2015). Feeding, Nutrition and Sustainability in Dairy Enterprises: The Case of Mediterranean Buffaloes (*Bubalus bubalis*). In *The Sustainability of Agro-Food and Natural Resource Systems in the Mediterranean Basin*, A. Vastola Ed., Springer, pp 57-64.
- [8] R. D. Córdor, L. Valli, G. De Rosa, A. Di Francia and R. De Lauretis, 2008. Estimation of the methane emission factor for the Italian Mediterranean buffalo. *Animal* (2008), 2:8, pp 1247–1253 & The Animal Consortium 2008, doi:10.1017/S1751731108002292.
- [9] Hu, E., Esther L., Babcock, E., Bialkowski, S., Jones, S., Tulle, M., 2014. Methods and Techniques for Measuring Gas Emissions from Agricultural and Animal Feeding Operations. *Critical Reviews in Analytical Chemistry* 44(3), 200-219.
- [10] Storm, I., Hellwing, A., Nielsen, N., 3 and Madsen, J., 2012. Methods for Measuring and Estimating Methane Emission from Ruminants. *Animals* 2012, 2, 160-183.

- [11] Griffith, D.W.T., Bryant, G.R., Hsu, D., Reisinger, A.R., 2008. Methane emissions from free-ranging cattle: comparison of tracer and Integrated horizontal flux techniques. *J. Environ. Qual.* 37, 582–591.
- [12] Laubach, J., Kelliher, F.M., 2005. Measuring methane emission rates of a dairy cow herd (II): results from a backward-Lagrangian stochastic model. *Agric. For. Meteorol.* 129, 137–150.
- [13] Harper, L.A., Denmead, O.T., Freney, J.R., Byers, F.M., 1999. Direct measurements of methane emissions from grazing and feed lot cattle. *J. Anim. Sci.* 77, 1392–1401.
- [14] Harper, L.A., Byers, F.M., Sharpe, R.R., 2002. Treatment effects on methane emissions from grazing cattle. In: Takahashi, J., Young, B.A. (Eds.), *Greenhouse Gases and Animal Agriculture*. Elsevier Science B.V., Amsterdam, The Netherlands, pp. 167–170.
- [15] Laubach, J., Kelliher, F.M., Knight, T.W., Clark, H., Molano, G., Cavanagh, A., 2008. Methane emissions from beef cattle—a comparison of paddock- and animal-scale measurements. *Aust. J. Exp. Agric.* 48, 132–137.
- [16] Ham, J., Johnson, K., 2010. Measuring methane emissions from cattle feedlots using open-path eddy covariance. In: *Proceedings of 4th Greenhouse Gases and Animal Agriculture Conference*, Banff, Canada, 3–8 October 2010, p. 92.
- [17] Harper, L.A.; Denmead, O.T.; Flesch, T.K. 2011. Micrometeorological techniques for measurement of enteric greenhouse gas emissions. *Anim. Feed Sci. Technol.* 2011, 166–167, 227–239.
- [18] Flesch T.K. (1996) The Footprint for Flux Measurements, from Backward Lagrangian Stochastic Models. In: Garratt J.R., Taylor P.A. (eds) *Boundary-Layer Meteorology 25th Anniversary Volume, 1970–1995*. Springer, Dordrecht
- [19] Haarlem, R. & Desjardins, Raymond & Gao, Zhiling & Flesch, T. & Li, Xiaolo & Haarlem, Van & Desjardins, Raymond & Gao, R & Flesch, Z & Li, T. (2008). Methane and ammonia emissions from a beef feedlot in western Canada for a twelve-day period in the fall. *Canadian Journal of Animal Science.* 88. 10.4141/CJAS08034.

- [20] Flesch, T.K., Harper, L.A., Desjardins, R.L., Gao, Z., Crenna, B.P., 2009. Multi-source emission determination using an inverse-dispersion technique. *Bound. Layer Meteorol.* 132, 11–30.
- [21] Harper, L.A., Flesch, T.K., Weaver, K.H., Wilson, J.D., 2010. The effect of biofuel production on swine farm ammonia and methane emissions. *J. Environ. Qual.* 39, 1984–1992
- [22] Harper, Lowry & Sharpe, Ron & Parkin, Tim. (2000). Gaseous Nitrogen Emissions from Anaerobic Swine Lagoons: Ammonia, Nitrous Oxide, and Dinitrogen Gas. *Journal of Environmental Quality - J ENVIRON QUAL.* 29. 10.2134/jeq2000.00472425002900040045x.
- [23] Flesch, T. & Wilson, J. & Harper, Lowry & Crenna, B. & Sharpe, R.. (2004). Deducing Ground-to-Air Emissions from Observed Trace Gas Concentrations: A Field Trial. *Journal of Applied Meteorology - J APPL METEOROL.* 43. 487-502. 10.1175/1520-0450(2004)043<0487:DGEFOT>2.0.CO;2.
- [24] Thomas K. Flesch, John D. Wilson, Lowry A. Harper, Brian P. Crenna, Estimating gas emissions from a farm with an inverse-dispersion technique, *Atmospheric Environment*, Volume 39, Issue 27, 2005, Pages 4863-4874, ISSN 1352-2310, <https://doi.org/10.1016/j.atmosenv.2005.04.032>.

Appendix A

Land-atmosphere exchange of N₂O, CH₄ and CO₂ from a Mediterranean rotation cropland

Daniele Gasbarra
CNR- ISAFOM, Ercolano (NA) Italy
Univ. degli Studi di Napoli Federico II
Dipartimento di Biologia, Napoli (IT)
daniele.gasbarra@isafom.cnr.it

Paul Di Tommasi
CNR- ISAFOM
Ercolano (NA) Italy
paul.ditommasi@cnr.it

Maurizio Tosca
CNR- ISAFOM
Ercolano (NA) Italy
maurizio.tosca@cnr.it

Daniela Famulari
CNR- ISAFOM
Ercolano (NA) Italy
daniela.famulari@cnr.it

Andrea Esposito
CNR- ISAFOM
Ercolano (NA) Italy
andrea.esposito@cnr.it

Enzo Magliulo
CNR- ISAFOM
Ercolano (NA) Italy
enzo.magliulo@cnr.it

Antonio Manco
CNR- ISAFOM, Ercolano (NA) Italy
Univ. degli Studi di Napoli Federico II
Dipartimento di Biologia, Napoli
antonio.manco@isafom.cnr.it

Luca Vitale
CNR- ISAFOM
Ercolano (NA) Italy
luca.vitale@cnr.it

Abstract— To assess the land atmosphere exchanges linked to agricultural management activities, we conducted two field campaigns over the ICOS-candidate ecosystem site of Borgo Cioffi, a rotation cropland in Southern Italy, measuring fluxes of CH₄ and CO₂ as well as N₂O, obtaining the temporal evolution of the exchange dynamics for the prevailing GHG. The interested crops were *Lolium italicum* and *Sorghum bicolor*, two fodder crops very common in the region. The results showed that the tilled field acted as a source for all GHGs in both cases.

Keywords— nitrous oxide (N₂O) emissions, methane (CH₄) emissions, Mediterranean, GHG fluxes.

I. INTRODUCTION

Agro-ecosystems play an important role in the global anthropogenic influence on climate (>12%), through the variation of carbon storage potential of the ecosystems, and exchanges of greenhouse gases – such as methane, nitrous oxide and carbon dioxide – between land and atmosphere. For N₂O, the impact increases to nearly 40% [1].

In agriculture, the most cost-effective mitigation options are cropland management, grazing land management, and restoration of organic soils: in this context, the assessment of the GHG impact of different managements of cropland becomes very important. Soil management and tillage, via the addition of fertilizers, plant residues, and changes to soil structure can impact on GHG emissions [2]. Greater soil disturbance, such as that caused by ploughing, can cause rapid respiration and loss of large amounts of soil carbon which would otherwise decompose more slowly [3]. Inversion ploughing will turn the soil upside down, but the actual disturbance depends on the depth of ploughing. Repeated mechanical operations cause soil microorganisms to become more compromised, and inversion can help oxygenate soil, making methane and nitrous oxide emissions from anaerobic soils less likely. The climatic impact of

different tillage systems is still poorly understood due to limited data availability (see e.g. [4]).

Here we present GHG flux measurements carried out on agricultural land nearby a commercial buffalo farm located in a Mediterranean environment, 5 km from the sea, in Southern Italy. The primary aim of this study was to identify and compare the most significant sources of GHGs from a typical cropland in a Mediterranean environment, with a particular focus on N₂O emissions from sources associated – directly and not – with fertiliser application, and management practices. Many past experiments have focussed on the release of N₂O from soils after the application of nitrogen fertilisers – which is the main cause of the rise in N₂O emissions since pre-industrial times [5]. Other factors affecting GHG emissions from agricultural soils, such as tillage and compaction, are less well documented, thus preventing effective assessment of their role in controlling GHG fluxes from the agricultural sector.

II. MATERIALS AND METHODS

A. The field site

The Borgo Cioffi field site (Bci-IT, shown in an aerial photo in Fig.1) is located near Eboli (SA), in the Southern Italian Campania region (40° 31' N, 14° 57' E) and is the European southernmost cropland observation candidate site of ICOS (Integrated Carbon Observation System) [6, 7]. The field station is located in a 15 ha field, irrigated by means of a centre pivot system. The main cultivated species are corn (*Zea mays*), sorghum (*Sorghum bicolor*) and *Alfalfa*, along with some winter grass crops (*Lolium italicum*), for fresh animal consumption, silage or haying. The cropland site is located nearby a water-buffalo farm (about 1000 animals). The farm area can be considered as representative of agricultural soils in this region where water buffalo form an important part of the animal husbandry.



Fig. 1. Map of the field site in Borgo Cioffi. N-NE of the EC tower is the water buffalo farm. The round shape on the ground traces the domain of the centre pivot irrigation system.

The soil at the site has an alluvial origin, deriving from the nearby Sele River, and it features a clay texture (clay: 52%; silt: 28%; sand: 20%), whereas in isolated patches localized in the SW area of the field, a coarse texture (clay: 14%; silt: 11% and sand: 75%) was detected. Soil pH is 7.5 and bulk density 1.2 g cm^{-3} , organic matter content $2.5 \pm 0.3\%$, as reported by previous studies [10,11].

N-fertiliser application rates have been approximately $300 \text{ kg-N ha}^{-1} \text{ yr}^{-1}$ (regional regulations impose a maximum of 340, including grazed areas). The fertilizer used is slurry produced by the nearby water-buffalos. According to the tillage classes, defined by France's National Institute for Agricultural Research (INRA) the measured tillage events on the field site can be defined as double-layer ploughing (inversion of the soil to a depth of ~15 cm and loosening to ~30 cm) and/or non-inversion (10–25 cm depth). Measurements took place over two different periods, characterized by two different crops. In the first period (30 October 2017 – 22 April 2018) *Lolium italicum*, grown for fodder, it constitutes the usual choice of winter crop in this region; in the second period (12 May – 20 August 2018), *Sorghum bicolor*, very common species of grain grown in this region, as it is drought- and heat- resistant species: also grown for fodder, it constitutes a common alternative to maize in scarcely irrigated areas. The management practices during the measurement periods are summarised in Table 1.

TABLE I AGRICULTURAL PRACTICES AT BORGO CIOFFI

Date	Crop Management			Tilling depth
	Event	Crop variety	N [kg ha^{-1}]	
10/10/17	Fertilisation	<i>Lolium italicum</i>	75	–
25/10/17	Fertilisation	<i>Lolium italicum</i>	75	–
28/10/17	Ploughing	<i>Lolium italicum</i>	–	35 cm
31/10/17	Harrowing and sowing	<i>Lolium italicum</i>	–	–
28/4 - 1/5/18	Fertilisation	<i>Sorghum bicolor</i>	75	–
15/5/18	Ploughing with incorporation	<i>Sorghum bicolor</i>	–	<20 cm
18/5/18	Fertilisation	<i>Sorghum bicolor</i>	75	–
17/6/18	Harrowing and sowing	<i>Sorghum bicolor</i>	–	–

B. Flux calculation and setup on the field

The land–atmosphere exchange of GHGs was measured by the eddy covariance technique, following the equation:

$$F_c = \overline{w' C'}$$
 (1)

Where F_c is the vertical turbulent flux of a gaseous concentration C , and w is the vertical component of the wind vector (see e.g. [8, 9]).

The eddy covariance station is setup approximately in the centre of the field, which has a rectangular shape, with dimensions of $300\text{m} \times 600\text{m}$. The fetch in the prevailing wind directions, southwest and northeast (sea breeze regime, as shown in Fig.2), is about 200 m. The height of the sonic anemometer varied from 2.15m to 2.60m according to vegetation growth stages. The terrain is flat with a gentle slope of approximately 2% toward south.

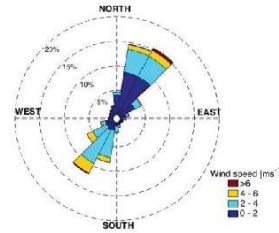


Fig. 2. Wind rose of the field site at Borgo Cioffi: a typical sea land breeze regime with North East to South West prevalent direction, with mean values ranging 0.5 to 9.4 m s^{-1} . Data refer to the whole measurement period.

A CW-QCLTILDAS (Aerodyne Research Inc., Billerica, MA, USA) was used for the fast, simultaneous measurement of N_2O , CH_4 and H_2O mixing ratios, whereas a LICOR 7200 (LiCor Inc., Lincoln, NE, USA) monitored CO_2 and H_2O : all gases were sampled at a rate of 10 Hz. The instrumentation was placed in an air-conditioned sea container. A Gill R3 Ultrasonic anemometer (Gill Instruments Ltd., Lymington, Hampshire, UK) functioning at 10 Hz was used to measure the wind vector. A heated and insulated PTFE sampling line of 32.6 m length ran from the sonic anemometer to the CW-QCL inside the container; air was drawn with a turbulent flow rate greater than 18 l/min. All systems logged data to a CR3000 Datalogger (Campbell Scientific Inc., Logan, UT, USA) by a custom-made program storing synchronous raw data.

III. RESULTS

A. Meteorology

In Fig.3 the meteorology of the second measurement period is shown as an example. Daily temperatures show mean values around 25°C during the summer period, while mean soil temperatures rise from 20°C to 23°C during summer. The lack of rainfall during summer at the site requires artificial irrigation, and soil water content follows the irrigation events on the crop, remaining below 35% volumetric water content throughout the observation period.

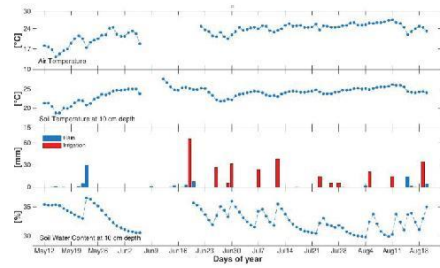


Fig. 3. Top to Bottom: air T; soil T; rainfall (blue) and irrigation (red) rates; volumetric soil water content at a depth of 10 cm. The data refer to the spring-summer field campaign over *Sorghum bicolor*.

B. GHG exchange

In Fig.4 the time series of N_2O daily fluxes recorded during the second field campaign shows an important emission feature, following the tillage, and the fertilisation events. Before the ploughing event, fluxes were close to zero; the fertilisation event triggered the highest response, while for both irrigation and tillage (any type of tilling) were followed by relative increase of emission.

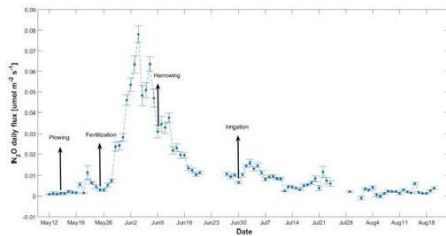


Fig. 4. Daily values of N_2O fluxes recorded during the second measurement campaign.

In order to underpin the causes of N_2O emission, we correlated N_2O fluxes to other environmental variables measured on site, and soil T showed the clearest relationship, as displayed in Fig. 5.

CO_2 fluxes showed that the field acts as a sink of C during the vegetated stages, with average daily net uptake values of $-2.5 \mu mol CO_2 m^{-2} s^{-1}$.

CH_4 average concentrations were 2052 ppb, well above the background atmospheric level of 1866 ppb recorded for 2019 [12]. This is explicable by the vicinity of the buffalo farm, an important source of methane influencing the area. No considerable emission fluxes of CH_4 were detected from either crops, however the spring-summer practices showed a short lived, small emission peak ($0.3 \mu mol CH_4 m^{-2} s^{-1}$) of CH_4 , that at present need further investigation for possible advection effects from the nearby source.

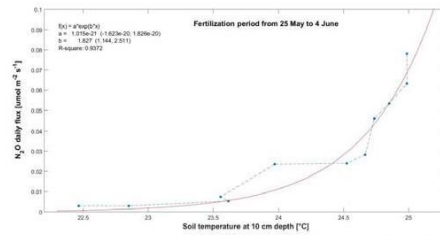


Fig. 5. N_2O daily fluxes plotted versus soil T as a potential driver variable.

IV. CONCLUSIONS

The measurement of eddy covariance fluxes allowed to have a continuous half-hourly dataset for description of the short-lived dynamics of the agricultural practices in a Mediterranean environment.

A preliminary analysis of the results gathered during two field campaigns over two rotational crops suggest that the tilled field acted as a source for all GHG in both cases: after tillage, for about 60 days, emission of CO_2 was predominant, until vegetation was re-established along with photosynthetic activity, reverting the field to CO_2 sink.

N_2O fluxes showed variability after every operation performed on the field, and emissions were recorded both after ploughing and harrowing of the field. The highest N_2O fluxes were observed following the spreading of buffalo slurry in the second campaign, where maximum emission reached $78 \text{ nmol } N_2O m^{-2} s^{-1}$ ten days after fertilisation. A very high variability was noted between the two campaigns: following the autumnal crop tillage the emissions were considerably lower, with a recorded maximum of $9 \text{ nmol } N_2O m^{-2} s^{-1}$. A possible explanation of the discrepancy is that the addition of organic nitrogen in the form of decaying plant matter (crop residues, incorporated during the second field campaign but not during the first) is a recognised potential source of N_2O following tillage, but the phenomenon is not well quantified [13, 14] and it would require more measurements.

Both CH_4 and N_2O emission fluxes were higher during the spring-summer event. However, the contribution of CH_4 from the crop was hardly detectable and needs further analysis.

REFERENCES

- [1] Intergovernmental Panel on Climate Change (IPCC): Climate Change 2013 – The Physical Science Basis: Working Group I Contribution to the Fifth Assessment Report of the Intergovernmental Panel on Climate Change, Cambridge University Press, Cambridge, available at: <http://ebooks.cambridge.org/ref/id/CBO9781107415324>, 2014.
- [2] Holder, A. J., McCalmont, J. P., Rowe, R., McNamara, N. P., Elias, D., & Donnison, I. S. (2019). Soil N_2O emissions with different reduced tillage methods during the establishment of Miscanthus in temperate grassland. *GCB Bioenergy*, 11(3), 539–549. <https://doi.org/10.1111/gcbb.12570>
- [3] Ecclestone, P. (2004). To plough or not to plough. *British Sugar Beet Review*, 72, 7–9.
- [4] Krauss, M., Ruser, R., Müller, T., Hansen, S., Mäder, P., & Gattinger, A. (2017). Impact of reduced tillage on greenhouse gas emissions and soil carbon stocks in an organic grass-clover ley - winter wheat

- cropping sequence. *Agriculture, Ecosystems and Environment*, 239, 324–333. <https://doi.org/10.1016/j.agee.2017.01.029>
- [5] Cowan, N. J., Levy, P. E., Famulari, D., Anderson, M., Drewer, J., Carozzi, M., ... Skiba, U. M. (2016). The influence of tillage on N₂O fluxes from an intensively managed grazed grassland in Scotland. *Biogeochemistry*, 13(16), 4811–4821. <https://doi.org/10.5194/bg-13-4811-2016>
- [6] <http://www.europe-fluxdata.eu/icos/home>
- [7] <http://www.icos-italy.it/network/borgocioffi.pdf>
- [8] Stull, R. B. "An introduction to boundary layer meteorology". Dordrecht: Kluwer Academic Publishers. J. Clerk Maxwell, A Treatise on Electricity and Magnetism, 3rd ed., vol. 2. Oxford: Clarendon, 1892, 1988, pp.68–73.
- [9] Kaimal, J. C., & Finnigan, J. J. (1994). Atmospheric boundary layer flows: their structure and measurement. In Book (Vol. 72). [https://doi.org/10.1016/0021-9169\(95\)90002-0](https://doi.org/10.1016/0021-9169(95)90002-0)
- [10] Ranucci, S., Bertolini, T., Vitale, L., Di Tommasi, P., Ottaiano, L., Oliva, M., ... Magliulo, V. (2011). The influence of management and environmental variables on soil N₂O emissions in a crop system in Southern Italy. *Plant and Soil*, 343(1–2), 83–96. <https://doi.org/10.1007/s11104-010-0674-x>
- [11] Vitale, L., di Tommasi, P., Arena, C., Oliva, M., Bertolini, T., Ranucci, S., ... Magliulo, V. (2011). Ecosystem carbon fluxes of a ryegrass and clover fodder crop in a Mediterranean environment. *Photosynthetica*, 49(3), 330–338. <https://doi.org/10.1007/s11099-011-0045-8>
- [12] https://www.esrl.noaa.gov/gmd/ccgg/trends_ch4/
- [13] Baggs, E. M., Stevenson, M., Pihlatie, M., Regar, A., Cook, H., and Cadisch, G.: Nitrous oxide emissions following application of residues and fertiliser under zero and conventional tillage, *Plant Soil*, 254, 361–370, doi:10.1023/A:1025593121839, 2003.
- [14] Mutegi, J. K., Munkholm, L. J., Petersen, B. M., Hansen, E. M., and Petersen, S. O.: Nitrous oxide emissions and controls as influenced by tillage and crop residue management strategy, *Soil Biol. Biochem.*, 42, 1701–1711, 2010.

Appendix B

FLUXNET-CH₄ SYNTHESIS ACTIVITY

Objectives, Observations, and Future Directions

SARA H. KNOX, ROBERT B. JACKSON, BENJAMIN POULTER, GAVIN MCNICOL,
ETIENNE FLUET-CHOUINARD, ZHEN ZHANG, GUSTAF HUGELIUS, PHILIPPE BOUSQUET, JOSEF G. CANADELL,
MARIELLE SAUNOIS, DARIO PAPALE, HOUSEN CHU, TREVOR F. KEENAN, DENNIS BALDOCCHI,
MARGARET S. TORN, IVAN MAMMARELLA, CARLO TROTTA, MIKA AURELA, GIL BOHRER,
DAVID I. CAMPBELL, ALESSANDRO CESCATTI, SAMUEL CHAMBERLAIN, JIQUAN CHEN, WEINAN CHEN,
SIGRID DENGEL, ANKUR R. DESAI, EUGENIE EUSKIRCHEN, THOMAS FRIBORG, DANIELE GASBARRA,
IGNACIO GODED, MATHIAS GOECKEDE, MARTIN HEIMANN, MANUEL HELBIG, TAKASHI HIRANO,
DAVID Y. HOLLINGER, HIROKI IWATA, MINSEOK KANG, JANINA KLATT, KEN W. KRAUSS, LARS KUTZBACH,
ANNALEA LOHILA, BHASKAR MITRA, TIMOTHY H. MORIN, MATS B. NILSSON, SHULI NIU, ASKO NOORMETS,
WALTER C. OECHEL, MATTHIAS PEICHL, OLLI PELTOLA, MICHELE L. REBA, ANDREW D. RICHARDSON,
BENJAMIN R. K. RUNKLE, YOUNGRYEL RYU, TORSTEN SACHS, KARINA V. R. SCHÄFER, HANS PETER SCHMID,
NARASINHA SHURPALI, OLIVER SONNENTAG, ANGELA C. I. TANG, MASAHITO UYEYAMA, RODRIGO VARGAS,
TIMO VESALA, ERIC J. WARD, LISAMARIE WINDHAM-MYERS, GEORG WOHLFAHRT, AND DONATELLA ZONA

We describe a new coordination activity and initial results for a global synthesis of eddy covariance CH₄ flux measurements.

Atmospheric methane (CH₄) is the second-most important anthropogenic greenhouse gas following carbon dioxide (CO₂) (Myhre et al. 2013). The concentration of CH₄ in the atmosphere today is about 2.5 times higher than in 1750 (Saunois et al. 2016a). The increase in atmospheric CH₄ has arisen from human activities in agriculture, energy production, and waste disposal, and from changes in natural CH₄ sources and sinks (Saunois et al. 2016a,b, 2017; Turner et al. 2019). Based on top-down atmospheric inversions, global CH₄ emissions for the decade of 2003–12 were an estimated ~420 Tg C yr⁻¹ (range 405–426 Tg C yr⁻¹) (Saunois et al. 2016a). However, some analyses suggest that uncertainties in global CH₄ sources and sinks are higher than those for CO₂,

and uncertainties from natural sources exceed those from anthropogenic emissions (Saunois et al. 2016a). In particular, the largest source of uncertainty in the global CH₄ budget is related to emissions from wetlands and inland waters (Saunois et al. 2016a; Melton et al. 2013; Bastviken et al. 2011). Wetland CH₄ emissions may contribute as much as 25%–40% of the global total and are a leading source of interannual variability in total atmospheric CH₄ concentrations (Bousquet et al. 2006; Chen and Prinn 2006; Saunois et al. 2016a).

Direct, ground-based measurements of in situ CH₄ fluxes with high measurement frequency are important for understanding the responses of CH₄ fluxes to environmental factors including climate,

AFFILIATIONS: KNOX—Department of Earth System Science, Stanford University, Stanford, California, and Department of Geography, The University of British Columbia, Vancouver, British Columbia, Canada; JACKSON—Department of Earth System Science, Woods Institute for the Environment, and Precourt Institute for Energy, Stanford University, Stanford, California; POLTER—Biospheric Sciences Laboratory, NASA Goddard Space Flight Center, Greenbelt, Maryland; McNICOL AND FLUET-CHOUINARD—Department of Earth System Science, Stanford University, Stanford, California; ZHANG—Department of Geographical Sciences, University of Maryland, College Park, College Park, Maryland; HUGELIUS—Department of Physical Geography, and Bolin Centre for Climate Research, Stockholm University, Stockholm, Sweden; BOUSQUET AND SAUNOIS—Laboratoire des Sciences du Climat et de l'Environnement, LSCE-IPSL, CEA-CNRS-UVSQ, Université Paris-Saclay, Gif-sur-Yvette, France; CANADELL—Global Carbon Project, Oceans and Atmosphere, CSIRO, Canberra, Australian Capital Territory, Australia; PAPAIE AND TROTTA—Dipartimento per la Innovazione nei Sistemi Biologici, Agroalimentari e Forestali, Università degli Studi della Tuscia, Largo dell'Università, Viterbo, Italy; CHU, TORN, AND DENGEL—Earth and Environmental Sciences Area, Lawrence Berkeley National Lab, Berkeley, California; KEENAN—Earth and Environmental Sciences Area, Lawrence Berkeley National Lab, and Department of Environmental Science, Policy and Management, University of California, Berkeley, Berkeley, California; BALDOCCHI AND CHAMBERLAIN—Department of Environmental Science, Policy and Management, University of California, Berkeley, Berkeley, California; MAMMARELLA—Institute for Atmospheric and Earth System Research/Physics, Faculty of Science, University of Helsinki, Helsinki, Finland; AURELA, LOHILA, AND PELTOLA—Finnish Meteorological Institute, Helsinki, Finland; BOHRER—Department of Civil, Environmental and Geodetic Engineering, The Ohio State University, Columbus, Ohio; CAMPBELL—School of Science, University of Waikato, Hamilton, New Zealand; CESCATTI AND GODED—European Commission, Joint Research Centre (JRC), Ispra, Italy; J. CHEN—Department of Geography, Environment, and Spatial Sciences, and Center for Global Change and Earth Observations, Michigan State, East Lansing, Michigan; W. CHEN AND NIU—Key Laboratory of Ecosystem Network Observation and Modeling, Institute of Geographic Sciences and Natural Resources Research, Chinese Academy of Sciences, Beijing, China; DESAI—Department of Atmospheric and Oceanic Sciences, University of Wisconsin–Madison, Madison, Wisconsin; EUSKIRCHEN—Institute of Arctic Biology, University of Alaska Fairbanks, Fairbanks, Alaska; FRIBORG—Department of Geosciences and Natural Resource Management, University of Copenhagen, Copenhagen, Denmark; GASBARRA—Department of Vegetal Biology, University of Napoli Federico II, and Institute for Mediterranean Agricultural and Forest Systems, CNR, Naples, Italy; GOECKEDE—Max Planck Institute for Biogeochemistry, Jena, Germany; HEIMANN—Max Planck Institute for Biogeochemistry, Jena, Germany, and Institute for Atmosphere and Earth System Research/Physics, Faculty of Science, University of Helsinki, Helsinki, Finland; HELBIG—School of Geography and Earth Sciences, McMaster University, Hamilton, Ontario, and Département de Géographie, Université de Montréal, Montréal, Quebec, Canada; HIRANO—Research Faculty of Agriculture, Hokkaido University, Sapporo, Japan; HOLLINGER—Northern Research Station, Forest Service, USDA, Durham, New Hampshire; IWATA—Department of Environmental Sciences, Shinshu

University, Matsumoto, Nagano, Japan; KANG—National Center for AgroMeteorology, Seoul, South Korea; KLATT—Institute of Meteorology and Climate Research, Karlsruhe Institute of Technology, Garmisch-Partenkirchen, Germany; KRAUSS AND WARD—Wetland and Aquatic Research Center, U.S. Geological Survey, Lafayette, Louisiana; KUTZBACH—Institute of Soil Science, Center for Earth System Research and Sustainability, Universität Hamburg, Hamburg, Germany; MITRA AND NOORMETS—Department of Ecosystem Science and Management, Texas A&M University, College Station, Texas; MORIN—Department of Environmental Resources Engineering, State University of New York College of Environmental Science and Forestry, Syracuse, New York; NILSSON AND PEICHL—Department of Forest Ecology and Management, Swedish University of Agricultural Sciences, Umeå, Sweden; OECHEL—Department of Biology, San Diego State University, San Diego, California, and Department of Physical Geography, University of Exeter, Exeter, United Kingdom; REBA—Delta Water Management Research Service, Agricultural Research Service, USDA, Jonesboro, Arkansas; RICHARDSON—School of Informatics, Computing, and Cyber Systems, and Center for Ecosystem Science and Society, Northern Arizona University, Flagstaff, Arizona; RUNKLE—Department of Biological and Agricultural Engineering, University of Arkansas, Fayetteville, Arkansas; RYU—Department of Landscape Architecture and Rural Systems Engineering, Seoul National University, Seoul, South Korea; SACHS—GFZ German Research Centre for Geoscience, Potsdam, Germany; SCHÄFER—Department of Biological Sciences, Rutgers, The State University of New Jersey, Newark, New Jersey; SCHMID—Atmospheric Environmental Research, Institute of Meteorology and Climatology, Karlsruhe Institute of Technology, Garmisch-Partenkirchen, Germany; SHURPALI—Biogeochemistry Research Group, Department of Biological and Environmental Sciences, University of Eastern Finland, Kuopio, Finland; SONNENTAG—Département de Géographie and Centre d'Études Nordiques, Université de Montréal, Montréal, Quebec, Canada; TANG—Sarawak Tropical Peat Research Institute, Kota Samarahan, Sarawak, Malaysia; UEYAMA—Graduate School of Life and Environmental Sciences, Osaka Prefecture University, Sakai, Japan; VARGAS—Department of Plant and Soil Sciences, University of Delaware, Newark, Delaware; VESALA—Institute for Atmospheric and Earth System Research/Physics, Faculty of Science, and Institute for Atmospheric and Earth System Research/Forest Sciences, Faculty of Agriculture and Forestry, University of Helsinki, Helsinki, Finland; WINDHAM-MYERS—Water Mission Area, U.S. Geological Survey, Menlo Park, California; WOHLFAHRT—Department of Ecology, University of Innsbruck, Innsbruck, Austria; ZONA—Department of Biology, San Diego State University, San Diego, California, and Department of Animal and Plant Sciences, University of Sheffield, Sheffield, United Kingdom
CORRESPONDING AUTHOR: Sara Knox,
 saraknox.knox@gmail.com

The abstract for this article can be found in this issue, following the table of contents.

DOI:10.1175/BAMS-D-18-0268.1

A supplement to this article is available online (10.1175/BAMS-D-18-0268.2)

In final form 11 June 2019

©2019 American Meteorological Society

For information regarding reuse of this content and general copyright information, consult the [AMS Copyright Policy](#).

for providing validation datasets for the land surface models used to infer global CH₄ budgets, and for constraining CH₄ budgets. Eddy covariance (EC) flux towers measure real-time exchange of gases such as CO₂, CH₄, water vapor, and energy between the land surface and the atmosphere. The EC technique has emerged as a widespread means of measuring trace gas exchange because it provides direct and near-continuous ecosystem-scale flux measurements without disturbing the soil or vegetation (Baldocchi 2003; Aubinet et al. 2012). There are more than 900 reported active and historical flux tower sites globally and approximately 7,000 site years of data collected (Chu et al. 2017). While most of these sites measure CO₂, water vapor, and energy exchange, the development of new and robust CH₄ sensors has resulted in a rapidly growing number of CH₄ EC measurements (Baldocchi 2014; Morin 2018), primarily in natural and agricultural wetlands (Petrescu et al. 2015).

Since the late 1990s, with a growing number of long-term, near-continuous EC measurements, the EC community has been well coordinated for integrating and synthesizing CO₂, water vapor and energy fluxes. This cross-site coordination resulted in the development of regional flux networks for Europe [EuroFlux, CarboEurope, and Integrated Carbon Observing System (ICOS)], Australia (OzFlux), North and South America (AmeriFlux, Large Biosphere Amazon, Fluxnet-Canada/Canadian Carbon Program, and MexFlux), Asia [AsiaFlux, ChinaFlux, KoFlux, and U.S.–China Carbon Consortium (USCCC)], and globally, FLUXNET (Papale et al. 2012; Baldocchi 2014). The resulting FLUXNET database (<http://fluxnet.fluxdata.org/>) has been used extensively to evaluate satellite measurements, inform Earth system models, generate data-driven CO₂ flux products, and provide answers to a broad range of questions about atmospheric fluxes related to ecosystems, land use and climate (Pastorello et al. 2017). FLUXNET has grown steadily over the past 25 years, enhancing our understanding of carbon, water and energy cycles in terrestrial ecosystems (Chu et al. 2017).

Similar community efforts and syntheses for CH₄ remain limited in part because EC measurements for CH₄ fluxes were rarer until recently. Whereas the earliest EC measurements of CO₂ fluxes date back to the late 1970s and early 1980s (Desjardins 1974; Anderson et al. 1984), the first EC CH₄ flux measurements only began in the 1990s (Verma et al. 1992; Shurpali and Verma 1998; Fan et al. 1992; Kim et al. 1999), with reliable, easy-to-deploy field sensors only becoming available in the past decade or so. EC CH₄ flux measurements became more feasible with advances

in sensor development, such as tunable diode laser absorption spectrometers, that allowed researchers to measure previously undetectable trace gas fluxes with higher signal to noise ratios (Rinne et al. 2007; McDermitt et al. 2011). After these new sensors were commercialized, and low-power, low-maintenance open-path sensors were developed that could be operated by solar panels in remote locations, the number of CH₄ flux tower measurements increased substantially (Baldocchi 2014; Morin 2018). The rapidly growing number of EC CH₄ flux measurements presents new opportunities for FLUXNET-type analyses and syntheses of ecosystem-scale CH₄ flux observations.

This manuscript describes initial results from a new coordination activity for flux tower CH₄ measurements organized by the Global Carbon Project (GCP) in collaboration with regional flux networks and FLUXNET. The goal of the activity is to develop a global database for EC CH₄ observations to answer regional and global questions related to CH₄ cycling. Here, we describe the objectives of the FLUXNET-CH₄ activity, provide an overview of the current geographic and temporal coverage of CH₄ flux measurements globally, present initial analyses exploring time scales of variability, uncertainty, trends, and drivers of CH₄ fluxes across 60 sites, and discuss future research opportunities for examining controls on CH₄ emissions and reducing uncertainties in the role of wetlands in the global CH₄ cycle.

FLUXNET-CH₄ SYNTHESIS OBJECTIVES AND TASKS.

This activity is part of a larger GCP effort to establish and better constrain the global methane budget (www.globalcarbonproject.org/methanebudget/index.htm), and is designed to develop a CH₄ database component in FLUXNET for a global synthesis of CH₄ flux tower data. To this end, we are surveying, assembling, and synthesizing data from the EC community, in coordination with regional networks, including AmeriFlux's 2019 "Year of Methane" (<http://ameriflux.lbl.gov/year-of-methane/year-of-methane/>), FLUXNET initiatives, and other complementary activities. In particular, this work is being carried out in parallel with the EU's Readiness of ICOS for Necessities of Integrated Global Observations (RINGO) project, which is working to standardize protocols for flux calculations, quality control and gap-filling for CH₄ fluxes (Nemitz et al. 2018). Methane-specific protocols are needed because of the added complexities and high variability of CH₄ flux measurements and dynamics (Nemitz et al. 2018).

Our approach is to include all currently available and future CH₄ flux tower observations in a global CH₄ database, including freshwater, coastal, natural, and managed ecosystems, as well as upland ecosystems that may be measuring CH₄ uptake by soils. The initiative is open to all members of the EC community. Database compilation began in 2017 and is ongoing. Data from sites in the Americas can be submitted to AmeriFlux (<http://ameriflux.lbl.gov/data/how-to-upload/download-data/>); otherwise, data can be submitted to the European Fluxes Database Cluster (www.europe-fluxdata.eu/home/sites-list).

In addition to many applications, an ultimate goal of the FLUXNET-CH₄ activity is to generate a publicly available, open-access, data-driven global CH₄ emissions product using similar machine-learning-based approaches used for CO₂ fluxes (Jung et al. 2009; Tramontana et al. 2016). The product will be based on mechanistic factors associated with CH₄ emissions and new spatiotemporal information on wetland area and dynamics for constraining CH₄-producing areas. This gridded product will provide an independent bottom-up estimate of global wetland CH₄ emissions to compare with estimates of global CH₄ emissions from land surface models and atmospheric inversions. Recent work has shown the potential to upscale EC CH₄ flux observations across northern wetlands, with predictive performance comparable to previous studies upscaling net CO₂ exchange (Peltola et al. 2019); however, our focus is on a globally gridded product.

The near-continuous, high-frequency nature of EC measurements also offers significant promise for improving our understanding of ecosystem-scale CH₄ flux dynamics. As such, this synthesis also aims to investigate the dominant controls on net ecosystem-scale CH₄ fluxes from hourly to interannual time scales across wetlands globally, and to characterize scale-emergent, nonlinear, and lagged processes of CH₄ exchange.

Methane is produced during decomposition under anaerobic or reducing conditions and is transported to the atmosphere via plant-mediated transport, ebullition, and diffusion (Bridgman et al. 2013). During transport, CH₄ can pass through unsaturated soil layers and be consumed or oxidized by aerobic bacteria (Wahlen 1993). Process-based biogeochemical models developed and applied at site, regional, and global scales simulate these individual processes with varying degrees of complexity (Bridgman et al. 2013; Melton et al. 2013; Poulter et al. 2017; Castro-Morales et al. 2018; Grant and Roulet 2002). The large range in predicted wetland CH₄ emissions rates suggests that there is both

substantial parameter and structural uncertainty in large-scale CH₄ flux models, even after accounting for uncertainties in wetland areas (Poulter et al. 2017; Saunio et al. 2016a; Melton et al. 2013; Riley et al. 2011). A global EC CH₄ database and associated environmental variables can help constrain the parameterization of process-based biogeochemistry models (Saunio et al. 2016a; Bridgman et al. 2013; Oikawa et al. 2017). Furthermore, a key challenge is evaluating globally applicable process-based CH₄ models at a spatial scale comparable to model grid cells (Melton et al. 2013; Riley et al. 2011). A globally gridded wetland CH₄ emissions product upscaled from EC fluxes can help resolve this issue by providing a scale-appropriate model evaluation dataset. As such, the global CH₄ database and gridded product will also be used to parameterize and benchmark the performance of land surface models of global CH₄ emissions, providing a unique opportunity for informing and validating biogeochemical models.

METHODS. Based on a survey of the EC community (announced via the fluxnet-community@george.lbl.gov and AmeriFlux-Community@lbl.gov listservs), information available in regional networks and FLUXNET, and the scientific literature, we estimate that at least 200 sites worldwide are currently applying the EC method for CH₄ flux measurements (Fig. 1). Here we focus on findings from across 60 of the ~110 sites currently committed to participating in our FLUXNET-CH₄ activity [Table A1 in the appendix and Table ES1 in the online supplemental material (<https://doi.org/10.1175/BAMS-D-18-0268.2>)]. Data from this initial set of sites were selected because they were publicly available or were contributed directly by site principal investigators (PIs). We will continue to engage the EC community more broadly and expand the database in the future.

Data standardization, gap-filling, and partitioning. We used similar data processing procedures as FLUXNET to standardize and gap-fill measurements, and in the case of net CO₂ exchange, partition fluxes across sites (<http://fluxnet.fluxdata.org/data/aboutdata/data-processing-101-pipeline-and-procedures/>). Standard quality assurance and quality control of the data were first performed by site PIs. In nearly all cases, data collected by the local tower teams were first submitted to the data archives hosted by the regional flux networks, where data are prescreened and formatted based on the regional network data protocols. Data from the regional networks then entered our flux processing procedure.

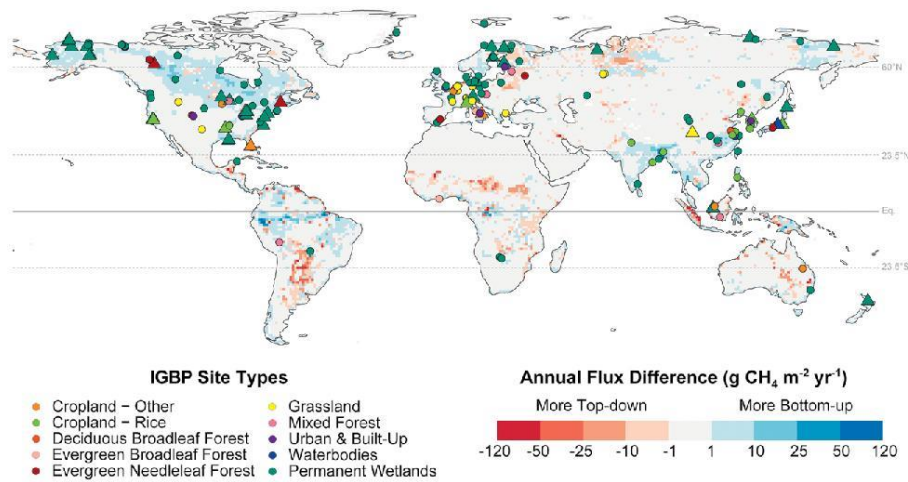


FIG. 1. Location of the 200 tower sites that report eddy covariance CH_4 flux measurements worldwide. Triangles indicate sites from which data are included in this manuscript, with circles indicating additional flux towers measuring CH_4 emissions. The colors of the markers represent the vegetation type based on the International Geosphere-Biosphere Programme (IGBP) definition. See Table ESI for a list of sites, their characteristics, and years of operation. Sites are overlaid over a map of the differences between the average CH_4 emissions over 2000–10 between top-down and bottom-up wetland CH_4 estimates. Top-down estimates are represented by the natural fluxes inventoried in NOAA's CarbonTracker (www.esrl.noaa.gov/gmd/ccgg/carbontracker-ch4/). Bottom-up emissions were produced from an ensemble of 11 Earth system model simulations (Poulter et al. 2017).

Within our processing procedure, data were first checked for obvious problems including unit errors, spikes, and out-of-range values based on visualization of the data and statistical metrics. Next, the data were filtered, gap-filled, and partitioned. Friction velocity (u_*) filtering, based on relating nighttime CO_2 fluxes to u_* , was implemented using the REdDyProc package (Wutzler et al. 2018) for R statistical software (R Core Team 2018, version 3.5.0), although in a few cases u_* filtering was performed by the site PIs. Gaps in meteorological variables including air temperature (TA), incoming shortwave (SW_{IN}) and longwave (LW_{IN}) radiation, vapor pressure deficit (VPD), pressure (PA), precipitation (P), and wind speed (WS) were filled with ERA-Interim (ERA-I) reanalysis data (Vuichard and Papale 2015). Gaps in CO_2 and latent and sensible heat fluxes were filled using the marginal distribution sampling method (Reichstein et al. 2005) using the REdDyProc package (Wutzler et al. 2018). Net CO_2 fluxes were partitioned into gross primary production (GPP) and ecosystem respiration (ER) using both the nighttime (Reichstein et al. 2005) and daytime (Lasslop et al. 2010) approaches also implemented in REdDyProc (Wutzler et al. 2018).

There are as yet no standards for gap-filling CH_4 flux measurements and this is an active and ongoing area of research (Nemitz et al. 2018). Gaps in CH_4 fluxes were filled using artificial neural networks (ANNs), as they have shown good performance for gap-filling CH_4 flux data (Dengel et al. 2013; Knox et al. 2015; Morin et al. 2014a; Nemitz et al. 2018; Goodrich et al. 2015). Details of the ANN routine are provided in Knox et al. (2016) and are summarized here briefly. The ANN routine was optimized for both generalizability and representativeness. To facilitate representativeness, explanatory data were divided into a maximum of 15 data clusters using the k -means algorithm. To avoid biasing toward conditions with better flux data coverage (e.g., summer and daytime), data used to train, test, and validate the ANN were proportionately sampled from these clusters. Several neural network architectures of increasing complexity were tested, ranging from one hidden layer with the number of nodes equal to the number of explanatory data variables (N) to two hidden layers with $1.5N$ and $0.75N$ nodes, respectively. The architecture of each neural network was initialized 10 times with random starting weights, and the initialization resulting in the lowest mean sampling

error was selected. The simplest architecture, whereby additional increases in complexity resulted in <5% reduction in mean squared error, was chosen and the prediction saved. This procedure was repeated with 20 resamplings of the data, and missing half hours were filled using the median prediction. A standard set of variables available across all sites were used to gap-fill CH₄ fluxes (Dengel et al. 2013), including TA, SW_{INT}, WS, PA, and sine and cosine functions to represent seasonality. These meteorological variables were selected since they are relevant to CH₄ exchange and were gap-filled using the ERA-I reanalysis data. Other variables related to CH₄ exchange such as water table depth (WTD) or soil temperature (TS) were not included as explanatory variables as they were not available across all sites or had large gaps that could not be filled using the ERA-I reanalysis data. These missing data for variables highlight some of the key challenges in standardizing CH₄ gap-filling methods across sites and emphasize the need for standardized protocols of auxiliary measurements across sites (cf. “Future research directions and needs” section) (Nemitz et al. 2018; Dengel et al. 2013). ANN gap-filling was performed using MATLAB (MathWorks 2018, version 9.4.0).

Annual CH₄ budgets represent gap-filled, half-hourly fluxes integrated over an entire year or growing season. If fluxes were only measured during the growing season, we assumed that fluxes outside of this period were negligible, although we acknowledge that cold season fluxes can account for as much as ~13%–50% of the annual CH₄ emissions in some locations (Zona et al. 2016; Treat et al. 2018b; Helbig et al. 2017a; Kittler et al. 2017).

Uncertainty estimation. ANNs were also used to estimate annual gap-filled and random uncertainty in CH₄ flux measurements (Richardson et al. 2008; Moffat et al. 2007; Anderson et al. 2016; Knox et al. 2018). Here, we focus on assessing the random error, but a full assessment of total flux measurement error also requires quantifying systematic error or bias (Baldocchi 2003). Systematic errors, due to incomplete spectral response, lack of nocturnal mixing, submesoscale circulations, and other factors are discussed elsewhere (Baldocchi 2003; Peltola et al. 2015) and are the focus of other ongoing initiatives.

Random errors in EC fluxes follow a double exponential (Laplace) distribution with a standard deviation varying with flux magnitude (Richardson et al. 2012, 2006). Model residuals of gap-filling algorithms such as ANNs provide a reliable, and conservative “upper limit,” estimate of the random

flux uncertainty (Moffat et al. 2007; Richardson et al. 2008). For half-hourly CH₄ flux measurements, random error was estimated using the residuals of the median ANN predictions. At each site, the probability density function (PDF) of the random flux measurement error more closely followed a double-exponential (Laplace) rather than normal (Gaussian) distribution, with the root-mean-square error (RMSE) for the Laplace distribution fitted to the PDF of random errors consistently lower than the normal distributed error. From half-hourly flux measurements, random error can also be estimated using the daily differencing approach (Richardson et al. 2012). Random error estimates [$\sigma(\delta)$], as expressed as the standard deviation of the double-exponential distribution with scaling parameter β , where $\sigma(\delta) = \sqrt{2}\beta$ (Richardson et al. 2006), were found to be nearly identical using the two approaches [$\sigma(\delta)_{\text{model residual}} = 1.0 \times \sigma(\delta)_{\text{daily differencing}} + 1.21$; $r^2 = 0.97$, $p < 0.001$], supporting the use of the model residual approach for estimating random error. As discussed below, $\sigma(\delta)$ scaled linearly with the magnitude of CH₄ fluxes at nearly all sites. To quantify random uncertainty of cumulative fluxes, we used a Monte Carlo simulation that randomly draws 1,000 random errors for every original measurement using $\sigma(\delta)$ binned by flux magnitude, and then computed the variance of the cumulative sums (Anderson et al. 2016). For gap-filled values, the combined gap-filling and random uncertainty was calculated from the variance of the cumulative sums of the 20 ANN predictions (Anderson et al. 2016; Oikawa et al. 2017; Knox et al. 2015). The annual cumulative uncertainty at 95% confidence was estimated by adding the cumulative gap-filling and random measurement uncertainties in quadrature (Richardson and Hollinger 2007; Anderson et al. 2016). Note that when reporting mean or median annual CH₄ fluxes across sites, error bars represent the standard error.

Wavelet-based time-scale decomposition. Methane fluxes are highly dynamic and vary across a range of time scales (Sturtevant et al. 2016; Koebsch et al. 2015). For example, in wetlands with permanent inundation, the seasonal variation of CH₄ exchange is predominantly controlled by temperature and plant phenology (Chu et al. 2014; Sturtevant et al. 2016). Ecosystem CH₄ exchange also varies considerably at both longer (e.g., interannual; Knox et al. 2016; Rinne et al. 2018) and shorter (e.g., weeks, days, or hours; Koebsch et al. 2015; Hatala et al. 2012; Schaller et al. 2018) time scales. Wavelet decomposition is a particularly useful tool for investigating scale in geophysical

and ecological analysis (Cazelles et al. 2008; Torrence and Compo 1998), because it can characterize both the time scale and location of patterns and perturbations in the data. Partitioning variability across temporal scales can help to isolate and characterize important processes (Schaller et al. 2018).

The maximal overlap discrete wavelet transform (MODWT) was used to decompose the time scales of variability in gap-filled CH_4 flux measurements, as described in Sturtevant et al. (2016). The MODWT allows the time series to be decomposed into the detail added from progressively coarser to finer scales and either summed or treated individually to investigate patterns across scales. We reconstructed the detail in the fluxes for dyadic scales 1 (2^1 measurements = 1 h) to 14 (2^{14} measurements = 341 days). Since patterns generated by ecological processes tend to occur over a scale range rather than at one individual scale, the detail over adjacent scales were summed to analyze four general time scales of variation (Sturtevant et al. 2016). These time scales included the “hourly” scale (1–2 h) representing perturbations such as the passage of clouds overhead and turbulent scales up to the spectral gap, the “diel” scale (4 h to 1.3 days) encompassing the diel cycles in sunlight and temperature, the “multiday” scale (2.7 to 21.3 days) reflecting synoptic weather variability or fluctuations in water levels, and the “seasonal” scale (42.7 to 341 days) representing the annual solar cycle and phenology. Data were wavelet decomposed into the hourly, diel, and multiday scales using the Wavelet Methods for Time Series Analysis (WMTSA) Wavelet Toolkit in MATLAB.

Statistical analysis. We tested for significant relationships between log-transformed annual CH_4 emissions and a number of covariates using linear mixed-effects models as described in Treat et al. (2018b). The predictor variables of CH_4 flux we evaluated included: biome or ecosystem type (categorical variables), and continuous biophysical variables including mean seasonal WTD, mean annual soil and air temperature (T_{MST} and T_{MAT} , respectively), net ecosystem exchange (NEE), GPP, and ER. When considering continuous variables, we focused on freshwater wetlands for comparison with previous CH_4 synthesis activities. Soil temperature was measured between 2 and 25 cm below the surface in different studies. The results below are presented for GPP and ER covariates that are partitioned using the nighttime flux partitioning algorithm (Wutzler et al. 2018; Reichstein et al. 2005), although similar findings were obtained using daytime partitioned estimates. Additionally, individual sites or

site years were excluded when gaps in measurements exceeded two consecutive months, which explains the differences in the number of sites and site years in the “Environmental controls on annual CH_4 emissions across freshwater wetland sites” section below.

Mixed-effects modeling was used because of the potential bias of having measurements over several years, with site included as a random effect in the analysis (Treat et al. 2018b). The significance of individual predictor variables was evaluated using a χ^2 test against a null model using only site as a random variable (Bates et al. 2015), with both models fit without reduced maximum likelihood. For multiple linear regression models, we used the model selection process outlined in Zuur et al. (2009). To incorporate annual cumulative uncertainty when assessing the significance of trends and differences in annual CH_4 fluxes across biomes and ecosystem types, we used a Monte Carlo simulation that randomly draws 1,000 annual cumulative uncertainties for each estimate of annual CH_4 flux. For each random draw the significance of the categorical variable was tested using a χ^2 test against the null model with only site as a random variable. We report the marginal r^2 (r_m^2), which describes the proportion of variance explained by the fixed factors alone (Nakagawa and Schielzeth 2013). The mixed-effects modeling was implemented using the lmer command from the lme4 package (Bates et al. 2015) for R statistical software.

RESULTS AND DISCUSSION. Geographic and temporal coverage of eddy covariance CH_4 flux measurements. We identified 200 sites worldwide that are applying the EC method for CH_4 (Fig. 1; Table ES1); wetlands (including natural, managed, and restored wetlands) comprise the majority of sites (59%), with rice agriculture (10%) as the second-most represented vegetation type. The predominance of wetland and rice paddy sites in the database is unsurprising because many studies are designed to target ecosystems expected to have relatively large CH_4 emissions. However, there are also sites in ecosystems that are typically smaller sources or even sinks of CH_4 such as upland forests (13%) and grasslands (8%). Additionally, six sites (~3%) are urban, with another five sites measuring CH_4 fluxes from open water bodies. Although identified sites span all continents except Antarctica, the majority are concentrated in North America and Europe, with a growing number of sites in Asia (Fig. 1; Table ES1).

Measurements of CH_4 fluxes cover a broad range of climates and a large fraction of wetland habitats (Fig. 2), with the tropics and tropical wetlands notably

underrepresented. As discussed below (see “Future research directions and needs” section), one important goal of FLUXNET and the regional networks is to increase site representativeness and extend measurements in undersampled regions. Increasing the number of tropical sites is particularly important for CH_4 because more than half of global CH_4 emissions are thought to come from this region (Saunois et al. 2016a; Dean et al. 2018). Furthermore, compared to northern wetlands, their biogeochemistry remains relatively poorly understood (Mitsch et al. 2009; Pangala et al. 2017). We expect the number of CH_4 flux sites and their geographic and temporal coverage to continue to increase, as has occurred through time for CO_2 , water vapor, and energy flux measurements in FLUXNET (Pastorello et al. 2017; Chu et al. 2017).

Long-term CH_4 flux time series are key to understanding the causes of year-to-year variability and

trends in fluxes (Chu et al. 2017; Euskirchen et al. 2017; Pugh et al. 2018). The longest continuous record of CH_4 flux measurements, from a fen in Finland (Rinne et al. 2018), is now ~14 years and ongoing (Table ES1). Three other sites have measurements exceeding 10 years; however, the median length is 5 years, with most sites established from 2013 onward (Table ES1). Longer time series are also important for both exploring the short- and long-term effects of extreme events on fluxes and tracking the response of disturbed or restored ecosystems over time (Pastorello et al. 2017). Furthermore, they can help address new and emerging science questions, such as quantifying CH_4 feedbacks to climate with rising temperatures and associated changes in ecosystem composition, structure and function (Helbig et al. 2017a,b; Dean et al. 2018), and the role of wetland emissions in atmospheric CH_4 variability (McNorton et al. 2016; Poulter et al. 2017).

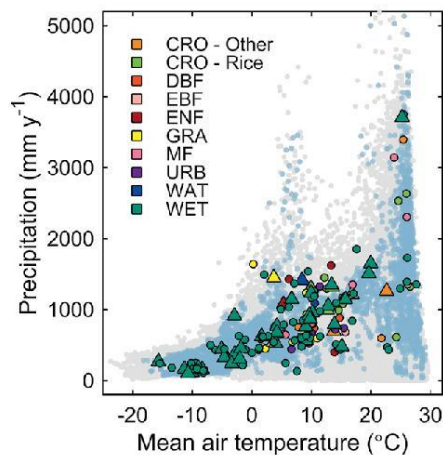


FIG. 2. Distribution of sites by mean annual air temperature and precipitation. Tower locations are shown as circles or triangles (see Fig. 1), with vegetation type in color based on the IGBP definitions (CRO = croplands; DBF = deciduous broadleaf forests; EBF = evergreen broadleaf forests; ENF = evergreen needleleaf forests; GRA = grasslands; MF = mixed forests; URB = urban and built-up lands; WAT = water bodies; WET = permanent wetlands). Gray dots represent annual mean temperature and total precipitation from the CRU TS 3.10 gridded climate dataset over the entire landmass (Harris et al. 2014), whereas blue dots represent grid cells with >25% wetland fraction as estimated using the Global Lakes and Wetlands Database (Lehner and Döll 2004). Temperature and precipitation grid cells included in this figure were averaged from 1981 to 2011, at 0.5° resolution.

CH₄ fluxes and trends across biomes and ecosystem types. Half-hourly and annual net CH_4 fluxes for the 60 sites currently included in the database exhibited strong variability across sites (Figs. 3 and 4). Across the dataset, the mean half-hourly CH_4 flux was greater than the median flux, indicating a positively skewed distribution with infrequent, large emissions (Fig. 3a), similar to findings from chamber-based syntheses (Olefeldt et al. 2013; Turetsky et al. 2014). Mean and median CH_4 fluxes were smaller at higher latitudes and larger at lower latitudes (Fig. 3b), comparable again to trends in CH_4 fluxes observed in predominantly chamber-based syntheses (Bartlett and Harriss 1993; Turetsky et al. 2014; Treat et al. 2018b).

The continuous nature of EC flux measurements is well suited for quantifying annual ecosystem-scale CH_4 budgets, along with accumulated uncertainty (cf. “Gap-filling performance and uncertainty quantification” section). Annual estimates of net CH_4 flux for each of the 60 sites in the flux tower database ranged from $-0.2 \pm 0.02 \text{ g C m}^{-2} \text{ yr}^{-1}$ for an upland forest site to $114.9 \pm 13.4 \text{ g C m}^{-2} \text{ yr}^{-1}$ for an estuarine freshwater marsh (Rey-Sanchez et al. 2018), with fluxes exceeding $40 \text{ g C m}^{-2} \text{ yr}^{-1}$ at multiple sites (Fig. 4b). These emissions are of a considerably broader range and have much higher annual values than in an earlier synthesis by Baldocchi (2014), which included published values from 13 sites (Fig. 4a); median annual CH_4 fluxes ($\pm \text{SE}$) in that study were $6.4 \pm 1.9 \text{ g C m}^{-2} \text{ yr}^{-1}$, compared with $10.0 \pm 1.6 \text{ g C m}^{-2} \text{ yr}^{-1}$ for our expanded database. Annual CH_4 sums in our database were positively skewed, with skewness increasing with additional observations due largely to the inclusion of

high CH_4 -emitting freshwater marsh sites (Fig. 4).

As suggested from Fig. 3b, annual wetland CH_4 emissions differed significantly among biomes, even when considering accumulated uncertainty [average Monte Carlo $\chi^2 = 13.4$ (12.1–14.7, 95% confidence interval), degrees of freedom (df) = 3, $p < 0.05$] (Table 1). Median CH_4 emissions were significantly lower for tundra wetlands ($2.9 \pm 1.3 \text{ g C m}^{-2} \text{ yr}^{-1}$) than temperate wetlands ($27.4 \pm 3.4 \text{ g C m}^{-2} \text{ yr}^{-1}$). Higher CH_4 emissions were observed from subtropical/tropical wetlands ($43.2 \pm 11.2 \text{ g C m}^{-2} \text{ yr}^{-1}$), based on only three site years of data; however, emphasizing the need for additional flux tower measurements in the tropics.

Whereas annual boreal/taiga wetland CH_4 emissions were comparable to values reported in a recent synthesis of predominantly chamber-based CH_4 flux measurements (Treat et al. 2018b), our tower-based measurements are $\sim 50\%$ lower and over 6 times higher for tundra and temperate wetlands, respectively (Table 1). The inconsistencies highlighted in Table 1 not only reflect the differences in the number and location of sites between datasets, but also the discrepancies resulting from different measurement

techniques. Several studies have noted considerable differences in CH_4 emissions measured using EC and chamber techniques, with estimates from chambers often higher than those from the EC measurements (Schrier-Uijl et al. 2010; Hendriks et al. 2010; Meijide et al. 2011; Krauss et al. 2016). This distinction highlights the need for additional studies investigating the systematic differences caused by the different spatial and temporal sampling footprints of these methods (Krauss et al. 2016; Morin et al. 2017; Windham-Myers et al. 2018; Xu et al. 2017). Characterizing discrepancies between measurement techniques may also help constrain bottom-up estimates of CH_4 emissions and reduce the disagreement of $\sim 15 \text{ Tg C yr}^{-1}$ between bottom-up ($139 \text{ Tg CH}_4 \text{ yr}^{-1}$) and top-down ($125 \text{ Tg CH}_4 \text{ yr}^{-1}$) estimates of CH_4 emissions from natural wetlands (Saunois et al. 2016a).

Annual CH_4 emissions also differed significantly across ecosystems [average Monte Carlo $\chi^2 = 45.5$ (39.3–50.1), df = 9, $p < 0.001$; Fig. 5], with median fluxes highest for freshwater marshes ($43.2 \pm$

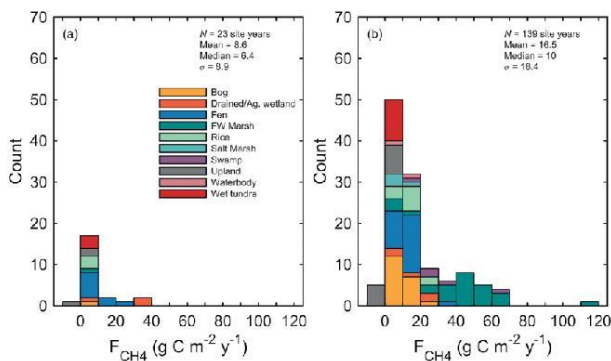


FIG. 4. (a) Histogram of annual CH_4 fluxes (F_{CH_4} ; $\text{g C m}^{-2} \text{ yr}^{-1}$) measured with eddy covariance and published in the synthesis by Baldocchi (2014), and (b) histogram of our annual CH_4 fluxes including additional site years of data estimated from the 60 sites listed in Table A1.

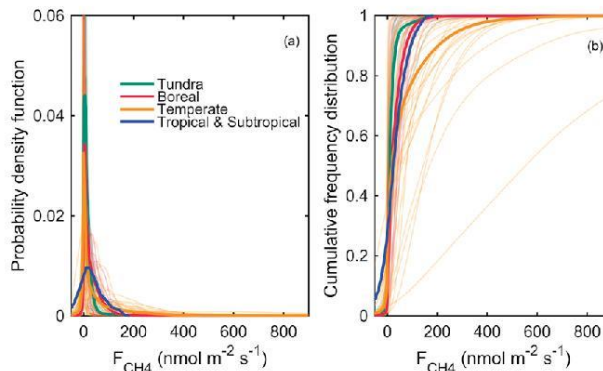


FIG. 3. (a) Probability density function, and (b) cumulative frequency distribution of half-hourly CH_4 flux (F_{CH_4}) data for sites currently included in the database (60 sites) aggregated by biome. Thin lines represent individual sites, whereas thicker lines present sites aggregated by biome. All cases are approximated by kernel density estimation. Note that whereas the x axis is scaled between -50 and $900 \text{ nmol m}^{-2} \text{ s}^{-1}$ for visualization purposes, some CH_4 fluxes exceed this range.

TABLE 1. Number of site years and characteristics of CH_4 fluxes ($\text{g C m}^{-2} \text{ yr}^{-1}$) currently included in the database. Fluxes are compared with measurements reported in a recent synthesis of predominantly chamber-based CH_4 flux measurements. Biome type was extracted from Olson et al. (2001) using site coordinates and includes tundra, boreal/taiga, temperate, and tropical/subtropical. Wetland CH_4 emissions differed significantly across biomes, with letters indicating significant differences ($\alpha = 0.05$) among biomes. Note that similar to our tower only dataset, values from Treat et al. (2018b) represent measured annual fluxes derived from a smaller dataset where measurements were made in the growing season and nongrowing season.

Biome	No. of site years	Median annual CH_4 flux	25th percentile	75th percentile	References
Tundra	10	2.9	1.8	4.2	This study—All sites
	10	2.9 ^a	1.8	4.2	This study—Wetlands
	31	5.6	1.0	11.4	Treat et al. (2018b)—All sites
	26	6.3	3.0	16.4	Treat et al. (2018b)—Wetlands
Boreal and taiga	35	8.3	4.1	10.9	This study—All sites
	30	9.5 ^{ab}	6.0	11.3	This study—Wetlands
	68	13.1	3.5	23.7	Treat et al. (2018b)—All sites
	67	13.2	3.6	23.7	Treat et al. (2018b)—Wetlands
Temperate	72	16.4	7.9	35.9	This study—All sites
	47	27.4 ^b	10.0	47.3	This study—Wetlands
	27	4.3	0.3	41.7	Treat et al. (2018b)—All sites
	25	5.3	0.8	42.2	Treat et al. (2018b)—Wetlands
Tropical and subtropical	3	43.2	20.0	46.8	This study—All sites
	3	43.2 ^{ab}	20.0	46.8	This study—Wetlands
	—	—	—	—	Treat et al. (2018b)—All sites
—	—	—	—	Treat et al. (2018b)—Wetlands	

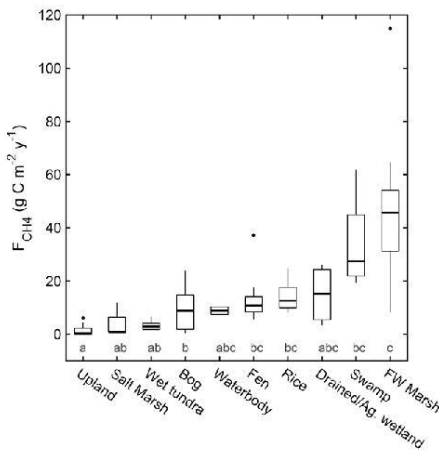


FIG. 5. Annual CH_4 fluxes (F_{CH_4} ; $\text{g C m}^{-2} \text{ yr}^{-1}$) among ecosystem types for the 60 sites currently included in the database (Table A1). Letters indicate significant differences ($\alpha = 0.05$) among ecosystem types. Median value, first quartile, and third quartile are presented in the boxes, and dots represent outliers, which are defined as observations more than 1.5 times the interquartile range away from the top or bottom of the box.

$4.2 \text{ g C m}^{-2} \text{ yr}^{-1}$) and lowest for upland ecosystems ($1.3 \pm 0.7 \text{ g C m}^{-2} \text{ yr}^{-1}$). Treat et al. (2018b) also observed the highest annual emissions in marshes and reported a similar median value for temperate marshes ($49.6 \text{ g C m}^{-2} \text{ yr}^{-1}$). Wet tundra and bogs had significantly lower annual emissions than marshes (Fig. 5), which in part reflects their presence in colder boreal and tundra systems, as well as differences in vegetation type, nutrient status, and hydrological regime (Treat et al. 2018b). Low median CH_4 emission was observed from salt marshes in our dataset ($0.8 \pm 2.9 \text{ g C m}^{-2} \text{ yr}^{-1}$), because high sulfate concentrations inhibit methanogenesis (Poffenbarger et al. 2011; Holm et al. 2016). Even drained wetlands converted to agricultural land can be large sources of CH_4 associated with seasonal flooding (Fig. 5). Median annual CH_4 flux from rice was $12.6 \pm 1.6 \text{ g C m}^{-2} \text{ yr}^{-1}$, which is slightly lower than the IPCC default value of $15 \text{ g C m}^{-2} \text{ yr}^{-1}$ (Sass 2003).

Environmental controls on annual CH_4 emissions across freshwater wetland sites. Using an integrated CH_4 flux database, we can begin to investigate the factors associated with varying CH_4 emissions across sites. We explored the effects of WTD , T_{MST} or T_{MAT} , NEE, GPP, and ER on annual CH_4 flux. At global scales,

T_{MAT} and T_{MST} were the most important predictors of annual CH_4 flux across wetland sites ($p < 0.001$ for each), with the fixed factor of T_{MAT} or T_{MST} explaining ~65% of the variation in log transformed annual CH_4 emission (Figs. 6a,b). Previous synthesis studies also observed a significant, but weaker, relationship between soil temperature and average CH_4 emissions across sites, explaining <15% of the variation in CH_4 flux in those studies (Olefeldt et al. 2013; Yvon-Durocher et al. 2014). However, our findings are consistent with numerous site-level studies that report a strong correlation between wetland CH_4 emissions and temperature, with nearly 95% of all EC studies reporting a significant relationship between temperature and CH_4 flux (Morin 2018). Across sites, Peltola et al. (2019) found that the most important predictor in a random forest model used to upscale EC CH_4 emissions across northern latitudes was temperature, again highlighting the importance of temperature in regulating CH_4 emissions within and across sites.

Water table depth has also commonly been identified as a key control on CH_4 emissions (Turetsky et al. 2014; Bubier et al. 2005), because higher water levels often inhibit oxygen availability and lower the soil reduction potential, making methanogenesis more thermodynamically favorable. Although predominantly chamber-based wetland CH_4 syntheses have found a positive relationship between WTD and average or annual CH_4 emissions across sites (Olefeldt et al. 2013; Turetsky et al. 2014; Treat et al. 2018b), we observed no significant relationship between mean WTD and annual CH_4 flux across all sites ($\chi^2 = 0.2$, $df = 1$, $p = 0.66$, $N_{sites} = 20$, $N_{site_yr} = 46$), even when considering WTD^2 or WTD^3 (Olefeldt et al. 2013). However, if we consider only sites where WTD was below the soil surface for part or all of the year (Fig. 6c, solid circles), we did observe a significant relationship with WTD ($p < 0.05$). Conversely, CH_4 emissions for permanently inundated sites showed no

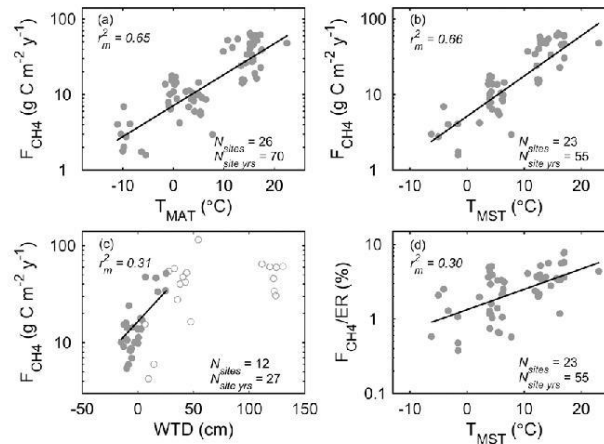


Fig. 6. Relationship between annual CH_4 flux (F_{CH_4}) and (a) mean annual air temperature (T_{MAT}) ($\chi^2 = 36.7$, $df = 1$, $p < 0.001$), (b) mean annual soil temperature (T_{MST}) ($\chi^2 = 32.3$, $df = 1$, $p < 0.001$) for freshwater wetlands, and (c) mean water table depth (WTD). While there was no significant relationship between mean annual WTD and annual CH_4 flux across all sites, there was a significant relationship if we consider only sites where WTD was below the soil surface for part or all of the year (solid circles) ($\chi^2 = 5.6$, $df = 1$, $p < 0.05$). Open circles in (c) indicate CH_4 emissions for permanently inundated sites. (d) Temperature dependence of the annual CH_4 :ER ratio ($\chi^2 = 12.0$, $df = 1$, $p < 0.001$). Lines represent the fitted values for the population.

significant relationship with WTD (Fig. 6c, open circles) ($\chi^2 = 0.5$, $df = 1$, $p = 0.50$, $N_{sites} = 13$, $N_{site_yr} = 19$). This result supports the finding that wetlands that are permanently inundated or exhibit little variation in WTD tend to show weak to no correlation between WTD and CH_4 emissions (Chu et al. 2014; Jackowicz-Korczyński et al. 2010; Rinne et al. 2007; Christensen et al. 2003); in contrast, wetlands with lower and more variable water levels often have a significant relationship between WTD and CH_4 emissions (Bubier et al. 2005; Treat et al. 2007). However, only half of the sites currently included in the database report water table position, and given the importance of WTD in regulating CH_4 exchange, it is critical to ensure that WTD is measured across all sites.

Gross primary production and ER were both significant positive predictors of annual CH_4 flux ($\chi^2 = 21.3$, $df = 1$, $p < 0.001$, $r_m^2 = 0.29$ and $\chi^2 = 17.1$, $df = 1$, $p < 0.001$, $r_m^2 = 0.25$, respectively, $N_{sites} = 26$, $N_{site_yr} = 64$), although there was no significant relationship between NEE and annual CH_4 flux ($\chi^2 = 0.9$, $df = 1$, $p = 0.33$, $N_{sites} = 2$, $N_{site_yr} = 64$). However, when considering GPP or ER in a multiple linear regression model with T_{MST} , including interaction terms (Chu

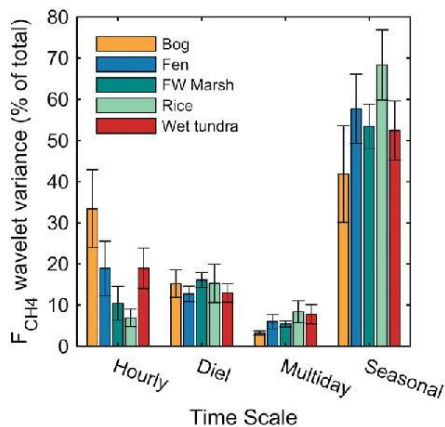


Fig. 7. Variance of CH₄ flux (F_{CH₄}) wavelet coefficients across time scales, as a percentage of the total variance, averaged by wetland type. Error bars represent the standard error. Note that only ecosystem types with at least 6 sites are shown here, including bogs, fens, freshwater (FW) marshes, rice paddies, and wet tundra.

et al. 2014), neither GPP nor ER were significant, suggesting that the observed relationship with GPP or ER was due to covariation with soil temperature and, possibly, other environmental drivers.

The strong temperature dependence of ecosystem-scale CH₄ emissions we observed across wetland sites is in line with the high temperature sensitivity of CH₄ emissions found across microbial to ecosystem scales (Yvon-Durocher et al. 2014). CH₄ emissions also have a higher temperature dependence than ER, such that the ratio of CH₄ to CO₂ emissions was found to increase markedly with seasonal increases in temperature (Yvon-Durocher et al. 2014). Similarly, we observed a significant increase in the ratio of annual CH₄ to ER along geographic temperature gradients, ranging from 0.4% to 7.9%, with a median value of 2.8% across the dataset (Fig. 6d). This relationship suggests that warming may result in a greater relative contribution of CH₄ to total carbon emissions from wetland ecosystems. With a growing FLUXNET CH₄ database, it will be possible to further explore the dominant controls on CH₄ fluxes within and across ecosystem types, as well as further investigate the temperature dependence of ecosystem-scale CH₄ exchange (Schipper et al. 2014; Arcus et al. 2016; Yvon-Durocher et al. 2014).

Time scales of variability. Methane fluxes exhibited strong variability over a range of time scales, with the

variation across time scales differing between wetland types (Fig. 7). As observed previously (Sturtevant et al. 2016), the seasonal time scale dominated CH₄ flux variability across wetland types, but was most pronounced in rice paddies, which have a distinct growing season, and least pronounced in bogs (Fig. 7). Across ecosystem types, variation was lowest at the multiday scale, although multiday CH₄ flux variation was slightly greater in rice paddies and wet tundra, potentially indicating greater water table fluctuations (Sturtevant et al. 2016), particularly at rice paddy sites, which are subject to seasonal drainage (Knox et al. 2016; Runkle et al. 2019). Whereas some studies report a strong diel pattern in CH₄ emissions from wetlands and rice paddies (Knox et al. 2016; Chu et al. 2014; Morin et al. 2014b; Kim et al. 1999), others have found little or no diel variation (Rinne et al. 2018; Jackowicz-Korczyński et al. 2010; Yagi and Minami 1990; Nadeau et al. 2013). Across wetland types, diel variation was greatest in freshwater marshes (Fig. 7), which is consistent with the observations that the vegetation at sites with a strong diel cycle of CH₄ emissions is typically dominated by species with convective gas flow such as *Phragmites australis* or *Typha* spp. (Brix et al. 1992; Chanton et al. 1993). Bogs, fens, and wet tundra showed the greatest variation at the hourly scale (Fig. 7). This is likely in part due to typically lower fluxes at these sites as hourly perturbations of turbulent time series are largely dominated by noise (Hollinger and Richardson 2005), as well as the fact that near-surface turbulence and short-term pressure fluctuations can strongly influence CH₄ exchange in these peat dominated ecosystems (Nadeau et al. 2013; Sachs et al. 2008).

Gap-filling performance and uncertainty quantification.

The performance of the neural networks varied strongly across sites (Fig. 8). Model r^2 , calculated from the median ANN prediction and observed fluxes at each site, ranged from ~0 to 0.92 across sites, with a median value of 0.41. Across sites, ANN performance was strongly linked to the percentage of total variance at diel and seasonal scales ($r^2 = 0.69$, $p < 0.001$), indicating that across the wide range of observed flux magnitudes, sites with a more distinct seasonal and diel pattern tended to be more predictable (Fig. 8). There was also a significant negative relationship between model r^2 and the percentage of total variance at the hourly scale across sites ($r^2 = 0.72$, $p < 0.001$), because, as noted previously, hourly perturbations are largely dominated by noise (Hollinger and Richardson 2005).

Knowledge of the random errors in half-hourly flux measurements is not only important for

evaluating the uncertainty in cumulative fluxes (e.g., daily, monthly, or annual) and comparing fluxes across tower sites, but it also needed to incorporate information about random flux errors in model-data synthesis activities (Richardson et al. 2006). As noted above, random flux error more closely followed a Laplace rather than Gaussian distribution. Within sites, $\sigma(\delta)$ was not constant, but rather nearly always scaled with the magnitude of CH_4 fluxes (Fig. 9a), as predicted from theory (Richardson et al. 2006). As observed for other fluxes (Richardson et al. 2006), both the slope and intercept of this relationship varied among sites, and depending on the sign of the flux (Fig. 9a). Across sites, random flux error therefore scaled linearly with the magnitude of mean CH_4 flux ($r^2 = 0.86$, $p < 0.001$), even when excluding the two highest CH_4 -emitting sites ($r^2 = 0.46$, $p < 0.001$) (Fig. 9b). Whereas closed-path CH_4 analyzers have been found to have lower random errors and instrument noise compared with open-path sensors (Peltola et al. 2014), there was no clear evidence of a systematic effect of the influence of closed- versus open-path sensors on random errors across sites (Fig. 9).

The total annual cumulative uncertainty in CH_4 fluxes, including both random and gap-filling errors, ranged from ± 0.01 to $\pm 13.4 \text{ g C m}^{-2} \text{ yr}^{-1}$, with a median value of $\pm 1.0 \text{ g C m}^{-2} \text{ yr}^{-1}$ at 95% confidence (Fig. 10a). Relative error decreased exponentially with flux magnitude, ranging from 1.5% to 60% in most cases (Fig. 10b), although a few sites where annual CH_4 sums were near zero had relative errors exceeding 200% (data not shown). The highest relative errors therefore tended to be associated with low CH_4 -emitting sites, such as upland sites and bogs, and the lowest relative errors were generally associated with high CH_4 -emitting sites such as freshwater marshes (Fig. 10b).

FUTURE RESEARCH DIRECTIONS AND NEEDS. Better quantification of CH_4 sources and sinks will improve estimates of regional and global CH_4 budgets and reduce uncertainties in the CH_4 cycle. In this general

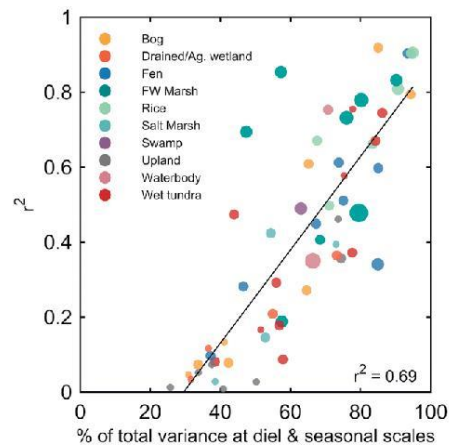


Fig. 8. Relationship between the correlation coefficient (r^2) calculated from the median ANN prediction and observed CH_4 fluxes at each site and the percentage of total variance at diel and seasonal scales ($r^2 = 0.69$, $p < 0.001$). Each site is color coded by ecosystem type. Sizes of the dots are proportional to the magnitude of mean CH_4 flux, where flux magnitude was aggregated into 10 bins for plotting.

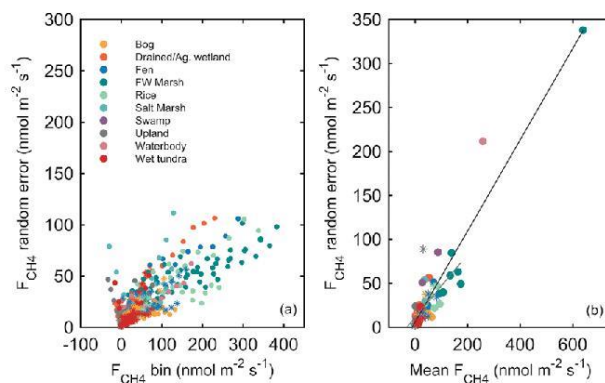


Fig. 9. (a) Scaling of F_{CH_4} random flux measurement error [$\sigma(\delta)$] with flux magnitude for all sites with a significant linear relationship between random error and flux magnitude (95% of all sites). Data at each site were placed into 10 bins (Oikawa et al. 2017). (b) Scaling of F_{CH_4} random flux measurement error, characterized by the standard deviation of the double-exponential distribution [$\sigma(\delta)$], with mean flux magnitude across sites. There was a significant linear relationship between $\sigma(\delta)$ and the magnitude of mean CH_4 flux [$\sigma(\delta) = 0.5 \times F_{\text{CH}_4} + 5.9$, $r^2 = 0.86$, $p < 0.001$], even when excluding the two highest CH_4 -emitting sites [$\sigma(\delta) = 0.4 \times F_{\text{CH}_4} + 11.3$, $r^2 = 0.46$, $p < 0.001$]. Note that circles represent sites with open-path CH_4 analyzers while asterisks represent sites with closed-path sensors.

context, high-frequency observations of ecosystem-scale CH_4 emissions should help constrain bottom-up CH_4 budgets, improve our understanding of the environmental factors controlling CH_4 fluxes, and inform and validate land surface models used to estimate global CH_4 fluxes. Unlike well-established efforts synthesizing CO_2 , water vapor, and energy observations, no such global data synthesis or initiative previously existed for CH_4 . The database presented here addresses this gap with the EC community by organizing the collection and aggregation of a global EC CH_4 database through FLUXNET.

EC flux data quality assessment.

Much of what has been learned within FLUXNET for CO_2 , water vapor, and energy measurements is informing, and should continue to inform, new efforts for CH_4 . Reliable EC measurements of CO_2 and water vapor fluxes have been conducted at hundreds of sites across broad regional networks (Papale et al. 2012), and substantial efforts have focused on developing best practices and harmonizing approaches across sites to ensure consistent, high-quality flux measurements (Aubinet et al. 1999; Reichstein et al. 2005; Moffat et al. 2007). CH_4 fluxes are often characterized by small fluxes with episodic spikes, and additional research is needed to ensure reliable measurements (Peltola et al. 2014, 2013), and refine and standardize methods and routines for data processing and quality checking (Nemitz et al. 2018; Schaller et al. 2018). Recent efforts provided guidance on instrument selection, setup and maintenance, and data processing for EC CH_4 flux measurements (Nemitz et al. 2018). However, with respect to instrument setup and data processing, more research is needed in best practices for storage flux quantification, despiking, and u_c filtering (Nemitz et al. 2018).

Gap-filling. Whereas neural networks have shown strong performance for gap-filling CH_4 fluxes (Dengel et al. 2013; Knox et al. 2016), our results reveal some of the challenges of gap-filling CH_4 fluxes at sites with low fluxes and/or a lack of seasonal and diel variation (Fig. 8). More research is therefore needed

for best practices for gap-filling to estimate annual CH_4 budgets (Nemitz et al. 2018). For example, there has yet to be a comprehensive analysis comparing a wide range of gap-filling approaches for CH_4 fluxes similar to the study by Moffat et al. (2007) for CO_2 exchange. While ANNs are one gap-filling method (Dengel et al. 2013; Shoemaker et al. 2014; Morin et al. 2014a), numerous other gap-filling approaches exist, including nonlinear regression techniques, mean diurnal variation, lookup tables, marginal distribution sampling, and the multiple imputation method (Moffat et al. 2007; Vitale et al. 2019). Future efforts should focus on systematically investigating these approaches across a range of sites to provide best practices for gap-filling CH_4 exchange.

Ancillary measurements. Along with research that addresses the challenges of measuring and processing EC CH_4 fluxes, key ancillary variables to help gap-fill, predict, and scale CH_4 fluxes should also be measured more comprehensively across sites. For instance, although WTD is known to strongly influence CH_4 emissions (Turetsky et al. 2014; Treat et al. 2018b), as noted above, only half of the sites currently included in the database report water table position. Generally, EC CH_4 measurements are implemented at sites also collecting CO_2 fluxes and common meteorological measurements used in the flux community; however, guidelines are only

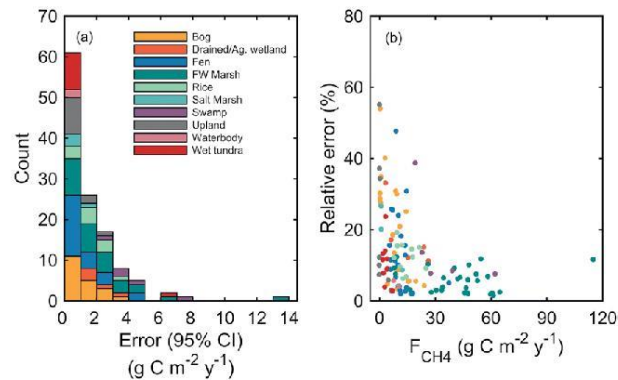


FIG. 10. (a) Histogram of total random error ($\text{g C m}^{-2} \text{yr}^{-1}$) in annual CH_4 flux at 95% confidence, where count refers to the number of site years of measurements. The cumulative gap-filling and random measurement uncertainties of gap-filled and original values were added in quadrature to estimate the total random uncertainty at each site. (b) Relationship between annual CH_4 flux ($\text{g C m}^{-2} \text{yr}^{-1}$) and relative error (i.e., total random error divided by flux magnitude; %).

beginning to emerge for which additional supporting variables should be collected at sites measuring CH_4 fluxes (Nemitz et al. 2018).

Measurements of variables beyond those relevant for CO_2 are needed to better understand and predict the complex and interacting processes of CH_4 production, consumption, and transport, the latter of which includes diffusion, ebullition, and plant-mediated transport. Guidance on the description of some basic variables affecting these processes is available through new protocols in the flux community detailing soil meteorological measurements, ancillary vegetation measurements, and site description, management and disturbance (Saunders et al. 2018; Op De Beeck et al. 2018; Gielen et al. 2018). These protocols provide guidance on variables such as soil temperature and soil moisture profiles, water table depth and snow depth, soil pH and soil type, bulk density, and livestock density. However, although WTD is an easily measured proxy for anaerobic conditions, direct and continuous measurement of redox potential and oxygen content in particular would be valuable additional measurements (Nemitz et al. 2018). Similarly, measuring variables such as conductivity, below-ground CH_4 concentrations, dissolved organic carbon concentrations, and the presence of alternative electron acceptors such as nitrate, iron, sulfate, and humic substances in the water and soil column would provide useful information for the interpretation of CH_4 emissions. Stable isotope analyses of CH_4 are also valuable as they provide important information on mechanisms of CH_4 production, transport, and oxidation (Chanton et al. 1997; Marushchak et al. 2016). Detailed information on soil microbial communities driving CH_4 production and consumption could also be helpful (Kwon et al. 2017). Vegetation biomass, species composition, and phenology are also important variables to consider, because plants are a primary source of carbon substrates for methanogenic metabolism, and they mediate CH_4 transport through aerenchymous tissue (Kwon et al. 2017; Joabsson et al. 1999; Carmichael et al. 2014). New guidance is now available for such measurements at flux tower locations (Gielen et al. 2018; Hufkens et al. 2018). Continuing to develop a consensus on best practices for ancillary measurements is important for interpreting, gap-filling, and upscaling CH_4 flux measurements.

Characterizing spatial variability. CH_4 fluxes exhibit finescale spatial variability that can span orders of magnitude within a landscape (Peltola et al. 2015; Marushchak et al. 2016; Desai et al. 2015; Treat et al.

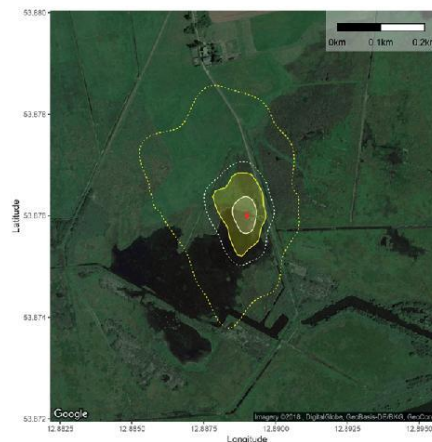


FIG. 11. Footprint climatology for a eutrophic shallow lake on a formerly drained fen in Germany (Zarnekow; DE-Zrk) illustrating the importance of footprint analysis for the interpretation of EC measurements of CH_4 . Here we used two footprint models, including the model of Kormann and Meixner (2001) (yellow) and Kljun et al. (2015) (white). The footprint climatology was calculated by aggregating all half-hour footprints within a year. The dashed lines enclose the areas aggregating to 80% of source areas, while solid lines enclose the 50% of source areas.

2018a; Iwata et al. 2018), attributable to heterogeneous soil properties and moisture conditions, vegetation composition, and land use (Davidson et al. 2016; Parmentier et al. 2011; Chamberlain et al. 2018). Furthermore, there is evidence that traditionally unmeasured surfaces (i.e., tree stems) are important sources of CH_4 to the atmosphere and could explain spatial heterogeneity within ecosystems (Barba et al. 2019). Accurately representing spatial heterogeneity and the relative fraction of uplands and wetlands is imperative for interpreting and predicting CH_4 emissions within many ecosystems, and for upscaling flux measurements regionally and globally as wetlands are hot spots for carbon cycling (Treat et al. 2018a; Tuovinen et al. 2019; Rößger et al. 2019). Flux footprint analysis characterizing the fractional coverage of the dominant surface types, particularly the fraction of open water and aerenchymatous plants, is important for interpreting EC CH_4 flux measurements and quantifying annual CH_4 budgets at spatially heterogeneous sites (Franz et al. 2016; Helbig et al. 2017a; Jammert et al. 2017) (Fig. 11). This integration can be achieved by combining CH_4 measurements, flux footprint analysis, and near-surface

TABLE A1. The ecosystem type is based on the classification of Olefeldt et al. (2013) and Treat et al. (2018b). Biome was based on the classification of Olson et al. (2001) and extracted using site coordinates. Vegetation type was based on the International Geosphere-Biosphere Programme (IGBP) definition. Salinity regime includes freshwater (FW) or saltwater (SW) wetlands. Disturbance is based on the classification of Turetsky et al. (2014). Data from all sites are publicly available, primarily through AmeriFlux and the European Database Cluster, and in a few cases, through other databases/repositories. Site DOIs are specified where applicable.

Site ID	Site name	Country	Lat (°N)	Lon (°E)	Biome	IGBP
US-JCs	Wet sedge tundra	U.S.	68.606	-149.311	Tundra	WET
SE-St1	Stordalen grassland (mire)	Sweden	68.350	19.050	Tundra	WET
SE-Sto	Stordalen Palsa bog	Sweden	68.356	19.050	Tundra	WET
RU-Vrk	Seida/Vorkuta	Russia	67.055	62.940	Tundra	WET
RU-Ch2	Chersky reference	Russia	68.617	161.351	Tundra	WET
RU-Che	Chersky	Russia	68.613	161.341	Tundra	WET
RU-SAM	Samoylov	Russia	72.374	126.496	Tundra	WET
US-NGB	NGEE Barrow	U.S.	71.280	-156.609	Tundra	WET
US-Beo	Barrow	U.S.	71.281	-156.612	Tundra	WET
US-Bes	Barrow	U.S.	71.281	-156.596	Tundra	WET
US-Atq	Atqasuk	U.S.	70.470	-157.409	Tundra	WET
US-Ivo	Ivotuk	U.S.	68.486	-155.750	Tundra	WET
—	Black spruce forest	U.S.	64.700	-148.320	Boreal forests/taiga	ENF
—	Rich fen	U.S.	64.704	-148.313	Boreal forests/taiga	WET
—	Thermokarst collapse scar bog	U.S.	64.700	-148.320	Boreal forests/taiga	WET
FI-Lom	Lompolojankka	Finland	67.997	24.209	Boreal forests/taiga	WET
SE-Deg	Degero	Sweden	64.182	19.557	Boreal forests/taiga	WET
CA-SCC	Scotty Creek—Peat plateau/collapse scar	Canada	61.308	-121.299	Boreal forests/taiga	ENF
CA-SCB	Scotty Creek bog	Canada	61.309	-121.299	Boreal forests/taiga	WET
US-NGC	NGEE Arctic Council	U.S.	64.861	-163.701	Boreal forests/taiga	WET
US-Uaf	University of Alaska Fairbanks	U.S.	64.866	-147.856	Boreal forests/taiga	WET
FI-Sii	Siikaneva I (FI-Sii)	Finland	61.833	24.193	Boreal forests/taiga	WET
FI-Si2	Siikaneva II	Finland	61.837	24.170	Boreal forests/taiga	WET
US-Myb	Mayberry wetland	U.S.	38.050	-121.765	Temperate	WET
US-Sne	Sherman Island restored wetland	U.S.	38.037	-121.755	Temperate	WET
US-Tw1	Twitchell west pond wetland	U.S.	38.107	-121.647	Temperate	WET
US-Tw4	Twitchell east end wetland	U.S.	38.103	-121.641	Temperate	WET
US-Twt	Twitchell rice	U.S.	38.109	-121.653	Temperate	CRO - Rice
US-Bi2	Bouldin Island corn	U.S.	38.109	-121.535	Temperate	CRO - Other
US-Bi1	Bouldin Island alfalfa	U.S.	38.102	-121.504	Temperate	CRO - Other
US-Snd	Sherman Island	U.S.	38.037	-121.754	Temperate	CRO - Other
US-OWC	Old Woman Creek	U.S.	41.380	-82.512	Temperate	WET
US-Orv	Olentangy River Wetland Research Park	U.S.	40.020	-83.018	Temperate	WET
NZ-Kop	Kopuatai	New Zealand	-37.388	175.554	Temperate	WET
IT-Cas	Castellaro	Italy	45.070	8.718	Temperate	CRO - Rice
US-WPT	Winous Point north marsh	U.S.	41.465	-82.996	Temperate	WET
US-CRT	Curtrice Walker-Berger cropland	U.S.	41.628	-83.347	Temperate	CRO - Other
US-Los	Lost Creek	U.S.	46.083	-89.979	Temperate	WET
JP-Mse	Mase paddy flux site (MSE)	Japan	36.054	140.027	Temperate	CRO - Rice
JP-Swl	Suwa Lake site	Japan	36.047	138.108	Temperate	WAT
IT-BCi	Borgo Cioffi	Italy	40.524	14.957	Temperate	CRO - Other
—	Hongyuan	China	32.800	102.550	Temperate	GRA
US-NC4	NC Alligator River	U.S.	35.788	-75.904	Temperate	WET
DE-SfN	Schechenfilz Nord	Germany	47.806	11.328	Temperate	WET
US-Ho1	Howland Forest (main tower)	U.S.	45.204	-68.740	Temperate	ENF
US-HRA	Humnoke farm rice field AWD, United States	U.S.	34.585	-91.752	Temperate	CRO - Rice
US-HRC	Humnoke farm rice field conventional, United States	U.S.	34.589	-91.752	Temperate	CRO - Rice
KR-CRK	Cheorwon rice paddy	South Korea	38.201	127.251	Temperate	CRO - Rice
DE-Zrk	Zarnekow	Germany	53.876	12.889	Temperate	WET
DE-Dgw	Dagowsee	Germany	53.151	13.054	Temperate	WAT
US-MRM	Marsh Resource Meadowlands Mitigation Bank	U.S.	40.816	-74.044	Temperate	WET
—	Bog Lake peatland	U.S.	47.530	-93.470	Temperate	WET
—	MacArthur Agro-Ecology Research Center	U.S.	27.163	-81.187	Temperate	CRO - Other
JP-BBY	Bibai bog	Japan	43.323	141.811	Temperate	WET
US-Stj	St. Jones Reserve	U.S.	39.088	-75.437	Temperate	WET
US-Srr	Suisun marsh—Rush Ranch	U.S.	38.201	-122.026	Temperate	WET
AT-Neu	Neustift	Austria	47.117	11.318	Temperate	GRA
US-LA2	Salvador WMA freshwater marsh	U.S.	29.859	-90.287	Tropical and subtropical	WET
US-LA1	Pointe-aux-Chenes brackish marsh	U.S.	29.501	-90.445	Tropical and subtropical	WET
MY-MLM	Maludam	Malaysia	1.454	111.149	Tropical and subtropical	WET

Ecosystem type	Wetland		Site PI	Data DOI/location
	Salinity	disturbance		
Wet tundra	FW	Undisturbed	Eugenie Euskirchen	DOI:10.17190/AMF/1246130
Fen	FW	Undisturbed	Thomas Friborg	European Fluxes Database Cluster
Bog	FW	Undisturbed	Thomas Friborg	European Fluxes Database Cluster
Wet tundra	FW	Undisturbed	Thomas Friborg	European Fluxes Database Cluster
Wet tundra	FW	Undisturbed	Mathias Goeckede	European Fluxes Database Cluster
Wet tundra	FW	Drying	Mathias Goeckede	European Fluxes Database Cluster
Wet tundra	FW	Undisturbed	Torsten Sachs	European Fluxes Database Cluster
Wet tundra	FW	Undisturbed	Margaret Torn	DOI:10.17190/AMF/1436326
Wet tundra	FW	Undisturbed	Donatella Zona	AmeriFlux
Wet tundra	FW	Undisturbed	Donatella Zona	AmeriFlux
Wet tundra	FW	Undisturbed	Donatella Zona	DOI:10.17190/AMF/1246029
Wet tundra	FW	Undisturbed	Donatella Zona	DOI:10.17190/AMF/1246067
Upland	—	—	Eugenie Euskirchen	www.lter.uaf.edu/data/data-detail/id/708
Fen	FW	Undisturbed	Eugenie Euskirchen	www.lter.uaf.edu/data/data-detail/id/708
Bog	FW	Undisturbed	Eugenie Euskirchen	www.lter.uaf.edu/data/data-detail/id/708
Fen	FW	Undisturbed	Annalea Lohila	European Fluxes Database Cluster
Fen	FW	Undisturbed	Matthias Peichl, Mats Nilsson	European Fluxes Database Cluster
Peat plateau	FW	—	Oliver Sonnentag	DOI:10.17190/AMF/1480303
Bog	FW	Undisturbed	Oliver Sonnentag	AmeriFlux
Wet tundra	FW	Undisturbed	Margaret Torn	AmeriFlux
Bog	FW	Undisturbed	Masahito Ueyama	DOI:10.17190/AMF/1480322
Fen	FW	Undisturbed	Timo Vesala, Ivan Mammarella	European Fluxes Database Cluster
Bog	FW	Undisturbed	Timo Vesala, Ivan Mammarella	European Fluxes Database Cluster
Marsh	FW	Wetting	Dennis Baldocchi	DOI:10.17190/AMF/1246139
Marsh	FW	Wetting	Dennis Baldocchi	DOI:10.17190/AMF/1418684
Marsh	FW	Wetting	Dennis Baldocchi	DOI:10.17190/AMF/1246147
Marsh	FW	Wetting	Dennis Baldocchi	DOI:10.17190/AMF/1246148
Rice	FW	—	Dennis Baldocchi	DOI:10.17190/AMF/1246151
Drained/agricultural wetland	FW	Drying	Dennis Baldocchi	DOI:10.17190/AMF/1419513
Drained/agricultural wetland	FW	Drying	Dennis Baldocchi	DOI:10.17190/AMF/1480317
Drained/agricultural wetland	FW	Drying	Dennis Baldocchi	DOI:10.17190/AMF/1246094
Marsh	FW	Undisturbed	Gil Bohrer	DOI:10.17190/AMF/1246094
Marsh	FW	Undisturbed	Gil Bohrer	DOI:10.17190/AMF/1246135
Bog	FW	Undisturbed	Dave Campbell	https://researchcommons.waikato.ac.nz/handle/10289/11393
Rice	FW	—	Alessandro Cescatti	European Fluxes Database Cluster
Marsh	FW	Wetting	Jiquan Chen, Housen Chu	DOI:10.17190/AMF/1246155
Upland	—	—	Jiquan Chen, Housen Chu	DOI:10.17190/AMF/1246156
Fen	FW	Undisturbed	Ankur Desai	DOI:10.17190/AMF/1246071
Rice	FW	—	Akira Miyata	European Fluxes Database Cluster
Waterbody	FW	Undisturbed	Hiroki lwata	European Fluxes Database Cluster
Upland	—	—	Vincenzo Magliulo	European Fluxes Database Cluster
Upland	—	—	Shuli Niu	European Fluxes Database Cluster
Swamp	FW	Undisturbed	Asko Noormets	DOI:10.17190/AMF/1480314
Bog	FW	Undisturbed	Hans Peter Schmid	European Fluxes Database Cluster
Upland	—	—	Andrew Richardson	DOI:10.17190/AMF/1246061
Rice	FW	—	Benjamin Runkle	AmeriFlux
Rice	FW	—	Benjamin Runkle	AmeriFlux
Rice	FW	—	Youngryel Ryu, Minseok Kang	European Fluxes Database Cluster
Fen	FW	Wetting	Torsten Sachs	European Fluxes Database Cluster
Waterbody	FW	Undisturbed	Torsten Sachs	European Fluxes Database Cluster
Salt marsh	SW	Wetting	Karina Schäfer	AmeriFlux
Fen	FW	Undisturbed	Shahi Verma	AmeriFlux
Drained/agricultural wetland	FW	Drying	Jed Sparks, Samuel Chamberlain	AmeriFlux
Bog	FW	Undisturbed	Masahito Ueyama	European Fluxes Database Cluster
Salt marsh	SW	Undisturbed	Rodrigo Vargas	DOI:10.17190/AMF/1480316
Salt marsh	SW	Undisturbed	Lisamarie Windham-Myers	DOI:10.17190/AMF/1418685
Upland	—	—	Georg Wohlfahrt	European Fluxes Database Cluster
Marsh	FW	Undisturbed	Ken Krauss	AmeriFlux
Salt marsh	SW	Undisturbed	Ken Krauss	AmeriFlux
Swamp	FW	Undisturbed	Angela Tang	DOI:10.5281/zenodo.1161966

(e.g., phenocams) and/or high-resolution drone or satellite remote sensing data, and should be common practice for all sites measuring CH₄ fluxes.

Spatial variability in ecosystem-scale CH₄ flux can further be examined by combining chamber and EC measurements, including manual and autochambers, multitower approaches, and airborne flux measurements (Peltola et al. 2015; Zona et al. 2016; Helbig et al. 2017a; Wolfe et al. 2018; Kohnert et al. 2018; Lai et al. 2014; McNicol et al. 2017). Integrating additional observations such as information on microbial communities, isotopic measurements, and laboratory incubation observations along with chamber and EC CH₄ flux measurements can further help explain CH₄ dynamics across scales (Angle et al. 2017; Chamberlain et al. 2018; Yang et al. 2017). However, as discussed above, additional research is needed to reconcile differences in fluxes measured across scales (Gioli et al. 2004; Holm et al. 2016; Meijide et al. 2011). Explicitly considering source area composition and spatial heterogeneity will provide enhanced process-based understanding of CH₄ fluxes and improve upscaled regional and global estimates of CH₄ emissions, which can help reconcile the discrepancy between bottom-up and top-down budgets (Saunois et al. 2016a; Morin et al. 2017; Davidson et al. 2016).

More sites in key regions. We expect the number of flux towers measuring CH₄ fluxes will continue to grow (Chu et al. 2017; Pastorello et al. 2017; Morin 2018), but our compilation of EC CH₄ flux sites highlights key underrepresented regions where future flux towers are needed or where more efforts are needed for existing but nonreporting towers to contribute to FLUXNET (Fig. 1). As noted previously, notable gaps include both tropical and subtropical regions, as well as eastern Canada, and the boreal forests of Russia. Figure 1 also provides guidance on where new towers could be strategically located to help reconcile differences between top-down and bottom-up estimates of wetland CH₄ emissions. In particular, substantial disagreements between top-down and bottom-up estimates are found over the Congo basin, the Inner Niger delta, the Orinoco River delta, the Marañón–Ucayali palm swamps, the Pantanal, the Ganges–Brahmaputra delta, Sumatra, the western Siberian lowlands, and the Hudson Bay lowlands (Fig. 1). However, the placement of new towers is a strong function of the scientific question being asked and research funding priorities, and therefore the optimal tower network could be different for different applications (Mahecha et al. 2017; Papale et al. 2015; Villarreal et al. 2018).

Better understanding and representing processes. One of the biggest challenges for understanding ecosystem functioning is resolving overlapping, asynchronous (i.e., lagged) and nonlinear processes (Sturtevant et al. 2016). This challenge is particularly relevant for interpreting continuous, ecosystem-scale measurements of CH₄ exchange where scale-specific, nonlinear, and lagged processes may dominate (Franz et al. 2016; Sturtevant et al. 2016; Knox et al. 2018). For instance, CH₄ emission responses to water table fluctuation can be nonlinear and lagged on the order of days to months (Goodrich et al. 2015; Sturtevant et al. 2016). CH₄ flux has also been observed to lag GPP by hours to days (Rinne et al. 2018; Hatala et al. 2012). Adequately representing these dynamics in process models is important, and further research is needed to better characterize the complex and nonlinear processes influencing ecosystem-scale CH₄ exchange across time scales.

The complex nature of CH₄ flux dynamics requires moving beyond traditional linear correlation and regression, and using methods such as wavelets, information theory, and Granger causality that are more tailored to address scale, nonlinearity, and lags directly (Stoy et al. 2005; Vargas et al. 2011; Schäfer et al. 2014; Knox et al. 2016; Detto et al. 2012). Through a USGS Powell Center working group activity, we will continue to investigate controls on CH₄ emissions within and across wetland types. To further explore interactions between ecosystem-scale CH₄ exchange and drivers across time scales, wavelet analysis will be combined with information theory to explore biosphere–atmosphere interactions regardless of form or asynchrony (Sturtevant et al. 2016; Knox et al. 2018; Chamberlain et al. 2018). By coupling wavelet decomposition with information theory, future research will investigate key controls on CH₄ fluxes across time scales, as well as the importance of nonlinearities and lags in predicting CH₄ flux dynamics. Future research will also use the global CH₄ database to parameterize and benchmark the performance of land surface models of global CH₄ emissions, providing a unique opportunity for informing and validating biogeochemical models.

Coordinating, organizing and improving the integration of CH₄ fluxes in regional networks and ultimately FLUXNET will bring us one step closer to achieving the goal of providing flux information “everywhere and all of the time” (Baldocchi 2008). In the long term, we hope to integrate the global eddy covariance CH₄ database with other methods for measuring CH₄ fluxes, such as chamber, aircraft, and satellite measurements. By integrating CH₄ flux

measurements, remote sensing, and modeling, we aim to better characterize CH₄ emissions from terrestrial ecosystems and ultimately reduce uncertainties in the global CH₄ cycle.

ACKNOWLEDGMENTS. This study was supported by the Gordon and Betty Moore Foundation through Grant GBMF5439 “Advancing Understanding of the Global Methane Cycle” to Stanford University supporting the Methane Budget activity for the Global Carbon Project (globalcarbonproject.org). This work was also conducted as a part of the Wetland FLUXNET Synthesis for Methane Working Group supported by the John Wesley Powell Center for Analysis and Synthesis of the U.S. Geological Survey. We acknowledge the following AmeriFlux sites for their data records: CA-SCC, CA-SCB, U.S.-Beo, U.S.-Bes, U.S.-Atq, U.S.-Ivo, U.S.-ICs, U.S.-NGB, U.S.-NGC, U.S.-Los, U.S.-NC4, U.S.-HRA, U.S.-HRC, U.S.-Myb, U.S.-Sne, U.S.-Tw1, U.S.-Tw4, U.S.-Twt, U.S.-Bi2, U.S.-Bi1, U.S.-Snd, U.S.-OWC, U.S.-ORv, U.S.-WPT, U.S.-CRT, U.S.-MRM, U.S.-Srr, U.S.-Uaf, U.S.-Ho1, U.S.-Stj, U.S.-LA2, U.S.-LA1. In addition, funding for AmeriFlux data resources were provided by the U.S. Department of Energy’s Office of Science. BRKR was supported by NSF Award 1752083. WCO and DZ acknowledge support from NSF 1204263 and 1702797; NASA ABoVE NNX15AT74A, NNX16AF94A, and NNX17AC61A; NOAA EPP NA16SEC4810008; EU Horizon 2020 No. 629 727890; and NERC UK NE/P002552/1. TFK and HC acknowledge support from the AmeriFlux Management Project. Any use of trade, firm, or product names is for descriptive purposes only and does not imply endorsement by the U.S. government. DP, IM, and TV thank the European Union for supporting the RINGO project funded by the Horizon 2020 Research and Innovation Programme under Grant Agreement 730944. The authors also thank Claire Treat, Nigel Roulet, and another anonymous reviewer for their helpful comments to improve the manuscript.

APPENDIX: SITES CURRENTLY INCLUDED IN THE DATABASE. Table A1 presents characteristics of sites currently included in the database.

REFERENCES

Anderson, D. E., S. B. Verma, and N. J. Rosenberg, 1984: Eddy correlation measurements of CO₂, latent heat, and sensible heat fluxes over a crop surface. *Bound.-Layer Meteor.*, **29**, 263–272, <https://doi.org/10.1007/BF00119792>.

Anderson, F. E., and Coauthors, 2016: Variation of energy and carbon fluxes from a restored temperate freshwater wetland and implications

for carbon market verification protocols. *J. Geophys. Res. Biogeosci.*, **121**, 777–795, <https://doi.org/10.1002/2015JG003083>.

Angle, J. C., and Coauthors, 2017: Methanogenesis in oxygenated soils is a substantial fraction of wetland methane emissions. *Nat. Commun.*, **8**, 1567, <https://doi.org/10.1038/s41467-017-01753-4>.

Arcus, V. L., E. J. Prentice, J. K. Hobbs, A. J. Mulholland, M. W. Van Der Kamp, C. R. Pudney, E. J. Parker, and L. A. Schipper, 2016: On the temperature dependence of enzyme-catalyzed rates. *Biochemistry*, **55**, 1681–1688, <https://doi.org/10.1021/acs.biochem.5b01094>.

Aubinet, M., and Coauthors, 1999: Estimates of the annual net carbon and water exchange of forests: The EUROFLUX methodology. *Adv. Ecol. Res.*, **30**, 113–175, [https://doi.org/10.1016/S0065-2504\(08\)60018-5](https://doi.org/10.1016/S0065-2504(08)60018-5).

—, T. Vesala, and D. Papale, 2012: *Eddy Covariance: A Practical Guide to Measurement and Data Analysis*. Springer, 438 pp.

Baldocchi, D. D., 2003: Assessing the eddy covariance technique for evaluating carbon dioxide exchange rates of ecosystems: Past, present and future. *Global Change Biol.*, **9**, 479–492, <https://doi.org/10.1046/j.1365-2486.2003.00629.x>.

—, 2008: ‘Breathing’ of the terrestrial biosphere: Lessons learned from a global network of carbon dioxide flux measurement systems. *Aust. J. Bot.*, **56**, 1–26, <https://doi.org/10.1071/BT07151>.

—, 2014: Measuring fluxes of trace gases and energy between ecosystems and the atmosphere—The state and future of the eddy covariance method. *Global Change Biol.*, **20**, 3600–3609, <https://doi.org/10.1111/gcb.12649>.

Barba, J., and Coauthors, 2019: Methane emissions from tree stems: A new frontier in the global carbon cycle. *New Phytol.*, **222**, 18–28, <https://doi.org/10.1111/nph.15582>.

Bartlett, K. B., and R. C. Harriss, 1993: Review and assessment of methane emissions from wetlands. *Chemosphere*, **26**, 261–320, [https://doi.org/10.1016/0045-6535\(93\)90427-7](https://doi.org/10.1016/0045-6535(93)90427-7).

Bastviken, D., L. J. Tranvik, J. A. Downing, P. M. Crill, and A. Enrich-Prast, 2011: Freshwater methane emissions offset the continental carbon sink. *Science*, **331**, 50, <https://doi.org/10.1126/science.1196808>.

Bates, D., M. Machler, B. Bolker, and S. Walker, 2015: Fitting linear mixed-effects models using lme4. *J. Stat. Software*, **67** (1), <https://doi.org/10.18637/jss.v067.i01>.

Bousquet, P., and Coauthors, 2006: Contribution of anthropogenic and natural sources to atmospheric methane variability. *Nature*, **443**, 439–443, <https://doi.org/10.1038/nature05132>.

- Bridgman, S. D., H. Cadillo-Quiroz, J. K. Keller, and Q. Zhuang, 2013: Methane emissions from wetlands: Biogeochemical, microbial, and modeling perspectives from local to global scales. *Global Change Biol.*, **19**, 1325–1346, <https://doi.org/10.1111/gcb.12131>.
- Brix, H., B. K. Sorrell, and P. T. Orr, 1992: Internal pressurization and convective gas flow in some emergent freshwater macrophytes. *Limnol. Oceanogr.*, **37**, 1420–1433, <https://doi.org/10.4319/lo.1992.37.7.1420>.
- Bubier, J., T. Moore, K. Savage, and P. Crill, 2005: A comparison of methane flux in a boreal landscape between a dry and a wet year. *Global Biogeochem. Cycles*, **19**, GB1023, <https://doi.org/10.1029/2004GB002351>.
- Carmichael, M. J., E. S. Bernhardt, S. L. Bräuer, and W. K. Smith, 2014: The role of vegetation in methane flux to the atmosphere: Should vegetation be included as a distinct category in the global methane budget? *Biogeochemistry*, **119**, 1–24, <https://doi.org/10.1007/s10533-014-9974-1>.
- Castro-Morales, K., T. Kleinen, S. Kaiser, S. Zaehle, F. Kit-Tler, M. J. Kwon, C. Beer, and M. Göckede, 2018: Year-round simulated methane emissions from a permafrost ecosystem in northeast Siberia. *Biogeosciences*, **15**, 2691–2722, <https://doi.org/10.5194/bg-15-2691-2018>.
- Cazelles, B., M. Chavez, D. Berteaux, F. Ménard, J. O. Vik, S. Jenouvrier, and N. C. Stenseth, 2008: Wavelet analysis of ecological time series. *Oecologia*, **156**, 287–304, <https://doi.org/10.1007/s00442-008-0993-2>.
- Chamberlain, S. D., and Coauthors, 2018: Soil properties and sediment accretion modulate methane fluxes from restored wetlands. *Global Change Biol.*, **24**, 4107–4121, <https://doi.org/10.1111/gcb.14124>.
- Chanton, J. P., G. J. Whiting, J. D. Happell, and G. Gerard, 1993: Contrasting rates and diurnal patterns of methane emission from emergent aquatic macrophytes. *Aquat. Bot.*, **46**, 111–128, [https://doi.org/10.1016/0304-3770\(93\)90040-4](https://doi.org/10.1016/0304-3770(93)90040-4).
- , —, N. E. Blair, C. W. Lindau, and P. K. Bollich, 1997: Methane emission from rice: Stable isotopes, diurnal variations, and CO₂ exchange. *Global Biogeochem. Cycles*, **11**, 15–27, <https://doi.org/10.1029/96GB03761>.
- Chen, Y.-H., and R. G. Prinn, 2006: Estimation of atmospheric methane emissions between 1996 and 2001 using a three-dimensional global chemical transport model. *J. Geophys. Res.*, **111**, D10307, <https://doi.org/10.1029/2005JD006058>.
- Christensen, T. R., and Coauthors, 2003: Factors controlling large scale variations in methane emissions from wetlands. *Geophys. Res. Lett.*, **30**, 1414, <https://doi.org/10.1029/2002GL016848>.
- Chu, H., J. Chen, J. F. Gottgens, Z. Ouyang, R. John, K. Czajkowski, and R. Becker, 2014: Net ecosystem methane and carbon dioxide exchanges in a Lake Erie coastal marsh and a nearby cropland. *J. Geophys. Res. Biogeosci.*, **119**, 722–740, <https://doi.org/10.1002/2013JG002520>.
- , D. D. Baldocchi, R. John, S. Wolf, and M. Reichstein, 2017: Fluxes all of the time? A primer on the temporal representativeness of FLUXNET. *J. Geophys. Res. Biogeosci.*, **122**, 289–307, <https://doi.org/10.1002/2016JG003576>.
- Davidson, S. J., V. L. Sloan, G. K. Phoenix, R. Wagner, J. P. Fisher, W. C. Oechel, and D. Zona, 2016: Vegetation type dominates the spatial variability in CH₄ emissions across multiple Arctic tundra landscapes. *Ecosystems*, **19**, 1116–1132, <https://doi.org/10.1007/s10021-016-9991-0>.
- Dean, J. F., and Coauthors, 2018: Methane feedbacks to the global climate system in a warmer world. *Rev. Geophys.*, **56**, 207–250, <https://doi.org/10.1002/2017RG000559>.
- Dengel, S., D. Zona, T. Sachs, M. Aurela, M. Jammet, F. J. W. Parmentier, W. Oechel, and T. Vesala, 2013: Testing the applicability of neural networks as a gap-filling method using CH₄ flux data from high latitude wetlands. *Biogeosciences*, **10**, 8185–8200, <https://doi.org/10.5194/bg-10-8185-2013>.
- Desai, A. R., and Coauthors, 2015: Landscape-level terrestrial methane flux observed from a very tall tower. *Agric. For. Meteorol.*, **201**, 61–75, <https://doi.org/10.1016/j.agrformet.2014.10.017>.
- Desjardins, R. L., 1974: A technique to measure CO₂ exchange under field conditions. *Int. J. Biometeor.*, **18**, 76–83, <https://doi.org/10.1007/BF01450667>.
- Detto, M., A. Molini, G. Katul, P. Stoy, S. Palmroth, and D. Baldocchi, 2012: Causality and persistence in ecological systems: A nonparametric spectral Granger causality approach. *Amer. Nat.*, **179**, 524–535, <https://doi.org/10.1086/664628>.
- Euskirchen, E. S., M. S. Bret-Harte, G. R. Shaver, C. W. Edgar, and V. E. Romanovsky, 2017: Long-term release of carbon dioxide from Arctic tundra ecosystems in Alaska. *Ecosystems*, **20**, 960–974, <https://doi.org/10.1007/S10021-016-0085-9>.
- Fan, S. M., and Coauthors, 1992: Micrometeorological measurements of CH₄ and CO₂ exchange between the atmosphere and subarctic tundra. *J. Geophys. Res.*, **97**, 16627–16643, <https://doi.org/10.1029/91JD02531>.
- Franz, D., F. Koebsch, E. Larmanou, J. Augustin, and T. Sachs, 2016: High net CO₂ and CH₄ release at a eutrophic shallow lake on a formerly drained fen. *Biogeosciences*, **13**, 3051–3070, <https://doi.org/10.5194/bg-13-3051-2016>.
- Gielen, B., and Coauthors, 2018: Ancillary vegetation measurements at ICOS ecosystem stations. *Int.*

- Agrophys.*, **10**, 645–664, <https://doi.org/10.1515/INTAG-2017-0048>.
- Gioli, B., and Coauthors, 2004: Comparison between tower and aircraft-based eddy covariance fluxes in five European regions. *Agric. For. Meteorol.*, **127**, 1–16, <https://doi.org/10.1016/j.agrformet.2004.08.004>.
- Goodrich, J. P., D. I. Campbell, N. T. Roulet, M. J. Clearwater, and L. A. Schipper, 2015: Overriding control of methane flux temporal variability by water table dynamics in a Southern Hemisphere, raised bog. *J. Geophys. Res. Biogeosci.*, **120**, 819–831, <https://doi.org/10.1002/2014JG002844>.
- Grant, R. F., and N. T. Roulet, 2002: Methane efflux from boreal wetlands: Theory and testing of the ecosystem model Ecosys with chamber and tower flux measurements. *Global Biogeochem. Cycles*, **16**, 1054, <https://doi.org/10.1029/2001GB001702>.
- Harris, I., P. D. Jones, T. J. Osborn, and D. H. Lister, 2014: Updated high-resolution grids of monthly climatic observations—The CRU TS3.10 dataset. *Int. J. Climatol.*, **34**, 623–642, <https://doi.org/10.1002/joc.3711>.
- Hatala, J. A., M. Detto, and D. D. Baldocchi, 2012: Gross ecosystem photosynthesis causes a diurnal pattern in methane emission from rice. *Geophys. Res. Lett.*, **39**, L06409, <https://doi.org/10.1029/2012GL051303>.
- Helbig, M., L. E. Chasmer, N. C. Kljun, W. L. Quinton, C. C. Treat, and O. Sonnentag, 2017a: The positive net radiative greenhouse gas forcing of increasing methane emissions from a thawing boreal forest-wetland landscape. *Global Change Biol.*, **23**, 2413–2427, <https://doi.org/10.1111/gcb.13520>.
- , W. L. Quinton, and O. Sonnentag, 2017b: Warmer spring conditions increase annual methane emissions from a boreal peat landscape with sporadic permafrost. *Environ. Res. Lett.*, **12**, 115009, <https://doi.org/10.1088/1748-9326/aa8c85>.
- Hendriks, D. M. D., J. van Huissteden, and A. J. Dolman, 2010: Multi-technique assessment of spatial and temporal variability of methane fluxes in a peat meadow. *Agric. For. Meteorol.*, **150**, 757–774, <https://doi.org/10.1016/j.agrformet.2009.06.017>.
- Hollinger, A. D., and A. D. Richardson, 2005: Uncertainty in eddy covariance measurements and its application to physiological models. *Tree Physiol.*, **25**, 873–885, <https://doi.org/10.1093/treephys/25.7.873>.
- Holm, G. O., B. C. Perez, D. E. McWhorter, K. W. Krauss, D. J. Johnson, R. C. Raynie, and C. J. Killebrew, 2016: Ecosystem level methane fluxes from tidal freshwater and brackish marshes of the Mississippi River delta: Implications for coastal wetland carbon projects. *Wetlands*, **36**, 401–413, <https://doi.org/10.1007/s13157-016-0746-7>.
- Hufkens, K., and Coauthors, 2018: Assimilating phenology datasets automatically across ICOS ecosystem stations. *Int. Agrophys.*, **32**, 677–687, <https://doi.org/10.1515/intag-2017-0050>.
- Iwata, H., R. Hirata, Y. Takahashi, Y. Miyabara, M. Itoh, and K. Iizuka, 2018: Partitioning eddy-covariance methane fluxes from a shallow lake into diffusive and ebullitive fluxes. *Bound.-Layer Meteorol.*, **169**, 413–428, <https://doi.org/10.1007/s10546-018-0383-1>.
- Jackowicz-Korczyński, M., T. R. Christensen, K. Bäckstrand, P. Crill, T. Friborg, M. Mastepanov, and L. Ström, 2010: Annual cycle of methane emission from a subarctic peatland. *J. Geophys. Res.*, **115**, G02009, <https://doi.org/10.1029/2008JG000913>.
- Jammet, M., S. Dengel, E. Kettner, F.-J. W. Parmentier, M. Wik, P. Crill, and T. Friborg, 2017: Year-round CH₄ and CO₂ flux dynamics in two contrasting freshwater ecosystems of the subarctic. *Biogeosciences*, **14**, 5189–5216, <https://doi.org/10.5194/bg-14-5189-2017>.
- Joabsson, A., T. R. Christensen, and B. Wallén, 1999: Vascular plant controls on methane emissions from northern peatforming wetlands. *Trends Ecol. Evol.*, **14**, 385–388, [https://doi.org/10.1016/S0169-5347\(99\)01649-3](https://doi.org/10.1016/S0169-5347(99)01649-3).
- Jung, M., M. Reichstein, and A. Bondeau, 2009: Towards global empirical upscaling of FLUXNET eddy covariance observations: Validation of a model tree ensemble approach using a biosphere model. *Biogeosciences*, **6**, 2001–2013, <https://doi.org/10.5194/BG-6-2001-2009>.
- Kim, J., S. B. Verma, and D. P. Billesbach, 1999: Seasonal variation in methane emission from a temperate Phragmites-dominated marsh: Effect of growth stage and plant-mediated transport. *Global Change Biol.*, **5**, 433–440, <https://doi.org/10.1046/j.1365-2486.1999.00237.x>.
- Kittler, F., M. Heimann, O. Kolle, N. Zimov, S. Zimov, and M. Göckede, 2017: Long-term drainage reduces CO₂ uptake and CH₄ emissions in a Siberian permafrost ecosystem. *Global Biogeochem. Cycles*, **31**, 1704–1717, <https://doi.org/10.1002/2017GB005774>.
- Kljun, N., P. Calanca, M. W. Rotach, and H. P. Schmid, 2015: A simple two-dimensional parameterisation for flux footprint prediction (FFP). *Geosci. Model Dev.*, **8**, 3695–3713, <https://doi.org/10.5194/gmd-8-3695-2015>.
- Knox, S. H., C. Sturtevant, J. H. Matthes, L. Koteen, J. Verfaillie, and D. Baldocchi, 2015: Agricultural peatland restoration: Effects of land-use change on greenhouse gas (CO₂ and CH₄) fluxes in the Sacramento-San Joaquin delta. *Global Change Biol.*, **21**, 750–765, <https://doi.org/10.1111/gcb.12745>.
- , J. H. Matthes, C. Sturtevant, P. Y. Oikawa, J. Verfaillie, and D. Baldocchi, 2016: Biophysical

- controls on interannual variability in ecosystem-scale CO₂ and CH₄ exchange in a California rice paddy. *J. Geophys. Res. Biogeosci.*, **121**, 978–1001, <https://doi.org/10.1002/2015JG003247>.
- , L. Windham-Myers, F. Anderson, C. Sturtevant, and B. Bergamaschi, 2018: Direct and indirect effects of tides on ecosystem-scale CO₂ exchange in a brackish tidal marsh in Northern California. *J. Geophys. Res. Biogeosci.*, **123**, 787–806, <https://doi.org/10.1002/2017JG004048>.
- Koebisch, F., G. Jurasinski, M. Koch, J. Hofmann, and S. Glatzel, 2015: Controls for multi-scale temporal variation in ecosystem methane exchange during the growing season of a permanently inundated fen. *Agric. For. Meteorol.*, **204**, 94–105, <https://doi.org/10.1016/j.agrformet.2015.02.002>.
- Kohnert, K., B. Juhls, S. Muster, S. Antonova, A. Serafimovich, S. Metzger, J. Hartmann, and T. Sachs, 2018: Toward understanding the contribution of waterbodies to the methane emissions of a permafrost landscape on a regional scale—A case study from the Mackenzie delta, Canada. *Global Change Biol.*, **24**, 3976–3989, <https://doi.org/10.1111/gcb.14289>.
- Kormann, R., and F. X. Meixner, 2001: An analytical footprint model for non-neutral stratification. *Bound.-Layer Meteorol.*, **99**, 207–224, <https://doi.org/10.1023/A:1018991015119>.
- Krauss, K. W., and Coauthors, 2016: Component greenhouse gas fluxes and radiative balance from two deltaic marshes in Louisiana: Pairing chamber techniques and eddy covariance. *J. Geophys. Res. Biogeosci.*, **121**, 1503–1521, <https://doi.org/10.1002/2015JG003224>.
- Kwon, M. J., and Coauthors, 2017: Plants, microorganisms, and soil temperatures contribute to a decrease in methane fluxes on a drained Arctic floodplain. *Global Change Biol.*, **23**, 2396–2412, <https://doi.org/10.1111/gcb.13558>.
- Lai, D. Y. F., T. R. Moore, and N. T. Roulet, 2014: Spatial and temporal variations of methane flux measured by autochambers in a temperate ombrotrophic peatland. *J. Geophys. Res. Biogeosci.*, **119**, 864–880, <https://doi.org/10.1002/2013JG002410>.
- Lasslop, G., M. Reichsten, D. Papale, A. D. R. Richardson, A. Arneeth, A. Barr, P. Stoy, and G. Wohlfahrt, 2010: Separation of net ecosystem exchange into assimilation and respiration using a light response curve approach: Critical issues and global evaluation. *Global Change Biol.*, **16**, 187–208, <https://doi.org/10.1111/j.1365-2486.2009.02041.x>.
- Lehner, B., and P. Döll, 2004: Development and validation of a global database of lakes, reservoirs and wetlands. *J. Hydrol.*, **296**, 1–22, <https://doi.org/10.1016/j.jhydrol.2004.03.028>.
- Mahecha, M. D., and Coauthors, 2017: Detecting impacts of extreme events with ecological in situ monitoring networks. *Biogeosciences*, **14**, 4255–4277, <https://doi.org/10.5194/bg-14-4255-2017>.
- Marushchak, M. E., and Coauthors, 2016: Methane dynamics in the subarctic tundra: Combining stable isotope analyses, plot- and ecosystem-scale flux measurements. *Biogeosciences*, **13**, 597–608, <https://doi.org/10.5194/bg-13-597-2016>.
- MathWorks, 2018: MATLAB, version 9.5. MathWorks.
- McDermitt, D., and Coauthors, 2011: A new low-power, open-path instrument for measuring methane flux by eddy covariance. *Appl. Phys.*, **102B**, 391–405, <https://doi.org/10.1007/s00340-010-4307-0>.
- McNicol, G., C. S. Sturtevant, S. H. Knox, I. Dronova, D. D. Baldocchi, and W. L. Silver, 2017: Effects of seasonality, transport pathway, and spatial structure on greenhouse gas fluxes in a restored wetland. *Global Change Biol.*, **23**, 2768–2782, <https://doi.org/10.1111/GCB.13580>.
- McNorton, J., and Coauthors, 2016: Role of regional wetland emissions in atmospheric methane variability. *Geophys. Res. Lett.*, **43**, 11 433–11 444, <https://doi.org/10.1002/2016GL070649>.
- Meijide, A., G. Manca, I. Goded, V. Magliulo, P. di Tommasi, G. Seufert, and A. Cescatti, 2011: Seasonal trends and environmental controls of methane emissions in a rice paddy field in northern Italy. *Biogeosciences*, **8**, 3809–3821, <https://doi.org/10.5194/bg-8-3809-2011>.
- Melton, J. R., and Coauthors, 2013: Present state of global wetland extent and wetland methane modelling: Conclusions from a model inter-comparison project (WETCHIMP). *Biogeosciences*, **10**, 753–788, <https://doi.org/10.5194/bg-10-753-2013>.
- Mitsch, W. J., A. Nahlik, P. Wolski, B. Bernal, L. Zhang, and L. Ramberg, 2009: Tropical wetlands: Seasonal hydrologic pulsing, carbon sequestration, and methane emissions. *Wetlands Ecol. Manage.*, **18**, 573–586, <https://doi.org/10.1007/S11273-009-9164-4>.
- Moffat, A. M., and Coauthors, 2007: Comprehensive comparison of gap-filling techniques for eddy covariance net carbon fluxes. *Agric. For. Meteorol.*, **147**, 209–232, <https://doi.org/10.1016/j.agrformet.2007.08.011>.
- Morin, T. H., 2018: Advances in the eddy covariance approach to CH₄ monitoring over two and a half decades. *J. Geophys. Res. Biogeosci.*, **124**, 453–460, <https://doi.org/10.1029/2018JG004796>.
- , G. Bohrer, R. P. M. Frasson, L. Naor-Azreli, S. Mesi, K. C. Stefanik, and K. V. R. Schäfer, 2014a: Environmental drivers of methane fluxes from an urban temperate wetland park. *J. Geophys. Res. Biogeosci.*, **119**, 2188–2208, <https://doi.org/10.1002/2014JG002750>.

- , —, L. Naor-Azrieli, S. Mesi, W. T. Kenny, W. J. Mitsch, and K. V. R. Schäfer, 2014b: The seasonal and diurnal dynamics of methane flux at a created urban wetland. *Ecol. Eng.*, **72**, 74–83, <https://doi.org/10.1016/j.ecoleng.2014.02.002>.
- , —, K. C. Stefanik, A. C. Rey-Sanchez, A. M. Matheny, and W. J. Mitsch, 2017: Combining eddy-covariance and chamber measurements to determine the methane budget from a small, heterogeneous urban floodplain wetland park. *Agric. For. Meteorol.*, **237–238**, 160–170, <https://doi.org/10.1016/j.agrformet.2017.01.022>.
- Myhre, G., and Coauthors, 2013: Anthropogenic and natural radiative forcing. *Climate Change 2013: The Physical Science Basis*, T. F. Stocker et al., Eds., Cambridge University Press, 659–740.
- Nadeau, D. F., A. N. Rousseau, C. Coursolle, H. A. Margolis, and M. B. Parlange, 2013: Summer methane fluxes from a boreal bog in northern Quebec, Canada, using eddy covariance measurements. *Atmos. Environ.*, **81**, 464–474, <https://doi.org/10.1016/j.atmosenv.2013.09.044>.
- Nakagawa, S., and H. Schielzeth, 2013: A general and simple method for obtaining R^2 from generalized linear mixed-effects models. *Methods Ecol. Evol.*, **4**, 133–142, <https://doi.org/10.1111/j.2041-210x.2012.00261.x>.
- Nemitz, E., and Coauthors, 2018: Standardisation of eddy-covariance flux measurements of methane and nitrous oxide. *Int. Agrophys.*, **32**, 517–549, <https://doi.org/10.1515/intag-2017-0042>.
- Oikawa, P. Y., and Coauthors, 2017: Evaluation of a hierarchy of models reveals importance of substrate limitation for predicting carbon dioxide and methane exchange in restored wetlands. *J. Geophys. Res. Biogeosci.*, **122**, 145–167, <https://doi.org/10.1002/2016JG003438>.
- Olefelt, D., M. R. Turetsky, P. M. Crill, and A. D. McGuire, 2013: Environmental and physical controls on northern terrestrial methane emissions across permafrost zones. *Global Change Biol.*, **19**, 589–603, <https://doi.org/10.1111/gcb.12071>.
- Olson, D. M., and Coauthors, 2001: Terrestrial ecoregions of the world: A new map of life on Earth. *BioScience*, **51**, 933–938, [https://doi.org/10.1641/0006-3568\(2001\)051\[0933:TEOTWA\]2.0.CO;2](https://doi.org/10.1641/0006-3568(2001)051[0933:TEOTWA]2.0.CO;2).
- Op De Beek, M., and Coauthors, 2018: Soil-meteorological measurements at ICOS monitoring stations in terrestrial ecosystems. *Int. Agrophys.*, **32**, 619–631, <https://doi.org/10.1515/intag-2017-0041>.
- Pangala, S. R., and Coauthors, 2017: Large emissions from floodplain trees close the Amazon methane budget. *Nature*, **552**, 230–234, <https://doi.org/10.1038/nature24639>.
- Papale, D., D. Agarwal, D. Baldocchi, R. Cook, J. B. Fisher, and C. van Ingen, 2012: Database maintenance, data sharing policy, collaboration. *Eddy Covariance: A Practical Guide to Measurement and Data Analysis*, M. Aubinet, T. Vesala, and D. Papale, Eds., Springer, 399–424.
- , and Coauthors, 2015: Effect of spatial sampling from European flux towers for estimating carbon and water fluxes with artificial neural networks. *J. Geophys. Res. Biogeosci.*, **120**, 1941–1957, <https://doi.org/10.1002/2015JG002997>.
- Parmentier, F. J. W., J. Van Huissteden, M. K. Van Der Molen, G. Schaepman-Strub, S. A. Karsanaev, T. C. Maximov, and A. J. Dolman, 2011: Spatial and temporal dynamics in eddy covariance observations of methane fluxes at a tundra site in northeastern Siberia. *J. Geophys. Res.*, **116**, G03016, <https://doi.org/10.1029/2010JG001637>.
- Pastorello, G. Z., D. Papale, H. Chu, C. Trotta, D. Agarwal, E. Canfora, D. Baldocchi, and M. Torn, 2017: A new data set to keep a sharper eye on land-air exchanges. *Eos, Trans. Amer. Geophys. Union*, **98**, <https://doi.org/10.1029/2017EO071597>.
- Peltola, O., I. Mammarella, S. Haapanala, G. Burba, and T. Vesala, 2013: Field intercomparison of four methane gas analyzers suitable for eddy covariance flux measurements. *Biogeosciences*, **10**, 3749–3765, <https://doi.org/10.5194/bg-10-3749-2013>.
- , and Coauthors, 2014: Evaluating the performance of commonly used gas analysers for methane eddy covariance flux measurements: The InGOS inter-comparison field experiment. *Biogeosciences*, **11**, 3163–3186, <https://doi.org/10.5194/bg-11-3163-2014>.
- , and Coauthors, 2015: Studying the spatial variability of methane flux with five eddy covariance towers of varying height. *Agric. For. Meteorol.*, **214–215**, 456–472, <https://doi.org/10.1016/j.agrformet.2015.09.007>.
- , and Coauthors, 2019: Monthly gridded data product of northern wetland methane emissions based on upscaling eddy covariance observations. *Earth Syst. Sci. Data*, **11**, 1263–1289, <https://doi.org/10.5194/essd-11-1263-2019>.
- Petrescu, A. M. R., and Coauthors, 2015: The uncertain climate footprint of wetlands under human pressure. *Proc. Natl. Acad. Sci. USA*, **112**, 4594–4599, <https://doi.org/10.1073/pnas.1416267112>.
- Poffenbarger, H., B. Needelman, and J. P. Megonigal, 2011: Salinity influence on methane emissions from tidal marshes. *Wetlands*, **31**, 831–842, <https://doi.org/10.1007/s13157-011-0197-0>.
- Poulter, B., and Coauthors, 2017: Global wetland contribution to 2000–2012 atmospheric methane growth

- rate dynamics. *Environ. Res. Lett.*, **12**, 094013, <https://doi.org/10.1088/1748-9326/aa8391>.
- Pugh, C. A., D. E. Reed, A. R. Desai, and B. N. Sulman, 2018: Wetland flux controls: How does interacting water table levels and temperature influence carbon dioxide and methane fluxes in northern Wisconsin? *Biogeochemistry*, **137**, 15–25, <https://doi.org/10.1007/s10533-017-0414-x>.
- R Core Team, 2018: R: A language and environment for statistical computing. R Foundation for Statistical Computing, www.R-project.org/.
- Reichstein, M., and Coauthors, 2005: On the separation of net ecosystem exchange into assimilation and ecosystem respiration: Review and improved algorithm. *Global Change Biol.*, **11**, 1424–1439, <https://doi.org/10.1111/j.1365-2486.2005.001002.x>.
- Rey-Sanchez, A. C., T. H. Morin, K. C. Stefanik, K. Wrighton, and G. Bohrer, 2018: Determining total emissions and environmental drivers of methane flux in a Lake Erie estuarine marsh. *Ecol. Eng.*, **114**, 7–15, <https://doi.org/10.1016/j.ecoleng.2017.06.042>.
- Richardson, A. D., and D. Y. Hollinger, 2007: A method to estimate the additional uncertainty in gap-filled NEE resulting from long gaps in the CO₂ flux record. *Agric. For. Meteorol.*, **147**, 199–208, <https://doi.org/10.1016/j.agrformet.2007.06.004>.
- , and Coauthors, 2006: A multi-site analysis of random error in tower-based measurements of carbon and energy fluxes. *Agric. For. Meteorol.*, **136**, 1–18, <https://doi.org/10.1016/j.agrformet.2006.01.007>.
- , and Coauthors, 2008: Statistical properties of random CO₂ flux measurement uncertainty inferred from model residuals. *Agric. For. Meteorol.*, **148**, 38–50, <https://doi.org/10.1016/j.agrformet.2007.09.001>.
- , M. Aubinet, A. G. Barr, D. Y. Hollinger, A. Ibrom, G. Lasslop, and M. Reichstein, 2012: Uncertainty quantification. *Eddy Covariance: A Practical Guide to Measurement and Data Analysis*, M. Aubinet, T. Vesala, and D. Papale, Eds., Springer, 173–209.
- Riley, W. J., Z. M. Subin, D. M. Lawrence, S. C. Swenson, M. S. Torn, L. Meng, N. M. Mahowald, and P. Hess, 2011: Barriers to predicting changes in global terrestrial methane fluxes: Analyses using CLM4Me, a methane biogeochemistry model integrated in CESM. *Biogeosciences*, **8**, 1925–1953, <https://doi.org/10.5194/bg-8-1925-2011>.
- Rinne, J., T. Riutta, M. Pihlatie, M. Aurela, S. Haapanala, J.-P. Tuovinen, E.-S. Tuittila, and T. Vesala, 2007: Annual cycle of methane emission from a boreal fen measured by the eddy covariance technique. *Tellus*, **59B**, 449–457, <https://doi.org/10.1111/j.1600-0889.2007.00261.x>.
- , and Coauthors, 2018: Temporal variation of ecosystem scale methane emission from a boreal fen in relation to temperature, water table position, and carbon dioxide fluxes. *Global Biogeochem. Cycles*, **32**, 1087–1106, <https://doi.org/10.1029/2017GB005747>.
- Rößger, N., C. Wille, G. Veh, J. Boike, and L. Kutzbach, 2019: Scaling and balancing methane fluxes in a heterogeneous tundra ecosystem of the Lena River delta. *Agric. For. Meteorol.*, **266–267**, 243–255, <https://doi.org/10.1016/j.agrformet.2018.06.026>.
- Runkle, B. R. K., K. Suvoč, M. L. Reba, C. W. Reavis, S. F. Smith, Y.-L. Chiu, and B. Fong, 2019: Methane emission reductions from the alternate wetting and drying of rice fields detected using the eddy covariance method. *Environ. Sci. Technol.*, **53**, 671–681, <https://doi.org/10.1021/acs.est.8b05535>.
- Sachs, T., C. Wille, J. Boike, and L. Kutzbach, 2008: Environmental controls on ecosystem-scale CH₄ emission from polygonal tundra in the Lena River delta, Siberia. *J. Geophys. Res.*, **113**, G00A03, <https://doi.org/10.1029/2007JG000505>.
- Sass, R., 2003: CH₄ emissions from rice agriculture. Good practice guidance and uncertainty management in national greenhouse gas inventories, IPCC Rep., 399–417.
- Saunders, M., and Coauthors, 2018: Importance of reporting ancillary site characteristics, and management and disturbance information at ICOS stations. *Int. Agrophys.*, **32**, 457–469, <https://doi.org/10.1515/intag-2017-0040>.
- Saunio, M., and Coauthors, 2016a: The global methane budget 2000–2012. *Earth Syst. Sci. Data*, **8**, 697–751, <https://doi.org/10.5194/essd-8-697-2016>.
- , R. B. Jackson, P. Bousquet, B. Poulter, and J. G. Canadell, 2016b: The growing role of methane in anthropogenic climate change. *Environ. Res. Lett.*, **11**, 120207, <https://doi.org/10.1088/1748-9326/11/12/120207>.
- , and Coauthors, 2017: Variability and quasi-decadal changes in the methane budget over the period 2000–2012. *Atmos. Chem. Phys.*, **17**, 11 135–11 161, <https://doi.org/10.5194/acp-17-11135-2017>.
- Schäfer, K. V. R., R. Tripathee, F. Artigas, T. H. Morin, and G. Bohrer, 2014: Carbon dioxide fluxes of an urban tidal marsh in the Hudson-Raritan estuary. *J. Geophys. Res. Biogeosci.*, **119**, 2065–2081, <https://doi.org/10.1002/2014JG002703>.
- Schaller, C., F. Kittler, T. Foken, and M. Göckede, 2018: Characterisation of short-term extreme methane fluxes related to non-turbulent mixing above an Arctic permafrost ecosystem. *Atmos. Chem. Phys.*, **19**, 4041–4059, <https://doi.org/10.5194/acp-19-4041-2019>.

- Schipper, L. A., J. K. Hobbs, S. Rutledge, and V. L. Arcus, 2014: Thermodynamic theory explains the temperature optima of soil microbial processes and high Q10 values at low temperatures. *Global Change Biol.*, **20**, 3578–3586, <https://doi.org/10.1111/gcb.12596>.
- Schrier-Uijl, A. P., P. S. Kroon, A. Hensen, P. A. Leffelaar, F. Berendse, and E. M. Veenendaal, 2010: Comparison of chamber and eddy covariance-based CO₂ and CH₄ emission estimates in a heterogeneous grass ecosystem on peat. *Agric. For. Meteorol.*, **150**, 825–831, <https://doi.org/10.1016/j.agrformet.2009.11.007>.
- Shoemaker, J. K., T. F. Keenan, D. Y. Hollinger, and A. D. Richardson, 2014: Forest ecosystem changes from annual methane source to sink depending on late summer water balance. *Geophys. Res. Lett.*, **41**, 673–679, <https://doi.org/10.1002/2013GL058691>.
- Shurpali, N. J., and S. B. Verma, 1998: Micrometeorological measurements of methane flux in a Minnesota peatland during two growing seasons. *Biogeochemistry*, **40**, 1–15, <https://doi.org/10.1023/A:1005875307146>.
- Stoy, P. C., G. G. Katul, M. B. S. Siqueira, J.-Y. Juang, H. R. McCarthy, H.-S. Kim, A. C. Oishi, and R. Oren, 2005: Variability in net ecosystem exchange from hourly to inter-annual time scales at adjacent pine and hardwood forests: A wavelet analysis. *Tree Physiol.*, **25**, 887–902, <https://doi.org/10.1093/treephys/25.7.887>.
- Sturtevant, C., B. L. Ruddell, S. H. Knox, J. Verfaillie, J. H. Matthes, P. Y. Oikawa, and D. Baldocchi, 2016: Identifying scale-emergent, nonlinear, asynchronous processes of wetland methane exchange. *J. Geophys. Res. Biogeosci.*, **121**, 188–204, <https://doi.org/10.1002/2015JG003054>.
- Torrence, C., and G. P. Compo, 1998: A practical guide to wavelet analysis. *Bull. Amer. Meteor. Soc.*, **79**, 61–78, [https://doi.org/10.1175/1520-0477\(1998\)079<0061:APGTWA>2.0.CO;2](https://doi.org/10.1175/1520-0477(1998)079<0061:APGTWA>2.0.CO;2).
- Tramontana, G., and Coauthors, 2016: Predicting carbon dioxide and energy fluxes across global FLUXNET sites with regression algorithms. *Biogeosciences*, **13**, 4291–4313, <https://doi.org/10.5194/bg-13-4291-2016>.
- Treat, C. C., J. L. Bubier, R. K. Varner, and P. M. Crill, 2007: Timescale dependence of environmental and plant-mediated controls on CH₄ flux in a temperate fen. *J. Geophys. Res.*, **112**, G01014, <https://doi.org/10.1029/2006JG000210>.
- , and Coauthors, 2018a: Tundra landscape heterogeneity, not interannual variability, controls the decadal regional carbon balance in the western Russian Arctic. *Global Change Biol.*, **24**, 5188–5204, <https://doi.org/10.1111/gcb.14421>.
- , A. A. Bloom, and M. E. Marushchak, 2018b: Non-growing season methane emissions—A significant component of annual emissions across northern ecosystems. *Global Change Biol.*, **24**, 3331–3343, <https://doi.org/10.1111/gcb.14137>.
- Tuovinen, J.-P., and Coauthors, 2019: Interpreting eddy covariance data from heterogeneous Siberian tundra: Land-cover-specific methane fluxes and spatial representativeness. *Biogeosciences*, **16**, 255–274, <https://doi.org/10.5194/bg-16-255-2019>.
- Turetsky, M. R., and Coauthors, 2014: A synthesis of methane emissions from 71 northern, temperate, and subtropical wetlands. *Global Change Biol.*, **20**, 2183–2197, <https://doi.org/10.1111/gcb.12580>.
- Turner, A. J., C. Frankenberg, and E. A. Kort, 2019: Interpreting contemporary trends in atmospheric methane. *Proc. Natl. Acad. Sci. USA*, **116**, 2805–2813, <https://doi.org/10.1073/pnas.1814297116>.
- Vargas, R., D. D. Baldocchi, M. Bahn, P. J. Hanson, K. P. Hosman, L. Kulmala, J. Pumpanen, and B. Yang, 2011: On the multi-temporal correlation between photosynthesis and soil CO₂ efflux: Reconciling lags and observations. *New Phytol.*, **191**, 1006–1017, <https://doi.org/10.1111/j.1469-8137.2011.03771.x>.
- Verma, S. B., F. G. Ullman, D. Billesbach, R. J. Clement, J. Kim, and E. S. Verry, 1992: Eddy correlation measurements of methane flux in a northern peatland ecosystem. *Bound.-Layer Meteorol.*, **58**, 289–304, <https://doi.org/10.1007/BF02033829>.
- Villarreal, S., M. Guevara, D. Alcaraz-Segura, N. A. Brunsell, D. Hayes, H. W. Loescher, and R. Vargas, 2018: Ecosystem functional diversity and the representativeness of environmental networks across the conterminous United States. *Agric. For. Meteorol.*, **262**, 423–433, <https://doi.org/10.1016/j.agrformet.2018.07.016>.
- Vitale, D., M. Bilancia, and D. Papale, 2019: A multiple imputation strategy for eddy covariance data. *J. Environ. Inform.*, **34**, 68–87, <https://doi.org/10.3808/jei.201800391>.
- Vuichard, N., and D. Papale, 2015: Filling the gaps in meteorological continuous data measured at FLUXNET sites with ERA-Interim reanalysis. *Earth Syst. Sci. Data*, **7**, 157–171, <https://doi.org/10.5194/essd-7-157-2015>.
- Wahlen, M., 1993: The global methane cycle. *Annu. Rev. Earth Planet. Sci.*, **21**, 407–426, <https://doi.org/10.1146/annurev.ea.21.050193.002203>.
- Windham-Myers, L., B. Bergamaschi, F. Anderson, S. Knox, R. Miller, and R. Fujii, 2018: Potential for negative emissions of greenhouse gases (CO₂, CH₄ and N₂O) through coastal peatland re-establishment: Novel insights from high frequency flux data at meter and kilometer scales. *Environ. Res. Lett.*, **13**, 045005, <https://doi.org/10.1088/1748-9326/aaae74>.

Conclusions

This work aimed to directly evaluate CH₄ emissions from different environments that characterize the whole territory of the Campania region (Southern Italy) by using different measurement approaches, in order to provide validation data for models as well as for national emission inventories.

A small research aircraft, the Sky Arrow ERA platform (see Chapter 1 for a full description) was setup and tested through several observational campaigns to provide regional field scale measurements of pollutants. Bio-meteorological observations and pollutants concentrations were measured on board the aircraft: with the recorded dataset, it was possible to parameterize meteorological and chemical dispersion models at high spatial resolution over the Campania region (Chapter 2). The results show that simultaneously using model simulations and measurements, we were successfully able to reproduce the dynamics of pollutants dispersion, and to understand the processes regulating the atmospheric circulation in a study area characterized by complex orography and dynamics.

The same Sky Arrow ERA platform has then been customised in order to estimate CH₄ emissions from four different landfills, closely located among each other, over a study domain of 5x5 km between the municipality of two main cities in Campania, Naples and Caserta (see Chapter 3). For this purpose, we developed a specific airborne payload able to measure CH₄ mixing ratios and wind components at high frequencies. The data from the measurement campaigns have been used to develop and test a novel airborne mass balance approach, able to distinguish the contribution of four different sources inside the same study domain. For this purpose, we computed CH₄ mass flows in combination with simulated CH₄ emissions obtained through a steady state Gaussian dispersion model. High emissions from the entire study area were measured, with a mean value of $252.5 \pm 54.2 \text{ g s}^{-1}$, while contributions from single landfills ranged from 17.5 to $40.1 \text{ g m}^{-2} \text{ day}^{-1}$.

In order to assess the contribution to the regional CH₄ emissions of the agricultural sector, we measured CH₄ emissions at a field scale by using micrometeorological techniques (see Chapter 4). The first part of the study aimed at establishing the role of crops, and it was conducted over a cultivated field in the Campania region (Salerno

province), where half yearly crop rotation is performed. The rotation allows to investigate the mean greenhouse gases fluxes for different crops cultivated, typical of the Mediterranean basin. The cropland site (Borgo Cioffi) can be considered a representative agricultural site of this region, both for type of the crops grown and for the landscape, being located nearby a water buffalo farm, which forms an important part of the animal husbandry of the Campania region, homeland of buffalo mozzarella.

Eddy covariance fluxes of GHG (CO_2 , N_2O , CH_4) were measured over two growing seasons, during 2017 and 2018: the results showed that both crops investigated (*Lolium italicum* and *Sorghum bicolor*) acted as a source for CH_4 and N_2O , and as a sink for CO_2 . Soil emissions magnitude of CH_4 and N_2O were higher for spring-summer cultivation compared to the winter one, although it can be concluded that no significant CH_4 fluxes from the soil were recorded during both measurement campaigns; furthermore, results showed that the CO_2 uptake from *Sorghum bicolor* was nearly double compared to *Lolium italicum*.

The second part of the study involved the application of backward Lagrangian simulations (by using the WindTrax model) in order to evaluate the CH_4 emissions coming from the livestock housing located at Borgo Cioffi, nearby the eddy covariance field. A 6-months time series of wind and CH_4 concentrations measured at the eddy covariance station were used as model input. While the CH_4 emitted by the crop can be considered negligible, by contrast, the Lagrangian simulations performed showed that the buffalo farm acts as a strong source for CH_4 , with a mean value of 18.3 kg CH_4 /hr that correspond to a release of about 5 g s^{-1} . This value is lower compared to the one obtained from landfills (about 200 g s^{-1}), but considering that livestock is spread over the whole Campania region the overall emission connected to these activities could be considered a serious environmental issue.

